Photoinduced Electron Transfer Dynamics in Ruthenium(II) Bis(terpyridine) Based Molecular Dyads and Triads

Dissertation
(kumulativ)

zur Erlangung des akademischen Grades doctor rerum naturalium
(Dr. rer. nat)

vorgelegt dem Rat der Chemisch-Geowissenschaftlichen Fakultät
der Friedrich-Schiller-Universität Jena

von Master of Science Yusen Luo
geboren am 19.05.1990 in Sichuan, China

Gutachter:

1. Prof. Dr. Benjamin Dietzek, Institut für Physikalische Chemie, Friedrich-Schiller-Universität Jena
2. Prof. Dr. Oliver S. Wenger, Departement Chemie, Universität Basel
3. Prof. Dr. Inke Siewert, Institut für Anorganische Chemie, Georg-August-Universität Göttingen

Tag der öffentlichen Verteidigung: 10. Juli 2019

Table of Content

Declaration on Authorship

Erklärung zu Eigenanteilen an Publikationen und Zweitpublikationsrechten bei einer kumulativen Dissertation

Für alle in dieser kumulativen Dissertation verwendeten Manuskripte liegen die notwendigen Genehmigungen der Verlage („Reprint permissions“) für die Zweitpublikation vor.

Die Co-Autoren der in dieser kumulativen Dissertation verwendeten Manuskripte sind sowohl über die Nutzung, als auch auf den folgenden Seiten Eigenanteile der weiteren Doktoranden/Doktorandinnen als Koautoren an den Publikationen und Zweitpublikationsrechten bei einer kumulativen Dissertation informiert und stimmen dem zu.

Die Anteile der Co-Autoren an den Publikationen sind in der Anlage aufgeführt.

Yusen Luo den Jena

…………………...

Ich bin mit der Abfassung der Dissertation als publikationsbasiert, d.h. kumulativ, einverstanden und bestätige die oben und auf den folgenden Seiten gegebenen Angaben. Eine entsprechend begründete Befürwortung mit Angabe des wissenschaftlichen Anteils des Doktoranden/der Doktorandin an den verwendeten Publikationen werde ich parallel an den Rat der Fakultät der Chemisch-Geowissenschaftlichen Fakultät richten.

Prof. Dr. Benjamin Dietzek den Jena

…………………..

[**P1**] Energy versus Electron Transfer: Controlling the Excitation Transfer in Molecular Triads.

Yusen Luo, Kevin Barthelmes, Maria Wächtler, Andreas Winter, Ulrich S. Schubert and Benjamin Dietzek
Chem. Eur. J., **2017**, *23*, 4917–4922.

Authors	YL	KB	MW	AW	USS	BD
Concept development		√		√	√	√
Synthesis		√				
Characterization	√					
Data analysis and processing	√					
Data interpretation	√		√			√
Preparation of the manuscript	√					√
Revision of the manuscript	√	√	√	√	√	√
Supervision of YL			√			√
Proposed publication equivalents	1.0					

[**P2**] Direct Detection of the Photoinduced Charge-Separated State in a Ru(II) Bis(terpyridine)–Polyoxometalate Molecular Dyad.

Yusen Luo, Maria Wächtler, Kevin Barthelmes, Andreas Winter, Ulrich S. Schubert and Benjamin Dietzek
Chem. Commun., **2018**, *54*, 2970–2973.

Authors	YL	MW	KB	AW	USS	BD
Concept development	√		√	√	√	√
Synthesis			√			
Characterization	√					
Data analysis and processing	√					
Data interpretation	√	√				√
Preparation of the manuscript	√					√
Revision of the manuscript	√	√	√	√	√	√
Supervision of YL		√				√
Proposed publication equivalents	1.0					

[**P3**] Coexistence of Distinct Intramolecular Electron Transfer Pathways in Polyoxometalate Based Molecular Triads.

Yusen Luo, Maria Wächtler, Kevin Barthelmes, Andreas Winter, Ulrich S. Schubert and Benjamin Dietzek
Phys. Chem. Chem. Phys., **2018**, *20*, 11740–11748.

Authors	YL	MW	KB	AW	USS	BD
Concept development	√		√	√	√	√
Synthesis			√			
Characterization	√					
Data analysis and processing	√					
Data interpretation	√	√				√
Preparation of the manuscript	√					√
Revision of the manuscript	√	√	√	√	√	√
Supervision of YL		√				√
Proposed publication equivalents	1.0					

[**P4**] Increased Charge Separation Rates with Increasing Donor-Acceptor Distance in Molecular Triads: The Effect of Solvent Polarity.

Yusen Luo, Kevin Barthelmes, Maria Wächtler, Andreas Winter, Ulrich S. Schubert and Benjamin Dietzek
J. Phys. Chem. C, **2017**, *121*, 9220−9229.

Authors	YL	KB	MW	AW	USS	BD
Concept development	√		√			√
Synthesis		√				
Characterization	√					
Data analysis and processing	√					
Data interpretation	√	√				√
Preparation of the manuscript	√					√
Revision of the manuscript	√	√	√	√	√	√
Supervision of YL			√			√
Proposed publication equivalents	1.0					

[**P5**] Superexchange on the Fast Lane – Intramolecular Electron Transfer in a Molecular Triad Occurs by Conformationally-Gated Superexchange.

Yusen Luo, Maria Wächtler, Kevin Barthelmes, Andreas Winter, Ulrich S. Schubert and Benjamin Dietzek

Chem. Commun., *Submitted.*

Chem. Commun., **2019**, *55,* 5251−5254.(Updated)

Authors	YL	MW	KB	AW	USS	BD
Concept development	√	√				√
Synthesis			√			
Characterization	√					
Data analysis and processing	√					
Data interpretation	√	√				√
Preparation of the manuscript	√					√
Revision of the manuscript	√	√	√	√	√	√
Supervision of YL		√				√
Proposed publication equivalents	1.0					

[**P6**] Remote Control of Electronic Coupling – Modification of Excited-State Electron Transfer Rates in Ru(tpy)$_2$-Based Donor-Acceptor Systems by Remote Ligand Design.

Yusen Luo, Jens H. Tran, Maria Wächtler, Martin Schulz, Kevin Barthelmes, Andreas Winter, Sven Rau, Ulrich S. Schubert and Benjamin Dietzek

Chem. Commun., **2019**, *55*, 2273−2276.

Authors	YL	JHT	MW	MS	KB	AW	SR	USS	BD
Concept development	√						√		√
Synthesis		√			√				
Characterization	√	√							
Data analysis and processing	√								
Data interpretation	√		√	√			√		√
Preparation of the manuscript	√	√							√
Revision of the manuscript	√	√	√	√	√	√	√	√	√
Supervision of YL			√						√
Proposed publication equivalents	1.0								

List of Abbreviations

Chemical terms

Ru	ruthenium
tpy	2, 2′:6′, 2″-terpyridine
PTZ	*N*-methylphenothiazine
exTTF	*p*-extended tetrathiafulvalene
C_{60}	*N*-methylfulleropyrrolidine
POM	polyoxometalate
PTZ–tpy	the terpyridine ligand connected with *N*-methylphenothiazine
exTTF–tpy	the terpyridine ligand connected with *p*-extended tetrathiafulvalene
tpy–C_{60}	the terpyridine ligand connected with *N*-methylfulleropyrrolidine
tpy–POM	the terpyridine ligand connected with polyoxometalate
ACN	acetonitrile
DCM	dichloromethane
DMF	*N,N*-dimethylformamid
DMSO	dimethyl sulfoxide

Methods and potophysical terms

UV	ultraviolet
Vis	visible
fs	femtosecond
ns	nanosecond
TA	transient absorption
RR	resonance Raman
SEC	spectroelectrochemistry
GSB	ground-state bleach

ESA	excited-state absorption
DAS	decay-associated spectra
OD	optical density
^{1}MLCT	singlet metal-to-ligand charge transfer
^{3}MLCT	triplet metal-to-ligand charge transfer
ET1	the first electron transfer step
ET2	the second electron transfer step
CSS	charge-separated state
CR	charge recombination
EnT	energy transfer
R_{DA}	donor-acceptor distance
λ	reorganization energy
H_{DA}	electronic coupling between donor and acceptor
$-\Delta G$	driving force for electron transfer
$\Delta G^{\ddagger}$	activation energy for electron transfer

1. Introduction

Because of the limited storage of fossil fuels and the long-term effects of burning them on the environment such as global warming and air pollution, development of clean and renewable energy is highly demanded.[1-3] Since solar radiation is the largest renewable energy source on earth, artificial photosynthesis, mimicking the natural photosynthesis to convert sunlight into chemical energies, has attracted extensive attention in the last two decades.[4-8] Learned from nature, the fundamental processes, *i.e.* light harvesting and electron transfer, should be integrated into the artificial systems. In this respect, multifunctional molecular assemblies which contain electron donors (D) and electron acceptors (A) have been constructed. Different to the noncovalent D/A assemblies, in which the intermolecular electron transfer rates might be limited by diffusion,[9,10] covalently linked D and A *via* molecular spacers have attracted remarkable interest (Figure 1.1a, a typical dyad structure).[11-15] These covalently linked D–A systems allow for tuning electron transfer dynamics at the molecular level, which on the other hand, serve as simple models for us to understand how electron transfer depends on the molecular structures. To achieve efficient solar-to-chemical energy conversion, the charge-separated states (CSS) should be efficiently generated and long-lived to react with external reactants (*e.g.* light-driving water splitting[16,17] and photochemical carbon dioxide reduction[18,19]) or to be transported into an external circuit (*e.g.* dye-sensitized solar cells[20,21]). However, compared to the natural photosynthesis, the efficiencies of charge separation in artificial (supra)molecular systems are generally low due to the existence of *e.g.* competitive decay pathways of the excited molecules and/or faster recombination rates of $D^{\bullet+}$ and $A^{\bullet-}$ pairs.[11-15,22]

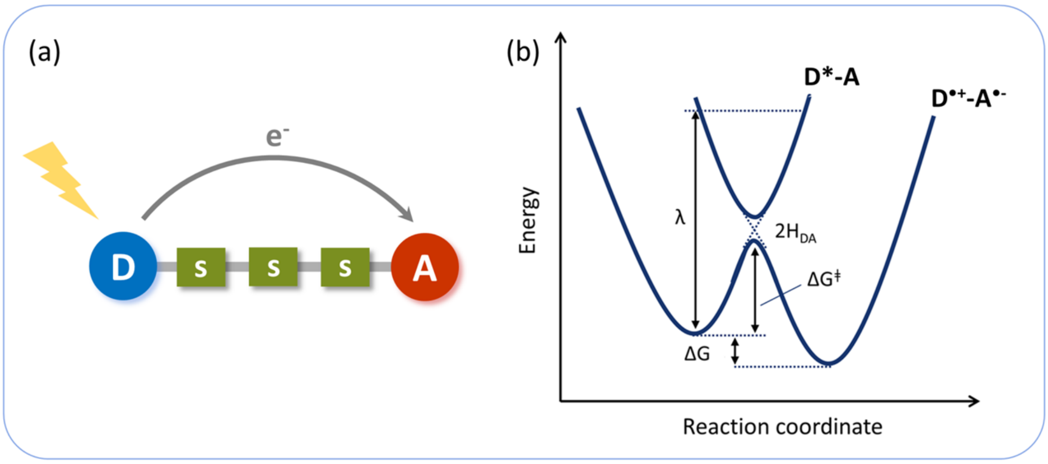

Figure 1.1. (a) Schematic representation of a typical molecular dyad structure contains an electron donor and an electron acceptor connected by molecular spacers (S). Upon excitation of the donor

electron transfer occurs. (b) The harmonic potential energy of the reactant (D*–A) and product states ($D^{\bullet+}$–$A^{\bullet-}$) for photoinduced electron transfer according to the Marcus theory.[23]

In order to optimize the artificial (supra)molecular systems for efficient solar-to-energy conversion, an in-depth understanding of how molecular structures influencing electron transfer rates is crucial. The correlation between electron transfer rates and the thermodynamic parameters is well-described by Marcus theory[23] (potential wells of the reactant (D*–A) and product ($D^{\bullet+}$–$A^{\bullet-}$) states for electron transfer see Figure 1.1b) which allows quantitative interpretation of the rate constants. That is, electron transfer rate (k_{ET}) is governed by reorganization energy (λ), electronic coupling (H_{DA}) and free energy change associated with electron transfer (*i.e.* driving force, –ΔG, usually written in this form to show a positive value):[5,11,13,14,23]

$$k_{ET} = \sqrt{\frac{\pi}{\hbar^2 \cdot \lambda \cdot k_B \cdot T}} \cdot |H_{DA}|^2 \cdot \exp\left(-\frac{(\lambda + \Delta G)^2}{4 \cdot \lambda \cdot k_B \cdot T}\right) \qquad (1)$$

where ħ is the reduced Plank constant, k_B is the Boltzmann constant and T is temperature. Therefore, the Marcus equation (eq 1) can be a valuable guide for the rational design of artificial (supra)molecular assemblies. To this end, it is necessary to understand how the molecular structure influences the three central parameters, λ, H_{DA} and –ΔG, which in turn determine k_{ET}.

1.1. Quantification of the Marcus' parameters

The driving force, –ΔG, can be estimated from electrochemical data according to the generally used form of Rehm-Weller equation:[9]

$$\Delta G = e\,(E_{D^+/D} - E_{A/A^-}) - E_{00} - \frac{e^2}{4\pi\varepsilon_0 \varepsilon R_{DA}} \qquad (2)$$

where $E_{D^+/D}$ and E_{A/A^-} represent the one-electron oxidation and reduction potential of D and A, respectively. E_{00} is the energy difference between the excited state (where the electron transfer takes place) and ground state. R_{DA} represents the D–A distance. In high polar solvents the last term in eq 2 is often neglected.[24,25] Thus, –ΔG is mainly determined by the nature of D and A. When turning to the reorganization energy λ, the Marcus dielectric continuum model indicates that the overall λ consists of inner-sphere (λ_i) and outer-sphere (λ_o) contributions (eq 3).[5,23,24,26,27] The latter inflects the energy necessary for the reorganization of the surrounding chemical environment (*e.g.* solvent molecules and counter-ions, eq 4) while the former represents the free energy change associated with the nuclear bond length changes within the reactant molecules.[5,26,27]

$$\lambda = \lambda_i + \lambda_o \tag{3}$$

$$\lambda_o = \frac{e^2}{4 \cdot \pi \cdot \varepsilon_0} \cdot \left(\frac{1}{2a_1} + \frac{1}{2a_2} - \frac{1}{R_{DA}}\right) \cdot \left(\frac{1}{n^2} - \frac{1}{\varepsilon_s}\right) \tag{4}$$

in the simplest model, D and A are treated as spheres with radius a_1 and a_2 (for more accurate prediction, D and A should be treated as ellipsoids[27]). a_1, a_2 and R_{DA} can be estimated from the optimized molecular structure. ε_0, n and ε_s are vacuum permittivity, refractive index and dielectric constant of the solvent, respectively. In general, λ_i is estimated to be 0.1–0.2 eV for large π-conjugated systems[27,28] and is treated as distance independent.[27] While λ_o depends strongly on solvent polarity, the size of D and A as well as the D–A distance. In a word, the nature of D and A, D–A distance and solvent polarity have significant effects on λ and –ΔG, and therefore k_{ET}.

H_{DA} cannot be easily estimated like λ and –ΔG described above. Conventionally, after acquiring the latter two parameters (based on eq 2–4) as well as k_{ET} from the time-resolved spectroscopy, H_{DA} values are extracted from eq 1. So far, the nature of D and A, the structure of the molecular spacer[29-34] and the molecular conformation[35,36] have been shown to drastically change H_{DA}: H_{DA} generally decreases with increasing R_{DA}[5,11,13,29,30]; The substituents on the spacer were found to change H_{DA} considerably. For example, Wenger and coworkers reported two dyads which have the same D, A and the same length of the molecular spacer, *i.e.* five repetitive *p*-xylene units.[33] Upon replacing the two $-CH_3$ groups on the middle ring by two $-OCH_3$ groups the hole transfer rate was found to be 55 times faster than the dyad with pure $-CH_3$ substituents.[33] It was ascribed to the significantly enhanced H_{DA} by the two $-OCH_3$ substituents on the molecular spacer.[33] As for the molecular conformation effect, Albinsson and coworkers reported on a (Zinc porphyrin)$_2$–fullerene (ZnP_2–C_{60}) dyad that electron transfer rate in perpendicular conformer was 10 times faster than that in planar conformer of the excited ZnP_2.[35] This was also attributed to the distinct H_{DA} in the two conformers.[35]

Considering the synergistic effects of the three Marcus parameters, studies pointed out that for two D–A systems with comparable H_{DA} and similar –ΔG for charge separation and charge recombination, the magnitude of λ is the pivotal parameter to determine k_{ET}.[5,37] As shown in Figure 1.2, for a small λ value, charge separation takes place close to the top region (where the electron transfer rate reaches a maximum) of the Marcus parabola meanwhile pushes the charge-recombination process into the deep Marcus inverted region leading to a relatively slow backward electron transfer.[5,37] On the contrary, a larger λ results in a much slower forward electron transfer rate which in turn decreases the charge-separation efficiency. In the meantime, the backward electron transfer is accelerated which shortens the lifetime of CSS. Hence, to achieve fast charge separation and slow charge recombination, small λ values of D–A systems are targeted.[5,37] To this end, structural rigid D, A as well as molecular spacers should be considered for constructing D–A assemblies.[5,37]

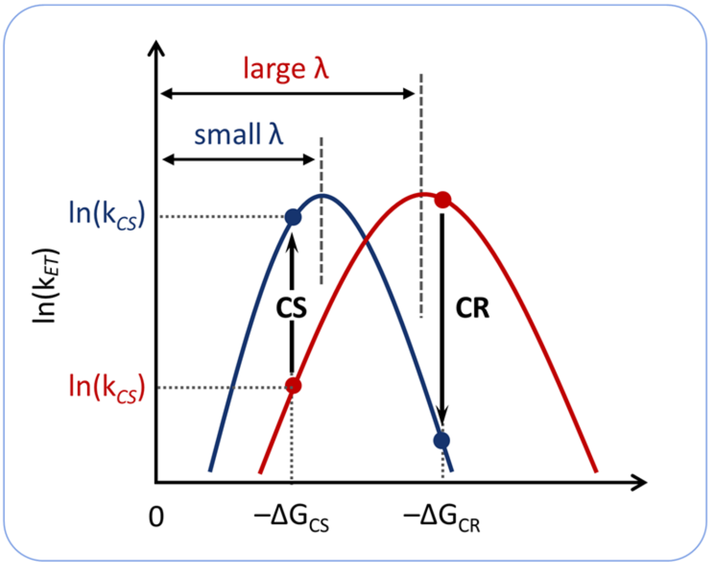

Figure 1.2. Driving force (–ΔG) dependence of ln(k_{ET}) with two distinct λ values, which was plotted by referring to ref 5 and 37. CS and CR represent charge separation and charge recombination, respectively.

1.2. The study of electron transfer mechanisms

Electron donors, *e.g.* porphyrin,[38,39] ferrocene,[40,41] π-extended tetrathiafulvalene (exTTF)[42,43] and phenothiazine (PTZ),[44,45] and electron acceptors, *e.g.* porphyrin,[28,46] perylene,[47,48] fullerene[44,49,50] and polyoxometalate (POM)[51,52] are frequently used in building D–A assemblies because of their good redox properties and relatively rigid structures. π-conjugated molecular spacers, *e.g.* oligo-*p*-phenylene (OP), oligo-*p*-phenyleneethenylene (OPE), oligo-*p*-phenylenevinylenes (OPV), oligo-thiophenes (OTP) and oligo-fluorene (OFL) are generally used to connect D and A.[5,53,54] The rigid structures of the π-conjugated molecular spacers not only yield small λ values but also can avoid the folded conformation of $D^{•+}$–$A^{•-}$ which would accelerate the charge-recombination process.[55-57] Concerning electron transfer through molecular spacers, both experimental and theoretical studies have indicated that either coherent superexchange or incoherent hopping is operative (Figure 1.3a, b).[11,13,14,53] Electron transfer *via* superexchange has to tunnel in one single step through the barrier imposed by the molecular spacers, and thus, no spacer-localized intermediate CSS can be formed even transiently (Figure 1.3a).[11,13,53] On the contrary, for hopping, the electron can be stepwise transported from D to A *via* the molecular spacers (Figure 1.3b).[11,13,53] The specific way of electron transfer is determined by the energy difference ΔE between the transition state (*i.e.* the crossing point of the two potential wells in Figure 1.1b) and the minimum of the spacer potential well (not shown in Figure 1.1b).[11,53] Due to the fact that ΔE is not readily quantifiable from the experiment, it is common to approximate ΔE as ΔE_{DB} (Figure 1.3a, b) which is the redox potential difference between the donor and spacer moieties (this can be estimated by electrochemistry).[13,14,58] When the energy of the spacer states is much higher than the donor state (*i.e.* large ΔE_{DB}, Figure 1.3a) coherent superexchange is operative. Typically, for superexchange H_{DA} decays exponentially with distance R_{DA}:

$$\mathrm{H_{DA}} = \mathrm{H_0} \cdot \exp(-\frac{\beta}{2} \cdot \mathrm{R_{DA}}) \qquad (5)$$

where H_0 represents the electronic coupling at van der Waals contact distance.[27,60] Combining eq 5 and eq 1, electron transfer rates *via* superexchange show exponential distance dependence as well:

$$\mathrm{k}_{ET} = \mathrm{k_0} \cdot e^{-\beta \cdot \mathrm{R_{DA}}} \qquad (6)$$

β is the attenuation factor. Hopping, on the other hand, requires the energy of the spacer states similar or lower than the donor state (*i.e.* small ΔE_{DB}, Figure 1.3b). This can be achieved by either extending the π-conjugation of the molecular spacer or by proper electronic substitution on it.[13,53] As a result, the molecular spacer becomes accessible for accepting an electron and spacer-localized intermediate CSS is generated. The incoherent hopping mechanism is reported to display a shallow distance dependence of electron transfer rates:[11,59]

$$\mathrm{k}_{ET} \propto \mathrm{N}^{-n} \ (n = 1\text{–}2) \qquad (7)$$

N is the number of subunits in a molecular spacer. Empirically, distance-dependent electron transfer rates, *i.e.* $\ln k_{ET}$ *vs.* R_{DA}, are often studied and the observed small β values (< 0.2 Å^{-1}) are attributed to predominant contributions from the hopping mechanism.[11,13,14,53] However, recent studies showed that differentiating electron transfer mechanisms by the magnitude of β-value may lead to misconceptions:[60,61] For example, Wasielewski and coworkers obtained a β-value of 0.34 Å^{-1} in 3,5-dimethyl-4-(9-anthracenyl) julolidine–fluorenone–naphthalene system at room temperature and a spacer-localized intermediate CSS was spectroscopically identified.[60] Thus, electron transfer by hopping was operative despite a relative high β-value (0.34 $Å^{-1}$).[60]

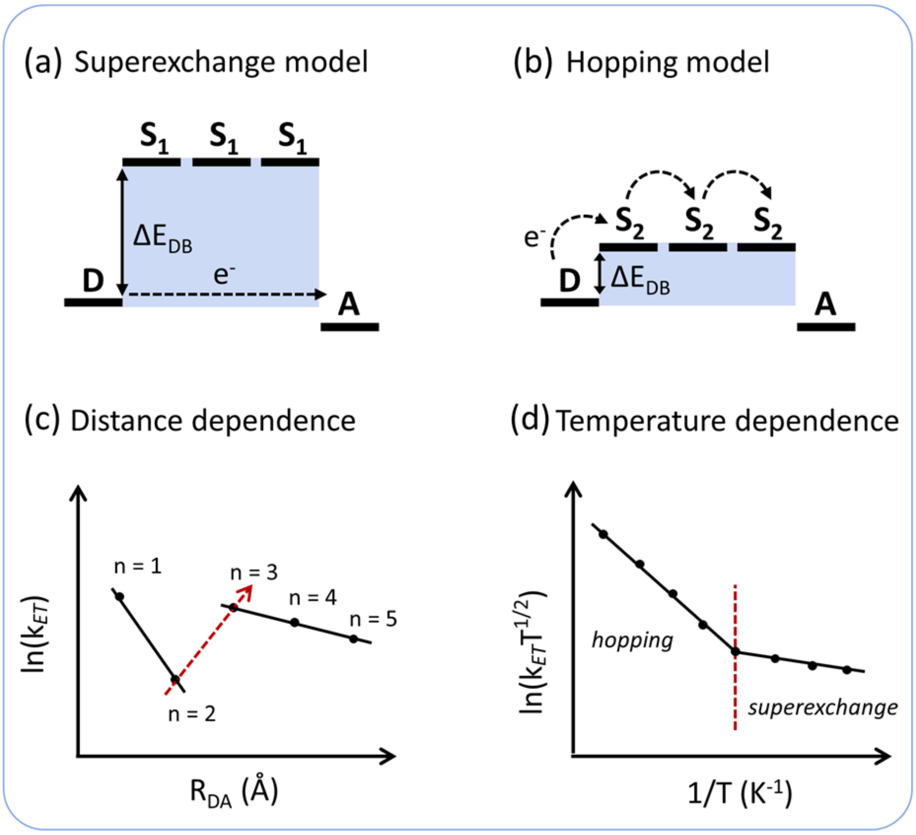

Figure 1.3. Exemplary illustration of the (a) coherent superexchange and (b) incoherent hopping mechanisms for electron transfer in D–A assemblies which contain three identical spacer fragments.[11,13,53] S_1 and S_2 represent two different molecular spacers which have different energetic levels. (c, d) Methods used in literature to understand the electron transfer mechanisms by studying the (c) distance dependent and (d) temperature dependent k_{ET}.

Considering the electron transfer mechanism for a specific D–A system, hopping is generally more efficient than superexchange at larger R_{DA} (eq 7 *vs.* eq 6, respectively). As a result, the appearance of slopes change at larger R_{DA} when studying $\ln k_{ET}$ *vs.* R_{DA} may imply a mechanism switch from superexchange to hopping.[62-70] For example, Wasielewki and coworkers reported TET–PPV_n–PI triads (n = 1–5, TET, PPV and PI represents tetracene, *p*-phenylenevinylene and pyromellitimide, respectively) which displayed a sharp increase of electron transfer rate from TET–PPV_2–PI to TET–PPV_3–PI (exemplarily shown in Figure 1.3c).[62] The resultant slopes change of the linear fit (according to eq 6) was rationalized by a mechanism transition from superexchange to hopping.[62] This conclusion was supported by the small energy gaps between the donor and spacer LUMOs when lengthening the spacer from TET–PPV_3–PI to TET–PPV_5–PI.[62]

Another approach to understand the electron transfer mechanisms is to investigate the temperature dependence of k_{ET} as reported in few studies.[61,71-75] In doing so, the Marcus equation (eq 1) is used in the following form:[61,71-75]

$$\ln(k_{ET} \cdot T^{\frac{1}{2}}) = \ln\left(\sqrt{\frac{\pi}{\hbar^2 \cdot \lambda \cdot k_B}} \cdot |H_{DA}|^2\right) - \frac{(\lambda + \Delta G)^2}{4 \cdot \lambda \cdot k_B \cdot T} \qquad (8)$$

$\ln(k_{ET}\cdot T^{1/2})$ *vs.* 1/T yields a single linear relationship. λ and H_{DA} can be extracted from the slope ($-\Delta G$ is estimated from the electrochemical data according to the Rehm-Weller equation, eq 2) and the intercept, respectively. According to the literature, a change in electron transfer mechanism would lead to deviations from the linearity when plotting $\ln(k_{ET}\cdot T^{1/2})$ *vs.* 1/T and hopping is considered to have stronger temperature dependence than superexchange (see Figure 1.3d).[61,71-75] For example, Guldi and coworkers reported a triad system containing an exTTF electron donor and a C_{60} electron acceptor connected by OPV spacer.[73] Plotting $\ln(k_{CR}\cdot T^{1/2})$ *vs.* 1/T yields two distinct sections in the temperature region of 350–272 K. The weaker temperature dependence of $\ln(k_{CR}\cdot T^{1/2})$ at 320–272 K suggested a superexchange mechanism being operative while the stronger temperature dependence of $\ln(k_{CR}\cdot T^{1/2})$ at 350–320 K indicated a thermally activated hopping mechanism to be dominant.[73] However, such analysis has to be conducted with care as temperature-induced changes in solvent's dielectric properties might cause λ, H_{DA} and $-\Delta G$ to become temperature-dependent quantities.[13,76,77] Considering this, Wasielewski pointed out that a positive activation cannot exclusively indicate a hopping mechanism while less activated behavior (*i.e.* flat slopes) alone cannot be conclusively attributed to superexchange.[77] Nonetheless, literature on quantitative analysis of the Marcus' parameters has concluded that electron transfer *via* hopping has stronger temperature dependence than electron transfer *via* superexchange.[61,71-75]

1.3. The work in this thesis

The thesis presents a fundamental research on molecular dyads and triads in which the photoinduced electron transfer dynamics is studied. The purpose of this work is to systemically study: 1) the influence of various factors such as the nature of D and A, D–A distance and solvent polarity on k_{ET}; 2) the mechanism of electron transfer, *i.e.* superexchange or hopping; 3) the influence of molecular structure on electronic coupling H_{DA} (which is an important factor controlling k_{ET} but less understood). In doing so, the well-studied *N*-methylphenothiazine (PTZ)[44,45] and π-extended tetrathiafulvalene (exTTF)[42,43] were chosen as electron donors and *N*-methylfulleropyrrolidine (C_{60})[44,49,50] and polyoxometalate (POM)[51,52] were used as electron acceptors. C_{60} and POM are ideal electron acceptors because both of them can store several electrons with very small structural change, *i.e.* small λ.[44,49-52] In addition, the reduced POM was found to be efficient photo-/electro-catalysts for proton reduction.[51,52] Considering all these selected D and A barely absorb the visible light, the incorporation of a photosensitizer is necessary to improve the absorption of solar irradiation.

Light harvesting is the "starting point" of any photochemical reactions and needs to be properly designed: With more light is absorbed the more charges are likely to be separated and consequently higher light-to-energy conversion efficiencies could be achieved.[5] In this respect, photoactive transition metal-polypyridyl complexes such as Ru(II), Os(II), Ir(III), and Cu(I) have been selected in constructing D–P–A systems.[12,78-80] The presence of metal/ligand interactions allows absorption of visible light *via* metal-to-ligand charge transfer (MLCT) transitions.[12,78-80] Due to the strong spin-orbital coupling induced by the heavy metal centers, ultrafast intersystem crossing (which usually occurs on a sub-100 fs timescale) from the singlet metal-to-ligand charge transfer (^{1}MLCT) excited state to the triplet metal-to-ligand charge transfer (^{3}MLCT) excited state was observed.[12,78-80] Thus upon excitation of the transition metal complex in D–P–A, electron transfer generally takes place from the ^{3}MLCT states leading to the CSS in triplet manifold.[44,88-90] The generated triplet CSS is longer lived than the corresponding singlet CSS, as the former has different spin multiplicities to the ground state. Another advantage of the transition metal complexes is their highly tunable optical and redox properties by changing the metal center or the functionalization of peripheral ligands.[78-80] By proper molecular design different electronic states, *e.g.* MLCT, metal-centered (MC), ligand-centered (LC), intraligand charge transfer (ILCT), ligand-to-ligand charge transfer (LLCT), with distinct reactivity can be accessed which have already shown the possibility to be used in photodynamic therapy.[81]

Until now, considerable attention has been paid to Ru(II) polypyridine due to their chemical robustness, ease of synthesis and relatively cheap starting materials.[82-85] In the family of Ru(II) polypyridine, complexes based on the tridentate ligands, *e.g.* 2,2':6',2''-terpyridine (tpy), are of particular interest due to its achiral nature and high symmetry which allows constructing linear structure without inducing geometrical and optical isomers.[82-84] Compared to another frequently used Ru photosensitizer, $[Ru(bpy)_3]^{2+}$, $[Ru(tpy)_2]^{2+}$ has relatively poor excited-state properties, *e.g.* a short excited-state lifetime of ^{3}MLCT state (τ = 0.25 ns[84] *vs.* 630 ns of $[Ru(bpy)_3]^{2+}$ in water[86]) and low quantum yield ($\leq 5 \times 10^{-6}$ *vs.* 0.062 of

$[Ru(bpy)_3]^{2+}$ at 25 °C).[84,86] This is owing to the existence of an excited-state deactivation pathway *via* the low-lying ^{3}MC state in $[Ru(tpy)_2]^{2+}$,[83,84,87] facilitating a non-radiative decay *via* the ^{3}MC state to ground state.[84] The small energy gap between ^{3}MLCT states and ^{3}MC ligand field states is due to the unfortunate bite angle of the tpy ligand which causes a distorted octahedral coordination sphere leading to weakened ligand field.[83,84,87] Prolonging the lifetimes of the ^{3}MLCT states in $[Ru(tpy)_2]^{2+}$-derived complexes has been achieved by increasing the energy gap between the ^{3}MC and ^{3}MLCT states: Either by using ligands with high ligand field strength (*e.g.* cyclometallated ligands or by substitution on tpy ligand to extend the π-conjugation) or using ligands with larger bite angles than tpy ligand.[84,87]

In this thesis, $[Ru(tpy)_2]^{2+}$ was chosen as the photosensitizer to facilitate the construction of linear molecular assemblies. The thesis will present a systematic investigation on D–Ru(tpy)$_2$–A dyads and triads that various factors such as the nature of D and A, D–A distance and solvent polarity on photoinduced electron transfer dynamics will be studied. To this end, electron donors such as PTZ and exTTF as well as electron acceptors such as C_{60} and POM were covalently linked to the 4'-position of tpy$_1$ and tpy$_2$ ligands, respectively (Figure 1.4). In the beginning of the work (**Chapter 2.1**), a model compound PTZ–Ru(tpy)$_2$–C_{60} is introduced. I will show that energy transfer (*i.e.* $PTZ\text{–}^3Ru(tpy)_2{*}\text{–}C_{60} \xrightarrow{EnT} PTZ\text{–}Ru(tpy)_2\text{–}^3C_{60}{*}$) and a two-step electron transfer (*i.e.* $PTZ\text{–}^3Ru(tpy)_2{*}\text{–}C_{60} \xrightarrow{ET1} PTZ^{\bullet+}\text{–}Ru(tpy)_2^{\bullet-}\text{–}C_{60} \xrightarrow{ET2} PTZ^{\bullet+}\text{–}Ru(tpy)_2\text{–}C_{60}^{\bullet-}$) take place upon excitation of the Ru(tpy)$_2$ photosensitizer. In general, the photochemistry of Ru(II) coordination complexes is discussed to start from the lowest thermalized ^{3}MLCT state.[88-90] However, the work here reveals that the initially populated two ^{1}MLCT excited states, instead of generating the lowest-lying ^{3}MLCT state, decay independently (*i.e. via* energy transfer and electron transfer). This observation holds true for the triad containing a different electron acceptor POM (*i.e.* PTZ–Ru(tpy)$_2$–POM, **Chapter 2.2**, Figure 1.4) and the triad containing a stronger electron donor exTTF (*i.e.* exTTF–Ru(tpy)$_2$–POM, **Chapter 2.2**, Figure 1.4).

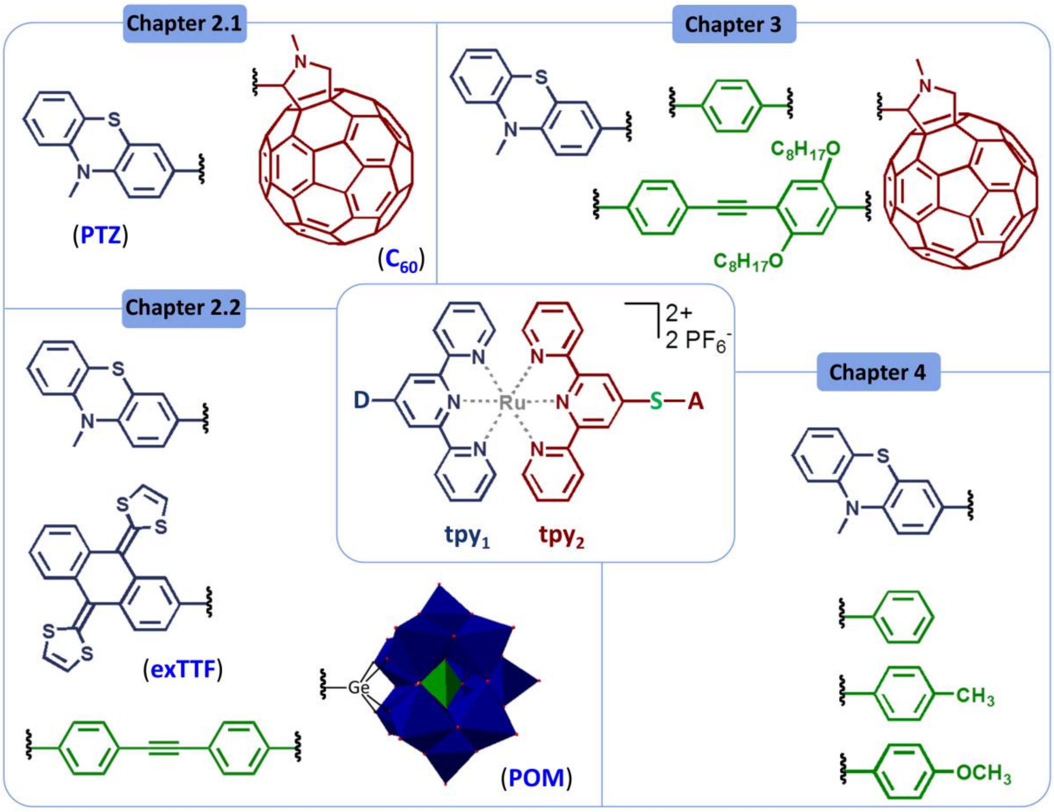

Figure 1.4. Overview of the molecular dyads and triads built on the $[Ru(tpy)_2]^{2+}$ photosensitizer in this thesis. Different colors are given to show which parts of the $[Ru(tpy)_2]^{2+}$ complex are connected to the specific molecular fragments (D, S and A).

In **Chapter 3**, the molecular structure of PTZ–Ru(tpy)$_2$–C$_{60}$ is extended by inserting two different molecular spacers between Ru(tpy)$_2$ and C$_{60}$ (Figure 1.4). The same decay pathways of the excited ^{3}MLCT states are observed in the longer triads, *i.e.* independent electron transfer (two-step) and energy transfer. The second electron transfer step (*i.e. ET2*, from Ru(tpy)$_2^{\bullet-}$ to C$_{60}$) *via* different lengths of the molecular spacer is the core of this chapter. The influence of distance and solvent polarity on the second electron transfer rates (k_{ET2}) will be evaluated. Afterwards, the underlying mechanism for *ET2* will be discussed based on the combined analysis of temperature- and distance-dependent k_{ET2}.

Chapter 4 will answer the question how the substitution pattern on the remote tpy$_2$ ligand could impact the electronic coupling between PTZ and Ru(tpy)$_2$. This remote-control effect, to the best of my knowledge, has not been explored for photoinduced excited-state electron transfer reactions. For this purpose, different substituents (*i.e.* –ph, –ph–CH$_3$ and –ph–OCH$_3$, Figure 1.4) were attached to the 4'-position of the tpy$_2$ ligand. The PTZ→^{3}Ru(tpy)$_2$* electron transfer will be studied as a function of temperature for differently substituted PTZ–Ru(tpy)$_2$ dyads and PTZ–Ru(tpy)$_2$–C$_{60}$ triads. All the compounds studied in this chapter have the same

D, D–A linkage and D–A distance. I will show that with a constant driving force, H_{DA} between PTZ and $Ru(tpy)_2$ can be significantly altered by the remote ligand design.

In short, the aim of this work is to figure out how the photoinduced electron transfer dynamics in D–$Ru(tpy)_2$–A systems can be affected by the structural variations. For this purpose several characterization techniques were used:

- fs / ns transient absorption (TA) spectroscopy.[81,87,91] The fs TA spectroscopy provides information on ultrafast photoinduced dynamics in the timescale from sub-ps to several ns. The ns TA spectroscopy characterizes the fate of a long-lived state populated upon excitation in the time range from ns to ms. To obtain the temperature dependent electron transfer rates in **Chapter 3** and **Chapter 4** a cryostat was used in the fs TA measurements.
- Spectroelectrochemistry (SEC) is a technique combining the UV/Vis absorption spectroscopy and electrochemistry.[92,93] This methodology is used to clarify the absorption features of one-electron oxidized and reduced species which can help interpret the fs / ns TA data.
- Resonance Raman (RR) spectroscopy[92,94] was utilized to characterize the electronic configurations of the ^{1}MLCT excited state which is the starting point of the photochemical reactions. RR probes dynamics in the Frank-Condon region which spans roughly the first 20 fs of the development in the excited state (*i.e.* ^{1}MLCT states herein).

2. $Ru(tpy)_2$ photosensitizer – excited state branching

Parts of this chapter are published in:

[**P1**] Y. Luo, K. Barthelmes, M. Wächtler, A. Winter, U. S. Schubert and B. Dietzek, Energy versus Electron Transfer: Controlling the Excitation Transfer in Molecular Triads. *Chem. Eur. J.*, **2017**, *23*, 4917–4922.

[**P2**] Y. Luo, M. Wächtler, K. Barthelmes, A. Winter, U. S. Schubert and B. Dietzek, Direct Detection of the Photoinduced Charge-Separated State in a Ru(II) Bis(terpyridine)–Polyoxometalate Molecular Dyad. *Chem. Commun.*, **2018**, *54*, 2970–2973.

[**P3**] Y. Luo, M. Wächtler, K. Barthelmes, A. Winter, U. S. Schubert and B. Dietzek, Coexistence of Distinct Intramolecular Electron Transfer Pathways in Polyoxometalate Based Molecular Triads. *Phys. Chem. Chem. Phys.*, **2018**, *20*, 11740–11748.

$[Ru(tpy)_2]^{2+}$ is a proper photosensitizer to construct linear D–P–A without inducing geometrical or optical isomers. Hence, a molecular dyad which contains a $[Ru(tpy)_2]^{2+}$ photosensitizer/electron donor and a *N*-methylfulleropyrrolidine (C_{60}) electron acceptor (*i.e.* $Ru(tpy)_2$–C_{60}) was previously designed and studied.[91] However, upon excitation of the ^{1}MLCT transition (λ_{ex} = 520 nm) only a fullerene triplet state ($^3C_{60}$*) was detected by fs/ns transient absorption (TA) spectroscopy.[91] The fs TA data revealed that $^3C_{60}$* was generated by triplet-triplet energy transfer from the thermalized ^{3}MLCT state.[91] In the first section of this chapter, an additional electron donor *N*-methylphenothiazine (PTZ) was incorporated into the $Ru(tpy)_2$–C_{60} dyad structure, *i.e.* triad **T1** (Scheme 2.1). The formation of a fully charge-separated state, *i.e.* $PTZ^{\bullet+}/C_{60}^{\bullet-}$ pair, is expected because the energy level of $PTZ^{\bullet+}$–$Ru(tpy)_2$ –$C_{60}^{\bullet-}$ (~1.4 eV according to the electrochemical data[95]) is lower than that of $^3C_{60}$* (1.5 eV).[44]

On the other hand, the photochemistry of Ru(II) coordination complexes is generally considered to start from the lowest ^{3}MLCT state because of the ultrafast intersystem crossing followed by rapid formation of the lowest thermalized ^{3}MLCT state.[88-90] However, for heteroleptic complexes, *e.g.* **T1**, immediately after photoexcitation the negative charges are delocalized on the two tpy ligands leading to the MLCT states into two different configurations which may have different photochemical properties. In doing so, **T1** was investigated at different excitation wavelengths by ns TA spectroscopy. To be specific, **T1** was excited at 520, 476 and 456 nm, *i.e.* throughout the MLCT band of $[Ru(tpy)_2]^{2+}$ photosensitizer, which would populate the two ^{1}MLCT states in different percentages. To provide insights into the distribution of ^{1}MLCT states over the individual coordinating ligands excitation wavelength dependent resonance Raman (RR) spectroscopy was employed. Investigation on **T1** reveals that the initially populated ^{1}MLCT states are distributed on the two differently functionalized tpy ligands. Instead of converting into the lowest-lying ^{3}MLCT state, the two distinct ^{3}MLCT states decay independently *via* electron transfer and energy transfer (*vide infra*). Namely a branching of the ^{3}MLCT states in $[Ru(tpy)_2]^{2+}$ photosensitizer is observed in **T1**.

2.1. Energy vs. electron transfer

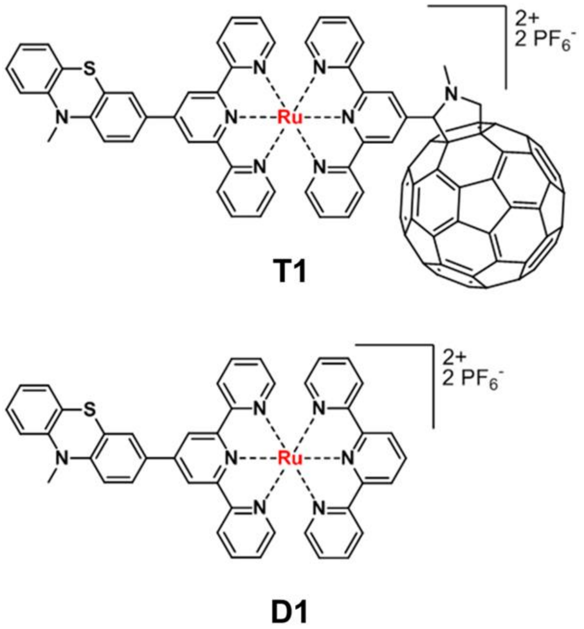

Scheme 2.1. Molecular triad **T1** and its reference dyad **D1** discussed in this section.

UV/Vis absorption and emission spectra. The UV/Vis absorption spectra of triad **T1** and dyad **D1** were collected in dichloromethane (Figure 2.1a). **D1** displays the characteristic spectral features well-known for Ru(II) polypyridyl complexes: The intense absorption bands in the UV region at 274 and 310 nm are attributed to the π-π transitions within tpy ligands and the substituent PTZ.[82-85,95] The absorption band in the visible region at 496 nm is typically for the Ru(II)-based MLCT transition.[82-85,95] **T1** exhibits stronger absorption in the wavelength range of 250–300 nm with an additional peak at 254 nm, which are attributed to the absorption of C_{60}.[95]

The interaction between ^{3}MLCT states and C_{60} are first gained from the steady-state emission spectra (Figure 2.1b): Upon excitation of ^{1}MLCT transition (λ_{ex} = 520 nm), **D1** shows a quite weak emission band at around 640 nm while the emission is totally quenched by the attachment of C_{60} which indicates the existence of additional decay channels of ^{3}MLCT states in **T1**.

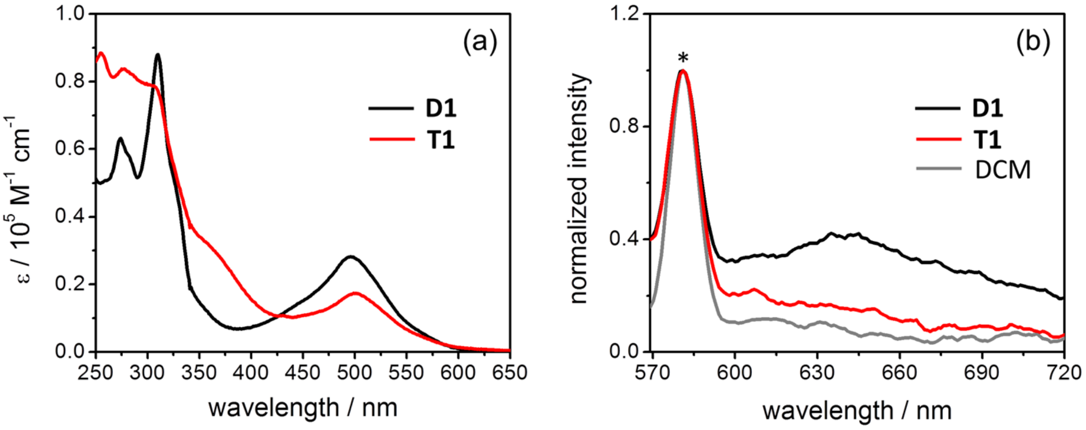

Figure 2.1. (a) UV/Vis absorption spectra and (b) emission spectra (isoabsorbing solutions at λ_{ex} = 520 nm) in aerated dichloromethane. The absorption spectra were taken from ref 95. The emission spectra were normalized to the Raman band (asterisk) of dichloromethane (DCM).

Photoinduced dynamics. The excitation wavelength-dependent photochemistry of **T1** is revealed by ns TA spectroscopy. The ns TA spectra obtained upon excitation at 520, 476 and 456 nm show two distinct excited-state absorption (ESA) bands at 590 and 700 nm (Figure 2.2a). The latter band is typical for the absorption of $^3C_{60}$* [44,91] which is supported by its extended lifetime in oxygen-free solution (320 ns in aerated solution *vs.* 1500 ns in deaerated solution, details see [**P1**]). The formation of $^3C_{60}$* is attributed to the triplet-triplet energy transfer from the ^{3}MLCT state as observed in dyad Ru(tpy)$_2$–C_{60}.[91] The band at 590 nm is assigned to the absorption of one-electron oxidized PTZ (*i.e.* PTZ$^{\bullet+}$). This is revealed by spectroelectrochemistry which displays three characteristic bands at 365, 473 and 580 nm for PTZ$^{\bullet+}$ (Figure 2.2c). The absorption of PTZ$^{\bullet+}$ at 365 nm is quite pronounced in **D1** but not in **T1** (Figure 2.2a). This is owing to the spectral overlap with the negative absorption of one-electron reduced C_{60} in the latter ($C_{60}^{\bullet-}$, Figure 2.2d). Hence, it indicates the formation of PTZ$^{\bullet+}$–Ru(tpy)$_2$–$C_{60}^{\bullet-}$ in **T1**. As a result, there are two states, *i.e.* PTZ$^{\bullet+}$–Ru(tpy)$_2$–$C_{60}^{\bullet-}$ and $^3C_{60}$*, generated in **T1** by electron transfer and energy transfer, respectively. The resultant long-lived states can also be disentangled according to their different lifetimes (Figure 2.2b, 20 *vs.* 320 ns, respectively). Notably, the relative intensities of the two ESA bands at 590 and 700 nm display strong excitation wavelength dependence (Figure 2.2a). In other words, the ratios between electron transfer and energy transfer depend on the excitation wavelengths: The absorption intensity at 590 nm, which represents the yield of PTZ$^{\bullet+}$–Ru(tpy)$_2$–$C_{60}^{\bullet-}$, decreases upon shifting the excitation to lower wavelengths (Figure 2.2a).

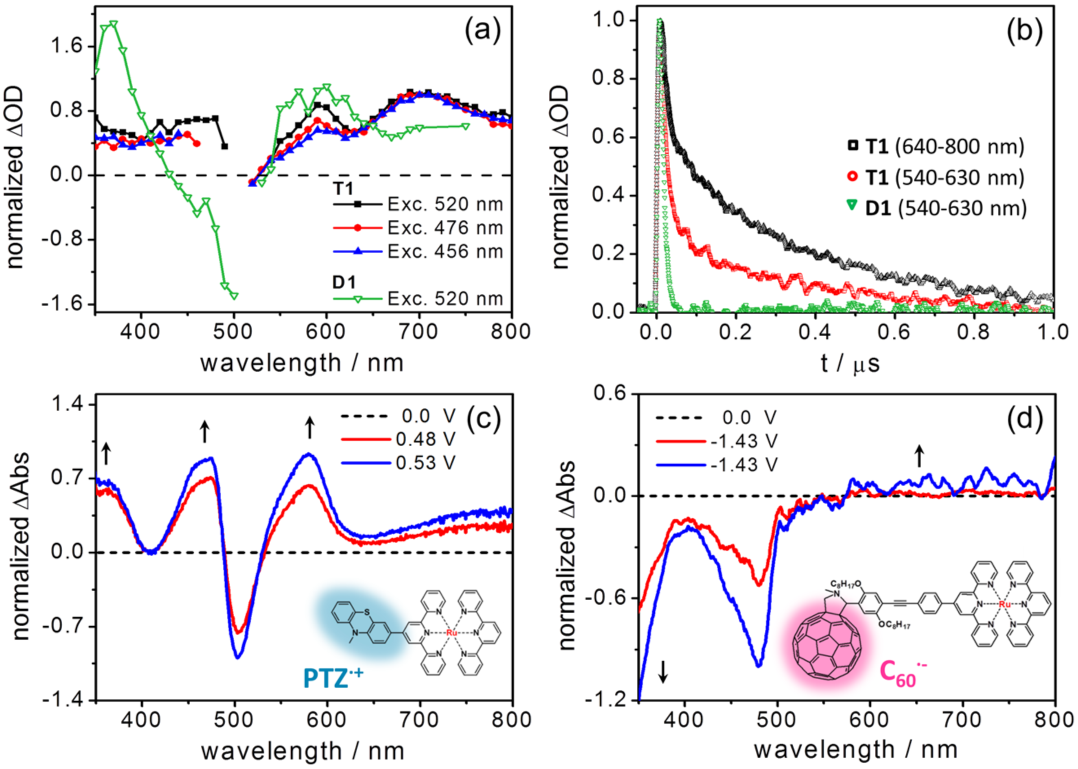

Figure 2.2. (a) Normalized TA spectra (at 700 nm) of **T1** at 15 ns upon excitation at 520, 476 and 456 nm in aerated dichloromethane. For comparison, the ns TA spectrum of **D1** at 15 ns upon excitation at 520 nm was arbitrarily scaled to fit the figure. (b) Normalized integrated kinetic traces at the spectral regions of the charge-separated state (540–630 nm) and $^{3}C_{60}$* (640–800 nm) of the ns TA data collected upon 520 nm excitation. Note: Because of the fast charge recombination of the charge-separated state in **D1**, its lifetime cannot be really determined using the time resolution (~10 ns) of the ns TA setup. (c) and (d) Normalized (by the absorption maxima at ground-state bleach, the blue one) spectroelectrochemical UV/Vis absorption difference spectra of (c) PTZ$^{\bullet+}$ and (d) $C_{60}^{\bullet-}$ in dichloromethane. Potentials are given *vs.* Fc$^{+/0}$.

To explore the origin of the excitation wavelength-dependent photochemistry, excitation wavelength-dependent RR spectra were recorded which could show how the distribution of ^{1}MLCT states changes with excitation wavelengths. In Figure 2.3a, PTZ and tpy associated bands were marked in different colors (the assignment was made based on the RR data of unsubstituted Ru(tpy)$_2$ complex[96] and *N*-methylphenothiazine[97,98]). Decreasing the excitation wavelength leads to decreased RR signals of PTZ associated bands. This means less ^{1}MLCT state distributed on the PTZ–tpy ligand (*i.e.* $^{1}\mathrm{MLCT}_{\mathrm{PTZ\text{-}tpy}}$) is populated which in turn results in a weaker PTZ$^{\bullet+}$–Ru(tpy)$_2$–$C_{60}^{\bullet-}$ associated band in ns TA spectra (Figure 2.2a and 2.3b). Combining the ns TA and RR results we conclude that the initially excited mixture of ^{1}MLCT states do not convert rapidly into the lowest-lying ^{3}MLCT state, from which a uniform photochemistry would be expected. Instead, the initially distinct ^{1}MLCT states give rise to distinct and slow photochemical response on the ns timescale.

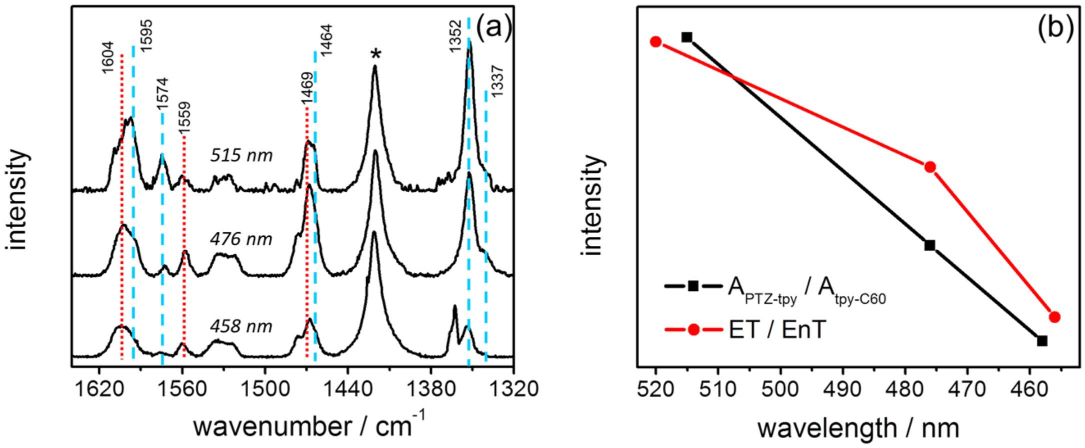

Figure 2.3. (a) Excitation wavelength-dependent resonance Raman (RR) spectra of **T1** in aerated dichloromethane. For comparison, the spectra were normalized to the solvent band at 1420 cm^{-1} (asterisk). Color code: Blue dashed line and red dotted line represents PTZ and tpy associated bands, respectively. (b) Ratios of the integrated band areas between the PTZ (namely PTZ–tpy ligand, $A_{PTZ\text{-}tpy}$) and tpy (namely tpy–C_{60} ligand, $A_{tpy\text{-}C60}$) associated RR bands as a function of excitation wavelengths (black line). The ratios between electron transfer (*ET*) and energy transfer (*EnT*) at certain excitation wavelengths are given for comparison (red line, this was obtained by comparing the integrated band area between 540–630 nm for *ET* and 630–800 nm for *EnT* shown in Figure 2.2a).

To elucidate the reason for the existence of two distinct decay pathways of the ^{3}MLCT states, the early events after photoexcitation were studied by fs TA spectroscopy. For **T1** and **D1**, the fs TA spectra (Figure 2.4a, c) at very short delay times, *e.g.* at 0.3 ps, display the typical spectral features of the ^{3}MLCT ESA of Ru(II) polypyridyl complexes: A strong ground-state bleach (GSB) at around 500 nm and two positive bands below 450 nm and above 550 nm.[87,91,99,100] At long delay times, *e.g.* at 1714 ps, consistent with the ns TA results (Figure 2.4a, at 15 ns), the fs TA spectrum of **T1** shows two distinct ESA bands at 470 and 585 nm associated with the absorption of $PTZ^{\bullet+}$ and one broad band at 700 nm related to the absorption of $^3C_{60}$* (Figure 2.4a). For **D1** at 1714 ps (Figure 2.4c), the fs TA spectrum displays two ESA bands of $PTZ^{\bullet+}$ at 365 and 590 nm which also match the ns TA spectra very well. Accordingly, the long-lived species (τ_{inf}) in decay-associated spectra (Figure 2.4b, d) represents $PTZ^{\bullet+}$–Ru(tpy)$_2$–$C_{60}^{\bullet-}$ and $^3C_{60}$* in **T1** (Figure 2.4b) and solely $PTZ^{\bullet+}$–Ru(tpy)$_2^{\bullet-}$ in **D1** (Figure 2.4d). The fastest process (τ_1 = 3 and 6 ps for **T1** and **D1**, respectively) leading to increased TA signals at 365 nm and 540–600 nm associated with the absorption of $PTZ^{\bullet+}$, and hence, is attributed to the electron transfer from PTZ to photo-oxidized Ru center. The second component (τ_2 = 20 and 515 ps for **T1** and **D1**, respectively), with typical ^{3}MLCT features, is assigned to the decay of ^{3}MLCT state either to $^3C_{60}$* state (**T1**) or to ground state (**D1**). The third component in **T1** (τ_3 = 457 ps) is characterized by decreased TA signals at 350–400 nm and above 550 nm. This is associated with the decay of the reduced tpy ligand (*i.e.* tpy$^{\bullet -}$)[99,100] in PTZ$^{\bullet +}$–Ru(tpy)$_2^{\bullet -}$–C$_{60}$. Additionally C$_{60}^{\bullet -}$ has a negative contribution below 400 nm (Figure 2.2d). Thus, τ_3 reflects electron-shifting from tpy$^{\bullet -}$ to C$_{60}$ to generate the fully charge-separated state, *i.e.* PTZ$^{\bullet +}$–Ru(tpy)$_2$–C$_{60}^{\bullet -}$.

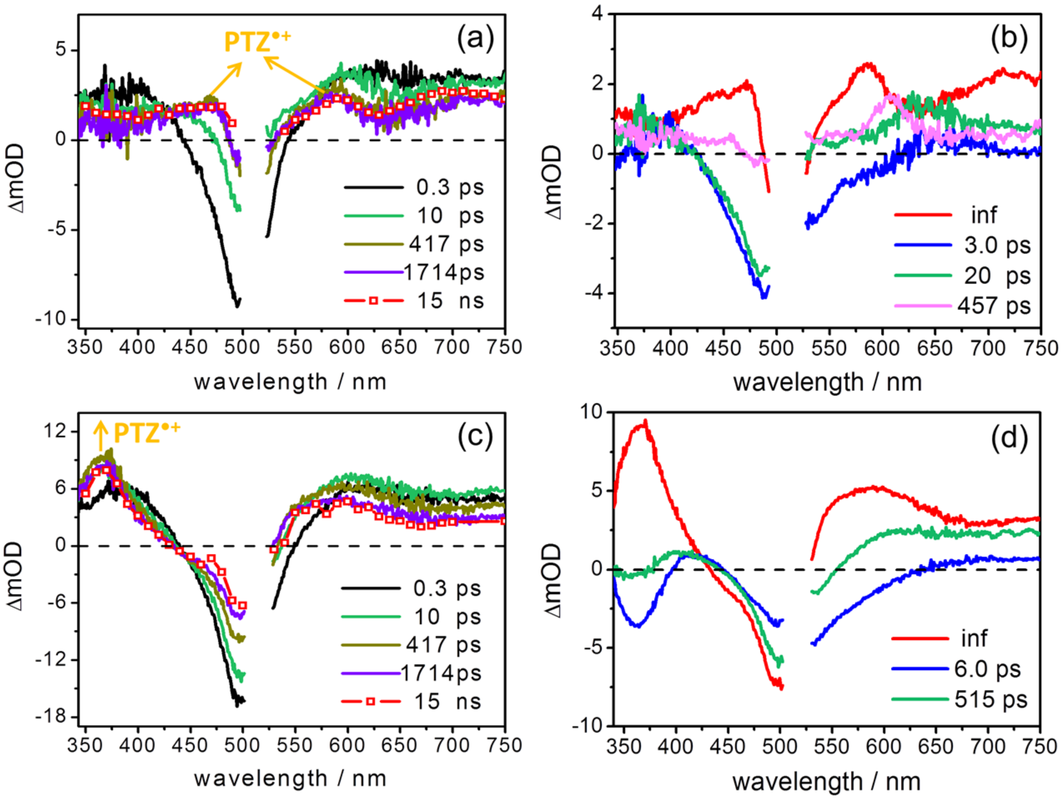

Figure 2.4. fs transient absorption spectra at selected delay times (a, c) and decay-associated spectra (b, d) of **T1** (a, b) and **D1** (c, d) in aerated dichloromethane upon excitation at 520 nm. For comparison, the ns TA spectrum recorded at 15 ns upon excitation at 520 nm was incorporated into the fs TA spectra (a, c). The ns TA spectrum was scaled according to the fs TA spectrum at 1714 ps.

Hence, there are two distinct kinetic relaxation pathways of the ^{3}MLCT states in **T1** and **D1**. In addition, the two relaxation pathways should occur from two separate ^{3}MLCT states, and thus, two distinct time constants for the decay of ^{3}MLCT states can be observed since they do not compete kinetically with each other. Combined with the ns TA and RR results, the relaxation scheme for **T1** and **D1** upon photoexcitation is proposed (Figure 2.5). The exchange interaction in the PTZ–tpy ligand, which is conjugated over a larger range, is comparably weaker than that in the tpy–C$_{60}$ ligand (or tpy ligand, **D1**). Thus, the energetic splitting between ^{1}MLCT$_{\text{PTZ-tpy}}$ and ^{3}MLCT$_{\text{PTZ-tpy}}$ is smaller than the energy gap between ^{1}MLCT$_{\text{tpy-C60}}$ and ^{3}MLCT$_{\text{tpy-C60}}$ (or between ^{1}MLCT$_{\text{tpy}}$ and ^{3}MLCT$_{\text{tpy}}$, **D1**).[101] Consequently, the energetic ordering of the ^{1}MLCT states determined by RR spectroscopy seems to be inverted in ^{3}MLCT manifold (Figure 2.5). For **T1** and **D1** the ultrafast 3 / 6 ps electron transfer process can kinetically compete with the interligand electron transfer (ILET, which is reported to be in the range of several ps for Ru(II) polypyridyl complexes[99,102,103] and causes the differently distributed ^{3}MLCT states towards the lowest-lying ^{3}MLCT state). As a result, two ^{3}MLCT states are generated which decay *via* different channels in distinct timescales (Figure 2.5). The observed results indicate that the generally accepted notion that all slow and function determining photochemistry in Ru-polypyridyl complexes stems from a single low-lying ^{3}MLCT state might have to be reconsidered especially for heteroleptic complexes which would have complex structures of MLCT states.

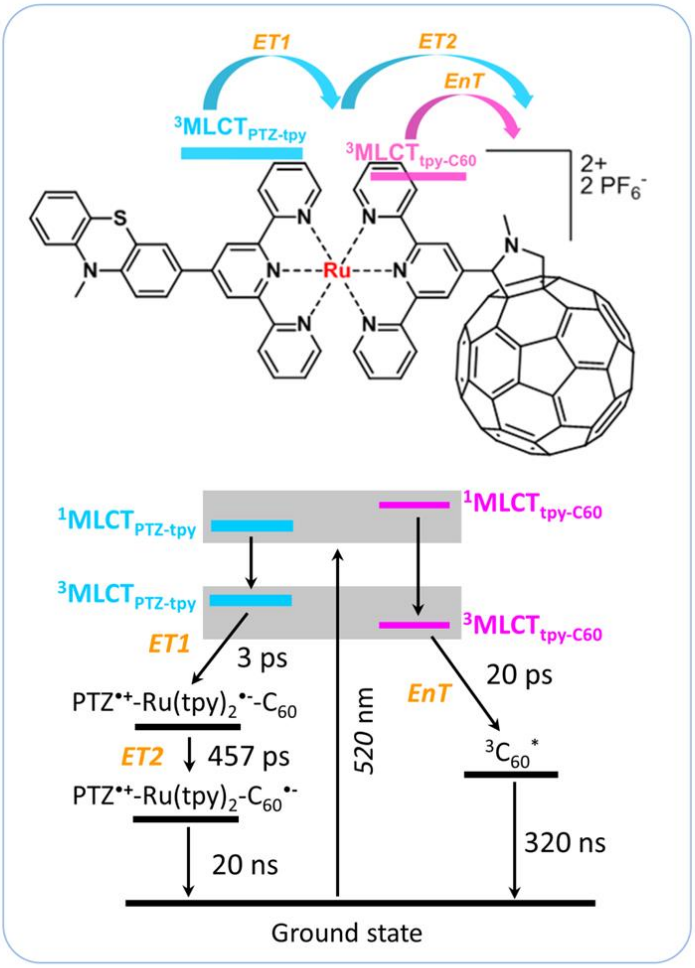

Figure 2.5. Simplified relaxation scheme for **T1**. *ET1* and *ET2* represent the first electron transfer, *i.e.* from ^{3}MLCT$_{PTZ\text{-}tpy}$ to PTZ$^{\bullet+}$–Ru(tpy)$_2^{\bullet-}$–C$_{60}$, and the second electron transfer, *i.e.* from PTZ$^{\bullet+}$–Ru(tpy)$_2^{\bullet-}$–C$_{60}$ to PTZ$^{\bullet+}$–Ru(tpy)$_2$–C$_{60}^{\bullet-}$, respectively. *EnT* represents energy transfer. **D1** only has *ET1*, *i.e.* from ^{3}MLCT$_{PTZ\text{-}tpy}$ to PTZ$^{\bullet+}$–Ru(tpy)$_2^{\bullet-}$ and instead of *EnT*, ^{3}MLCT$_{tpy}$ decays directly to ground state. For the MLCT states, the thicker bar indicates a higher population of the MLCT state upon excitation at 520 nm as indicated by resonance Raman spectroscopy.

2.2. The directionality of electron transfer

Studies on **T1** reveal that photoexcitation of the asymmetric –tpy–Ru–tpy– photosensitizer (due to the unequal substitution on tpy ligands) leads to differently distributed negative charges on the two tpy ligands and the resultant distinct ^{3}MLCT states decay independently. This observation motivated us to further investigate –tpy–Ru–tpy– based asymmetric D–Ru(tpy)$_2$–A systems. In this section, C_{60} was replaced by a Keggin-type polyoxometalate ($[PW_{11}O_{39}Ge]^{4-}$) and a molecular spacer was incorporated to slow down the backward electron transfer (*i.e.* **PTZ-Ru-POM**, Scheme 2.2). In addition, a much stronger electron donor π-extended tetrathiafulvalene (exTTF) was used instead of PTZ (*i.e.* **exTTF-Ru-POM**, Scheme 2.2) to increase the driving force for charge separation.

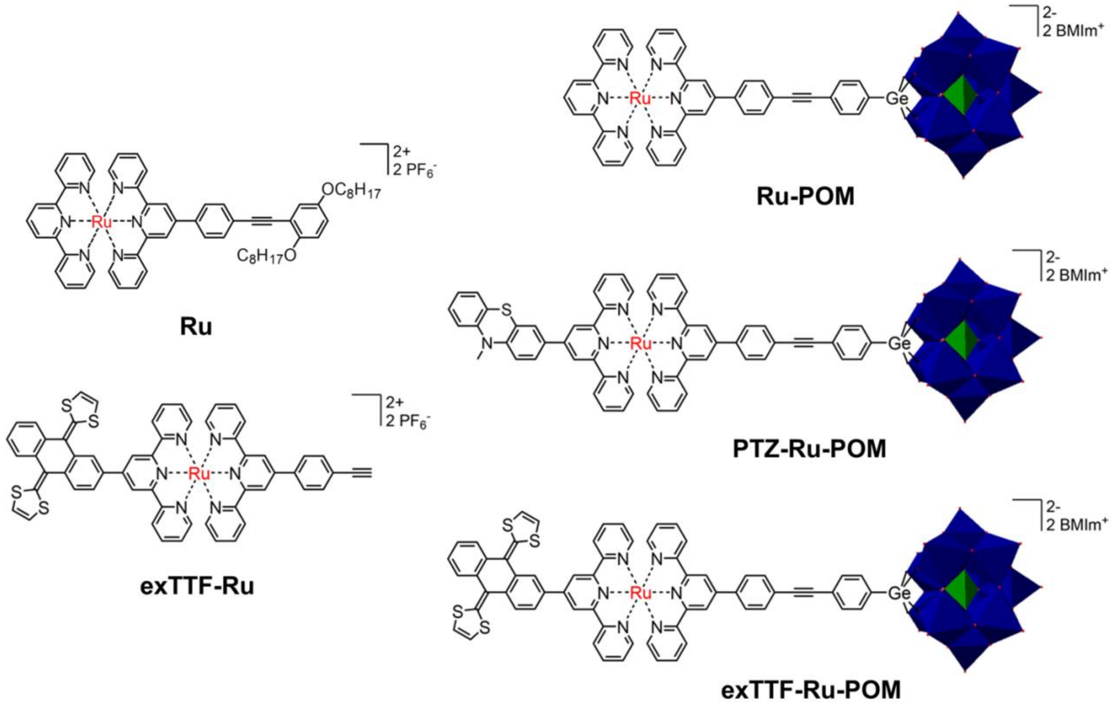

Scheme 2.2. Molecular triads and its reference dyads discussed in this section. POM is $[PW_{11}O_{39}Ge]^{4-}$ and $BMIm^+$ stands for the 1-butyl-3-methyl-*1H*-imidazol-3-ium cation. Color code: WO_6 octahedron, blue; PO_4 tetrahedron, green.

Note: *I would like to point out that **T1**, **D1** and their derivatives will be discussed throughout this thesis (**Chapter 2–Chapter 4**), so the simplest nomenclature was used. While for the POM-based system a detailed nomenclature was employed to specify each compound.*

UV/Vis absorption and emission spectra. Due to the limited solubility of the POM, the UV/Vis absorption spectra were measured in dimethyl sulfoxide (DMSO, Figure 2.6a). All Ru(II) compounds show the typical absorption features of $[Ru(tpy)_2]^{2+}$ as discussed for Figure

2.1a. The additional band at around 262 nm in **Ru-POM**, **PTZ-Ru-POM** and **exTTF-Ru-POM** is attributed to the absorption of the POM (grey line, Figure 2.6a). Next to the tpy-absorption band at 314 nm, there is a shoulder at 360 nm for **Ru**, **Ru-POM**, **PTZ-Ru-POM** and **exTTF-Ru-POM**, which is associated with the π-π transitions in the molecular spacer.[104,105] Furthermore, the attachment of PTZ and exTTF causes a distinct red shift of the MLCT band (ca. 15 nm) compared to **Ru**. This is due to the extended electron delocalization between tpy and PTZ / exTTF orbitals.[104,105] The absorption band at 435 nm in **exTTF-Ru** (and also in **exTTF-Ru-POM** but less prominent) is owing to the absorption of the exTTF moiety.[106,107]

First insight into the interaction of the individual units in the dyads and triads is gained from the emission spectra. Upon excitation of ^{1}MLCT transition (λ_{ex} = 520 nm) the emission of **Ru-POM** is decreased by 15% compared to the intrinsically rather weak emission of the mono-ruthenium complex **Ru**. This indicates an oxidative quenching pathway of the ^{3}MLCT states in **Ru-POM**. With an additional electron donor PTZ (**PTZ-Ru-POM**) a further quenched emission is observed, *i.e.* the emission intensity is reduced by 40% compared to **Ru**. For the compounds containing a stronger electron donor exTTF, the emission is fully quenched. This points to a reductive quenching pathway of the ^{3}MLCT states being operative in **PTZ-Ru-POM**, **exTTF-Ru-POM** and **exTTF-Ru**.

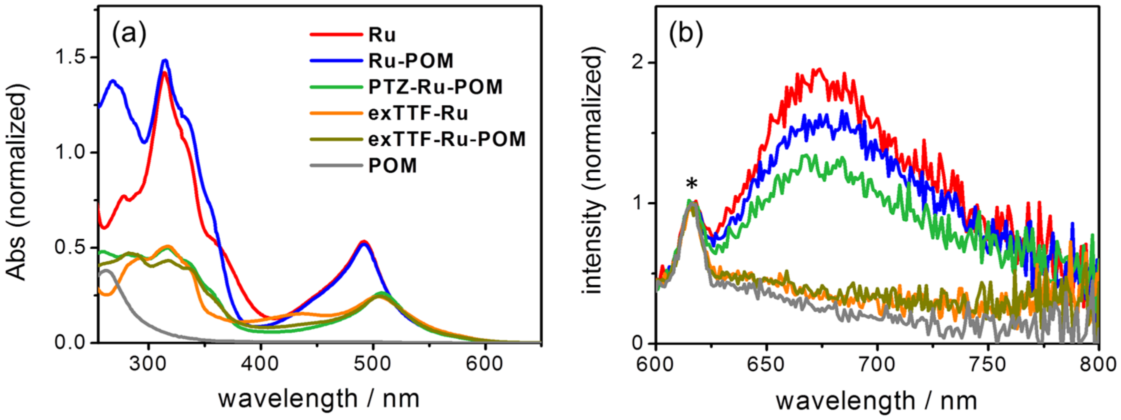

Figure 2.6. (a) UV/Vis absorption spectra and (b) emission spectra (isoabsorbing solutions at λ_{ex} = 520 nm) in aerated DMSO. The emission spectra were normalized to the Raman band of DMSO (asterisk, grey line) and share the same color code to (a). The extinction coefficients of the absorption spectra were reported in ref 104.

Photoinduced dynamics. To explore the deactivation processes of the ^{3}MLCT states in these Ru(II) compounds, fs TA spectroscopy with a short (up to 1.8 ns) and long (up to 9.5 ns) optical delay line was employed. The excitation wavelength was kept at 520 nm.

Interpretation of the fs TA data for **PTZ-Ru-POM** can be done by referring to **D1** (*i.e.* PTZ-Ru) and **Ru-POM**. Selected results of **D1** (Figure 2.7c) and **Ru-POM** (Figure 2.7d) from fs TA data are shown in terms of decay-associated spectra (DAS) since the spectral features of **D1** in DMSO are quite similar to that in DCM (Figure 2.4c) and **Ru-POM** do not show distinct spectral changes within the experimental window (~9.5 ns). For **D1**, the two processes, *i.e.* electron transfer (τ_1 = 23 ps) and relaxation of ^{3}MLCT$_{\text{tpy}}$ state (τ_2 = 1310 ps), are decelerated in DMSO compared to that in DCM (Figure 2.4d). τ_3 = 4300 ps represents the charge recombination of PTZ$^{\bullet+}$–Ru(tpy)$_2^{\bullet-}$. For **Ru-POM**, the fastest component (τ_1 = 1.3 ps) is assigned to the vibrational cooling and interligand electron transfer within the ^{3}MLCT manifold.[87] As a result, a thermalized ^{3}MLCT state is formed, for which the excess electron density is localized on the ligand with the lowest accepting orbitals, *i.e.* the extended tpy–POM ligand (*i.e.* ^{3}MLCT$_{\text{tpy-POM}}$ state). The second component (τ_2 = 5400 ps) describes the decay of the thermalized ^{3}MLCT$_{\text{tpy-POM}}$ state. Furthermore, a small offset is required in order to account quantitatively for the data (τ_{inf} in Figure 2.7b, which will be discussed later).

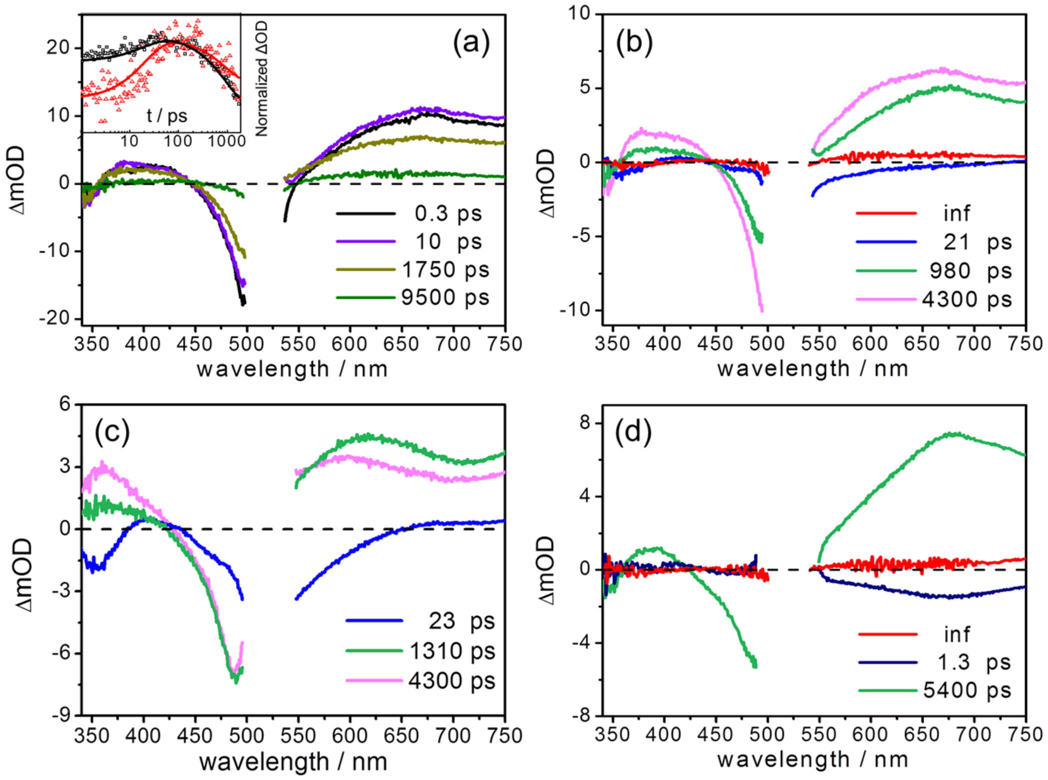

Figure 2.7. (a) fs transient absorption spectra at selected delay times upon excitation at 520 nm in aerated DMSO for **PTZ-Ru-POM**. Decay-associated spectra of (b) **PTZ-Ru-POM**, (c) **D1** (*i.e.* PTZ-Ru) and (d) **Ru-POM** obtained from the global fit of the fs TA data. Inset: normalized (at 105 ps) integrated kinetics at spectral region 360–370 nm (red) and 580–590 nm (black) where the PTZ$^{\bullet+}$ dominates.

For **PTZ-Ru-POM**, between 0.3 and 10 ps, a slight increase of the TA signal is observed at around 366 and 590 nm which is indicative of the formation of $PTZ^{•+}$ (Figure 2.2c). The TA signal increase is clearly shown in the integrated kinetics at 360–370 nm and at 580–590 nm where the $PTZ^{•+}$ dominates (Inset in Figure 2.7a). Thus, $PTZ^{•+}$ is generated within the first 100 ps indicating the population of a charge-separated state. Correspondingly, the first component in DAS (τ_1 = 21 ps, Figure 2.7b), which owns a similar spectral shape and kinetics to that of **D1** (τ_1 = 23 ps, Figure 2.7 c), is assigned to the formation of $PTZ^{•+}$–$Ru(tpy)_2^{•-}$–POM from a ^{3}MLCT state. τ_3 = 4300 ps reveals an absorption shoulder at 590 nm indicating the recombination of $PTZ^{•+}$–$Ru(tpy)_2^{•-}$–POM. Apparently, **PTZ-Ru-POM** and **D1** have very similar rate constants for the formation and recombination of the $PTZ^{•+}/Ru(tpy)_2^{•-}$ radical pair. τ_2 = 980 ps resembles the second component observed in **Ru-POM** (τ_2 = 5400 ps, Figure 2.7d), and thus, is attributed to the decay of the $^3MLCT_{tpy\text{-}POM}$ state. Additionally, a small offset is needed to completely describe the fs TA data. Notably, the decay of the $^3MLCT_{tpy\text{-}POM}$ state (*i.e.* 980 ps) is relatively slow compared to the electron transfer process (*i.e.* 21 ps). Considering the relaxation model developed for PTZ–Ru–C_{60} triad (Figure 2.5), **PTZ-Ru-POM** has independent decay pathways originating from the individual ^{3}MLCT states which do not kinetically compete with each other: The ^{3}MLCT state distributed on the PTZ–tpy ligand (*i.e.* $^3MLCT_{PTZ\text{-}tpy}$ state) undergoes reductive quenching (*i.e.* electron transfer) to generate $PTZ^{•+}$–$Ru(tpy)_2^{•-}$–POM while the ^{3}MLCT state distributed on the tpy–POM ligand (*i.e.* $^3MLCT_{tpy\text{-}POM}$ state) decays separately.

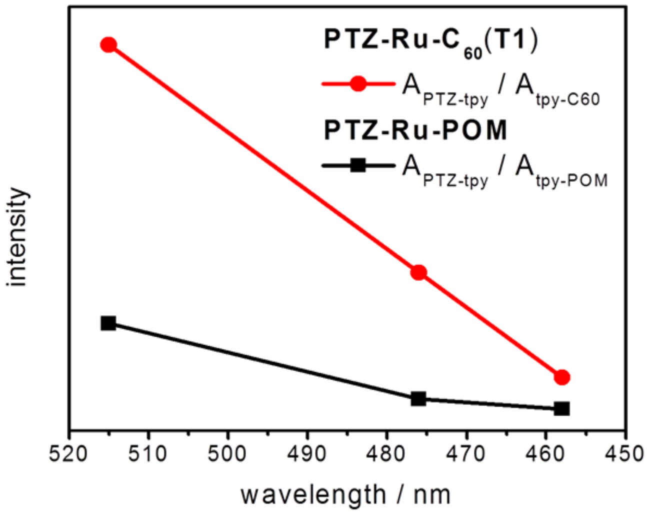

Figure 2.8. Ratios of the integrated band areas between the PTZ ($A_{PTZ\text{-}tpy}$) and tpy ($A_{tpy\text{-}C60}$ for **T1** and $A_{tpy\text{-}POM}$ for **PTZ-Ru-POM**) associated RR bands as a function of excitation wavelengths. Note: The red line (**T1**) was taken directly from Figure 2.3b.

The similarity of the initially populated MLCT states in **PTZ-Ru-POM** and **T1** (*i.e.* PTZ–Ru–C_{60}) is demonstrated by the excitation wavelength-dependent RR spectra (Figure 2.8, RR spectra of **PTZ-Ru-POM**, see [**P3**]): Decreasing the excitation wavelength from 515 to 458 nm leads to decreased RR signals of PTZ associated bands both in **PTZ-Ru-POM** and **T1** (Figure 2.8). This indicates a decreased excess electron density shift towards the PTZ–tpy ligand during ^{1}MLCT transition. However, the energetic ordering of the MLCT states is considered to be inverted in the triplet manifold as already deduced for **T1**, *i.e.* the ^{3}MLCT$_{\text{tpy-POM}}$ state is considered to be energetically lower than the ^{3}MLCT$_{\text{PTZ-tpy}}$ state, and thus, a relatively slow decay of the ^{3}MLCT$_{\text{tpy-POM}}$ state (980 ps) can be observed.

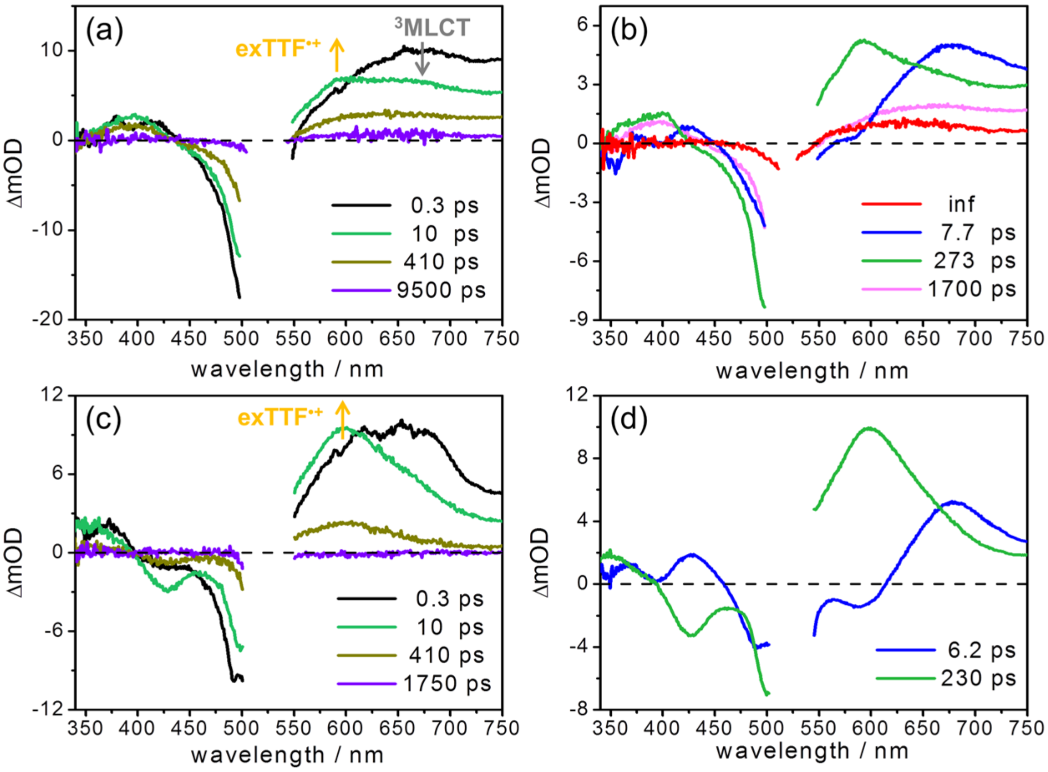

Figure 2.9. fs transient absorption spectra at selected delay times (a, c) and decay-associated spectra (b, d) of **exTTF-Ru-POM** (a, b) and **exTTF-Ru** (c, d) in aerated DMSO upon excitation at 520 nm.

This observation holds true for **exTTF-Ru-POM** which contains the stronger electron donor exTTF ($E_{\text{exTTF}+/0}$ = –0.16 V while $E_{\text{PTZ}+/0}$ = 0.37 V *vs.* Fc$^{+/0}$ in DMF, electrochemical data see [**P3**]). From 0.3 to 10 ps, the ESA of ^{3}MLCT state decreases meanwhile a new band appears at 595 nm (Figure 2.9a). This new band is attributed to the absorption of exTTF$^{•+}$ which displays two negative peaks at 360 and 430 nm accompanied with two broad absorption bands at around 610 and 660 nm in dichloromethane.[107] Correspondingly, the first component (τ_1 = 7.7 ps) in Figure 2.9b shows decreased TA signals at 370 and 430 nm indicating the formation of exTTF$^{\bullet+}$.[107] Hence, exTTF$^{\bullet+}$–Ru(tpy)$_2^{\bullet-}$–POM is generated with a time constant of 7.7 ps. The second component (τ_2 = 273 ps), which leads to a decreased TA signal at 595 nm and the recovery of bleach at 430 nm, is attributed to the recombination of exTTF$^{\bullet+}$–Ru(tpy)$_2^{\bullet-}$–POM. These assignments are supported by the fs TA data of the reference dyad **exTTF-Ru** which shows the formation and recombination of exTTF$^{\bullet+}$–Ru(tpy)$_2^{\bullet-}$ with a time constant of 6.2 and 230 ps, respectively (Figure 2.9c and d). The slow process in **exTTF-Ru-POM** (τ_3 = 1700 ps, Figure 2.9b), which reveals a spectral shape similar to the third component observed in **PTZ-Ru-POM**, is assigned to the decay of the ^{3}MLCT$_{\text{tpy-POM}}$ state. As a consequence, a branching decay of the ^{3}MLCT states is observed irrespective of which electron donors (PTZ or exTTF) were used. Namely, the ^{3}MLCT$_{\text{PTZ-tpy}}$ (or ^{3}MLCT$_{\text{exTTF-tpy}}$) state undergoes reductive quenching to populate a charge-separated state while the ^{3}MLCT$_{\text{tpy-POM}}$ state decays separately.

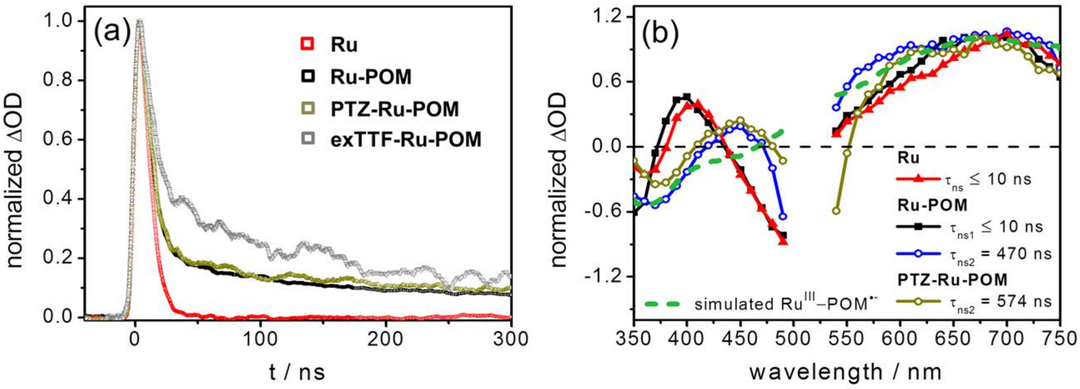

Figure 2.10. (a) Normalized integrated kinetic trace of the ns TA data (λ_{ex} = 520 nm) at the wavelength region between 540 and 750 nm. (b) Selected normalized (at 680 nm) global fit results of the ns TA data. For **PTZ-Ru-POM** only the long-lived species is shown here. The green dashed line shows the simulated absorption spectrum of Ru^{III}(tpy)$_2$–POM$^{\bullet-}$ which is the sum of the spectrum of one-electron oxidized **Ru** and one-electron reduced **POM**. All data shown here were collected in aerated DMSO.

Interestingly, the ^{3}MLCT$_{\text{tpy-POM}}$ state in **Ru-POM**, **PTZ-Ru-POM** and **exTTF-Ru-POM** does not decay to ground state directly. Instead, two kinetically distinct processes of the ns TA data are observed (Figure 2.10a). This is different to **Ru** in which the ^{3}MLCT$_{\text{tpy-POM}}$ state decays mono-exponentially within 50 ns (Figure 2.10a). It indicates that POM provides an additional decay channel for the ^{3}MLCT$_{\text{tpy-POM}}$ state in **Ru-POM**, **PTZ-Ru-POM** and **exTTF-Ru-POM**. Selected global fit results of the ns TA data are shown in Figure 2.10b. **Ru-POM** yields a short-lived component, τ_{ns1} ≤ 10 ns, which has a much stronger contribution to the overall ns decay (91%) than the long-lived species (τ_{ns2} = 470 ns, 9%

contribution). The short-lived component in **Ru-POM** resembles the decay kinetics as well as the spectral features of **Ru** (Figure 2.10b), and thus, is attributed to the decay of the ^{3}MLCT$_{\text{tpy-POM}}$ state. However, the relaxation of the ^{3}MLCT$_{\text{tpy-POM}}$ state does not exclusively repopulate the ground state but a small fraction decays *via* the POM-associated intermediate state (whose decay is associated with τ_{ns2}). The τ_{ns2} species, whose lifetime is insensitive to the existence of oxygen (470 ns in aerated solution *vs.* 570 ns in deaerated solution, for ns TA data in deaerated solution see supporting information of [**P2**]), is assigned to the charge-separated state Ru$^{\text{III}}$(tpy)$_2$–POM$^{\bullet-}$ which is further supported by the SEC simulation of the absorption of Ru$^{\text{III}}$(tpy)$_2$–POM$^{\bullet-}$ (green dashed line, Figure 2.10b, which was obtained by simply adding up the absorption of Ru$^{\text{III}}$(tpy)$_2$ and POM$^{\bullet-}$). Similar results are observed for **PTZ-Ru-POM** and **exTTF-Ru-POM** which also generate a relatively short-lived component ($\tau_{\text{ns1}} \leq 10$ ns, not shown here, similar spectral shape to the τ_{ns1} species in **Ru-POM**) and a long-lived species ($\tau_{\text{ns2}} = 574$ and 320 ns, respectively). Figure 2.10b exemplarily shows the long-lived species ($\tau_{\text{ns2}} = 574$ ns) in **PTZ-Ru-POM**, which apparently resemble the τ_{ns2} species in **Ru-POM**. This implies that instead of the fully charge-separated state, *i.e.* PTZ$^{\bullet+}$–Ru(tpy)$_2$–POM$^{\bullet-}$, τ_{ns2} refers to the decay of a partially charge-separated state, *i.e.* PTZ–Ru$^{\text{III}}$(tpy)$_2$–POM$^{\bullet-}$.

The oxidative quenching rate of the ^{3}MLCT$_{\text{tpy-POM}}$ state in **PTZ-Ru-POM** can be estimated by $k_{ET} = 1/\tau - 1/\tau_0$, $\tau = 0.98$ ns (Figure 2.7b) and $\tau_0 = 6.5$ ns in **Ru** (determined by the long optical delay line, see supporting information of [**P2**]). This yields a POM reduction rate of $k_{ET} = 8.7 \times 10^7$ s^{-1} (*i.e.* 1.2 ns). While for **exTTF-Ru-POM** no emission is observed (Figure 2.6b), and thus, the electron transfer from the ^{3}MLCT$_{\text{tpy-POM}}$ state to exTTF–Ru$^{\text{III}}$(tpy)$_2$–POM$^{\bullet-}$ is characterized by $\tau_3 = 1.7$ ns as shown in Figure 2.9b. The observation of such an oxidative quenching of the ^{3}MLCT state is quite interesting because a relatively slow intramolecular electron transfer occurs (with time constants of 1.2 and 1.7 ns) despite the short excited-state lifetime of the Ru(tpy)$_2$ photosensitizer. Combining the fs TA results, we conclude that there are two directions of electron transfer in **PTZ-Ru-POM** and **exTTF-Ru-POM** (Figure 2.11):

- The ^{3}MLCT$_{\text{PTZ-tpy}}$ (or ^{3}MLCT$_{\text{exTTF-tpy}}$) state undergoes fast electron transfer (tens of ps) from PTZ (or exTTF) to ^{3}Ru(tpy)$_2$* to generate PTZ$^{\bullet+}$–Ru(tpy)$_2^{\bullet-}$–POM (or exTTF$^{\bullet+}$–Ru(tpy)$_2^{\bullet-}$–POM).
- While the ^{3}MLCT$_{\text{tpy-POM}}$ state decays *via* slow electron transfer (in ns timescale) from ^{3}Ru(tpy)$_2$* to POM to form PTZ–Ru$^{\text{III}}$(tpy)$_2$–POM$^{\bullet-}$ (or exTTF–Ru$^{\text{III}}$(tpy)$_2$–POM$^{\bullet-}$).

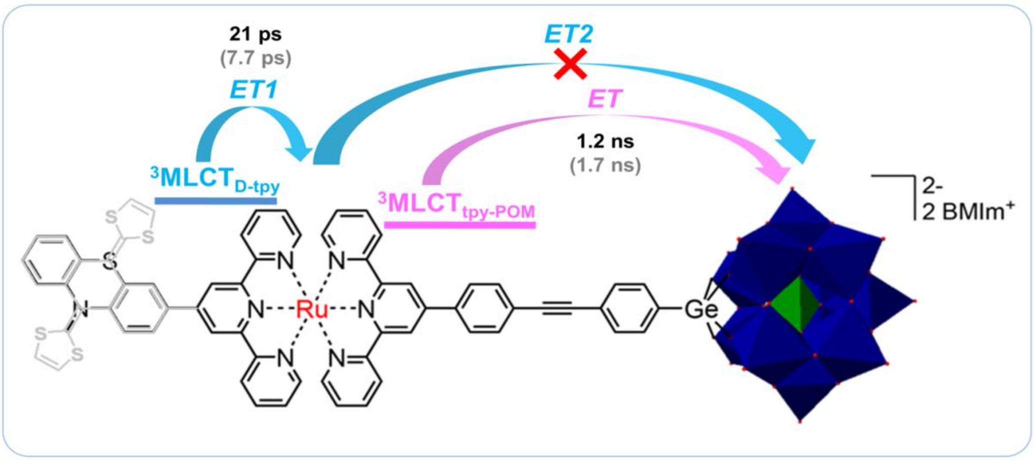

Figure 2.11. Schematic illustration of the different relaxation pathways which are determined by the specific ^{3}MLCT states excited. The grey color denotes the triad containing exTTF donor.

The fully charge-separated state, *i.e.* PTZ$^{\bullet+}$–Ru(tpy)$_2$–POM$^{\bullet-}$ or exTTF$^{\bullet+}$–Ru(tpy)$_2$–POM$^{\bullet-}$, is not formed no matter which electron donor is used (Figure 2.11). Nevertheless, this further electron-shifting process (*i.e. ET2* in Figure 2.11) is energetically downhill with a free Gibbs energy change of $-\Delta G = 0.21$ and 0.14 eV (for detailed calculation see [**P3**]) for **PTZ-Ru-POM** and **exTTF-Ru-POM**, respectively. This might be due to that the activation barrier for *ET2* (Figure 2.11) is still too high for the electron to overcome. To corroborate this speculation, in the next step the photoinduced electron transfer processes should be studied by temperature dependent fs TA spectroscopy, *e.g.* to see if the fully charge-separated state could be formed upon increasing the temperature.

To sum up, the D–Ru(tpy)$_2$–A systems presented in this chapter highlight the effects of the electronically and structurally distinct ^{3}MLCT states in Ru(tpy)$_2$ on the subsequent decay pathways. It is found that instead of generating the lowest-lying ^{3}MLCT state the two different ^{3}MLCT states decay *via* separate channels. In PTZ–Ru(tpy)$_2$–C$_{60}$ system, selective electron transfer and energy transfer towards C$_{60}$ can be achieved by tuning the excitation wavelength. While in PTZ–Ru(tpy)$_2$–POM system, the directionality of electron transfer is determined by the specific ^{3}MLCT excited. Thus, these results point out that the general picture that the slow photochemistry in Ru(II)-polypyridyl complexes originates from the lowest-lying ^{3}MLCT state might have to be revisited to account for more complex coordination spheres of the photosensitizers.

3. Electron transfer rates: distance, solvent polarity and temperature dependence

Parts of this chapter are published in:

[P4] Y. Luo, K. Barthelmes, M. Wächtler, A. Winter, U. S. Schubert and B. Dietzek, Increased Charge Separation Rates with Increasing Donor-Acceptor Distance in Molecular Triads: The Effect of Solvent Polarity. *J. Phys. Chem. C*, **2017**, *121*, 9220−9229.

[P5] Y. Luo, M. Wächtler, K. Barthelmes, A. Winter, U. S. Schubert and B. Dietzek, Superexchange on the Fast Lane – Intramolecular Electron Transfer in a Molecular Triad Occurs by Conformationally-Gated Superexchange. *Chem. Commun.*, **2019**, *55*, 5251−5254.

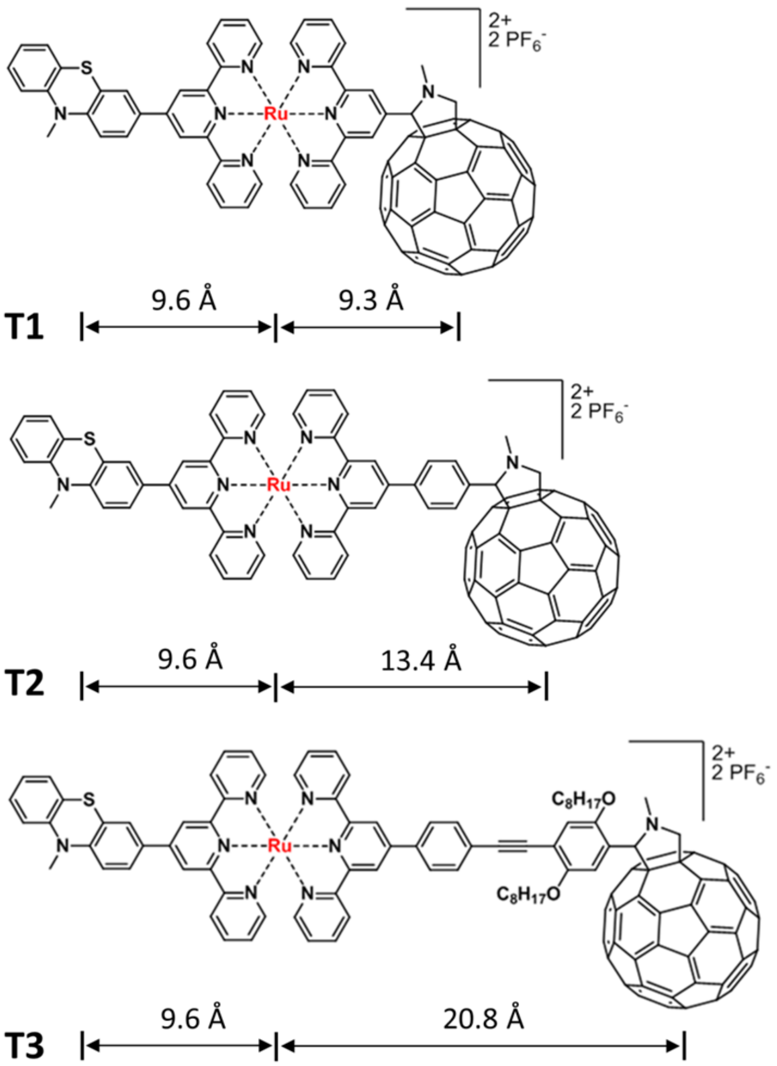

Scheme 3.1. Molecular triads **T1**–**T3** studied in this chapter. Different molecular spacers were inserted between Ru(tpy)$_2$ and C$_{60}$ to vary the distance for electron transfer. The center-to-center distance was obtained from the optimized molecular structure.[95]

For efficient solar-to-energy conversion, exploring the way to increase the charge-separation efficiencies (*i.e.* fast forward electron transfer) and to improve the stability of CSS (*i.e.* slow backward electron transfer) is of great importance. Various factors, *e.g.* solvent, D–A distance and the nature of the molecular spacer, have been shown to significantly impact electron transfer rates.[11-15] The influence of solvent is reflected either by polarity (*e.g.* which could change the driving force for electron transfer)[108-110] or viscosity[111,112] or by hydrogen-bonding with the CSS (*e.g.* which could slow down the backward electron transfer).[113-115] D–A distance, which can be tuned by adjusting the lengths of the molecular spacers, is of particular interest.[5,11,13,14,53] Studies have found that electron transfer through molecular spacer is mediated by either coherent superexchange or incoherent hopping (or the combination of them).[11,13,14,53,116] Extending the π-conjugated molecular spacer not only increases the D–A distance but also could reduce the energetic levels of the spacer states which makes the spacer energetically accessible for accepting an electron. As a result, a mechanism switch from superexchange to hopping was observed.[62-70]

This chapter presents the investigation on the electron transfer dynamics in three D–P–A triads (**T1**–**T3**, Scheme 3.1). Two different lengths of the molecular spacer were inserted between $Ru(tpy)_2$ and C_{60} in **T1**. Studies on **T1** (**Chapter 2**) reveal a two-step electron transfer process (*ET1* and *ET2*) and an energy transfer (*EnT*) process taking place upon photoexcitation of $Ru(tpy)_2$ (Figure 2.5). This chapter will only focus on *ET2* to elucidate how the second electron transfer rates (k_{ET2}) depend on the $Ru(tpy)_2$–C_{60} distance and the effect of solvent polarity on it. To this end, k_{ET2} was studied in dichloromethane ($\varepsilon = 8.93$)[108,117] and acetonitrile ($\varepsilon = 35.9$)[108,117] by fs TA spectroscopy. Furthermore, the stability of the fully CSS, *i.e.* $PTZ^{\bullet+}$–$Ru(tpy)_2$–$C_{60}^{\bullet-}$, was evaluated in the two solvents by ns TA spectroscopy. Finally, to shed light on the mechanism for *ET2*, k_{ET2} was recorded by temperature-dependent fs TA spectroscopy.

3.1. Distance and solvent polarity dependence

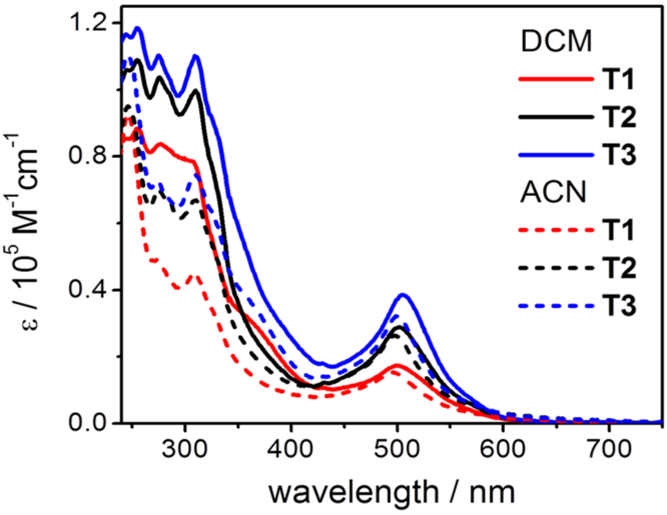

Figure 3.1. (a) UV/Vis absorption spectra of **T1**–**T3** in aerated dichloromethane (DCM, solid lines) and acetonitrile (ACN, dashed lines) recorded at room temperature.[95]

UV/Vis absorption spectra. **T2** and **T3** show similar spectral features as observed for **T1**: The broad band in the visible region at around 500 nm is due to the MLCT transitions. Compared to **T1** (peaked at 500 nm) the MLCT band is slightly red-shifted to 502 nm for **T2** and to 505 nm for **T3** which is due to the extended π-conjugation on the tpy ligand.[95] The UV region is dominated by the intense π-π transitions in tpy, PTZ and the molecular spacer. Increasing the solvent polarity from dichloromethane to acetonitrile leads to a slightly blue-shifted MLCT band for **T1**–**T3**. In both solvents, no emission from the photo-excited Ru complex was found for **T1**–**T3** (emission spectra see supporting information of [**P4**]).

3.1.1. The forward electron transfer – *ET2*

Photoinduced dynamics. For comparison with the results obtained for **T1** (dichloromethane, **Chapter 2**), the excitation wavelength for **T2** and **T3** was kept at 520 nm. Figure 3.2 exemplarily shows the fs TA spectra of **T2** and **T3** in dichloromethane: The fs TA spectrum at 0.3 ps shows typical absorption features of the ^{3}MLCT states in Ru(tpy)$_2$ complexes, *i.e.* GSB at around 500 nm and two ESA bands at 340–450 nm and 530–750 nm. Notably, the ESA band in the wavelength region of 340–450 nm undergoes distinct red-shift from 380 nm in **T2** to 415 nm in **T3**. This is owing to the extended π-π conjugation at the 4'-position of the tpy ligand.[91,99,105] At 1714 ps, **T2** shows a quite similar spectral shape to that in **T1** (Figure 2.4a): The absorption of PTZ$^{\bullet+}$ is visible at 473 and 590 nm while $^3C_{60}$* absorbs at around 700 nm. For **T3** the fs TA spectrum at 1714 ps is relatively unstructured but the peak at 590 nm for

$PTZ^{•+}$ is still discernable. Three components and an offset corresponding to the long-lived species are needed to fit the fs TA data for **T2** and **T3** (Figure 3.2b and d). The assignment of each component follows the model proposed for **T1** (Figure 2.5). That is, the first (τ_1 = 4 and 7 ps for **T2** and **T3**, respectively) and the third component (τ_3 = 535 and 794 ps for **T2** and **T3**, respectively) are assigned to *ET1* and *ET2*, respectively. The second component (τ_2 = 63 and 89 ps for **T2** and **T3**, respectively) is attributed to the energy transfer step (*i.e. EnT*). Apparently, the rates of *ET2* and *EnT* decrease with increasing $Ru(tpy)_2$–C_{60} distance (Figure 3.2b and d). In addition, changing the solvent from dichloromethane (DCM) to acetonitrile (ACN) does not introduce significant spectral changes to **T1**–**T3**. However, the rates of *ET2* (*i.e.* k_{ET2}) depend on the solvent polarity. Table 3.1 lists the time and rate constants as well as the driving force for *ET2* in **T1**–**T3**. $R_{Ru\text{-}C60}$ represents the center-to-center distance which was obtained from the optimized molecular structures (Scheme 3.1).[95]

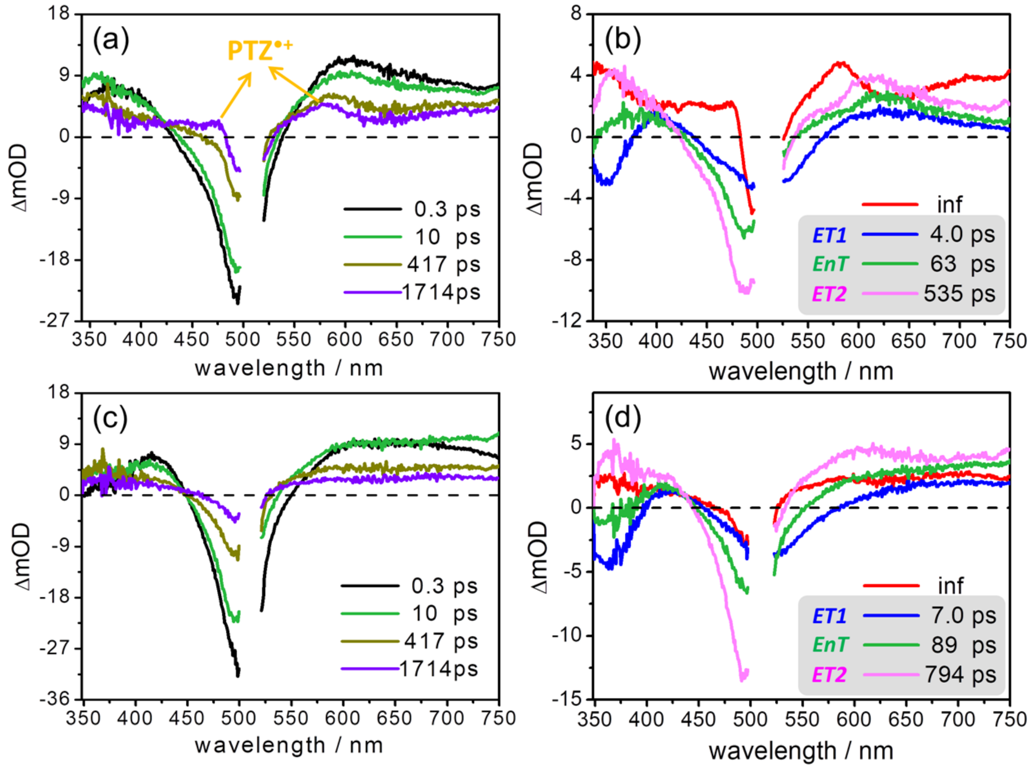

Figure 3.2. fs transient absorption spectra at selected delay times (a, c) and decay-associated spectra (b, d) of **T2** (a, b) and **T3** (c, d) in aerated dichloromethane upon excitation at 520 nm. The assignment of each time constant is shown in the grey box.

compound	$R_{Ru\text{-}C60}$ / Å	–ΔG / eV		τ_{ET2} / ps		$k_{ET2}\times10^{9}$ / s^{-1}	
		DCM	ACN	DCM	ACN	DCM	ACN
T1	9.3	0.56	0.72	457	716	2.2	1.4
T2	13.4	0.43	0.66	535	585	1.9	1.7
T3	20.8	0.40	0.55	794	480	1.3	2.1

Table 3.1. Summary of the driving force (–ΔG), time constants and the corresponding rate constants for *ET2* in dichloromethane (DCM) and acetonitrile (ACN) for **T1**–**T3**. The values of –ΔG was obtained according to the electrochemical data (see [**P4**]) based on eq 2.

Notably, k_{ET2} shows distinct distance dependence in solvents with different polarities. In DCM, k_{ET2} decreases with increasing $R_{Ru\text{-}C60}$, while in ACN, k_{ET2} increases by a factor of 1.5 from the shortest triad **T1** to the longest triad **T3** (Table 3.1). This behavior is graphically reflected in Figure 3.3 (according to the linearization of eq 6, $\ln k_{ET}$ *vs.* R_{DA}) that a negative slope (–0.046 $Å^{-1}$) in DCM and a positive slope (+0.034 $Å^{-1}$) in ACN are generated. Thus, the distance dependence of k_{ET2} in **T1**–**T3** can be switched by changing the solvent polarity. That is, a phenomenological positive β-value (+0.046 $Å^{-1}$) in DCM and a negative β-value (–0.034 $Å^{-1}$) in ACN are yielded.

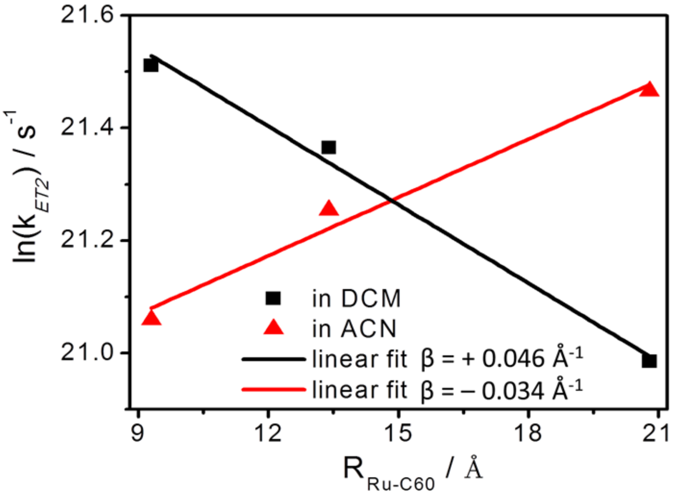

Figure 3.3. Distance dependence of the second electron transfer rates ($\ln k_{ET2}$) for **T1**–**T3** in dichloromethane (DCM) and acetonitrile (ACN).

To rationalize the changed sign of the phenomenological β-value by changing the solvent, one might consider the following equation which relates β to the spacer length, r_0, the energy gap between the donor and spacer states, Δ, and the electronic coupling within the subunits in the spacer, *v*:[11,13,14,53,58]

$$\beta = \frac{2}{r_0}\ln\left|\frac{\Delta}{v}\right| \quad (9)$$

However, Albinsson and coworkers pointed out that for a structurally-related OPE (*i.e.* oligo(*p*-phenyleneethynylene)s) spacer $\Delta/v \gg 1$.[34] This would only result in positive β-values according to eq 9. On the other hand, eq 9 may become invalid for this triad system since the molecular spacer in **T3** cannot be treated as identical subunits according to the superexchange model.[5,11,13,53] Furthermore, Albinsson and coworkers suggested a *local β value* based on a modified superexchange model that treats the spacers as a single tunneling barrier of width and height which can explain the unusual, non-exponential distance dependence of electronic coupling (*i.e.* H_{DA}).[34] This modified model indicates that if the variation of the energy of the spacer states with distance is large then the *local β value* is negative.[34] Nevertheless, the behavior observed in ACN where the electron transfer rates increase with extended donor-acceptor distance is quite interesting and rare reported in literature. Wenger and coworkers observed a similar trend and they attributed this unusual distance dependence to the interplay between λ (reorganization energy) and H_{DA} based on the Marcus theory and the superexchange model.[24,27,29] The distance dependence of electron transfer rates were simulated under various parameters function (*i.e.* β, λ, H_{DA}, $-\Delta G$).

On the basis of the method reported by Wenger and coworkers,[27] the distance dependence of k_{ET} as a function of diverse parameters in our system was simulated. Figure 3.4 exemplarily shows the different distance dependence of k_{ET} in the two solvents which display that in a certain R_{DA} region k_{ET} decreases / increases with increasing distance in DCM / ACN, and thus, different slopes with opposite signs can be generated (according to eq 6). However, the simulation cannot quantitatively describe our experimental results within a reasonable breadth of parameters, which might be the reason that only positive β-values and exponential distance dependence of H_{DA} (eq 5) were considered in this simulation. This indicates that the frequently used relation (eq 6) is oversimplified for our system because eq 6 is derived from the assumption that the distance dependences of $-\Delta G$ and λ are weak (so the exponential term in Marcus equation, *i.e.* eq 1, is constant with distance).[27] However, apparently the distance dependence of the driving force $-\Delta G$ for *ET2* cannot be ignored (Table 3.1). Thus, either an extended model accounting for the non-exponential distance dependent H_{DA}[34] or a different electron transfer mechanism, *i.e.* the contribution from incoherent hopping, may have to be taken into account. In **Chapter 3.2**, the electron transfer mechanism for *ET2* will be discussed.

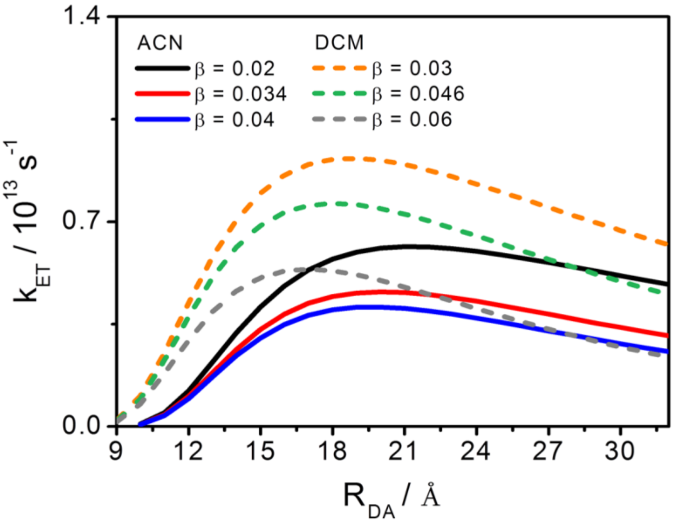

Figure 3.4. Distance dependence of k_{ET} resulting from the Marcus equation and superexchange model.[27] The parameters used for simulation are as follows: (i) the outer-sphere reorganization energy was estimated by eq 4: ACN, n = 1.3416, ε = 35.9 and DCM, n = 1.4212, ε = 8.93. a_1 = 9.6 Å and a_2 = 4.5 Å: *ET2* occurs from an intermediate state $PTZ^{\bullet+}$–$Ru(tpy)_2^{\bullet-}$–C_{60}, the electron density is thought to be delocalized over the conjugated PTZ and Ru complex unities, and thus the radius of the donor (a_1) was estimated to be 9.6 Å according to the optical molecular structure. The inner-sphere reorganization energy λ_i = 0.1 eV and usually is considered as distance independent. (ii) H_0 = 100 cm^{-1} is taken from ref 27. (iii) Driving forces $-\Delta G$ is 1.0 eV and 0.8 eV in DCM and ACN, respectively. The values of $-\Delta G$ are based on the fact that the absolute values of $-\Delta G$ in DCM are ca. 25% higher than that in ACN (Table 3.1). It should be pointed out that in practice $-\Delta G$ is also distance dependent, but in this simulation we assumed $-\Delta G$ is constant with distance.

3.1.2. The backward electron transfer – the stability of CSS

The fs TA data shown above reveal that the fully charge-separated state $PTZ^{\bullet+}$–$Ru(tpy)_2$–$C_{60}^{\bullet-}$ is generated in **T1**–**T3**. This conclusion is further corroborated by ns TA spectroscopy (discussed in this section). The ns TA spectra of **T2** and **T3** resemble the spectral features of **T1** (Figure 2.2a), which show the $PTZ^{\bullet+}$ and $^3C_{60}$* associated ESA band at 590 and 700 nm, respectively (Figure 3.5). However, the relative intensities of the two bands (corresponding to electron transfer and energy transfer) as well as the lifetime of $PTZ^{\bullet+}$–$Ru(tpy)_2$–$C_{60}^{\bullet-}$ change with the D–A distance and solvent polarity. For example, at 20 ns the ratio between the bands at 590 and 700 nm (I_{ET} / I_{EnT}) decreases from 1.36 (**T2**) to 0.65 (**T3**) in DCM (Figure 3.5). At the same time $PTZ^{\bullet+}$–$Ru(tpy)_2$–$C_{60}^{\bullet-}$ and $^3C_{60}$* decay faster in **T2** than **T3**. Time constants of the charge recombination for **T1**–**T3** in the two solvents are summarized in Table 3.2. I would like to point out that due to the fast charge recombination of $PTZ^{\bullet+}$–$Ru(tpy)_2$–$C_{60}^{\bullet-}$ in **T1** in ACN, the exact time constant cannot be obtained under the time resolution (~10 ns) of the setup.

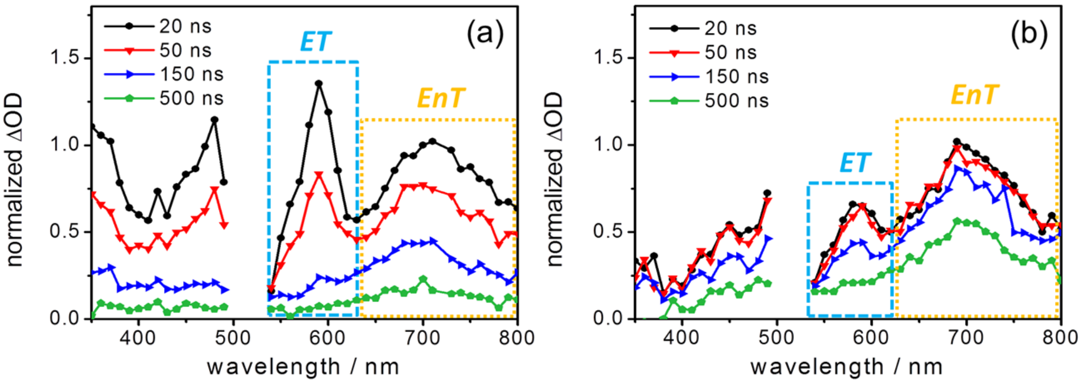

Figure 3.5. ns transient absorption spectra at selected delay times of **T2** (a) and **T3** (b) in aerated dichloromethane upon excitation at 520 nm. For comparison, all spectra were normalized to the absorption maximum at 700 nm at 20 ns.

		τ_{CR} / ns		I_{ET} / I_{EnT}	
compound	$R_{PTZ\text{-}C60}$ / Å	DCM	ACN	DCM	ACN
T1	18.3	20	< 10	2.5	–
T2	22.9	52	19	3.1	3.3
T3	30.1	180	94	0.6	2.1

Table 3.2. Summary of time constants for charge recombination (τ_{CR}) of PTZ$^{\bullet+}$–Ru(tpy)$_2$–C$_{60}$$^{\bullet-}$ and the comparison between absorption intensities of PTZ$^{\bullet+}$–Ru(tpy)$_2$–C$_{60}$$^{\bullet-}$ and $^3C_{60}{}^*$ in aerated dichloromethane (DCM) and acetonitrile (ACN) for **T1**–**T3**. The center-to-center distance $R_{PTZ\text{-}C60}$ was estimated from the optimized molecular structures.[95]

From Table 3.2 some conclusions can be drawn:

- Distance effect: In DCM and ACN, the lifetime of PTZ$^{\bullet+}$–Ru(tpy)$_2$–C$_{60}$$^{\bullet-}$ becomes longer from **T1** to **T3**. In other words, a slower backward electron transfer rate is achieved with a larger D–A distance. This in turn corroborates the formation of the fully charge-separated state PTZ$^{\bullet+}$–Ru(tpy)$_2$–C$_{60}$$^{\bullet-}$ instead of the partially charge-separated state PTZ$^{\bullet+}$–Ru(tpy)$_2$$^{\bullet-}$–C$_{60}$ (otherwise similar lifetimes would be expected).
- Polarity effect: Charge recombination is faster in a high polar solvent, *i.e.* ACN, than that in a low polar solvent, *i.e.* DCM for all the triads.
- The yield of PTZ$^{\bullet+}$–Ru(tpy)$_2$–C$_{60}$$^{\bullet-}$ differs with triads and solvent polarity. The yield in **T2** is the highest and is barely influenced by solvent polarity. However, for **T3** the yield of PTZ$^{\bullet+}$–Ru(tpy)$_2$–C$_{60}$$^{\bullet-}$ is increased by a factor of 3 in ACN compared to DCM. The influence of solvent polarity on the yield of PTZ$^{\bullet+}$–Ru(tpy)$_2$–C$_{60}$$^{\bullet-}$ in **T3** could be rationalized by the distinct kinetics for *ET1* in ACN and DCM (2.0 *vs.* 7.0 ps, respectively, for the fs TA data in ACN see [**P4**]). Compared to *ET1* in ACN (with a

time constant of 2 ps), *ET1* in DCM (with a time constant of 7 ps) becomes less competitive with the interligand electron transfer which would convert ^{3}MLCT$_{\text{PTZ-tpy}}$ to ^{3}MLCT$_{\text{tpy-C60}}$ state to generate $^3C_{60}$* (see model in Figure 2.5). As a result, a smaller percentage of the ^{3}MLCT$_{\text{PTZ-tpy}}$ state undergoes *ET1* in DCM than that in ACN, which leads to less PTZ$^{\bullet+}$–Ru(tpy)$_2$–C$_{60}$$^{\bullet-}$ in DCM. While for **T2**, the time constants for *ET1* in ACN and DCM are quite similar (*i.e.* 6 and 4 ps, respectively, for the fs TA data in ACN see [**P4**]). Thus, nearly identical yields of PTZ$^{\bullet+}$–Ru(tpy)$_2$–C$_{60}$$^{\bullet-}$ in the two solvents are obtained in **T2**.

In short, the studies on **T1**–**T3** reveal that both forward and backward electron transfer rates can be altered by the D–A distance and solvent polarity. The backward electron transfer rates are found to decrease with increasing D–A distance independent of solvent polarity while the forward electron transfer (*ET2*) shows opposing distance dependence which is controlled by the solvent polarity.

3.2. Temperature dependence: Electron transfer mechanism

The results shown above indicate that the generally used β-values for distinguishing between superexchange and hopping may become invalid in some cases, *e.g.* a negative β-value is obtained in ACN (Figure 3.3). Furthermore, the rather small β-value (0.046 Å^{-1}) in DCM would normally be attributed to a hopping mechanism.[11,13,14,53] However, as mentioned in **Chapter 1**, differentiating electron transfer mechanisms by the magnitude of β-value may lead to misconceptions as pointed out by Wasielewski and Albinsson.[60,61] Thus in this section, to gain insights into the electron transfer mechanism underlying *ET2* temperature-dependent k_{ET2} will be studied which according to literature is another way (apart from the distance-dependent studies) to understand the electron transfer mechanisms.[61,71-75] To this end, fs TA spectroscopy was performed from 300 to 230 K in DCM. Furthermore, as discussed in **Chapter 1**, changes in solvent dielectric properties (which would make λ and –ΔG to become temperature-dependent) might superimpose the changes caused by a switch in electron transfer mechanisms.[61,71-75] Herein, the discussion of temperature-dependent k_{ET2} will be conducted with the consideration of the temperature-dependent solvent properties. With the analysis of the distance- and temperature-dependent k_{ET2} the electron transfer mechanism for *ET2* can be understood.

Photoinduced dynamics as a function of temperature. The fs TA spectra of **T1**–**T3** were collected upon excitation at 520 nm in the temperature range of 300–230 K in DCM. Figure

3.6 exemplarily shows fs TA spectra recorded at 270 K for **T1**–**T3** which are quite similar to that recorded at room temperature (Figure 3.2 and Figure 2.4a for **T1**). Owing to the fact that the fs TA spectra do not display significant changes upon decreasing temperature (for each compound), the model developed at room temperature (see Figure 2.5) can be applied to analyze the temperature dependent data. Namely, three kinetic components and an offset were used to account for the data in the temperature range between 300 and 230 K. Apparently, time constants for *ET1*, *ET2* as well as *EnT* are temperature dependent. In this section we still focus on *ET2* with the aim of elucidating the electron transfer mechanism (the temperature dependence of *ET1* will be discussed in **Chapter 4**). Time constants for *ET2* as a function of temperature are listed in Table 3.3.

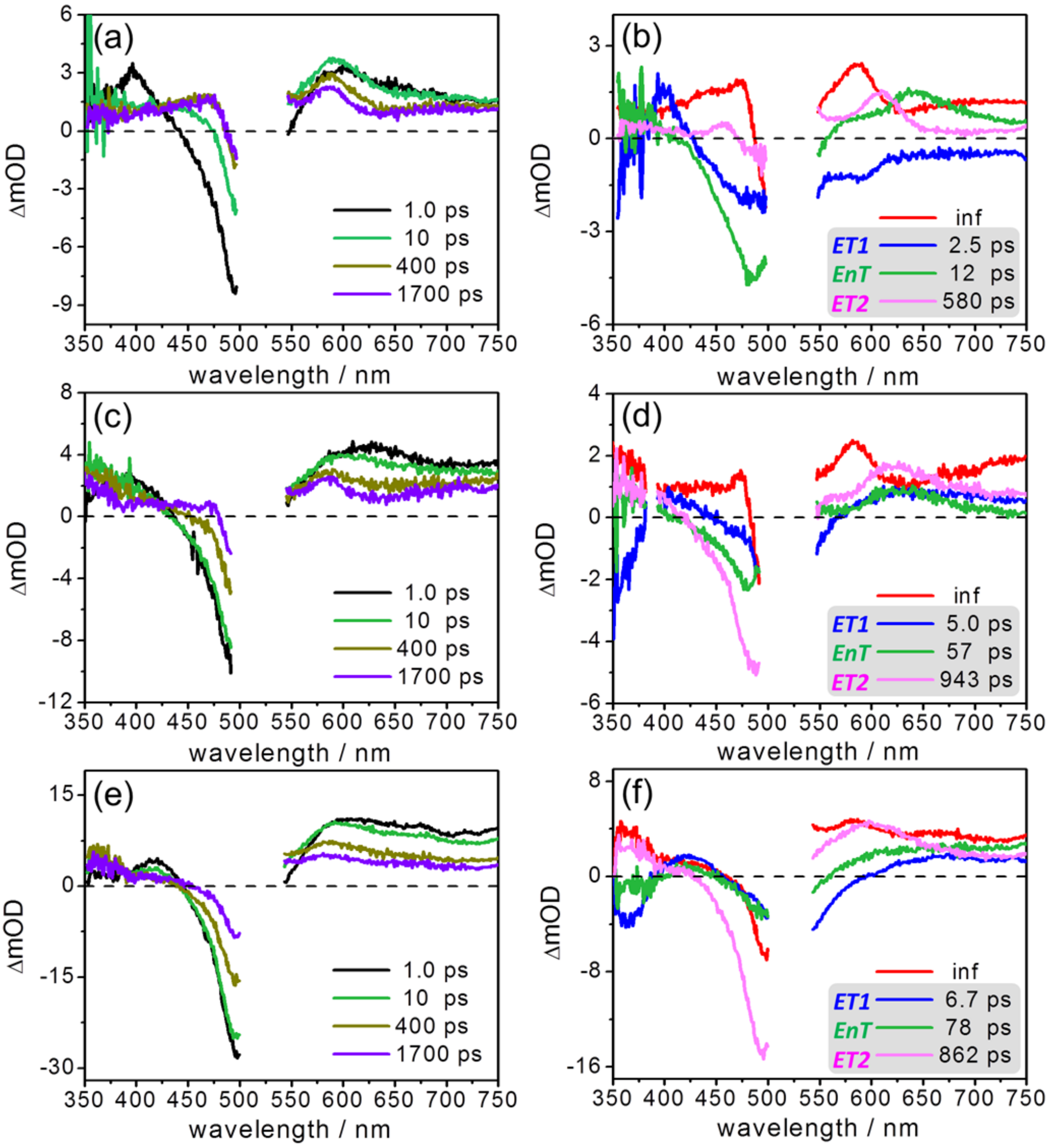

Figure 3.6. fs transient absorption spectra at selected delay times (a, c, e) and decay-associated spectra (b, d, f) of **T1** (a, b), **T2** (c, d) and **T3** (e, f) in aerated dichloromethane upon excitation at 520 nm at 270 K.

T / K	τ_{ET2} / ps			k_{ET2} ×10^9 / s^{-1}		
	T1	**T2**	**T3**	**T1**	**T2**	**T3**
300	334	500	690	2.99	2.00	1.45
280	421	569	740	2.38	1.76	1.35
270	580	943	862	1.72	1.06	1.16
260	712	996	850	1.40	1.00	1.18
250	774	1267	924	1.29	0.79	1.08
240	886	–	943	1.13	–	1.06
230	–	1615	1006	–	0.62	0.99

Table 3.3. Temperature dependence of the time constants (τ_{ET2}) and the corresponding rate constants (k_{ET2}) for the second electron transfer process (*ET2*) in **T1**–**T3**.

Basically, τ_{ET2} increases with decreasing temperatures indicating decelerated electron transfer rates (k_{ET2}) at lower temperatures (Table 3.3). Consistent with the result at room temperature in DCM (Figure 3.3), k_{ET2} decreases with increasing D–A distance at 300 and 280 K. However, when further decreasing the temperatures k_{ET2} in **T3** becomes larger than that in **T2** (Table 3.3). The distance dependence of k_{ET2} at different temperatures is depicted in Figure 3.7a (based on eq 6). That is, at 300 and 280 K $\ln k_{ET2}$ displays a single linear relation with distance $R_{Ru\text{-}C60}$. However, upon decreasing the temperature from 270 K to 230 K a minimal k_{ET2} is observed at **T2**. In other words, electron transfer rates do not decay exponentially with increasing D–A distance in the temperature range between 270 and 230 K. Such appearance of a slope change is attributed to a switch in electron transfer mechanism from superexchange (**T1** and **T2**) to hopping (**T3**).[62-70] To get further information on the electron transfer mechanism in the entire investigated temperature range, the temperature dependence of k_{ET2} is evaluated by eq 8 (Figure 3.7b). In doing so, we explicitly take into account the temperature dependence of the solvent's dielectric properties. Both λ (estimated by eq 3–4) and activation energy $\Delta G^{\ddagger}$, *i.e.* $(\lambda+\Delta G)^2/4\lambda$, are nearly temperature independent for *ET2*: From 300 to 230 K, λ and $(\lambda+\Delta G)^2/4\lambda$ show changes smaller than 2% and 8%, respectively (details see supporting information of [**P5**]). Thus, the solvent itself would not induce significant deviations to the Marcus analysis (eq 8). Figure 3.7b illustrates that k_{ET2} can be well described by the Marcus equation (eq 8) and no slope-changes indicating different electron transfer mechanisms in different temperature ranges are apparent.[61,71-75] Accordingly, combined with the results from Figure 3.7a, we conclude that from 300 to 230 K electron transfer in **T1** and **T2** occurs *via* superexchange while incoherent hopping must be dominant in **T3**. Hopping being operative in **T3** can be understood by the long conjugated molecular spacer between $Ru(tpy)_2$ and C_{60}. Extension of the π-conjugation could reduce the energetic levels of the spacer states which makes the spacer available for accepting an electron.[13,53,62] In addition, structural changes of the molecular spacer in the excited state should be considered especially for the long conjugated π-system which might impact the distance- and temperature dependence of k_{ET}. Literature has reported that electron transfer can be gated by the torsional motion in molecular spacers.[118-120] For **T3** this would relate to the torsional motion in the alkoxy substituted oligo(*p*-phenyleneethynylene)s molecular spacer. However, the activation energy $\Delta G^{\ddagger}$ for *ET2* in **T3** extracted from Figure 3.7b is only 0.04 eV (Table 3.4), which is ten times smaller than the calculated torsional barrier (0.3–0.6 eV, depending on the actual theoretical method used) for related oligo(*p*-phenyleneethynylene)s molecular spacers.[121,122] Hence, *ET2* in **T3** does not appear to be gated by the torsional dynamics of the ligand system.

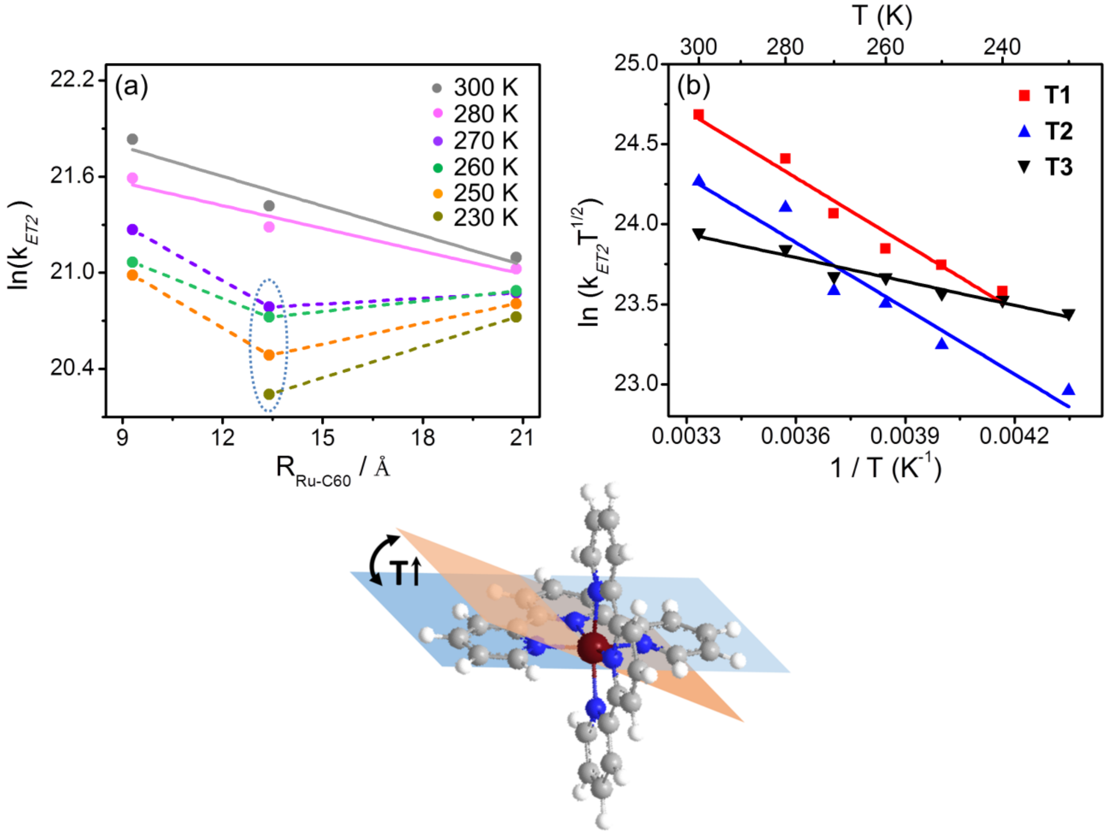

Figure 3.7. (a) Plots of ln(k_{ET2}) *vs.* the center-to-center distance for *ET2* ($R_{Ru\text{-}C60}$). The solid line represents the linear fit of the data at 300 and 280 K which yield the attenuation factor β = 0.060 and 0.048 $Å^{-1}$, respectively. The dashed lines are given to show the trend of electron transfer rates as a function of distance. (b) Plots of ln(k_{ET2}·$T^{1/2}$) *vs.* 1/T for *ET2* in **T1**–**T3** with the corresponding linear fit. Bottom: Simplified graphical representation of the temperature-activated geometry of Ru photosensitizer for superexchange. Color code: Red Ru, blue N, grey C.

	ET2		
	T1	**T2**	**T3**
$-\Delta G$ / eV	0.56	0.43	0.40
λ / eV	1.36	1.17	0.77
H_{DA} / cm^{-1}	35	28	5
$\Delta G^{‡}$ / eV	0.1	0.1	0.04

Table 3.4. Summary of driving force ($-\Delta G$), reorganization energy (λ), electronic coupling (H_{DA}) and activation energy ($\Delta G^{‡}$) obtained from the experimental results displayed in Figure 3.7b for *ET2* in **T1**–**T3**. $-\Delta G$ was calculated based on eq 2 and electrochemical data reported in ref 95.

Noteworthily, *ET2* in **T3**, taking place *via* hopping, has weaker temperature dependence (*i.e.* a flatter slope) than the superexchange in **T1** and **T2** (Figure 3.7b). Owing to $\lambda > |-\Delta G|$ (Table 3.4) *ET2* occurs in the Marcus normal region for **T1**–**T3**. Hence, the weak temperature dependence of k_{ET2} in **T3** is not due to the electron transfer occurring in the Marcus inverted region where k_{ET} shows very weak or even no temperature dependence.[76,118] To the best of my knowledge, this is the first observation of superexchange having stronger temperature dependence than hopping in structurally-related systems: Molecular assemblies containing electron donors π-extended tetrathiafulvalenes (exTTF), phenothiazine (PTZ), porphyrin, ferrocene and electron acceptors fullerene (C_{60}), perylene.[61,71-75] All these studies on temperature-dependent electron / hole transfer rates pointed out that incoherent hopping is more sensitive to temperature change than coherent superexchange.[61,71-75] Nevertheless, none of these studies in literature is concerned with Ru-polypyridyl photosensitizers. For this type of photosensitizers, upon excitation, the negative charges are distributed on the ligands which have specific mutual orientation. Thus, I would correlate the observation of the pronounced thermally activated superexchange in **T1** and **T2** to the specific geometry of the –tpy–Ru–tpy– photosensitizer. According to the relaxation model in Figure 2.5, *ET2* takes place from the reduced tpy ligand, *i.e.* $PTZ^{\bullet+}$–$tpy^{\bullet-}$–Ru–tpy–C_{60}, to C_{60} acceptor. However, the orbitals carrying the excess charges on the PTZ–tpy ligand are spatially orthogonal to the orbitals on the tpy–C_{60} ligand (Figure 3.7, bottom). Superexchange requires orbital overlap.[53] Thus, *ET2 via* superexchange can only occur in the thermally activated structures, *i.e.* slightly distorted geometries of –tpy–Ru–tpy– (Figure 3.7, bottom). As a result, electron transfer *via* superexchange in **T1** and **T2** is more sensitive to temperature change than electron hopping in **T3**. While for the temperature-dependent studies in literature, electron transfer takes place from rather planar organic photosensitizers, *i.e.* excited C_{60}, porphyrin and perylene derivatives,[61,71-75] the thermal population of a specific conformation of the photosensitizers is not necessarily needed to trigger electron transfer *via* superexchange. Thus, generally k_{ET} *via* superexchange shows weaker temperature dependence than hopping.[61,71-75] The finding in our system highlights the effect of the specific geometrical structures of the –tpy–Ru–tpy– photosensitizer on the electron transfer dynamics in D–Ru(tpy)$_2$–A triad.

In this chapter, the influence of D–A distance and solvent polarity on electron transfer rates k_{ET2} is discussed. Interestingly, inverted distance dependence of k_{ET2} is observed in **T1**–**T3** by simply changing the solvent polarity. The numerical simulation based on the Marcus theory (eq 1) and superexchange model (eq 5) can only qualitatively describe the distinct distance dependence of k_{ET2} observed here. This points to either a model extension (*e.g.* by employing non-exponential distance dependent H_{DA}) or a different electron transfer mechanism should be considered. Subsequently, k_{ET2} was studied as a function of temperature by fs TA spectroscopy to understand the electron transfer mechanism underlying *ET2*. The combined analysis of distance- and temperature-dependent k_{ET2} indicates that from 300 to 230 K incoherent hopping is the dominant mechanism for **T3** while coherent superexchange is operative in **T1** and **T2** despite a rather small β-value (0.046 Å^{-1}) is observed at room temperature (in dichloromethane). The studies here are in agreement with recent reports[60,61] that conclusions on the specific electron transfer mechanism cannot be made solely based on the β-value. Noteworthily, a weaker temperature dependence of hopping as compared to superexchange is observed. This is rationalized by the specific geometrical and electronic structure of the Ru(tpy)$_2$ photosensitizer. Hence, the generally reported temperature sensitivity that hopping has stronger temperature dependence than superexchange should not be the criterion for distinguishing the two mechanisms.

4. Electronic coupling: The remote substituent effects

Parts of this chapter are published in:

[**P5**] Y. Luo, M. Wächtler, K. Barthelmes, A. Winter, U. S. Schubert and B. Dietzek, Superexchange on the Fast Lane – Intramolecular Electron Transfer in a Molecular Triad Occurs by Conformationally-Gated Superexchange. *Chem. Commun.*, **2019**, *55,* 5251–5254.

[**P6**] Y. Luo, J. H. Tran, M. Wächtler, M. Schulz, K. Barthelmes, A. Winter, S. Rau, U. S. Schubert and B. Dietzek, Remote Control of Electronic Coupling – Modification of Excited-State Electron Transfer Rates in Ru(tpy)$_2$-Based Donor-Acceptor Systems by Remote Ligand Design. *Chem. Commun.*, **2019**, *55*, 2273–2276.

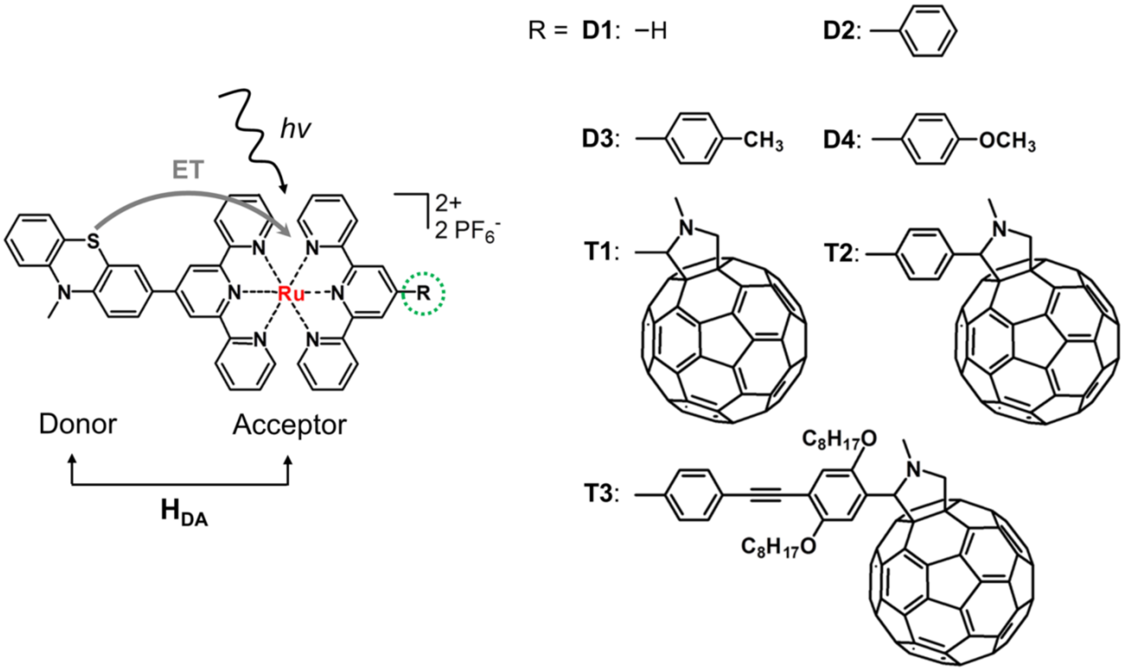

Scheme 4.1. Molecular dyads **D1**–**D4** and triads **T1**–**T3** studied in this chapter. Herein the photoinduced electron transfer from PTZ to photo-excited Ru complex is of interest.

From the temperature dependent fs TA data of **T1**–**T3** (**Chapter 3.2**), we have found that the time constants for the first electron transfer process (*i.e. ET1*) are different albeit the D–A distance, chemical linkage and –ΔG are quite similar amongst the triads. It seems that the substitution pattern on the second tpy ligand has an impact on the electronic interaction between PTZ and photo-excited Ru complex (*i.e.* H_{DA}, Scheme 4.1), and thus k_{ET1}. This observation motivated us to systematically investigate how the functionalization on the remote tpy ligand of the Ru(tpy)$_2$ complex could affect H_{DA} underlying the electron transfer from PTZ to Ru(tpy)$_2$*, *i.e. ET1*. Literature has reported such remote effects for mixed-valence Ru^{II}/Ru^{III} complexes that the properties of intervalence charge-transfer (IVCT) transitions were altered by the remote ligands:[123,124] With nearly identical –ΔG the electronic coupling underlying the IVCT was changed by 20%.[123] However, this work only considered the ground-state properties.[123] In this chapter, three new dyads **D2**–**D4** based on the molecular structure of **D1** were designed (Scheme 4.1). Herein, I focus on the electron transfer from PTZ to photo-excited Ru complex, *i.e.* PTZ→Ru(tpy)$_2$*. I will show that H_{DA} between PTZ and Ru(tpy)$_2$ can be tuned by the substituents on the remote tpy ligand in spite of the same D, D–A distance, D–A linkage as well as similar –ΔG for PTZ→Ru(tpy)$_2$* in all compounds.

UV/Vis absorption spectroscopy. The UV/Vis absorption spectra of **D1** and **T1**–**T3** are shown before (Figure 2.1a and Figure 3.1, respectively). For **D2**–**D4** similar spectral features as that of **D1** are observed (Figure 4.1). The UV/Vis absorption spectra display intense absorption bands associated with the π-π transitions in tpy ligands and the substituents in the UV region along with a moderate MLCT band at around 500 nm. With the attachment of a phenyl ring (–ph), *i.e.* **D2**, the MLCT band experiences a slight red-shift (4 nm) compared to **D1**, which is due to the slightly delocalized MLCT states in **D2**.[87,91,99] By adding a strong electron-donating group methoxyl (–OCH$_3$) on the phenyl ring, the MLCT band undergoes further red-shift (4 nm) compared to that in **D2**. This is due to the enhanced π character of the tpy–ph bond at ground state that the –OCH$_3$ group makes the dihedral angle between tpy and ph smaller leading to more delocalized negative charges in **D3** compared to **D2**.[125]

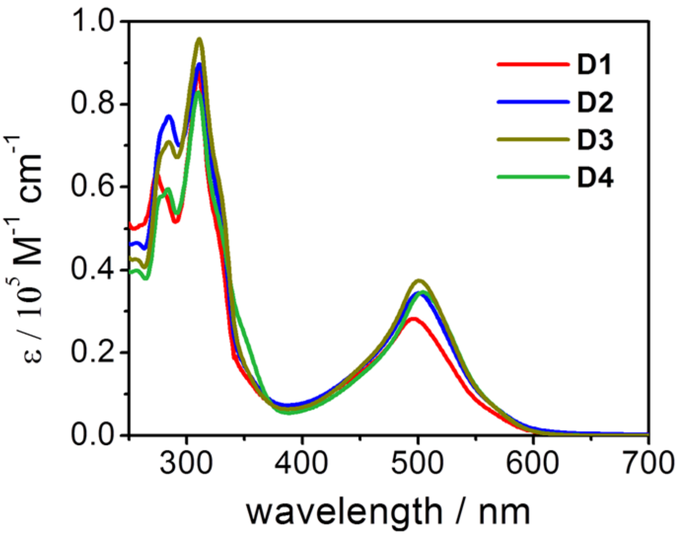

Figure 4.1. (a) UV/Vis absorption spectra of **D1**–**D4** in dichloromethane (DCM) at room temperature. The spectrum and extinction coefficient of **D1** were taken from ref 95.

Photoinduced dynamics as a function of temperature. The fs TA spectra of **D1**–**D4** were collected upon excitation at 520 nm in the temperature region of 300–240 K. For each compound, the characteristics of the fs TA spectra do not display significant changes upon decreasing the temperature, and thus, the interpretation of fs TA data of **D1**–**D4** can follow the model developed for **D1** at room temperature (Figure 2.5). Exemplarity, the fs TA spectra of **D1**–**D4** at 270 K are displayed in Figure 4.2 (the fs TA spectra of **T1**–**T3** at 270 K are shown in **Chapter 3**, Figure 3.6). Concerning the dyads, two kinetic components and an offset corresponding to the long-lived species are sufficient to describe all the fs TA data. According to Figure 2.5, the long-lived species in decay-associated spectra (Figure 4.2b, d, f and h) represents the charge recombination of $PTZ^{\bullet+}$–$Ru(tpy)_2^{\bullet-}$; the first component (τ_1; from 5.2 to 7.1 ps for **D1**–**D4**, respectively) describes the PTZ→$Ru(tpy)_2$* electron transfer; the second component (τ_2; from 404 to 920 ps for **D1**–**D4**, respectively) is attributed to the decay of ^{3}MLCT state distributed on the tpy–R ligand (*i.e.* $^3MLCT_{tpy\text{-}R}$ state, R represents the substituents shown in Scheme 4.1) to ground state. Apparently, the lifetime of the $^3MLCT_{tpy\text{-}R}$ state increases from **D1** to **D4** at the same temperature. This is due to the stabilized $^3MLCT_{tpy\text{-}R}$ state because of the increased π-conjugation.[99] To figure out how H_{DA} between PTZ and $Ru(tpy)_2$ could be impacted by the remote tpy–R ligand, we focus on the PTZ→$Ru(tpy)_2$* electron transfer for which all dyads and triads have the same donor, donor-acceptor distance and donor-acceptor linkage (for **T1**–**T3** it is the *ET1* process).

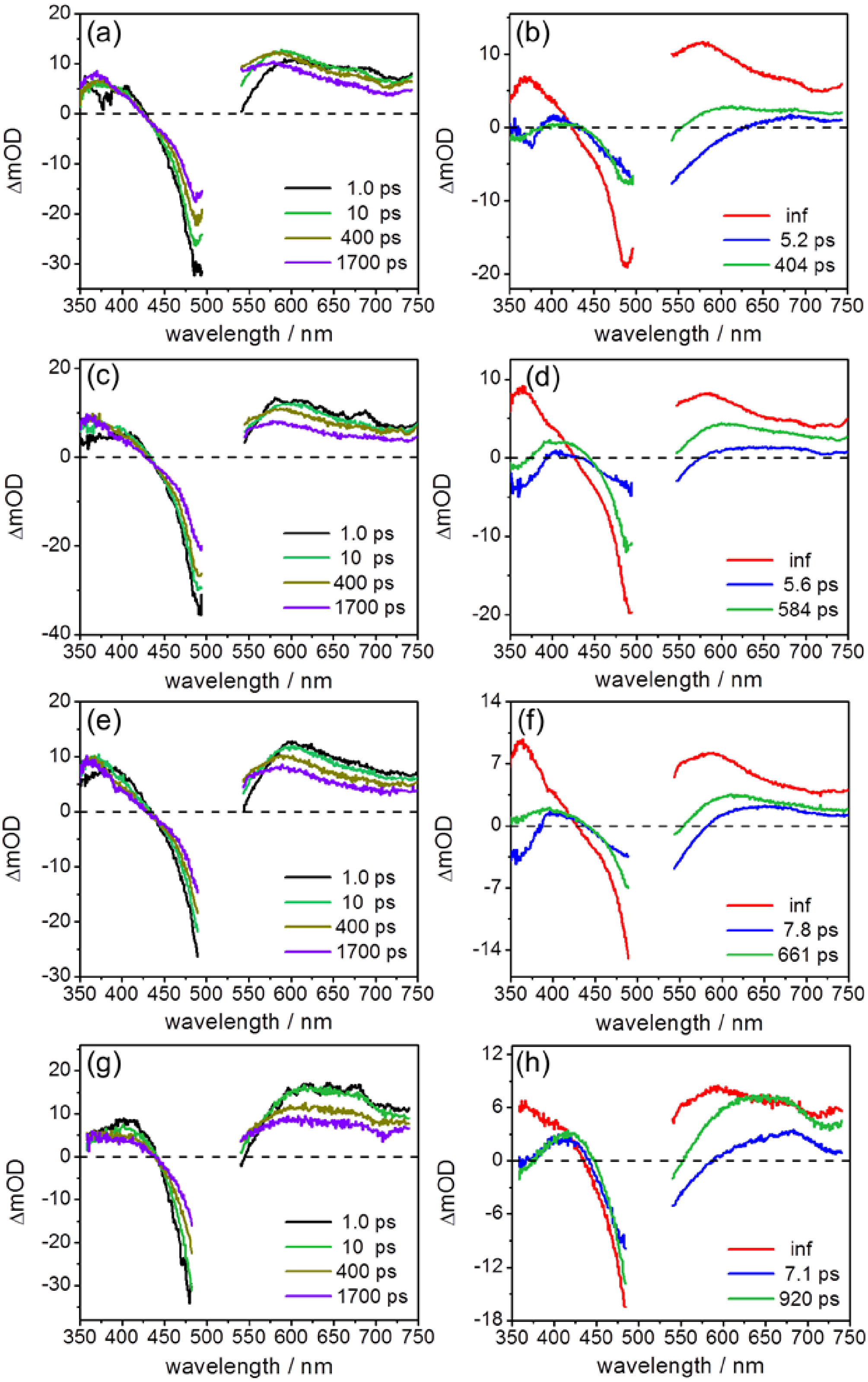

Figure 4.2. fs transient absorption spectra at selected delay times (a, c, e and g) and decay-associated spectra (b, d, f and h) of **D1** (a, b), **D2** (c, d), **D3** (e, f) and **D4** (g, h) in aerated dichloromethane upon excitation at 520 nm at 270 K.

	$\tau_{PTZ\rightarrow Ru(tpy)2}$ / ps						
	D1	**D2**	**D3**	**D4**	**T1**	**T2**	**T3**
300	5.0	4.6	6.4	5.1	2.0	3.8	3.7
280	5.4	5.2	7.5	5.6	2.2	3.2	6.0
270	5.2	5.6	7.8	7.1	2.5	5.0	6.7
260	6.4	5.9	8.3	9.3	3.2	5.3	7.6
250	7.1	6.8	9.2	12.6	2.9	4.7	9.0
240	8.3	7.6	10.8	–	3.5	–	10.0
230	–	–	–	–	–	6.0	14.0

Table 4.1. Temperature dependence of the time constants for the PTZ→Ru(tpy)$_2$* electron transfer process in **D1**–**D4** and **T1**–**T3**.

Time constants for PTZ→Ru(tpy)$_2$* electron transfer in **D1**–**D4** and **T1**–**T3** as a function of temperature are summarized in Table 4.1. In general, decelerated electron transfer rates (k_{ET} is used instead of k_{ET1} for **T1**–**T3** in this chapter) upon decreasing the temperatures are observed. It should be noted that the time constants for PTZ→Ru(tpy)$_2$* electron transfer are in the same timescale of rotational motion around the tpy–ph bond which was reported to be some-ps for Ru(tpy)$_2$-derived complexes.[91,126,127] This indicates that the PTZ→Ru(tpy)$_2$* electron transfer is likely accompanied by planarization of the tpy–ph ligand in **D2**–**D4** and **T2**–**T3**. To obtain H_{DA} values underlying PTZ→Ru(tpy)$_2$* electron transfer, the reformed Marcus equation was employed (eq 8). As shown in Figure 4.3, plotting $\ln(k_{ET}{\cdot}T^{1/2})$ *vs.* 1/T yields a single line for each compound. Parameters such as $-\Delta G$, λ, H_{DA} and $\Delta G^{\ddagger}$ extracted from Figure 4.3 are summarized in Table 4.2.

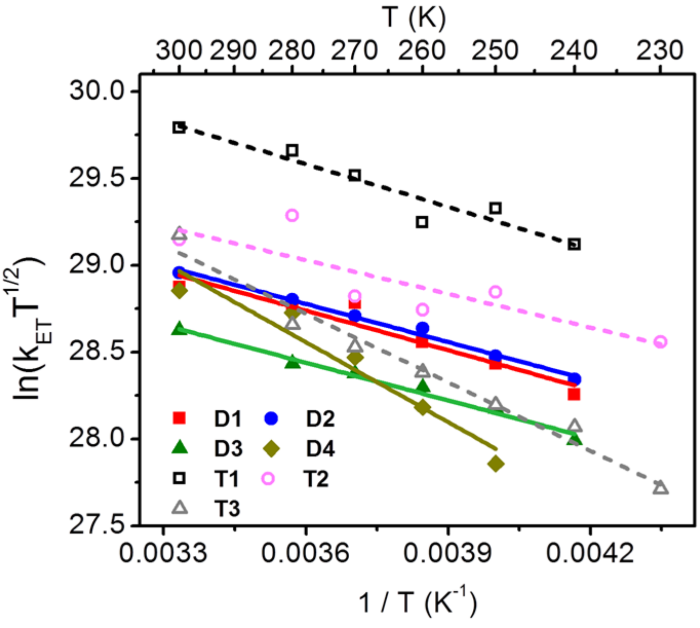

Figure 4.3. Plots of ln $(k_{ET}{\cdot}T^{1/2})$ *vs.* 1/T with the corresponding linear fit.

	PTZ→Ru(tpy)$_2$*						
	D1	**D2**	**D3**	**D4**	**T1**	**T2**	**T3**
$-\Delta G$ / eV	0.29	0.26	0.25	0.24	0.23	0.26	0.24
λ /eV	0.72	0.67	0.65	0.95	0.67	0.63	0.86
H_{DA} / cm^{-1}	94	90	74	371	157	86	265
$\Delta G^{\ddagger}$ / eV	0.064	0.063	0.062	0.13	0.072	0.054	0.11

Table 4.2. Summary of driving force ($-\Delta G$), reorganization energy (λ), electronic coupling (H_{DA}) and activation energy ($\Delta G^{\ddagger}$) extracted from the linear fit in Figure 4.3 for the PTZ→Ru(tpy)$_2$* electron transfer process.

It is apparent that $-\Delta G$ for PTZ→Ru(tpy)$_2$* electron transfer is quite similar within dyads and triads, *i.e.* only slight changes from 0.23 eV in **T1** to 0.29 eV in **D1** are observed (Table 4.2). The λ values for **D1**–**D3** and **T1**–**T2** are also rather similar due to the identical donor, donor-acceptor distance and the mutual orientation. However, **D4** and **T3** exhibit quite different λ values which are roughly 40% and 30% higher than others, respectively. It indicates that the inner-sphere reorganization energy (λ_i) must be significantly changed since the outer-sphere reorganization energy (λ_o) is not supposed to vary a lot according to the dielectric continuum model (eq 3–4). Notably, H_{DA} values are quite different among the dyads and triads which can be roughly divided into three regions: **D4** and **T3**, with the strongly electron-donating substituents $-OCH_3$ and $-OC_8H_{17}$, show the highest H_{DA} values (370~260 cm^{-1}); **T1** with a directly connected electron-withdrawing group $-C_{60}$ reveals a moderate coupling value (157 cm^{-1}); For **D1**–**D3** and **T2** the H_{DA} values are significantly lower (*i.e.* 90~70 cm^{-1}). These observations reveal that the substitution on the remote tpy ligand can significantly alter the electronic interaction between PTZ and photo-excited Ru complex. For example, the electron rich group $-OCH_3$ in **D4** increases the electronic coupling by a factor of 4 compared to **D3** despite of the minimal structural differences.

Since H_{DA} is mainly determined by the electronic structure of the molecular fragments involved, any changes of charge densities within the donor or acceptor would change H_{DA} values.[128] Thus, the influence of the substituent –R on charge densities is considered, which was previously investigated by theoretical calculations.[125,129] These studies focused on the ground-[125] and ^{1}MLCT excited-state[129] properties of two Ru(tpy)$_2$ derivatives in which a strong electron-donating ($-NH_2$) and electron-withdrawing ($-NO_2$) group was attached to the 4'-position of one tpy ligand *via* a phenyl spacer (–ph), respectively. Calculations illustrated that:

- $-NH_2$ substituent (electron-donating): A shortened tpy–ph bond and a smaller dihedral angel between tpy and ph in the ground state of the Ru complex was observed.[125] Moreover, significant charge depletion instead of accumulation at –ph–NH_2 moiety upon the ^{1}MLCT transition was shown.[129]

- –NO_2 substituent (electron-withdrawing): It facilitates long-range charge delocalization both in the ground- and excited-state albeit a relative larger tpy–ph dihedral angle in the ground state.[125,129]

In other words, opposing contributions of –NH_2 and –NO_2 to ground- and excited-state properties of $Ru(tpy)_2$ were found. Within the series of dyads and triads, the various H_{DA} values are tentatively explained as follows:

- (**D4** and **T3**) *vs.* (**D2**, **D3** and **T2**). The electron rich substituents –OCH_3 and –OC_8H_{17} in **D4** and **T3** give rise to the highest H_{DA} for PTZ→$Ru(tpy)_2$* electron transfer, which is accompanied by distinct increase of λ values (Table 4.2). The increased λ values in **D4** and **T3** is rationalized by the decreased tpy–ph bond length and smaller tpy–ph dihedral angle induced by the strong electron-donating groups (–OCH_3 and –OC_8H_{17}).[125] Thus, λ_i related to the free energy change associated with bond length changes upon electron transfer must be different.[26] On the other hand, the strong electron-donating groups change the electronic nature of the $Ru(tpy)_2$*. That is, the negative charges on the remote tpy ligand in **D4** and **T3** are more localized than that in **D2**, **D3** and **T2**. Hence, increased H_{DA} for PTZ→$Ru(tpy)_2$* electron transfer is observed. In addition, **T3** shows a lower H_{DA} value than **D4** (*i.e.* 265 *vs.* 371 cm^{-1}). This could be the reason that the two –OC_8H_{17} groups in **T3** have a longer distance to the tpy ligand than –OCH_3 in **D4**, and thus, a relative weak electronic effect on H_{DA} is observed in **T3**. Furthermore, there could be an additional contribution from the electron-withdrawing group –C_{60} in **T3** which pulls the negative charges away from the tpy ligand leading to further reduced charge densities adjacent to Ru. Under these combined effects, a relatively small H_{DA} value is observed in **T3** compared to **D4**.
- **D1** *vs.* **T1** (94 *vs.* 157 cm^{-1}). There is no planarization process within the remote tpy ligand for the two compounds. Replacing the –H atom by –C_{60} increases H_{DA} by 70%. It was found that the attachment of –C_{60} shifts the Ru^{III}/Ru^{II} oxidation anodically by 120 mV compared to **D1**.[95] The shifted HOMO apparently affects the electronic levels on the PTZ–tpy ligand and thus increases the coupling underlying the PTZ→$Ru(tpy)_2$* electron transfer.

The studies presented in this chapter reveal the possibility to modulate H_{DA} between the

PTZ donor and Ru(tpy)$_2$ acceptor *via* changing the substituent –R on the remote tpy ligand. Altering the electronic nature of the photo-excited Ru(tpy)$_2$, either by localization of the excited-state within the ligand sphere (*i.e.* by using strong electron-donating substituents) or by modifying the HOMO level of the Ru(II) center, impacts the electronic coupling for photoinduced electron transfer in structurally-related dyads and triads. Hence, the work provides an additional design parameter for transition-metal complexes based D–P–A systems in which achieving efficient and specific electron transfer paths is key to improve functions.

5. Summary

One aspect of artificial photosynthesis pays attention to the fundamental research on simple models (*e.g.* D–P–A triads) to understand how electron transfer rates depend on the molecular structures. This in turn provides guidelines to the design of more complex multi-component systems with specific functions. Considering the photosensitizers, Ru(II) polypyridyl complexes have drawn much attention due to the relatively wide absorption of the solar irradiation spanning from the UV (*i.e.* π-π transitions within the ligands) to the visible region (*via* metal-to-ligand charge transfer, MLCT). Apart from that, favorable properties of Ru(II) polypyridyl complexes, such as chemical robustness, ease of synthesis, relatively cheap starting materials, highly tunable optical and redox properties, also make them outstanding. In general, the photochemistry of Ru(II) polypyridyl complexes is discussed to starts from the lowest-lying ^{3}MLCT state. For efficient charge separation the ^{3}MLCT states should live long enough that the subsequent electron transfer can compete with the decay of the ^{3}MLCT states to ground state. In this respect, $Ru(tpy)_2$ is normally not considered as a good photosensitizer because of its intrinsic short ^{3}MLCT state lifetime which is roughly three orders of magnitude shorter than that in $Ru(bpy)_3$.

However, in this thesis, $Ru(tpy)_2$ was used as the photosensitizer to construct linear structures without inducing geometrical and optical isomers. The presented results show that charge separation takes place (from ps to ns timescales depending on the nature of D and A) in spite of the relatively short excited-state lifetime of the photosensitizer. The work provides a systematic investigation on the photoinduced electron transfer dynamics in $Ru(tpy)_2$ based molecular dyads and triads. **Chapter 2** focuses on the photochemistry of $Ru(tpy)_2$ heteroleptic complexes, especially the relaxation of the initially populated distinct ^{1}MLCT states. **Chapter 3** pays attention to the photoinduced electron transfer rates and their dependence on D–A distance and solvent polarity. Furthermore, the underlying mechanism for electron transfer is discussed *via* the combined analysis of distance- and temperature-dependent electron transfer rates. In **Chapter 4**, tuning of the electronic coupling between PTZ donor and $Ru(tpy)_2$ acceptor through the substitution pattern on a remote site (*i.e.* the second tpy ligand) is achieved.

In **Chapter 2**, three structurally related molecular triads are studied. First of all (**Chapter 2.1**), the photoinduced dynamics in model triad **T1** (*i.e.* PTZ–$Ru(tpy)_2$–C_{60}, see Figure 5.1) are discussed. It reveals that the initially generated two MLCT states, instead of populating the lowest-lying ^{3}MLCT state, decay *via* fast electron transfer (*ET*) and relatively slow energy transfer, respectively (Figure 5.1). This independent decay model is still valid for triads PTZ–Ru(tpy)$_2$–POM and exTTF–Ru(tpy)$_2$–POM (**Chapter 2.2**, also see Figure 5.1) in which two directions of electron transfer occurring in different timescales are identified. This is due to the ultrafast electron transfer occurs from a relatively high-lying ^{3}MLCT state (*i.e.* ^{3}MLCT$_{\text{D-tpy}}$ state, Figure 5.1), which can kinetically compete with the interligand charge transfer that typically leads to the lowest-lying ^{3}MLCT state.

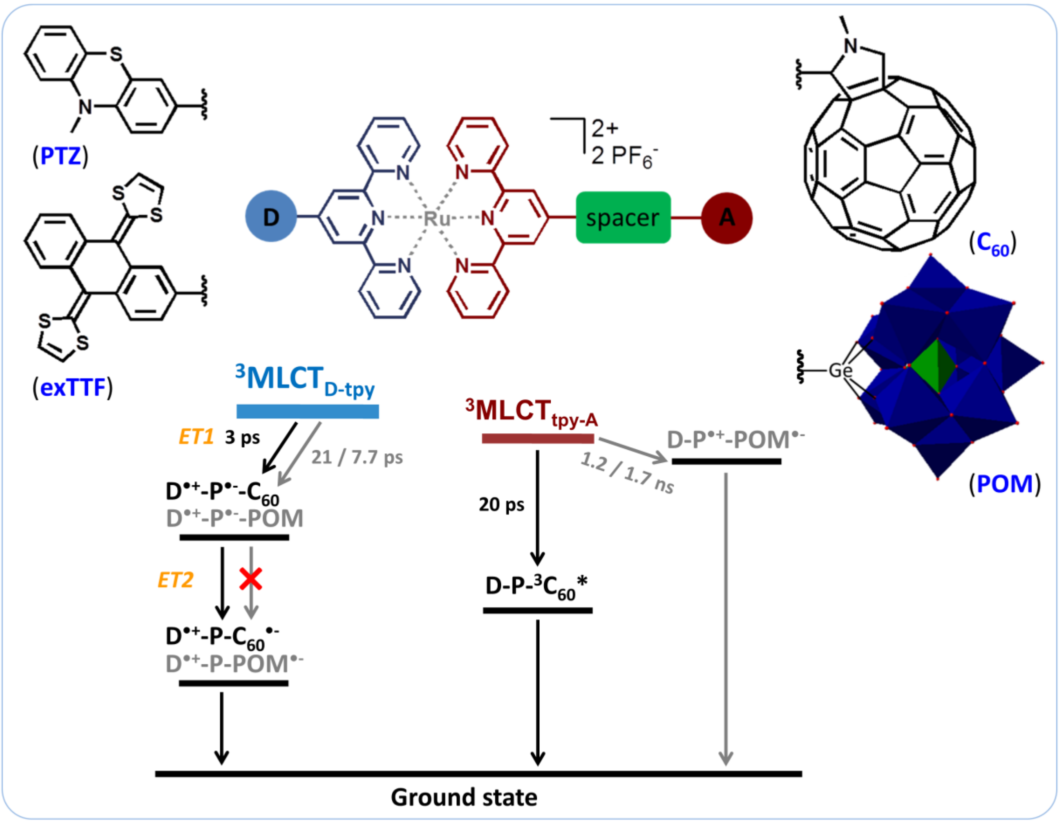

Figure 5.1. Simplified relaxation model upon excitation of the Ru(tpy)$_2$ photosensitizer in D–Ru(tpy)$_2$–A triads. Only the time constants related to the decay of ^{3}MLCT states are shown. The black arrows stand for the decay pathways for **T1** (D: PTZ, A: C_{60}) that except for the energy transfer, the fully charge-separated state is formed *via* the first (*ET1*) and second electron transfer (*ET2*) process. The grey arrows display the relaxation channels for **PTZ-Ru-POM** (time constants: grey left) and **exTTF-Ru-POM** (time constants: grey right). In this figure, P represents the Ru(tpy)$_2$ photosensitizer.

The studies (Figure 5.1) reveal that for heteroleptic Ru(tpy)$_2$ complex, photoexcitation would lead to differently distributed charges within the coordination sphere of the Ru(II) and the resultant MLCT states decay *via* different channels. This finding is interesting and important because the specific electron transfer does not kinetically compete with other processes, *e.g.* energy transfer, which would decrease the charge-separation efficiencies. Instead, the initial distribution of the specific MLCT states, which can be tuned by the excitation wavelength, determines the upper limit of molecules that can undergo intramolecular electron transfer (Figure 5.1). These results have important implications for the design of transition metal complexes based molecular assemblies with respect to a specifically targeted response to photoexcitation. In this case the distribution of the MLCT states should be considered.

Furthermore, for POM based molecular triads, no fully charge-separated state, *i.e.* $PTZ^{\bullet+}$–$Ru(tpy)_2$–$POM^{\bullet-}$ and $exTTF^{\bullet+}$–$Ru(tpy)_2$–$POM^{\bullet-}$, is not formed no matter which electron donor is used (**Chapter 2.1**, also Figure 5.1). Thus, it might be more useful to increase the driving force between $Ru(tpy)_2$ and POM to facilitate electron shifting from $Ru(tpy)_2^{\bullet-}$ to POM than tuning the electron donor. For the next step, either a different photosensitizer, *e.g.* a Ir(III) polypyridyl complex or a different POM which is easier to be reduced than the POM studied here, would be a promising way. Furthermore, it would be interesting to see if $PTZ^{\bullet+}$–$Ru(tpy)_2$–$POM^{\bullet-}$ and $exTTF^{\bullet+}$–$Ru(tpy)_2$–$POM^{\bullet-}$ can be formed when increasing the temperature.

Chapter 3.1 focuses on the photoinduced electron transfer rates and their dependence on D–A distance and solvent polarity. To this end, except for **T1**, two structurally-extended triads **T2** and **T3** are involved. The second electron transfer process (*i.e. ET2* in Figure 5.1) is of particular interest. It reveals that the distance dependence of k_{ET2} can be switched by changing the solvent polarity. Upon increasing the D–A distance, a decreased k_{ET2} is observed in dichloromethane while in acetonitrile k_{ET2} becomes faster for a longer distance. Up to now, the latter behavior is rarely reported in literature despite theory has predicated a regime in which the electron-transfer rates can increase with increasing D–A distance. The numerical simulation, based on the Marcus equation and a superexchange model reported by Wenger group[27], can only qualitatively rationalize the distinct distance dependence of k_{ET2}. This gives us a hint that either a model extension to account for a non-exponential distance dependent H_{DA} or the contribution from a different electron transfer mechanism, *i.e.* hopping, might have to be taken into account.

Next, the electron transfer mechanism for *ET2* in **T1**–**T3** is discussed in **Chapter 3.2**. For this purpose, k_{ET2} was recorded as a function of temperature (from 300 to 230 K). The combined analysis of distance- and temperature-dependent k_{ET2} indicate that superexchange is operative in **T1** and **T2** while hopping dominates in the longest triad **T3**. It is noteworthy that

ET2 via superexchange shows stronger temperature dependence than hopping, which is opposite to literature report. This is the first observation of superexchange having stronger temperature dependence than hopping, which is rationalized by the specific geometrical and electronic structure of the $Ru(tpy)_2$ photosensitizer. Hence, the presented studies indicate that the general observation that hopping has stronger temperature dependence than superexchange should not be treated as the only criterion for differentiating between the two mechanisms. Instead, the specific nature of the photosensitizer may have to be considered. The next step we could do is to increase the temperature above 300 K. Higher temperature facilitates the vibration of the two tpy ligands which in principle, according to the speculation here, will help the superexchange process in **T1** and **T2**. Additionally, it also would be interesting to see how k_{ET2} behaves in acetonitrile as a function of temperature since opposing distance dependence of k_{ET2} is observed in the two solvents.

The work in **Chapter 4** provides a new way to tune the electronic coupling between donor and acceptor (H_{DA}). Remarkable difference in H_{DA} between methoxyl- and methyl-substituted D–A dyads has been reported in literature, but in all these studies the molecular spacer was the one to be modified. In this chapter, distinct H_{DA} values underlying PTZ→$Ru(tpy)_2$* electron transfer in PTZ–$Ru(tpy)_2$–R dyads and triads are observed, which are altered by the substitution (*i.e.* –R) on the remote tpy ligand (which does not link the PTZ donor and Ru(II) core). Especially, with a constant driving force, H_{DA} between the PTZ donor and $Ru(tpy)_2$ acceptor is increased by a factor of four through changing –R from $–CH_3$ to $–OCH_3$. Furthermore, the direct attachment of $–C_{60}$ on the remote tpy ligand also increases the H_{DA} value compared to the dyad with a bare remote tpy ligand. This observation points out that changing the electronics in the photo-excited $Ru(tpy)_2$*, either by delocalization of the charges within the ligand sphere or by modifying the HOMO level of the Ru(II) ion can tune the H_{DA}. This finding provides an additional design parameter for molecular systems, in which realizing efficient and specific electron transfer paths is key to improved function. In the next step, it would be very interesting to study how the H_{DA} values would change by placing the $–OCH_3$ group at the *ortho*- and *meta*-position of the phenyl ring (to compare with the $–OCH_3$ group at the *para*-position studied here), or to see if the H_{DA} values can be increased by simply increasing the number of $–OCH_3$.

In short, the presented results extend our understanding of the properties of $Ru(tpy)_2$ photosensitizer, which highlight the importance of the distribution of MLCT states on the following decay pathways (**Chapter 2**) as well as the influence of the specific molecular geometry of Ru(tpy)$_2$ on the electron transfer dynamics (**Chapter 3** and **Chapter 4**). Both aspects are closely related to the functionalization of the peripheral ligands of the photosensitizer, which may provide important hint to the design of more complex multi-component systems in the future.

6. Zusammenfassung

Ein Aspekt der künstlichen Photosynthese ist die Grundlagenforschung an einfachen Modellen (z.B. D-P-A Triaden), um den Zusammenhang zwischen Molekularstrukturen und Elektronenübergängen zu verstehen. Dies liefert wiederum Richtlinien für das Design komplexerer Mehrkomponentensysteme mit spezifischen Funktionen. Bei den Photosensibilisatoren haben die Ru(II)-Polypyridylkomplexe aufgrund der relativ breiten Absorption von Sonnenlicht, die von UV Strahlung (d.h. π-π Übergänge innerhalb der Liganden) bis in den sichtbaren Bereich (*via* Metall-zu-Ligand Charge Transfer, MLCT) reicht, große Aufmerksamkeit erregt. Darüber hinaus zeichnen sich Ru(II)-Polypyridylkomplexe durch ihre günstigen Eigenschaften, wie chemische Beständigkeit, einfache Synthese, verhältnismäßig billige Ausgangsmaterialien, sowie hochabstimmbare optische und Redoxeigenschaften aus. Im Allgemeinen wird die Photochemie von Ru(II)-Polypyridylkomplexen ausgehend vom energetisch niedrigsten ^{3}MLCT-Zustand diskutiert. Für eine effiziente Ladungstrennung sollten die ^{3}MLCT-Zustände so lange leben, dass der nachfolgende Elektronentransfer mit dem Zerfall der ^{3}MLCT-Zustände in den Grundzustand konkurrieren kann. In dieser Hinsicht wird $Ru(tpy)_2$ normalerweise nicht als guter Photosensibilisator angesehen, da seine intrinsisch kurze ^{3}MLCT-Zustandslebensdauer etwa drei Größenordnungen kürzer ist als die von $Ru(bpy)_3$.

Dennoch wurde in dieser Arbeit $Ru(tpy)_2$ als Photosensibilisator verwendet, um lineare Strukturen zu konstruieren, ohne hierbei geometrische und optische Isomere zu erzeugen. Die vorgestellten Ergebnisse zeigen, dass trotz der relativ kurzen Lebensdauer des Photosensibilisators eine Ladungstrennung (von ps- bis ns-Zeitskalen je nach Art von Donor und Akzeptor) stattfindet. Die Arbeit bietet eine systematische Untersuchung der photoinduzierten Elektronentransferdynamik in $Ru(tpy)_2$-basierten molekularen Dyaden und Triaden. **Kapitel 2** konzentriert sich auf die Photochemie von $Ru(tpy)_2$ heteroleptischen Komplexen, insbesondere die Relaxation der zunächst populierten unterschiedlichen ^{1}MLCT-Zustände. In **Kapitel 3** wird auf die photoinduzierten Elektronentransferraten und deren Abhängigkeit von D-A-Abstand und Lösungsmittelpolarität eingegangen. Darüber hinaus wird der zugrunde liegende Mechanismus für den Elektronentransfer durch die kombinierte Analyse von distanz- und temperaturabhängigen Elektronentransferraten diskutiert. In **Kapitel 4** wird die Abstimmung der elektronischen Kopplung zwischen PTZ-Donor und $Ru(tpy)_2$-Akzeptor durch das Substitutionsmuster an einer entlegenen Stelle (d.h. dem zweiten tpy-Liganden) erreicht.

In **Kapitel 2** werden drei strukturell verwandte molekulare Triaden untersucht. Zunächst (**Kapitel 2.1**) wird die photoinduzierte Dynamik in der Modelltriade **T1** (d.h. PTZ-Ru(tpy)$_2$-C$_{60}$, siehe Abbildung 6.1) diskutiert. Es zeigt sich, dass die ursprünglich erzeugten zwei MLCT-Zustände durch schnellen Elektronentransfer (ET) bzw. relativ langsamen Energietransfer zerfallen (Abbildung 6.1), anstatt den niedrigsten ^{3}MLCT-Zustand zu bevölkern. Dieses unabhängige Zerfallsmodell gilt weiterhin für die Triaden PTZ-Ru(tpy)$_2$-POM und exTTF-Ru(tpy)$_2$-POM (**Kapitel 2.2**, siehe auch Abbildung 6.1), in denen zwei Richtungen des Elektronentransfers in unterschiedlichen Zeitabständen identifiziert wurden. Dies liegt daran, dass der ultraschnelle Elektronentransfer aus einem verhältnismäßig hochliegenden ^{3}MLCT-Zustand (d.h. ^{3}MLCT$_{\text{D-tpy}}$-Zustand, Abbildung 6.1) erfolgt, der mit dem Interligand-Ladungstransfer, der typischerweise zum niedrigsten ^{3}MLCT-Zustand führt, kinetisch konkurrieren kann.

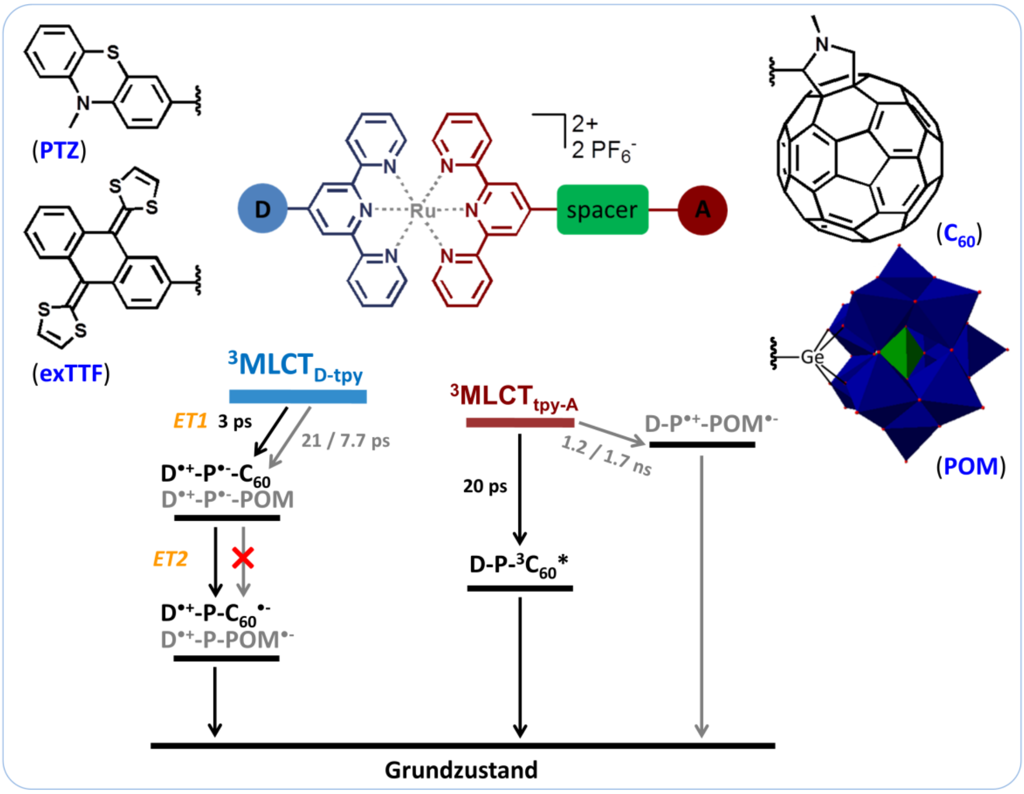

Abbildung 6.1. Vereinfachtes Relaxationsmodell nach Anregung des Ru(tpy)$_2$ Photosensibilisators in D–Ru(tpy)$_2$–A Triaden. Es werden nur die Zeitkonstanten gezeigt, die sich auf den Zerfall von ^{3}MLCT-Zuständen beziehen. Die schwarzen Pfeile stellen die Zerfallspfade für **T1** (D: PTZ, A: C$_{60}$) dar, das bis auf den Energietransfer des vollständig ladungsgetrennten Zustands durch den ersten (*ET1*) und zweiten Elektronentransfer (*ET2*) Prozess gebildet wird. Die grauen Pfeile zeigen die Relaxationskanäle für **PTZ-Ru-POM** (Zeitkonstanten: grau links) und **exTTF-Ru-POM** (Zeitkonstanten: grau rechts). In dieser Abbildung stellt P den Ru(tpy)$_2$ Photosensibilisator dar.

Die Studien (Abbildung 6.1) zeigen, dass für den heteroleptischen Ru(tpy)$_2$-Komplex die Photoanregung zu unterschiedlich verteilten Ladungen innerhalb der Koordinationssphäre des Ru(II) führen würde und die resultierenden MLCT-Zustände über verschiedene Kanäle zerfallen. Dieser Befund ist interessant und wichtig, da der spezifische Elektronentransfer nicht kinetisch mit anderen Prozessen konkurriert, z.B. dem Energietransfer, was die Effizienz der Ladungsseparation verringern würde. Stattdessen bestimmt die Anfangsverteilung der spezifischen MLCT-Zustände, die durch die Anregungswellenlänge beeinflusst werden kann, den oberen Grenzwert der Moleküle, die für einen intramolekularen Elektronentransfer infrage kommen (Abbildung 6.1). Diese Ergebnisse liefern wichtige Erkenntnisse für das Design von Übergangsmetallkomplexen mit molekularen Anordnungen in Bezug auf spezifische Reaktion nach Photoanregung. In diesem Fall sollte die Verteilung der MLCT-Zustände berücksichtigt werden.

Darüber hinaus wird für POM-basierte molekulare Triaden kein vollständig ladungsgetrennter Zustand, d.h. PTZ$^{\bullet+}$-Ru(tpy)$_2$-POM$^{\bullet-}$ und exTTF$^{\bullet+}$-Ru(tpy)$_2$-POM$^{\bullet-}$, gebildet, unabhängig davon, welcher Elektronendonor verwendet wird (**Kapitel 2.1**, auch Abbildung 6.1). Daher könnte es sinnvoller sein, die Antriebskraft zwischen Ru(tpy)$_2$ und POM zu erhöhen, um den Elektronenwechsel von Ru(tpy)$_2^{\bullet-}$ zu POM zu erleichtern, als den Elektronendonor zu modifizieren. Für den nächsten Schritt wäre entweder ein anderer Photosensibilisator wie z.B. ein Ir(III)-Polypyridylkomplex oder ein anderer POM, der leichter zu reduzieren ist als der hier untersuchte POM, ein vielversprechender Weg. Darüber hinaus wäre es interessant zu sehen, ob PTZ$^{\bullet+}$-Ru(tpy)$_2$-POM$^{\bullet-}$ und exTTF$^{\bullet+}$-Ru(tpy)$_2$-POM$^{\bullet-}$ bei Temperaturerhöhung gebildet werden können.

Kapitel 3.1 konzentriert sich auf die photoinduzierten Elektronentransferraten und deren Abhängigkeit von D-A-Abstand und Lösungsmittelpolarität. Zu diesem Zweck sind, mit Ausnahme von **T1**, zwei strukturell erweiterte Triaden **T2** und **T3** beteiligt. Von besonderem Interesse ist der zweite Elektronenübertragungsprozess (z.B. *ET2* in Abbildung 6.1). Es zeigt sich, dass die Abstandsabhängigkeit von k_{ET2} durch Änderung der Lösungsmittelpolarität geschaltet werden kann. Mit zunehmender D-A-Distanz wird bei Dichlormethan ein verminderter k_{ET2}-Wert beobachtet, während bei Acetonitril k_{ET2} über eine längere Distanz schneller wird. Bisher wird letzteres Verhalten in der Literatur nur selten berichtet, obwohl die Theorie ein System vorausgesagt hat, in dem die Elektronentransferraten mit zunehmender D-A-Distanz zunehmen können. Die numerische Simulation, die auf der Marcus-Gleichung und einem von der Wenger-Gruppe[27] berichteten Superaustauschmodell basiert, kann die unterschiedliche Entfernungsabhängigkeit von k_{ET2} nur qualitativ rationalisieren. Dies gibt uns einen Hinweis darauf, dass entweder eine Modellerweiterung zur Berücksichtigung einer nicht exponentiellen entfernungsabhängigen H_{DA} (die elektronische Kopplung zwischen Donor und Akzeptor) oder der Beitrag eines anderen Elektronenübertragungsmechanismus, d.h. des *Hoppings*, berücksichtigt werden muss.

Als nächstes wird der Elektronenübertragungsmechanismus für *ET2* in **T1**-**T3** in **Kapitel 3.2** beschrieben. Zu diesem Zweck wurde k_{ET2} als Funktion der Temperatur (von 300 bis 230 K) aufgezeichnet. Die kombinierte Analyse von entfernungs- und temperaturabhängigem k_{ET2} zeigt, dass der *Superexchange* in **T1** und **T2** wirksam ist, während das *Hopping* in der längsten Triade **T3** dominiert. Bemerkenswert ist, dass *ET2* über den *Superexchange* eine stärkere Temperaturabhängigkeit aufweist als das *Hopping*, was der Literatur widerpricht. Dies ist die erste Beobachtung eines *Superexchanges* mit stärkerer Temperaturabhängigkeit als das *Hopping*, welches durch die spezifische geometrische und elektronische Struktur des $Ru(tpy)_2$-Photosensibilisators rationalisiert wird. Daher deuten die vorgestellten Studien darauf hin, dass die allgemein beobachtete Temperaturempfindlichkeit, nicht als das einzige Kriterium für die Unterscheidung zwischen den beiden Mechanismen behandelt werden sollte. Stattdessen kann die spezifische Beschaffenheit des Photosensibilisators berücksichtigt werden. Der nächste mögliche Schritt wäre, die Temperatur auf über 300 K zu erhöhen. Eine höhere Temperatur erleichtert die Vibration der beiden tpy-Liganden, was nach den vorliegenden Spekulationen im Prinzip dem *Superexchange* Prozess in **T1** und **T2** helfen wird. Darüber hinaus wäre es auch interessant zu sehen, wie sich k_{ET2} in Acetonitril als Funktion der Temperatur verhält, da in den beiden Lösungsmitteln eine entgegengesetzte Abstandsabhängigkeit von k_{ET2} beobachtet wird.

Die Arbeit in **Kapitel 4** bietet einen neuen Weg, die elektronische Kopplung zwischen Donor und Akzeptor (H_{DA}) einzustellen. Bemerkenswerte Unterschiede der H_{DA} zwischen Methoxyl- und methylsubstituierten D-A-Dyaden wurden in der Literatur berichtet, aber in all diesen Studien war der molekulare Abstandshalter derjenige, der modifiziert werden musste. In diesem Kapitel werden verschiedene H_{DA}-Werte beobachtet, die dem Elektronentransfer von PTZ→$Ru(tpy)_2$* in PTZ-$Ru(tpy)_2$-R Dyaden und Triaden zugrunde liegen, die durch die Substitution (d.h. -R) am entlegenen tpy-Liganden (der den PTZ-Donor und den Ru(II)-Kern nicht verbindet) verändert werden. Insbesondere bei konstanter Antriebskraft wird die H_{DA} zwischen dem PTZ-Donor und dem $Ru(tpy)_2$-Akzeptor durch die Änderung –des Restes von -CH_3 auf -OCH_3 um den Faktor vier erhöht. Darüber hinaus erhöht die direkte Bindung von -

C_{60} an den entfernten tpy-Liganden auch den H_{DA}-Wert im Vergleich zur Dyade mit einem unsubstituierten entlegenen tpy-Liganden. Diese Beobachtung weist darauf hin, dass ein Wechsel der Elektronik im photoangeregten $Ru(tpy)_2$*, entweder durch Verlagerung der Ladungen innerhalb der Ligandensphäre oder durch Änderung des HOMO-Niveaus des Ru(II)-Ions, die H_{DA} verändern kann. Dieser Befund stellt einen zusätzlichen Designparameter für molekulare Systeme dar, bei dem die Realisierung effizienter und spezifischer Elektronenübertragungswege der Schlüssel zu einer verbesserten Funktion ist. Im nächsten Schritt wäre es sehr interessant zu untersuchen, wie sich die H_{DA}-Werte ändern würden, indem man die $-OCH_3$-Gruppe an der *ortho*- und *meta*-Position des Phenylrings platziert (im Vergleich zur $-OCH_3$-Gruppe an der hier untersuchten *para*-Position), oder ob die H_{DA}-Werte durch einfache Erhöhung der Anzahl von $-OCH_3$ erhöht werden können.

Kurz gesagt, die vorgestellten Ergebnisse erweitern unser Verständnis für die Eigenschaften des $Ru(tpy)_2$-Photosensibilisators, die die Bedeutung der Verteilung von MLCT-Zuständen auf den folgenden Relaxationspfaden (**Kapitel 2**) sowie den Einfluss der spezifischen Molekulargeometrie von $Ru(tpy)_2$ auf die Elektronentransferdynamik (**Kapitel 3** und **Kapitel 4**) hervorheben. Beide Aspekte stehen in engem Zusammenhang mit der Funktionalisierung der peripheren Liganden des Photosensibilisators, die einen wichtigen Hinweis auf das Design komplexerer Mehrkomponentensysteme in der Zukunft geben können.

Bibliography

[1]. M. Z. Jacobson, *Earth's Future*, **2017**, *5*, 948–952.

[2]. M. N. Anwara, A. Fayyaza, N. F. Sohaila, M. F. Khokharb, M. Baqara, W. D. Khana, K. Rasoolc, M. Rehand, A. S. Nizamid, *J. Environ. Manage.*, **2018**, *226*, 131–144.

[3]. A. M. Abdalla, S. Hossain, O. B. Nisfindy, A. T. Azad, M. Dawood, A. K. Azad, *Energy Convers. Manage.*, **2018**, *165*, 602–627.

[4]. M. D. Kärkäs, O. Verho, E. V. Johnston, B. Åkermark, *Chem. Rev.*, **2014**, *114*, 11863–120001.

[5]. M. Rudolf, S. V. Kirner, D. M. Guldi, *Chem. Soc. Rev.*, **2016**, *45*, 612–630.

[6]. N. S. Lewis, *Science*, **2016**, *351*, aad1920.

[7]. L. Hammarström, *Faraday Discuss.*, **2017**, *198*, 549–560.

[8]. F. Kuttassery, S. Mathew, S. N. Remello, A. Thomas, K. Sano, Y. Ohsaki, Y. Nabetani, H. Tachibana, H. Inoue, *Coord. Chem. Rev.*, **2018**, *377*, 64–72.

[9]. D. Rehm, A. Weller, *Isr. J. Chem.*, **1970**, *8*, 259–271.

[10]. M. Tachiya, S. Murata, *J. Phys. Chem.*, **1992**, *96*, 8441–8444.

[11]. M. Natali, S. Campagna, F. Scandola, *Chem. Soc. Rev.*, **2014**, *43*, 4005–4018.

[12]. O. S. Wenger, *Coord. Chem. Rev.*, **2015**, *282–283*, 150–158.

[13]. M. Gilbert, B. Albinsson, *Chem. Soc. Rev.*, **2015**, *44*, 845–862.

[14]. C. Schubert, J. T. Margraf, T. Clark, D. M. Guldi, *Chem. Soc. Rev.*, **2015**, *44*, 988–998.

[15]. N. T. La Porte, J. F. Martinez, S. Chaudhuri, S. Hedström, V. S. Batista, M. R. Wasielewski, *Coord. Chem. Rev.*, **2018**, *361*, 98–119.

[16]. S. Tschierlei, M. Presselt, C. Kuhnt, A. Yartsev, T. Pascher, V. Sundström, M. Karnahl, M. Schwalbe, B. Schäfer, S. Rau, M. Schmitt, B. Dietzek, J. Popp, *Chem. Eur. J.*, **2009**, *15*, 7678–7688.

[17]. S. Fukuzumi, Y. Yamada, T. Suenobu, K. Ohkubo, H. Kotani, *Energy Environ. Sci.*, **2011**, *4*, 2754–2766.

[18]. J. F. Martinez, N. T. La Porte, C. M. Mauck, M. R. Wasielewski, *Faraday Discuss.*, **2017**, *198*, 235–249.

[19]. Y. Kuramochi, O. Ishitani, H. Ishida, *Coord. Chem. Rev.*, **2018**, *373*, 333–356.

[20]. J. R. Pinzon, D. C. Gasca, S. G. Sankaranarayanan, G. Bottari, T. Torres, D. M. Guldi, L. Echegoyen, *J. Am. Chem. Soc.*, **2009**, *131*, 7727–7734.

[21]. B. R. Gautam, R. Younts, W. T. Li, L. Yan, E. Danilov, E. Klump, I. Constantinou, F. So, W. You, H. Ade, K. Gundogdu, *Adv. Energy Mater.*, **2016**, *6*, 1501032.

[22]. K. A. Mazzio, C. K. Luscombe, *Chem. Soc. Rev.*, **2015**, *44*, 78–90.

[23]. R. A. Marcus, N. Sutin, *Biochim. Biophys. Acta*, **1985**, *811*, 265–322.

[24]. M. Kuss-Petermann, O. S. Wenger, *J. Am. Chem. Soc.*, **2016**, *138*, 1349−1358.

[25]. H. Imahori, K. Tamaki, D. M. Guldi, C. Luo, M. Fujitsuka, O. Ito, Y. Sakata, S. Fukuzumi, *J. Am. Chem. Soc.*, **2001**, *123*, 2607−2617.

[26]. G. J. Kavarnos, N. J. Turro, *Chem. Rev.*, **1986**, *86*, 401–449.

[27]. M. Kuss-Petermann, O. S. Wenger, *Phys. Chem. Chem. Phys.*, **2016**, *18*, 18657–18664.

[28]. E. Göransson, J. Boixel, J. Fortage, D. Jacquemin, H.-C. Becker, E. Blart, L. Hammarström, F. Odobel, *Inorg. Chem.*, **2012**, *51*, 11500–11512.

[29]. M. Kuss-Petermann, O. S. Wenger, *Angew. Chem. Int. Ed.*, **2016**, *55*, 815–819.

[30]. T. Higashino, T. Yamada, M. Yamamoto, A. Furube, N. V. Tkachenko, T. Miura, Y. Kobori, R. Jono, K. Yamashita, H. Imahori, *Angew. Chem. Int. Ed.*, **2016**, *55*, 629–633.

[31]. C. Lambert, G. Nöll, J. Schelter, *Nat. Mater.*, **2002**, *1*, 69–73.

[32]. R. N. Sampaio, E. J. Piechota, L. Troian-Gautier, A. B. Maurer, K. Hu, P. A. Schauer, A. D. Blair, C. P. Berlinguette, G. J. Meyer, *Proc. Natl. Acad. Sci. U.S.A.*, **2018**, *115*, 7248–7253.

[33]. D. Hanss, M. E. Walther, O. S. Wenger, *Chem. Commun.*, **2010**, *46*, 7034–7036.

[34]. M. P. Eng, B. Albinsson, *Angew. Chem. Int. Ed.*, **2006**, *45*, 5626–5629.

[35]. M. U. Winters, J. Kärnbratt, H. E. Blades, C. J. Wilson, M. J. Frampton, H. L. Anderson, B. Albinsson, *Chem. Eur. J.*, **2007**, *13*, 7385–7394.

[36]. Y. Zhao, X. Li, Z. Wang, W. Yang, K. Chen, J. Zhao and G. G. Gurzadyan, *J. Phys. Chem. C*, **2018**, *122*, 3756–3772.

[37]. S. Fukuzumi, K. Ohkubo and T. Suenobu, *Acc. Chem. Res.*, **2014**, *47*, 1455–1464.

[38]. J. Petersson, M. Eklund, J. Davidsson, L. Hammarström, *J. Am. Chem. Soc.*, **2009**, *131*, 7940–7941.

[39]. M. Wielopolski, G. M. Rojas, C. Pol, L. Brinkhaus, G. Katsukis, M. R. Bryce, T. Clark, D. M. Guldi, *ACS Nano*, **2010**, *4*, 6449–6462.

[40]. S.-H. Lee, A. G. Larsen, K. Ohkubo, Z.-L. Cai, J. R. Reimers, S. Fukuzumi, M. J. Crossley, *Chem. Sci.*, **2012**, *3*, 257–269.

[41]. M. Natali, M. Ravaglia, F. Scandola, J. Boixel, Y. Pellegrin, E. Blart, F. Odobel, *J. Phys. Chem. C*, **2013**, *117*, 19334–19345.

[42]. S. Wenger, P.-A. Bouit, Q. Chen, J. Teuscher, D. D. Censo, R. Humphry-Baker, J.-E. Moser, J. L. Delgado, N. Martín, S. M. Zakeeruddin, M. Grätzel, *J. Am. Chem. Soc.*, **2010**, *132*, 5164–5169.

[43]. Y. Takano, M. A. Herranz, N. Martín, S. G. Radhakrishnan, D. M. Guldi, T. Tsuchiya, S. Nagase, T. Akasaka, *J. Am. Chem. Soc.*, **2010**, *132*, 8048–8055.

[44]. S.-H. Lee, C. T.-L. Chan, K. M.-C. Wong, W. H. Lam, W.-M. Kwok, V. W.-W. Yam, *J. Am. Chem. Soc.*, **2014**, *136*, 10041–10052.

[45]. T. Kamimura, K. Ohkubo, Y. Kawashima, S. Ozako, K. Sakaguchi, S. Fukuzumi, F. Tani, *J. Phys. Chem. C*, **2015**, *119*, 25634–25650.

[46]. J. Wiberg, L. Guo, K. Pettersson, D. Nilsson, T. Ljungdahl, J. Mårtensson, B. Albinsson, *J. Am. Chem. Soc.*, **2007**, *129*, 155–163.

[47]. I. A. Howard, F. Laquai, P. E. Keivanidis, R. H. Friend, N. C. Greenham, *J. Phys. Chem. C*, **2009**, *113*, 21225–21232.

[48]. S. T. J. Ryan, R. M. Young, J. J. Henkelis, N. Hafezi, N. A. Vermeulen, A. Hennig, E. J. Dale, Y. Wu, M. D. Krzyaniak, A. Fox, W. M. Nau, M. R. Wasielewski, J. F. Stoddart, O. A. Scherman, *J. Am. Chem. Soc.*, **2015**, *137*, 15299–15307.

[49]. S. V. Kirner, C. Henkel, D. M. Guldi, J. D. M. Jr, D. I. Schuster, *Chem. Sci.*, **2015**, *6*, 7293–7304.

[50]. M. Yamamoto, J. Fohlinger, J. Petersson, L. Hammarström, H. Imahori, *Angew. Chem. Int. Ed.*, **2017**, *56*, 3329–3333.

[51]. B. Matt, C. Coudret, C. Viala, D. Jouvenot, F. Loiseau, G. Izzet, A. Proust, *Inorg. Chem.*, **2011**, *50*, 7761–7768.

[52]. A. Yokoyama, T. Kojima, K. Ohkubo, M. Shiro, S. Fukuzumi, *J. Phys. Chem. A*, **2011**, *115*, 986–997.

[53]. O. S. Wenger, *Chem. Soc. Rev.*, **2011**, *40*, 3538–3550.

[54]. J. R. Winkler, H. B. Gray, *J. Am. Chem. Soc.*, **2014**, *136*, 2930−2939.

[55]. D. M. Guldi, M. Prato, *Acc. Chem. Res.*, **2000**, *33*, 695−703.

[56]. A. Harriman, K. J. Elliott, M. A. H. Alamiry, L. Le Pleux, M. Severac, Y. Pellegrin, E. Blart, C. Fosse, C. Cannizzo, C. R. Mayer, F. Odobel, *J. Phys. Chem. C*, **2009**, *113*, 5834–5842.

[57]. Y.-T. Kao, X. Guo, Y. Yang, Z. Liu, A. Hassanali, Q.-H. Song, L. Wang, D. Zhong, *J. Phys. Chem. B*, **2012**, *116*, 9130−9140.

[58]. M. E. Walther, O. S. Wenger, *ChemPhysChem*, **2009**, *10*, 1203–1206.

[59]. J. Jortner, M. Bixon, T. Langenbacher, M. E. Michel-Beyerle, *Proc. Natl. Acad. Sci. U.S.A.*, **1998**, *95*, 12759–12765.

[60]. A. B. Ricks, K. E. Brown, M. Wenninger, S. D. Karlen, Y. A. Berlin, D. T. Co, M. R. Wasielewski, *J. Am. Chem. Soc.*, **2012**, *134*, 4581−4588.

[61]. M. G. Gatty, A. Kahnt, L. J. Esdaile, M. Hutin, H. L. Anderson, B. Albinsson, *J. Phys. Chem. B*, **2015**, *119*, 7598−7611.

[62]. W. B. Davis, W. A. Svec, M. A. Ratner, M. R. Wasielewski, *Nature*, **1998**, *396*, 60−63.

[63]. J. Jiang, A. Alsam, S. Wang, S. M. Aly, Z. Pan, O. F. Mohammed, K. S. Schanze, *J. Phys. Chem. A*, **2017**, *121*, 4891−4901.

[64]. E. A. Weiss, M. J. Ahrens, L. E. Sinks, A. V. Gusev, M. A. Ratner, M. R. Wasielewski, *J. Am. Chem. Soc.*, **2004**, *126*, 5577–5584.

[65]. T. Miura, R. Carmieli, M. R. Wasielewski, *J. Phys. Chem. A*, **2010**, *114*, 5769–5778.

[66]. N. Renaud, M. A. Harris, A. P. N. Singh, Y. A. Berlin, M. A. Ratner, M. R. Wasielewski, F. D. Lewis, F. C. Grozema, *Nat. Chem.*, **2016**, *8*, 1015–1021.

[67]. A. Paul, R. M. Watson, E. Wierzbinski, K. L. Davis, A. Sha, C. Achim, D. H. Waldeck, *J. Phys. Chem. B*, **2010**, *114*, 14140–14148.

[68]. X. Zhao, C. Huang, M. Gulcur, A. S. Batsanov, M. Baghernejad, W. Hong, M. R. Bryce, T. Wandlowski, *Chem. Mater.*, **2013**, *25*, 4340−4347.

[69]. D. Bu, Y. Xiong, Y. N. Tan, M. Meng, P. J. Low, D.-B. Kuang, C. Y. Liu, *Chem. Sci.*, **2018**, *9*, 3438–3450.

[70]. C. E. Smith, S. O. Odoh, S. Ghosh, L. Gagliardi, C. J. Cramer, C. Daniel Frisbie, *J. Am. Chem. Soc.*, **2015**, *137*, 15732–15741.

[71]. A. Kahnt, J. Kärnbratt, L. J. Esdaile, M. Hutin, K. Sawada, H. L. Anderson, B. Albinsson, *J. Am. Chem. Soc.*, **2011**, *133*, 9863–9871.

[72]. V. Lloveras, J. Vidal-Gancedo, T. M. Figueira-Duarte, J.-F. Nierengarten, J. J. Novoa, F. Mota, N. Ventosa, C. Rovira, J. Veciana, *J. Am. Chem. Soc.*, **2011**, *133*, 5818–5833.

[73]. F. Giacalone, J. L. Segura, N. Martín, D. M. Guldi, *J. Am. Chem. Soc.*, **2004**, *126*, 5340–5341.

[74]. M. Wielopolski, G. de Miguel Rojas, C. van der Pol, L. Brinkhaus, G. Katsukis, M. R. Bryce, T. Clark, D. M. Guldi, *ACS Nano*, **2010**, *4*, 6449–6462.

[75]. G. Yzambart, A. Zieleniewska, S. Bauroth, T. Clark, M. R. Bryce, D. M. Guldi, *J. Phys. Chem. C*, **2017**, *121*, 13557−13569.

[76]. J. Kroon, H. Oevering, J. W. Verhoeven, J. M. Warman, A. M. Oliver, M. N. Paddon-Row, *J. Phys. Chem.*, **1993**, *97*, 5065–5069.

[77]. R. H. Goldsmith, O. DeLeon, T. M. Wilson, D. Finkelstein-Shapiro, M. A. Ratner, M. R. Wasielewski, *J. Phys. Chem. A*, **2008**, *112*, 4410–4414.

[78]. P. P. Lainé, S. Campagna, F. Loiseaub, *Coord. Chem. Rev.*, **2008**, *252*, 2552–2571.

[79]. Y. Zhang, M. Schulz, M. Wächtler, M. Karnahl, B. Dietzek, *Coord. Chem. Rev.*, **2018**,

356, 127–146.

[80]. O. S. Wenger, *Coord. Chem. Rev.*, **2009**, *253*, 1439–1457.

[81]. C. Reichardt, T. Sainuddin, M. Wächtler, S. Monro, S. Kupfer, J. Guthmuller, S. Gräfe, S. McFarland, B. Dietzek, *J. Phys. Chem. A*, **2016**, *120*, 6379−6388.

[82]. M. Maestri, N. Armaroli, V. Balzani, E. C. Constable, A. M. W. Cargill Thompson, *Inorg. Chem.*, **1995**, *34*, 2159−2161.

[83]. E. Baranoff, J.-P. Collin, L. Flamigni, J.-P. Sauvage, *Chem. Soc. Rev.*, **2004**, *33*, 147–155.

[84]. A. K. Pal, G. S. Hanan, *Chem. Soc. Rev.*, **2014**, *43*, 6184–6197.

[85]. K. Barthelmes, A. Winter, U. S. Schubert, *Dalton Trans.*, **2016**, *45*, 14855–14882.

[86]. J. V. Caspar, T. J. Meyer, *J. Am. Chem. Soc.*, **1983**, *105*, 5583–5590.

[87]. M. Wächtler, J. Kübel, K. Barthelmes, A. Winter, A. Schmiedel, T. Pascher, C. Lambert, U. S. Schubert, B. Dietzek, *Phys. Chem. Chem. Phys.*, **2016**, *18*, 2350–2360.

[88]. J.-P. Sauvage, J.-P. Collin, J.-C. Chambron, S. Guillerez, C. Coudret, V. Baltani, F. Barigelletti, L. D. Cola, L. Flamigni, *Chem. Rev.*, **1994**, *94*, 993–1019.

[89]. A. T. Yeh, C. V. Shank, J. K. McCusker, *Science*, **2000**, *289*, 935–938.

[90]. A. Cannizzo, F. van Mourik, W. Gawelda, G. Zgrablic, C. Bressler, M. Chergui, *Angew. Chem. Int. Ed.*, **2006**, *45*, 3174–3176.

[91]. K. Barthelmes, J. Kübel, A. Winter, M. Wächtler, C. Friebe, B. Dietzek, U. S. Schubert, *Inorg. Chem.*, **2015**, *54*, 3159–3171.

[92]. L. Zedler, S. Kupfer, I. R. de Moraes, M. Wächtler, R. Beckert, M. Schmitt, J. Popp, S. Rau, B. Dietzek, *Chem. Eur. J.*, **2014**, *20*, 3793–3799.

[93]. Y. Zhang, S. Kupfer, L. Zedler, J. Schindler, T. Bocklitz, J. Guthmuller, S. Rau, B. Dietzek, *Phys. Chem. Chem. Phys.*, **2015**, *17*, 29637–29646.

[94]. M. Wächtler, J. Guthmuller, L. González, B. Dietzek, *Coord. Chem. Rev.*, **2012**, *256*, 1479–1508.

[95]. K. Barthelmes, A. Winter, U. S. Schubert, *Eur. J. Inorg. Chem.*, **2016**, 5132–5142.

[96]. K. Heinze, K. Hempel, S. Tschierlei, M. Schmitt, J. Popp, S. Rau, *Eur. J. Inorg. Chem.*, **2009**, *21*, 3119–3126.

[97]. R. E. Hester, K. P. J. Williams, *J. Chem. Soc. Perkin II*, **1981**, *5*, 852–859.

[98]. M. A. Palafox, M. Gil, J. L. Nunez, G. Tardajos, *Int. J. Quantum Chem.*, **2002**, *89*, 147–171.

[99]. J. T. Hewitt, P. J. Vallett, N. H. Damrauer, *J. Phys. Chem. A*, **2012**, *116*, 11536–11547.

[100]. A. M. Brown, C. E. McCusker, J. K. McCusker, *Dalton Trans.*, **2014**, *43*, 17635–

17646.

[101]. W. R. Browne, W. Henry, P. Passaniti, M. T. Gandolfi, R. Ballardini, C. M. O'Connor, C. Brady, C. G. Coates, J. G. Vosa, J. J. McGarvey, *Photochem. Photobiol. Sci.*, **2007**, *6*, 386–396.

[102]. G. Benkö, J. Kallioinen, P. Myllyperkiö, F. Trif, J. E. I. Korppi-Tommola, A. P. Yartsev, V. Sundström, *J. Phys. Chem. B*, **2004**, *108*, 2862–2867.

[103]. M. T. Indelli, M. Orlandi, C. Chiorboli, M. Ravaglia, F. Scandola, F. Lafolet, S. Welter, L. De Cola, *J. Phys. Chem. A*, **2012**, *116*, 119–131.

[104]. K. Barthelmes, M. Sittig, A. Winter, U. S. Schubert, *Eur. J. Inorg. Chem.*, **2017**, 3698–3706.

[105]. F. Chaignon, J. Torroba, E. Blart, M. Borgström, L. Hammarström, F. Odobel, *New J. Chem.*, **2005**, *29*, 1272–1284.

[106]. A. E. Jones, C. A. Christensen, D. F. Perepichka, A. S. Batsanov, A. Beeby, P. J. Low, M. R. Bryce, A.W. Parker, *Chem. Eur. J.*, **2001**, *7*, 973–978.

[107]. D. M. Guldi, L. Sánchez, N. Martín, *J. Phys. Chem. B*, **2001**, *105*, 7139–7144.

[108]. J. Hankache, O. S. Wenger, *Phys. Chem. Chem. Phys.*, **2012**, *14*, 2685–2692.

[109]. M. Krzeszewski, E. M. Espinoza, C. Cervinka, J. B. Derr, J. A. Clark, D. Borchardt, G. J. O. Beran, D. T. Gryko, V. I. Vullev, *Angew. Chem. Int. Ed.*, **2018**, *57*, 12365–12369.

[110]. S.-Y. Kim, Y.-J. Cho, H.-J. Son, D. W. Cho, S. O. Kang, *J. Phys. Chem. A*, **2018**, *122*, 3391−3397.

[111]. B. Bleisteiner, T. Marian, S. Schneider, A. M. Brouwer, J. W. Verhoeven, *Phys. Chem. Chem. Phys.*, **2001**, *3*, 2070−2079.

[112]. J. V. Lockard, M. R. Wasielewski, *J. Phys. Chem. B*, **2007**, *111*, 11638−11641.

[113]. J. Hankache, O. S. Wenger, *Chem. Eur. J.*, **2012**, *18*, 6443–6447.

[114]. J. Hankache, M. Niemi, H. Lemmetyinen, O. S. Wenger, *J. Phys. Chem. A*, **2012**, *116*, 8159−8168.

[115]. K. Kawai, Y. Osakada, T. Takada, M. Fujitsuka, T. Majima, *J. Am. Chem. Soc.*, **2004**, *126*, 12843–12846.

[116]. G. Li, N. Govind, M. A. Ratner, C. J. Cramer, L. Gagliardi, *J. Phys. Chem. Lett.*, **2015**, *6*, 4889−4897.

[117]. G. W. Kauffman, P. C. Jurs, *J. Chem. Inf. Comput. Sci.*, **2001**, *41*, 408–418.

[118]. A. M. Scott, M. R. Wasielewski, *J. Am. Chem. Soc.*, **2011**, *133*, 3005–3013.

[119]. W. B. Davis, M. A. Ratner, M. R. Wasielewski, *J. Am. Chem. Soc.*, **2001**, *123*, 7877–7886.

[120]. E. A. Weiss, M. J. Tauber, R. F. Kelley, M. J. Ahrens, M. A. Ratner, M. R. Wasielewski, *J. Am. Chem. Soc.*, **2005**, *127*, 11842–11850.

[121]. P. V. James, P. K. Sudeep, C. H. Suresh, K. G. Thomas, *J. Phys. Chem. A*, **2006**, *110*, 4329–4337.

[122]. N. Li, K. Jia, S. Wang, A. Xia, *J. Phys. Chem. A*, **2007**, *111*, 9393–9398.

[123]. J.-Y. Shao, Y.-W. Zhong, *Chem. Eur. J.*, **2014**, *20*, 8702–8713.

[124]. Y.-W. Zhong, Z.-L. Gong, J.-Y. Shao, J. Yao, *Coord. Chem. Rev.*, **2016**, *312*, 22–40.

[125]. M. Presselt, B. Dietzek, M. Schmitt, S. Rau, A. Winter, M. Jäger, U. S. Schubert, J. Popp, *J. Phys. Chem. A*, **2010**, *114*, 13163–13174.

[126]. P. P. Laine, F. Bedioui, F. Loiseau, C. Chiorboli, S. Campagna, *J. Am. Chem. Soc.*, **2006**, *128*, 7510–7521.

[127]. R. Siebert, D. Akimov, M. Schmitt, A. Winter, U. S. Schubert, B. Dietzek, J. Popp, *ChemPhysChem*, **2009**, *10*, 910–919.

[128]. C.-P. Hsu, *Acc. Chem. Res.*, **2009**, *42*, 509–518.

[129]. J. Preiß, M. Jäger, S. Rau, B. Dietzek, J. Popp, T. Martínez, M. Presselt, *ChemPhysChem*, **2015**, *16*, 1395–1404.

Acknowledgement

I want to express my heartfelt thanks to all the people who have helped, supported and accompanied me during the past four years. When I look back I have to say studying abroad for the doctoral degree is not easy, but worth. I am very clear that without others' help I cannot reach here smoothly.

First and foremost, I truly want to thank **Prof. Dr. Benjamin Dietzek** for giving me this opportunity to work in his group on such an interesting topic. I appreciate for his time, patience and guidance for each time data and manuscript discussion. The efficient discussion plays a key role in our achievements, which I am very grateful.

I would like to thank **Dr. Maria Wächtler** for her help in data and manuscript discussion as well. I have to admit that for my first year I really felt nervous to discuss with Benjamin alone. Her participation made me feel much better. Meanwhile, I appreciate her introduction and tutorial guidance to the fs / ns transient absorption setup for my first measurement in the lab.

I thank **Dr. Denis Akimov** for his help and support in fs transient absorption setup maintenance and alignment. I still remember one time I was working in the lab for roughly two weeks and the TOPAS needed to be checked, aligned and optimized for each day. Many thanks to his patience and help.

I thank the colleagues from the Institute of Organic Chemistry and Macromolecular Chemistry (IOMC) in Jena for the excellent collaborations, especially **Prof. Dr. Ulrich S. Schubert**, **Dr. Andreas Winter**, and **Dr. Kevin Barthelmes** for the sample synthesis as well as the comments on our joint manuscripts. In this context, I also need to thank **Dr. Martin Schultz** and **Jens H. Tran** in our group for the sample synthesis (compounds in Chapter 4) and their help in the lab at IPC and IAAC. In addition, I thank all other colleagues and collaborators I worked with in the side projects including the group of **Prof. Dr. Sven Rau** (Uni Ulm) and **Prof. Dr. Carsten Streb** (Uni Ulm).

Furthermore, I want to give my special thanks to all the colleagues in Group Dietzek, in particular, **Dr. Mathias Micheel** (for the discussion and help in fs / ns transient absorption spectroscopy; the help to handle the cryostat); **Dr. Linda Zedler** and **Dr. Ying Zhang** (for their help in spectroelectrochemistry); **Dr. Christian Reichardt** (for the help in resonance Raman spectroscopy and proofreading of the Summary and Zusammenfassung part); **Julian**

Schindler and **Kilian Schneider** (for the help in fs transient absorption spectroscopy); **Tingsen Ming** (for the help in getting and carrying liquid nitrogen for so many times). I would like to thank **Philipp Traber** (Uni Jena) for his corrections in the Zusammenfassung part.

Many thanks to the **China Scholarship Council (CSC)** for the financial support to my doctoral study.

Last but not least, I want to sincerely thank my family and friends. Especial thanks to my boyfriend **Dengpeng Huang** (Uni Hannover) for his company, understanding and support for the past six years. Thanks for joining me to come to Germany for the doctoral study. I am very happy and lucky to share this cool experience with you.

Curriculum Vitae

Personal Information

Name	Yusen Luo
Date of birth	19.05.1990
Nationality	Chinese

University Education

09/2015–present	Doctoral candidate, Group of Prof. Benjamin Dietzek, Leibniz Institute of Photonic Technology (IPHT) and Friedrich Schiller University, Jena, Germany
03/2014–05/2015	Master studies (exchange program), Group of Prof. Yuliang Li, Institute of Chemistry Chinese Academy of Sciences (ICCAS), Beijing, China Thesis: *Synthesis, Self-Assembly and Optical Properties of Intramolecular Charge-Transfer Compounds*
09/2012–03/2014	Master studies, Group of Prof. Wensheng Yang, Jilin University, Changchun, China Topic: *Synthesis and Growth Mechanism Studies of Gold Nanoflowers*
09/2008–06/2012	Bachelor studies, Department of Chemistry, Jilin University, Changchun, China Thesis: *Mechanism and Characterization of Gold Nanoplates Synthesized by Sodium Citrate as the Reducing and Capping Agent* (supervised by Prof. Wensheng Yang)

Teaching Experience

2018–2019	Electrochemistry MCEU 1.3, Practicum
2017–2018	Electrochemistry MCEU 1.3, Practicum
2016–2017	MedPho–P1, Practicum

Jena, March 18, 2019 Yusen Luo

Lists of publications

Peer-reviewed publications

[1]. Y. Luo, M. Wächtler, K. Barthelmes, A. Winter, U. S. Schubert and B. Dietzek, Superexchange on the Fast Lane – Intramolecular electron transfer in a molecular triad occurs by conformationally-gated superexchange. *Chem. Commun.*, **2019**, *55*, 5251–5254.

[2]. Y. Luo, J. H. Tran, M. Wächtler, M. Schulz, K. Barthelmes, A. Winter, S. Rau, U. S. Schubert and B. Dietzek, Remote Control of Electronic Coupling – Modification of Excited-State Electron-Transfer Rates in Ru(tpy)$_2$-Based Donor-Acceptor Systems by Remote Ligand Design. *Chem. Commun.*, **2019**, *55*, 2273–2276.

[3]. Y. Luo, M. Wächtler, K. Barthelmes, A. Winter, U. S. Schubert and B. Dietzek, Direct Detection of the Photoinduced Charge-Separated State in a Ru(II) Bis(terpyridine)–Polyoxometalate Molecular Dyad. *Chem. Commun.*, **2018**, *54*, 2970–2973.

[4]. Y. Luo, M. Wächtler, K. Barthelmes, A. Winter, U. S. Schubert and B. Dietzek, Coexistence of Distinct Intramolecular Electron Transfer Pathways in Polyoxometalate Based Molecular Triads. *Phys. Chem. Chem. Phys.*, **2018**, *20*, 11740–11748.

[5]. Y. Luo, K. Barthelmes, M. Wächtler, A. Winter, U. S. Schubert and B. Dietzek, Increased Charge Separation Rates with Increasing Donor-Acceptor Distance in Molecular Triads: The Effect of Solvent Polarity. *J. Phys. Chem. C*, **2017**, *121*, 9220−9229.

[6]. Y. Luo, K. Barthelmes, M. Wächtler, A. Winter, U. S. Schubert and B. Dietzek, Energy versus Electron Transfer: Controlling the Excitation Transfer in Molecular Triads. *Chem. Eur. J.*, **2017**, *23*, 4917–4922.

Publications during the Master studies

[7]. Y. Luo, C. Yuan (co-author), J. Xu, Y. Li, H. Liu, S. Semin, T. Rasing, W. Yang and Y. Li, Controlling Growth of Molecular Crystal Aggregates with Distinct Linear and Nonlinear Optical Properties. *ACS Appl. Mater. Interfaces*, **2017**, *9*, 30862−30871.

[8]. Y. Luo, Z. Xue, Y. Li, H. Liu, W. Yang and Y. Li, Controllable Growth of Organic Nanostructures from 0D to 1D with Different Optical Properties. *RSC Adv.*, **2015**, *5*, 100457−100463.

[9]. Y. Luo, X. Ji, J. Zhuang and W. Yang, Controlled Formation of Gold Nanoflowers by Reduction of Tetrachloroauric Acid with Thermally Treated Glucosein Alkaline Solution. *Colloids and Surfaces A: Physicochem. Eng. Aspects*, **2014**, *463*, 28−36.

Conference contributions

[1]. Talk, "*Influence of Donor-Acceptor Distance Variation on Photoinduced Electron and Energy Transfer in Ruthenium(II) Bis(terpyridine) Fullerene Triads*", 25th Lecture Conference on Photochemistry, **2016**, Jena, Germany.

[2]. Talk, "*Energy vs. Electron Transfer: Ultrafast Photoinduced Dynamics in Molecular Triads*", 1st Förster Resonance Energy Transfer and Beyond, **2018**, Warsaw, Poland.

Selbständigkeitserklärung

Ich erkläre, dass ich die vorliegende Arbeit selbständig und unter Verwendung der angegebenen Hilfsmittel, persönlichen Mitteilungen und Quellen angefertigt habe.

Declaration of originality

I certify that the work presented here is, to the best of my knowledge and belief, original and the result of my own investigations, except as acknowledged, and has not been submitted, either in part or whole, for a degree at this or any other university.

Jena, March 18, 2019 Yusen Luo

Publications P1–P6

[P1] Energy versus Electron Transfer: Controlling the Excitation Transfer in Molecular Triads

Reproduced with permission from: Y. Luo, K. Barthelmes, M. Wächtler, A. Winter, U. S. Schubert and B. Dietzek, "Energy versus Electron Transfer: Controlling the Excitation Transfer in Molecular Triads", *Chem. Eur. J.*, **2017**, *23*, 4917–4922. Copyright © WILEY-VCH Verlag GmbH & Co. KGaA, Weinheim.

ChemPubSoc Europe
DOI: 10.1002/chem.201700413
CHEMISTRY A European Journal
Full Paper

Photochemistry

Energy versus Electron Transfer: Controlling the Excitation Transfer in Molecular Triads

Yusen Luo,[a, b] Kevin Barthelmes,[c, d] Maria Wächtler,[b] Andreas Winter,[c, d] Ulrich S. Schubert,[c, d] and Benjamin Dietzek*[a, b, c]

Abstract: The photochemistry of Ru^{II} coordination compounds is generally discussed to originate from the lowest lying triplet metal-to-ligand charge-transfer state (^{3}MLCT). However, when heteroleptic complexes are considered, for example, in the design of molecular triads for efficient photoinduced charge separation, a complex structure of ^{1}MLCT states, which can be populated in a rather narrow spectral window (typically around 450 nm) is to be considered. In this contribution we show that the localization of MLCT excited states on different ligands can affect the following ps to ns decay pathways to an extent that by tuning the excitation wavelength, intermolecular energy transfer from a Ru^{II}–terpyridine unit to a fullerene acceptor can be favored over electron transfer within the molecular triad. These results might have important implications for the design of molecular dyads, triads, pentads and so forth with respect to a specifically targeted response of these complexes to photoexcitation.

Introduction

Photoinduced electron transfer and the resultant intra- and intermolecular charge-separated states (CSS) play pivotal roles in natural and artificial photosynthesis.[1] Generally fast and efficient formation of a long-lived CSS is targeted.[2] In this respect, molecular design aims to directly affect electron transfer rates by making use of factors such as the donor-acceptor distance,[3] the chemical nature of spacers[4] and molecular conformations.[5] Following such strategies has led to improved charge-separation efficiencies and prolonged lifetimes of CSS. $[Ru(tpy)_2]^{2+}$ complexes (tpy = 2, 2′:6′, 2′′-terpyridine), which facilitate the construction of linear molecular triads (and pentads and so forth) without introducing isomers, are frequently used as photosensitizers and primary photoactivated electron donors.[6] It is a general notion in transition-metal complexes based donor–acceptor assemblies that intramolecular electron or energy transfer starts from the lowest ^{3}MLCT (metal-to-ligand charge transfer) excited state, which is rapidly formed upon intersystem crossing from the photoexcited ^{1}MLCT states.[7]

In this manuscript, we report mechanistically distinct yet coexisting decay pathways (i.e. electron transfer and energy transfer) in a molecular triad which is comprised of a phenothiazine donor, a Ru–terpyridine (tpy) photocenter and a fullerene (energy and electron) acceptor. The chemical structures of the investigated triad, **PTRuC$_{60}$**, and a dyad, **PTRu**, which serves as reference system, are shown in Scheme 1.[8] The ratio to which the individual transfer channels are effective upon photoexcitation can be controlled by changing the excitation wavelength, that is, by preferential excitation of either of the MLCT states associated with the two structurally (and hence electronically) distinct tpy ligands coordinating the Ru ion.[9] We show that these distinct MLCT states have different propensities to promote electron or energy transfer, which would affect the performance of a potential device in dependence on the excitation conditions.[11b,c]

Results and Discussion

To illustrate the excitation-wavelength-dependent photochemistry of the triad, Figure 1 depicts the results of nanosecond (ns) transient absorption (TA) experiments. The data of **PTRuC$_{60}$** was recorded upon excitation at 520, 476, and 456 nm, that is, throughout the MLCT band of the Ru–tpy core. The ns TA data of **PTRuC$_{60}$** shows two distinct

---

[a] *Y. Luo, Prof. Dr. B. Dietzek*
Institute of Physical Chemistry and Abbe Center of Photonics
Friedrich-Schiller-University Jena
Helmholtzweg 4
07743 Jena (Germany)

[b] *Y. Luo, Dr. M. Wächtler, Prof. Dr. B. Dietzek*
Leibniz Institute of Photonic Technology (IPHT)
Albert-Einstein-Strasse 9
07745 Jena (Germany)
E-mail: benjamin.dietzek@leibniz-ipht.de

[c] *K. Barthelmes, Dr. A. Winter, Prof. Dr. U. S. Schubert, Prof. Dr. B. Dietzek*
Jena Center for Soft Matter (JCSM)
Friedrich-Schiller-University Jena
Philosophenweg 7
07743 Jena (Germany)

[d] *K. Barthelmes, Dr. A. Winter, Prof. Dr. U. S. Schubert*
Laboratory of Organic and Macromolecular Chemistry (IOMC)
Friedrich-Schiller-University Jena
Humboldtstrasse 10
07743 Jena (Germany)

Supporting information for this article can be found under: http://dx.doi.org/10.1002/chem.201700413.

© 2017 Wiley-VCH Verlag GmbH & Co. KGaA, Weinheim

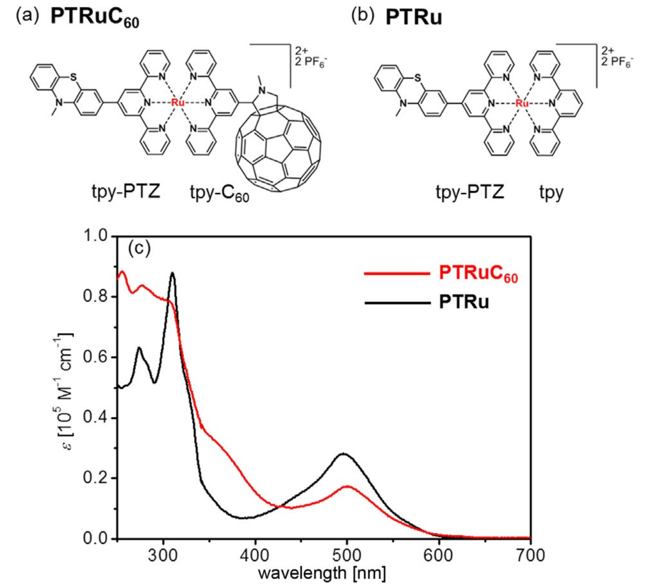

Scheme 1. Molecular structures of (a) triad **PTRuC$_{60}$** and (b) reference dyad **PTRu**. The terpyridine (tpy) ligands connecting with *N*-methylphenothiazine (PTZ) and *N*-methylfulleropyrrolidine (C$_{60}$) are named as tpy–PTZ and tpy–C$_{60}$ respectively. (c) Steady-state absorption spectra of the triad **PTRuC$_{60}$** and dyad **PTRu** in dichloromethane.

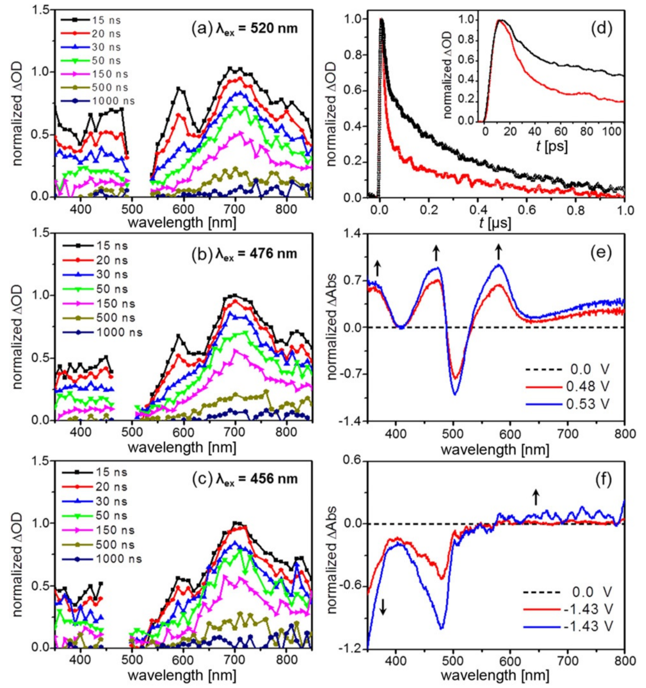

Figure 1. Nanosecond transient absorption spectra at selected times of **PTRuC$_{60}$** upon excitation at (a) 520 nm, (b) 476 nm, (c) 456 nm in aerated dichloromethane. For comparison, the ns TA spectra were normalized by the absorption maxima of $^3C_{60}$* (at 700 nm at 15 ns). (d) Normalized integrated kinetic traces at the spectral regions of the CSS (540–630 nm, red) and $^3C_{60}$*(640–850 nm, black) of the ns TA data upon excitation at 520 nm. The inset shows enlargement of the time region up to 100 ps. Spectroelectrochemical UV/Vis absorption difference spectra of (e) $PTZ^{\cdot +}$ and (f) $C_{60}^{\cdot -}$ collected in dichloromethane by oxidation of **PTRu** and reduction of **RuC$_{60}$** respectively. Potentials are given versus $Fc^{+/0}$. The spectra were normalized by the absorption maxima of the ground state bleach (the blue one). For reference **RuC$_{60}$**, the data in (f) were smoothed. The raw data and molecular structure are shown in Supporting Information Figure S2.

excited-state absorption bands centered at 590 and 700 nm (Figure 1 a–c). The latter indicates the formation of fullerene triplet state ($^3C_{60}$*)[10] and the former is due to the absorption of the one-electron-oxidized phenothiazine donor ($PTZ^{\cdot +}$), indicating the formation of a charge-separated state (CSS). This assignment is supported by UV/Vis spectroelectrochemistry (SEC) on the reference dyad: Upon one-electron oxidation of **PTRu**, that is, formation of the $PTZ^{\cdot +}$ unit, three maxima arise at 365, 473, and 580 nm, which are accompanied by a loss of ^{1}MLCT intensity (Figure 1 e). In the ns data the formation of the CSS, that is, formation of the PTZ radical cation, is visible by following the band at 580 nm. The $PTZ^{\cdot +}$ absorption, which is expected at 365 nm, is not pronounced in the ns TA data owing to the spectral overlap with the strong negative absorption of $C_{60}^{\cdot -}$ below 400 nm (Figure S1). The latter feature is illustrated by UV/Vis SEC upon reduction of a **RuC$_{60}$** model dyad:[12] Electrochemical reduction of the fullerene unit causes a rise of weak, featureless absorption from 550 to 800 nm together with a strong negative absorption below 400 nm (Figure 1 f and Supporting Information Figure S2). Altogether these results indicate the formation of the fully CSS ($PTZ^{\cdot +}$–P–$C_{60}^{\cdot -}$).

This conclusion is further supported by the ns transient absorption (TA) spectra of the dyad **PTRu** (without C$_{60}$) upon excitation at 520 nm (Figure 2). The shape of the ns TA spectra matches the UV/Vis SEC of the oxidized PTZ (Figure 1 e) very well, that is, they feature an intense absorption peak at 365 nm and another broad absorption above 540 nm. In the ns TA spectra (e.g. at 15 ns) there appears a shoulder at around 470 nm which is also related to the absorption of $PTZ^{\cdot +}$. However due to the strong ground state bleach, this peak appears not particularly pronounced. Hence, upon photoexcitation of the dyad a CSS ($PTZ^{\cdot +}$–$P^{\cdot -}$) is generated but displaying an intense absorption at 365 nm (Figure 2). This observation supports the assignment of forming the fully CSS ($PTZ^{\cdot +}$–P–$C_{60}^{\cdot -}$) in the triad **PTRuC$_{60}$** which does not show structured absorption at 365 nm due to the presence of reduced C$_{60}$ (Figure 1 a–c).

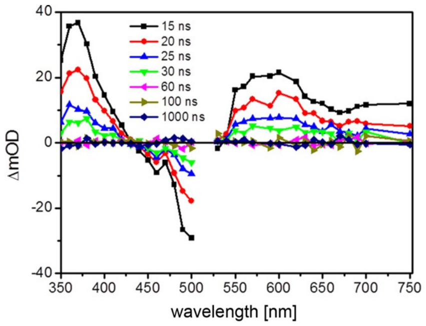

Figure 2. Nanosecond transient absorption spectra at selected times of dyad **PTRu** upon excitation at 520 nm in aerated dichloromethane.

The final states in triad **PTRuC$_{60}$** resulting from either intramolecular energy or electron transfer are not only spectrally distinct but can be disentangled based on their characteristic lifetimes: Integrated kinetic traces over the two bands are

© 2017 Wiley-VCH Verlag GmbH & Co. KGaA, Weinheim

shown in Figure 1 d and Supporting Information Figure S4, that is, kinetics recorded in the spectral region characteristic for the CSS (540–630 nm) and the $^3C_{60}$* (640–850 nm). Global fits of the ns TA data (Figure S5) also yield two species: a short-lived one ($\tau_{ns1} = 20$ ns) mainly dominates at 590 nm (absorption of $PTZ^{\cdot+}$) and a longer-lived one ($\tau_{ns2} = 320$ ns) at around 700 nm (assigned to $^3C_{60}$*). The assignment is corroborated by experiments in the absence of oxygen (Figure S6), which shows that τ_{ns2} increases fivefold in the absence of oxygen, whereas τ_{ns1} is insensitive to the presence of oxygen in solution. Thus τ_{ns1} and τ_{ns2} describe the decay of the fully CSS and $^3C_{60}$* in **PTRuC$_{60}$**, respectively.

As it is immediately apparent from Figure 1 a–c, the relative intensities of the two prominent bands in the ns TA spectra—and hence the ratio between energy and electron transfer—depend on the excitation wavelengths within the MLCT manifold. For illustrating of the energy versus electron transfer ratio as a function of excitation wavelength the ns TA spectra were normalized by the corresponding absorption maximum of $^3C_{60}$* (at 700 nm at 15 ns). Apparently the absorption intensity of the CSS band decreases when shifting the excitation to low wavelength (Figure 1 a to Figure 1 c). The excitation-wavelength dependence effects are also reflected in the global fitting results of the ns TA data: Upon decreasing the excitation wavelength the intensity of the CSS absorption band decreases by a factor 2.5 (see Supporting Information Figure S5).

To explore the origin of the excitation-wavelength dependent ns photochemistry, excitation-wavelength-dependent resonance Raman (RR) spectra were recorded, which provide insight into the distribution of ^{1}MLCT excited states over the individual coordinating ligands.[11] RR spectroscopy is a very effective method to trace changes in electron density distribution upon optical excitation. In RR only modes which are coupled to the electronic transitions can be largely enhanced (i.e., Frank–Condon active modes). Thus, this feature has been utilized to probe dynamics in the Frank–Condon region which spans roughly the first 20 fs of the development in the excited state[11d] (i.e. the ^{1}MLCT states in the structures investigated here) and hence delivers intrinsically only information on this time range. Thus RR is an optical–spectroscopic tool to characterize the "starting point" of all photochemical reactions. All RR spectra display PTZ (blue dotted line) and tpy (red dashed line) associated bands (Figure 3). The mode assignment was based on RR data of the unsubstituted $[Ru(tpy)_2](PF_6)_2$ complex[13] and *N*-methylphenothiazine (Supporting Information Table S1).[14] As apparent from the experimental data (see inset in Figure 3) the relative signal intensities of RR bands associated with PTZ and tpy change with excitation wavelengths. Decreasing excitation wavelengths from 515 to 458 nm results in decreased RR signals of PTZ associated bands ($\tilde{\nu} = 1595$, 1574, and 1352 cm^{-1}) and shoulders (at 1464 and 1337 cm^{-1}). Hence, the data show that upon shifting the excitation wavelength different portions of MLCT states associated with the tpy–PTZ and the tpy–C$_{60}$ ligand are populated. Decreasing the excitation wavelengths leads to a decreased excess-electron density shift towards the tpy–PTZ ligand during the initial MLCT transition (see Figure 1). This excitation condition, on the other hand, leads to a comparatively lower absorption of the CSS in the ns-data, that is, indicating that less electron transfer takes place (see Figure 1). In turn, under such excitation conditions, that is, excitation of the MLCT$_{tpy-C60}$ state causes energy transfer to happen more preferentially, that is, the absorption band of $^3C_{60}$* becomes more prominent in the ns transient absorption data. This is remarkable, as it shows that the population of the two distinct MLCT states (which are disentangled with respect to the vertical $S_0 \rightarrow MLCT_{tpy-C60}/MLCT_{tpy-PTZ}$ transition based on the RR data) leads to distinct slow photochemical responses, that is, the initially excited mixture of MLCT states does not convert rapidly into a single low-lying ^{3}MLCT state, from which a uniform photochemistry is subsequently observed. Instead, the initial population of a distinct MLCT state causes a distinct and slow photochemical response on the ns timescale, that is, the initially populated MLCT excited states distribution determines the subsequent decay pathways.

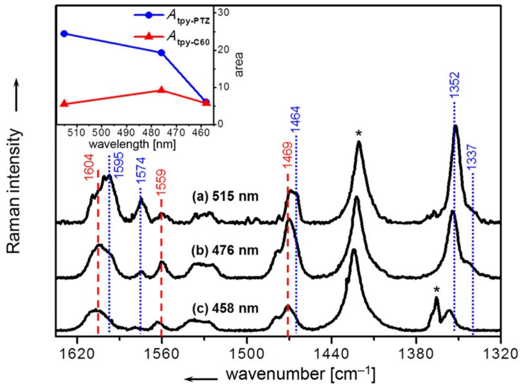

Figure 3. Resonance Raman spectra of **PTRuC$_{60}$** in dichloromethane with excitation wavelengths at (a) 515, (b) 476 and (c) 458 nm. For comparison the spectra were normalized to the solvent, dichloromethane, band (asterisks) at 1420 cm^{-1} and the modes showing distinct differences in signal intensities upon variation of the excitation wavelengths were marked. Color code: PTZ-associated bands in blue dotted line, tpy-associated bands in red dashed line. Inset: band areas of the PTZ (namely tpy–PTZ ligand, $A_{tpy-PTZ}$, blue) and tpy ($A_{tpy-C60}$, red) associated bands as a function of excitation wavelengths. Resonance Raman spectra collected for the reference dyad **PTRu** display a similar trend (see Supporting Information Figure S7).

To obtain a detailed picture of the photoinduced dynamics mechanistically connecting the initial photoexcited MLCT state with the long-lived states probed by ns TA spectroscopy, femtosecond (fs) TA spectroscopy was performed. The respective data were obtained upon excitation at 520 nm for both **PTRuC$_{60}$** and **PTRu**. For both compounds, the differential absorption spectra (Figure 4 a, c) are dominated by three features, namely ground state bleach in the wavelength region of the ^{1}MLCT absorption (at ca. 500 nm) and excited-state absorption (ESA) from 340 to 450 nm and from 540 up to 735 nm. The absorptive features of the ESA in Figure 4 have ^{3}MLCT-character because the ultrafast intersystem crossing of the initially excited ^{1}MLCT state to ^{3}MLCT state happens in a sub-100 fs time scale[15] which is limited by the resolution of the setup. To be specific, the fs TA spectra (Figure 4 a, c) recorded at short delay times (i.e. at 0.3 ps) show the typical characteristics of ^{3}MLCT ESA of $[Ru(tpy)_2]^{2+}$ complexes, that is, a broad and rather

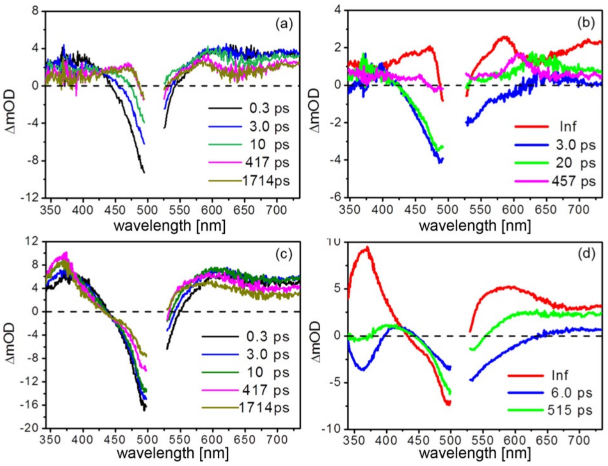

Figure 4. Transient absorption spectra (left) at selected delay times and decay-associated spectra (right) resulting from the global fit upon excitation at 520 nm in dichloromethane for triad **PTRuC$_{60}$** (a, b) and dyad **PTRu** (c, d).

unstructured absorption above 550 nm.[15] Another peak in the differential absorption data at 385 nm is assigned to the absorption of tpy$^{\cdot-}$.[15] For **PTRuC$_{60}$** at long delay times (i.e. after 417 ps, Figure 4a) the band at 385 nm has decayed to a flat, featureless absorption along with the formation of three distinct peaks at 473, 585, and 700 nm, which matches the ns TA spectra very well (Figure 1a). Furthermore, from 10 to 400 ps, the band at 600 nm blue shifts to 585 nm and remains unchanged up to 1700 ps. This spectral features indicate the shift of electron density to other parts of the molecule, that is, forming the fully CSS (PTZ$^{\cdot+}$–P–C$_{60}^{\cdot-}$). For **PTRu**, the band at 385 nm undergoes a blue-shift to 365 nm (at 10 ps) which indicates the formation of the PTZ$^{\cdot+}$ (Figure 1e), namely the process from the ^{3}MLCT excited state to the CSS (PTZ$^{\cdot+}$–P$^{\cdot-}$).

Quantitative interpretation of fs TA data is based on the decay-associated spectra (DAS) (Figure 4b, d).[16] DAS are based on global multiexponential fits of the fs TA data corresponding to a specific kinetic model. The obtained characteristic time constants (τ) describe the kinetics of the excited state relaxation processes and each component in DAS represents the spectral weight associated with each process.[17] The assignment of the time constants for **PTRuC$_{60}$** (Figure 4b) is done in accordance to **PTRu** (Figure 4d). For **PTRu**, two kinetic components and an offset corresponding to the long-lived species (longer than the experimentally accessible time scale of the setup) are used to fit the fs TA data (Figure 4d). The long-lived species (τ_{inf}), as has been discussed in the ns time-resolved TA experiment (Figure 2), represents the CSS (PTZ$^{\cdot+}$–P$^{\cdot-}$). For picosecond (ps) processes, the first component ($\tau_1 = 6$ ps) is attributed to the formation of the CSS (PTZ$^{\cdot+}$–P$^{\cdot-}$) describing an increase of positive signal amplitude at the positions of the absorption feature of the oxidized PTZ. The second component ($\tau_2 = 515$ ps) reveals a spectral shape that resembles the transient spectrum of ^{3}MLCT excited state and is in the same order of magnitude as ^{3}MLCT lifetimes reported for similar [Ru(tpy)$_2$]$^{2+}$ complexes.[15] Hence, it reflects the decay of ^{3}MLCT state to the ground state. For **PTRuC$_{60}$**, the global fit results in three kinetic components and an offset corresponding to the long-lived species (Figure 4b). Again the long-lived species (τ_{inf}) represent the mixture of the fully CSS and ^{3}C$_{60}$*, which already have been observed in the ns TA spectra (Figure 1a). The ultrafast component ($\tau_1 = 3$ ps) resembles very closely the features of the first component ($\tau_1 = 6$ ps) in **PTRu** and is therefore assigned to the formation of the intermediate CSS, that is, PTZ$^{\cdot+}$–P$^{\cdot-}$–C$_{60}$. The second component ($\tau_2 = 20$ ps) with a spectral shape similar to the ESA of ^{3}MLCT state is attributed to the energy transfer step from ^{3}MLCT excited state to ^{3}C$_{60}$*. The third component is characterized by an absorption at 600 nm, which contributes the shift to 585 nm (the long-lived species) reflecting the process from the intermediate CSS to the fully CSS (PTZ$^{\cdot+}$–P–C$_{60}^{\cdot-}$).

Hence, in the fs time-resolved experiments, we observe two distinct kinetic relaxation pathways for **PTRuC$_{60}$**: one is the formation of the fully charge-separated state and the other is energy transfer from a ^{3}MLCT excited state to form the ^{3}C$_{60}$* state likely by Dexter-type energy transfer, which for a structurally similar system was found to be active in transferring energy from a Ru–tpy photoactive center to a C$_{60}$ energy acceptor.[12] Furthermore, literature has pointed out that triplet–triplet energy transfer in related structures proceeds exclusively via the Dexter-type energy transfer.[2] This type of energy transfer proceeds via a super-exchange mechanism and requires orbital overlap.[18] In the **PTRuC$_{60}$**, the ^{3}MLCT state of the Ru-photocenter is the energy donor, in view of its molecular structure, orbital overlap between the directly connected tpy–C$_{60}$ ligand and C$_{60}$ can be expected to be stronger than that of the tpy–PTZ ligand and C$_{60}$ (which is relatively far away). Thus, it is reasonable to consider that the ^{3}MLCT$_{\text{tpy–C60}}$ excited state transfers energy to C$_{60}$ to form ^{3}C$_{60}$* whereas the ^{3}MLCT$_{\text{tpy–PTZ}}$ excited state is specific to generate the CSS. In addition, the observed fast kinetic components, that is, 20 ps for energy transfer and 3 ps for formation of the intermediate CSS in the electron transfer pathway, can kinetically compete with ILET (interligand electron transfer), which causes the thermalization of MLCT states initially localized on different ligands towards the lowest MLCT state. ILET in related Ru$^{\text{II}}$ polypyridyl complexes is reported to be in the range of several ps.[15,19,20] The actually observed rate for this process depends on the relative energies of the two MLCT states and the solvent environment. The exchange interaction in the tpy–PTZ ligand, which is conjugated over a larger range, is comparably weaker than in the tpy–C$_{60}$ ligand. Hence, the energetic splitting between the ^{1}MLCT$_{\text{tpy–C60}}$ (which is probed in the RR spectra) and the ^{3}MLCT$_{\text{tpy–C60}}$ is larger than the energy gap between the ^{1}MLCT$_{\text{tpy–PTZ}}$ and ^{3}MLCT$_{\text{tpy–PTZ}}$.[21] As a consequence, the energetic ordering of the ^{1}MLCT states (as determined from the dispersion in the RR data) is assumed to become inverted in the triplet manifold. The same situation holds true for the **PTRu** dyad, that is, the ^{3}MLCT$_{\text{tpy}}$ is energetically lower than the ^{3}MLCT$_{\text{tpy–PTZ}}$ state. Hence, slow ground state recovery is observed (as well as comparatively slow energy transfer in the triad **PTRuC$_{60}$**) despite the fact that the formation of the charge separated states in either of the systems should be kinetically favored. However, the initial distribution of ^{1}MLCT states determines the upper limit of molecules that can actually undergo intramolecular electron transfer.

Hence, the combined fs/ns TA and RR data lead to the conclusion that the decay pathway depends on the specific MLCT state excited and the ratios vary with excitation wavelength. The decay processes of the triad and the dyad after photoexcitation are summarized in Scheme 2. Thus, the observed results indicate that the generally accepted picture that all (slow and function determining) photochemistry in Ru–polypyridine complexes stems from a single low-lying ^{3}MLCT state might have to be revisited to account for more complex coordination spheres which give rise to electronically and structurally distinct MLCT states.[11b,c]

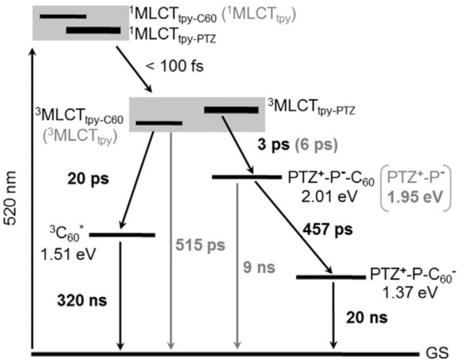

Scheme 2. Energy-level diagram of **PTRuC$_{60}$** and **PTRu** is developed by electrochemical, resonance Raman and fs/ns TA data. Note: for dyad **PTRu** different energy levels, time constants and relaxation pathways were marked in light grey. The energy of $^3C_{60}$* in triad **PTRuC$_{60}$** is 1.51 eV.[10] For the MLCT states in the grey boxes, the thicker black bar indicates higher population of the MLCT state upon excitation at 520 nm.

Conclusion

Aside from tuning the donor–acceptor distances, the nature of the spacers, or the driving forces for charge transfer, it is shown herein that the excitation wavelength for the photoactive unit might provide an additional—up to now scarcely employed— handle to tune the photo-chemistry and -physics of coordination compounds. This can happen not only on a sub-ps timescale but (more importantly) on the chemically more relevant nanosecond timescale.

Experimental Section

Spectroelectrochemical measurements were performed in a home-built three-electrode thin-layer cell with a path length of 1 mm (Bioanalytical System).[22] The three-electrode setup consists of a transparent platinum mesh working electrode, a platinum wire counter electrode and an Ag/AgCl reference electrode. Potentials were tuned using a PC-controlled potentiostat. All potentials given in the manuscript refer to ferrocene as standard. The corresponding UV/Vis spectra were recorded on a double-beam Cary 5000 UV/Vis spectrometer (Varian, USA) at room temperature. Both the oxidative and reductive SEC were reversible by obtaining the recovered initial sample absorption when a zero voltage cycle being applied to the working electrode.

Femtosecond (fs) transient absorption spectra were collected by using a previously reported home-built pump-probe laser system which is based on an amplified Ti: Sapphire oscillator (Libra, Coherent Inc.[23] **PTRuC$_{60}$** and **PTRu** were excited by pump pulse centered at 520 nm (TOPASwhite, Lightconversion Ltd.) with a duration of 110 fs. The power of the pump beam was kept at 0.3 mW before samples and the beam diameter of the pump is 0.38 mm inside the sample volume. A white light supercontinuum generated by a rotating CaF$_2$ plate is used to probe the samples in a wide spectral range (340–800 nm). The probe beam is delayed in time with respect to the pump beam by means of an optical delay line and the polarization between probe and pump is set at the magic angle (54.7°). Steady-state absorption spectra (Jasco, V-530 spectrometer) were collected before and after each transient absorption measurement to ensure sample integrity. Each solution (optical density ca. 0.2 at the excitation wavelength) was kept in a 1 mm quartz cuvette. Transient absorption data were displayed after chirp correction. The transient absorption data was analyzed by a global multi-exponential fit after exclusion of a temporal window of 200 fs around time-zero in order to avoid contributions of the coherent-artifact region to the data analysis. Furthermore, a spectral band of 20 nm around the pump-wavelength is omitted from the data analysis due to pump-scatter in this spectral range.

Nanosecond (ns) transient absorption spectra[12] were collected to study the long-lived species appearing in fs transient absorption data. The pump pulses centered at 456, 476, and 520 nm were produced by a Continuum Surelite OPO Plus which is pumped by an Nd: YAG laser system (pulse duration 5 ns, repetition rate 10 Hz). The probe light is provided by a 75 W xenon arc lamp. Spherical concave mirrors are used to focus the probe beam into the samples and then send the beam to the monochromator (Acton, Princeton Instruments). The probe light is detected by a Hamamatsu R928 photomultiplier. The signal is amplified and processed by a commercially available detection system (Pascher Instruments AB). For the excitation-wavelength-dependent measurements, each sample was fresh prepared and the optical density (ca. 0.37) at the excitation wavelengths (456, 476, and 520 nm) was kept the same. For all measurements, the power of the pump beam was kept at 0.35 mJ. Oxygen-free solution was prepared by at least four freeze–pump–thaw cycles. All measurements were performed in 1 cm path length fluorescence cuvettes. A spectral band of 20 nm around the pump wavelength is omitted from the data analysis due to pump-scatter in this spectral range.

Resonance Raman spectra were recorded with a conventional 90° scattering arrangement.[24] Excitation wavelengths at 458, 476 and 515 nm (Model Coherent Innova 300C MotoFreD Ion Laser) were used which are equal or very close to the excitation wavelengths performed in ns transient absorption experiments. Optical density at the excitation wavelength of samples was kept at ca. 0.2 in 1 mm quartz cuvette. A rotating cell was utilized to prevent sample decomposition. No changes in the absorption band were observed before and after the RR measurements.

Acknowledgements

This research is funded by the Deutsche Forschungsgemeinschaft (DFG, Grant Nos. SCHU1229-16/1 and DI1517-3/1) and the China Scholarship Council (CSC, Y. L.). The authors thank Dr. Martin Presselt and Julian Schindler for helpful discussions.

Conflict of interest

The authors declare no conflict of interest.

Keywords: charge-separated state · charge transfer · electron transfer · MLCT excited states · ruthenium

[1] a) T. M. Clarke, J. R. Durrant, *Chem. Rev.* **2010**, *110*, 6736–6767; b) M. D. Kärkäs, O. Verho, E. V. Johnston, B. Åkermark, *Chem. Rev.* **2014**, *114*, 11863–12001.

[2] M. Rudolf, S. V. Kirner, D. M. Guldi, *Chem. Soc. Rev.* **2016**, *45*, 612–630.

[3] a) M. P. Eng, B. Albinsson, *Angew. Chem. Int. Ed.* **2006**, *45*, 5626–5629; *Angew. Chem.* **2006**, *118*, 5754–5757; b) M. Kuss-Petermann, H. Wolf, D. Stalke, O. S. Wenger, *J. Am. Chem. Soc.* **2012**, *134*, 12844–12854; c) M. Kuss-Petermann, O. S. Wenger, *Angew. Chem. Int. Ed.* **2016**, *55*, 815–819; *Angew. Chem.* **2016**, *128*, 826–830; d) T. Higashino, T. Yamada, M. Yamamoto, A. Furube, N. V. Tkachenko, T. Miura, Y. Kobori, R. Jono, K. Yamashita, H. Imahori, *Angew. Chem. Int. Ed.* **2016**, *55*, 629–633; *Angew. Chem.* **2016**, *128*, 639–643.

[4] a) D. M. Guldi, M. Maggini, S. Mondini, G. Scorrano, M. Prato, *Proc. SPIE, Fullerenes and Photonics IV*, **1997**, *3142*, 96–103; b) S. Castellanos, A. A. Vieira, B. M. Illescas, V. Sacchetti, C. Schubert, J. Moreno, D. M. Guldi, S. Hecht, N. Mártin, *Angew. Chem. Int. Ed.* **2013**, *52*, 13985–13990; *Angew. Chem.* **2013**, *125*, 14235–14240; c) J. Sukegawa, C. Schubert, X. Z. Zhu, H. Tsuji, D. M. Guldi, E. Nakamura, *Nat. Chem.* **2014**, *6*, 899–905.

[5] a) M. Gilbert, L. J. Esdaile, M. Hutin, K, Sawada, H. L. Anderson, B. Albinsson, *J. Phys. Chem. C* **2013**, *117*, 26482–26492; b) S. V. Kirner, C. Henkel, D. M. Guldi, J. D. M. Jr, D. I. Schuster, *Chem. Sci.* **2015**, *6*, 7293–7304; c) K. E. Spettel, N. H. Damrauer, *J. Phys. Chem. C* **2016**, *120*, 10815–10829.

[6] a) E. Baranoff, J. P. Collin, L. Flamigni, J. P. Sauvage, *Chem. Soc. Rev.* **2004**, *33*, 147–155; b) R. Siebert, A. Winter, M. Schmitt, J. Popp, U. S. Schubert, B. Dietzek, *Macromol. Rapid Commun.* **2012**, *33*, 481–497; c) M. Wächtler, J. Kübel, K. Barthelmes, A. Winter, A. Schmiedel, T. Pascher, C. Lambert, U. S. Schubert, B. Dietzek, *Phys. Chem. Chem. Phys.* **2016**, *18*, 2350–2360.

[7] a) J.-P. Sauvage, J.-P. Collin, J.-C. Chambron, S. Guillerez, C. Coudret, V. Baltani, F. Barigelletti, L. D. Cola, L. Flamigni, *Chem. Rev.* **1994**, *94*, 993–1019; b) A. T. Yeh, C. V. Shank, J. K. McCusker, *Science* **2000**, *289*, 935–938; c) S. Wallin, J. Davidsson, J. Modin, L. Hammarström, *J. Phys. Chem. A* **2005**, *109*, 4697–4704; d) A. Cannizzo, F. van Mourik, W. Gawelda, G. Zgrablic, C. Bressler, M. Chergui, *Angew. Chem. Int. Ed.* **2006**, *45*, 3174–3176; *Angew. Chem.* **2006**, *118*, 3246–3248; e) M. Polson, C. Chiorboli, S. Fracasso, F. Scandola, *Photochem. Photobiol. Sci.* **2007**, *6*, 438–443.

[8] K. Barthelmes, A. Winter, U. S. Schubert, *Eur. J. Inorg. Chem.* **2016**, 5132–5142. The synthesis, photophysical, and electrochemical properties of the investigated molecules were reported in this paper. MLCT emission for the triad is totally quenched and the dyad only shows very weak emission.

[9] a) C. Chiorboli, M. A. J. Rodgers, F. Scandola, *J. Am. Chem. Soc.* **2003**, *125*, 483–491; b) D. L. Ashford, W. Song, J. J. Concepcion, C. R. K. Glasson, M. K. Brennaman, M. R. Norris, Z. Fang, J. L. Templeton, T. J. Meyer, *J. Am. Chem. Soc.* **2012**, *134*, 19189–19198.

[10] D. M. Guldi, M. Prato, *Acc. Chem. Res.* **2000**, *33*, 695–703.

[11] a) M. Wächtler, J. Guthmuller, L. Gonzálezd, B. Dietzek, *Coord. Chem. Rev.* **2012**, *256*, 1479–1508; b) S. Tschierlei, M. Karnahl, M. Presselt, B. Dietzek, J. Guthmuller, L. González, M. Schmitt, S. Rau, J. Popp, *Angew. Chem. Int. Ed.* **2010**, *49*, 3981–3984; *Angew. Chem.* **2010**, *122*, 4073–4076; c) M. Wächtler, J. Guthmuller, S. Kupfer, M. Maiuri, D. Brida, J. Popp, S. Rau, G. Cerullo, B. Dietzek, *Chem. Eur. J.* **2015**, *21*, 7668–7674.

[12] K. Barthelmes, J. Kübel, A. Winter, M. Wächtler, C. Friebe, B. Dietzek, U. S. Schubert, *Inorg. Chem.* **2015**, *54*, 3159–3171.

[13] K. Heinze, K. Hempel, S. Tschierlei, M. Schmitt, J. Popp, S. Rau, *Eur. J. Inorg. Chem.* **2009**, 3119–3126.

[14] a) R. E. Hester, K. P. J. Williams, *J. Chem. Soc. Perkin Trans. 2* **1981**, 852–859; b) M. A. Palafox, M. Gil, J. L. Nunez, G. Tardajos, *Int. J. Quantum Chem.* **2002**, *89*, 147–171.

[15] J. T. Hewitt, P. J. Vallett, N. H. Damrauer, *J. Phys. Chem. A* **2012**, *116*, 11536–11547.

[16] J. Schindler, S. Kupfer, M. Wächtler, J. Guthmuller, S. Rau, B. Dietzek, *ChemPhysChem* **2015**, *16*, 1061–1070.

[17] R. Berera, R. Grondelle, J. T. M. Kennis, *Photosynth. Res.* **2009**, *101*, 105–118.

[18] F. Chaignon, J. Torroba, E. Blart, M. Borgström, L. Hammarström, F. Odobel, *New J. Chem.* **2005**, *29*, 1272–1284.

[19] G. Benkö, J. Kallioinen, P. Myllyperkiö, F. Trif, J. E. I. Korppi-Tommola, A. P. Yartsev, V. Sundström, *J. Phys. Chem. B* **2004**, *108*, 2862–2867.

[20] M. T. Indelli, M. Orlandi, C. Chiorboli, M. Ravaglia, F. Scandola, F. Lafolet, S. Welter, L. De Cola, *J. Phys. Chem. A* **2012**, *116*, 119–131.

[21] W. R. Browne, W. Henry, P. Passaniti, M. T. Gandolfi, R. Ballardini, C. M. O'Connor, C. Brady, C. G. Coates, J. G. Vosa, J. J. McGarvey, *Photochem. Photobiol. Sci.* **2007**, *6*, 386–396.

[22] a) L. Zedler, J. Guthmuller, I. R. de Moraes, S. Krieck, M. Schmitt, J. Popp, B. Dietzek, *J. Phys. Chem. C* **2013**, *117*, 6669–6677; b) Y. Zhang, S. Kupfer, L. Zedler, J. Schindler, T. Bocklitz, J. Guthmuller, S. Raud, B. Dietzek, *Phys. Chem. Chem. Phys.* **2015**, *17*, 29637–29646.

[23] a) R. Siebert, A. Winter, U. S. Schubert, B. Dietzek, J. Popp, *Phys. Chem. Chem. Phys.* **2011**, *13*, 1606–1617; b) J. Kübel, R. Schroot, M. Wächtler, U. S. Schubert, B. Dietzek, M. Jäger, *J. Phys. Chem. C* **2015**, *119*, 4742–4751.

[24] L. Zedler, J. Guthmuller, I. R. Moraes, S. Kupfer, S. Krieck, M. Schmitt, J. Popp, S. Raue, B. Dietzek, *Chem. Commun.* **2014**, *50*, 5227–5229.

Manuscript received: January 27, 2017
Accepted Article published: February 15, 2017
Final Article published: March 23, 2017

© 2017 Wiley-VCH Verlag GmbH & Co. KGaA, Weinheim

CHEMISTRY
A European Journal

Supporting Information

Energy versus Electron Transfer: Controlling the Excitation Transfer in Molecular Triads

Yusen Luo,[a, b] Kevin Barthelmes,[c, d] Maria Wächtler,[b] Andreas Winter,[c, d] Ulrich S. Schubert,[c, d] and Benjamin Dietzek*[a, b, c]

chem_201700413_sm_miscellaneous_information.pdf

Table of Contents

Spectrum of the fully CSS ($PTZ^{\cdot+}$-$C_{60}^{\cdot-}$)

For the absorption features of oxidized PTZ in the main manuscript, we would like to point out that compared with the pristine PTZ radical cation reported elsewhere the maximum absorption is at ca. 520 nm,[1] the absorption of $PTZ^{\cdot+}$(at 580 nm) in our systems appears red-shifted. This is explained by an increased delocalization of the excess charge in $PTZ^{\cdot+}$ due to the conjugation of the tpy ligand in the 3-position of the donor. This assumption is supported by literature which shows that the absorption of $PTZ^{\cdot+}$ is very sensitive to the substitution patterns.[2] By simply adding up the absorption of $PTZ^{\cdot+}$ and $C_{60}^{\cdot-}$ the spectrum of the fully CSS ($PTZ^{\cdot+}$-$C_{60}^{\cdot-}$) can be obtained. Note that the absorption of $PTZ^{\cdot+}$ at 365 nm is not that pronounced owing to the negative absorption of $C_{60}^{\cdot-}$.

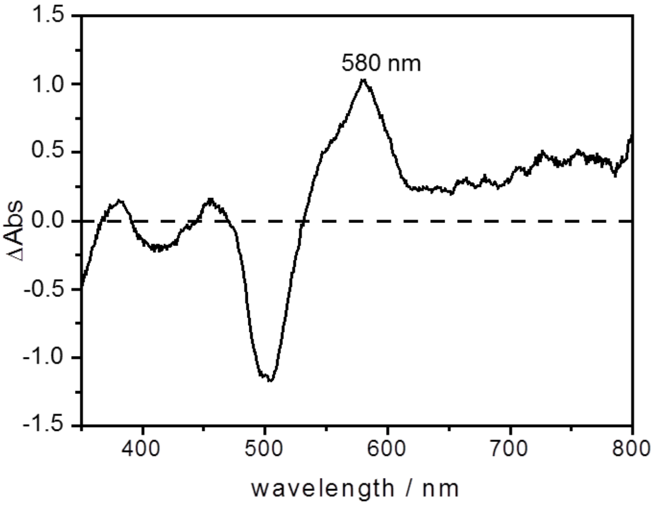

Figure S1. Spectrum of the fully CSS ($PTZ^{\cdot+}$-$C_{60}^{\cdot-}$) obtained by summing up the oxidized ($PTZ^{\cdot+}$) and reduced ($C_{60}^{\cdot-}$) spectroelectrochemical UV-Vis spectra in the main text (Figure 1e, f). The oxidized and reduced spectra were normalized at the absorption maxima of ground state bleach before addition.

Reductive SEC-UV/Vis spectra of **RuC$_{60}$**

For the reductive SEC, reference compound **RuC$_{60}$** (Figure S2a) containing a C_{60}, octyloxy functionalized *para*-phenyleneethynylene spacer and a $[Ru\ (tpy)_2]^{2+}$ complex without electron donor PTZ was used.[3] The SEC absorption difference spectra of $C_{60}^{\cdot -}$ were smoothed by the method of adjacent-averaging of 20 points of window. For comparison, the original and smoothed spectra are showed in Figure S2b.

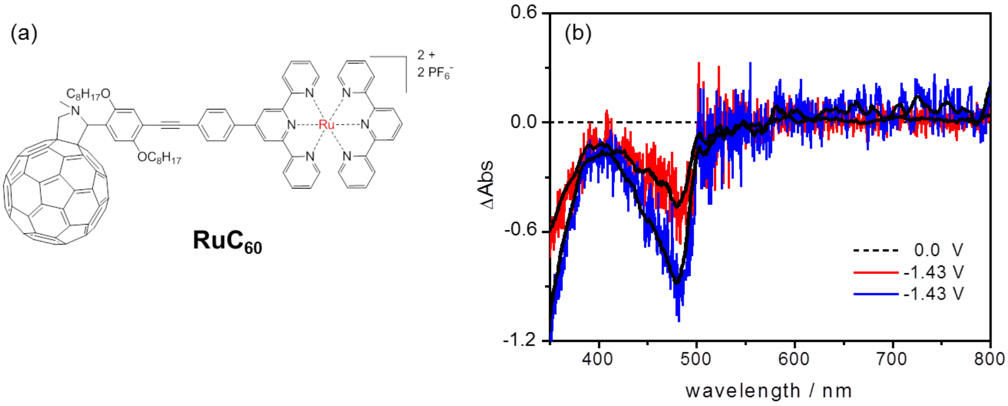

Figure S2. (a) Molecular structure of the **RuC$_{60}$** used for the reductive spectroelectrochemistry and (b) comparison of the raw (red and blue ones) and corresponding smoothed spectra (black curves within the raw spectra).

Global fit result of the ns TA data of **PTRu**

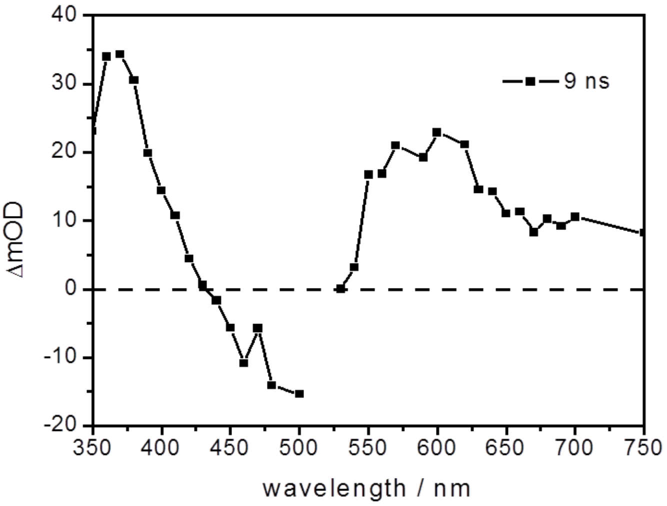

Figure S3. Global fit result of the ns TA data of **PTRu** upon excitation at 520 nm in aerated DCM gives out only one species with a life time of ~9 ns (limited by the time resolution of our detection system).

Integrated kinetic traces of the ns TA data of **PTRuC$_{60}$**

Integrated kinetic traces over the two bands, *i.e.* the spectral region specific to the CSS (540-630 nm) and $^3C_{60}^*$ (640-850 nm) in the ns TA spectra of **PTRuC$_{60}$** upon different excitation wavelengths were obtained. Clearly, two decay processes on different timescales were observed which further illustrate two different final states after photoexcitation. From the normalized spectra the excitation-wavelength dependent properties were apparent. Upon shifting the excitation to low wavelength the intensity of the CSS trace decreases (from Figure S4a to S4c).

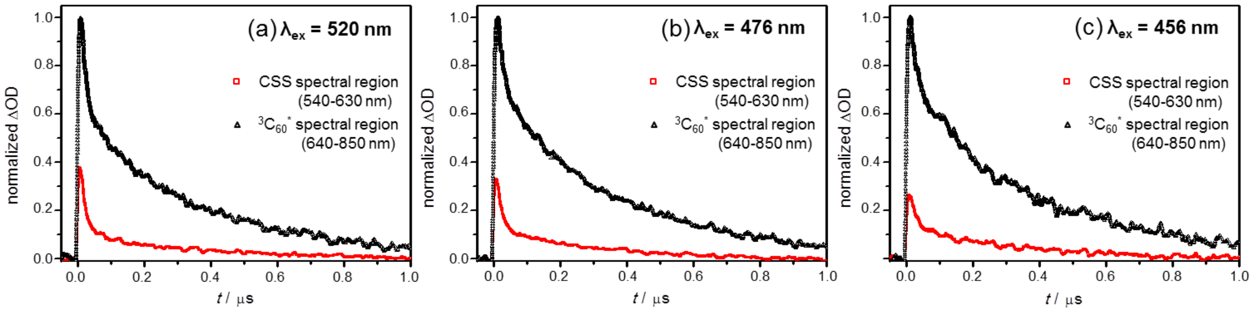

Figure S4. Integrated kinetic traces over the two bands which belong to the CSS (540-630 nm, red square) and $^3C_{60}^*$ (640-850 nm, black triangle) of the ns transient absorption data of **PTRuC$_{60}$** upon excitation at (a) 520, (b) 476 and (c) 456 nm in aerated DCM. The data were normalized by the corresponding maximum of the kinetic trance of $^3C_{60}^*$.

Global fits of the ns TA data of **$PTRuC_{60}$**

The global fits of the ns TA data of **$PTRuC_{60}$** upon varying excitation wavelengths yields two species: the relative short one (τ_{ns1} = 20 ns) mainly dominates at 590 nm (the absorption of $PTZ^{\cdot+}$) and the longer one (τ_{ns2} = 320 ns) dominates at 700 nm which is assigned to the fully CSS and $^3C_{60}^*$ respectively (as has been discussed in the main text). The excitation-wavelength dependent effects are more prominently displayed in the global fitting results, *e.g.* upon decreasing the excitation wavelength from 520 to 456 nm, the intensity of the CSS absorption band decreases by 2.5 times (all spectra were normalized by the absorption maximum of $^3C_{60}^*$).

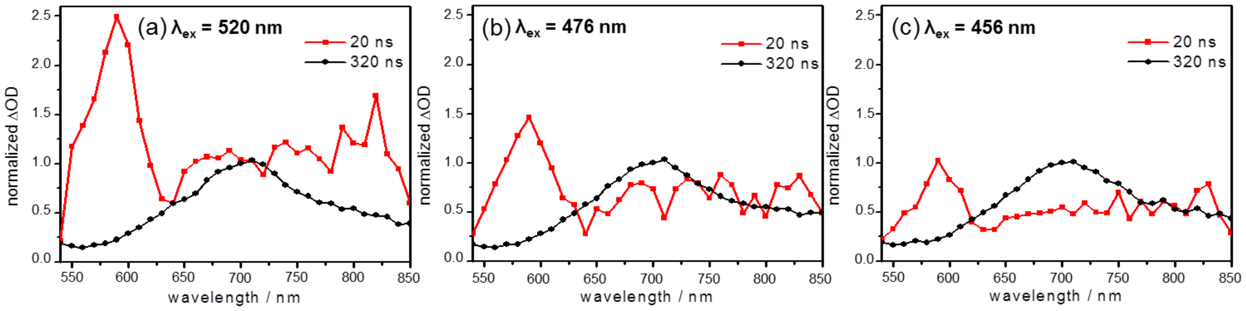

Figure S5. Global fit results of the ns transient absorption data of **$PTRuC_{60}$** upon excitation at (a) 520, (b) 476 and (c) 456 nm in aerated DCM. All spectra were normalized by the corresponding absorption maximum of $^3C_{60}^*$ (at 700 nm) and only show the spectral region above 540 nm where displays significant characteristics. The ratio of the absorption maxima between CSS and $^3C_{60}^*$ is (a) 2.5, (b) 1.4 and (c) 1.0.

Nanosecond TA spectra of **PTRuC$_{60}$** without oxygen

The existence of $^3C_{60}{}^*$ was corroborated by comparing the kinetic traces at 700 nm with and without oxygen based on the principle that triplet states of organic molecules would be quenched by triplet oxygen, reducing the lifetimes of excited states intensively.[3] Comparing the ns data recorded for **PTRuC$_{60}$** in the presence (Figure 1a, d, Figure S5a) and absence (Figure S6) of oxygen, it is apparent that τ_{ns1} is barely changed (20 ns and 26 ns respectively). However, τ_{ns2} revealing a strong influence of oxygen concentration in solution which increases by a factor of 5 is assigned to the decay of $^3C_{60}{}^*$ state.

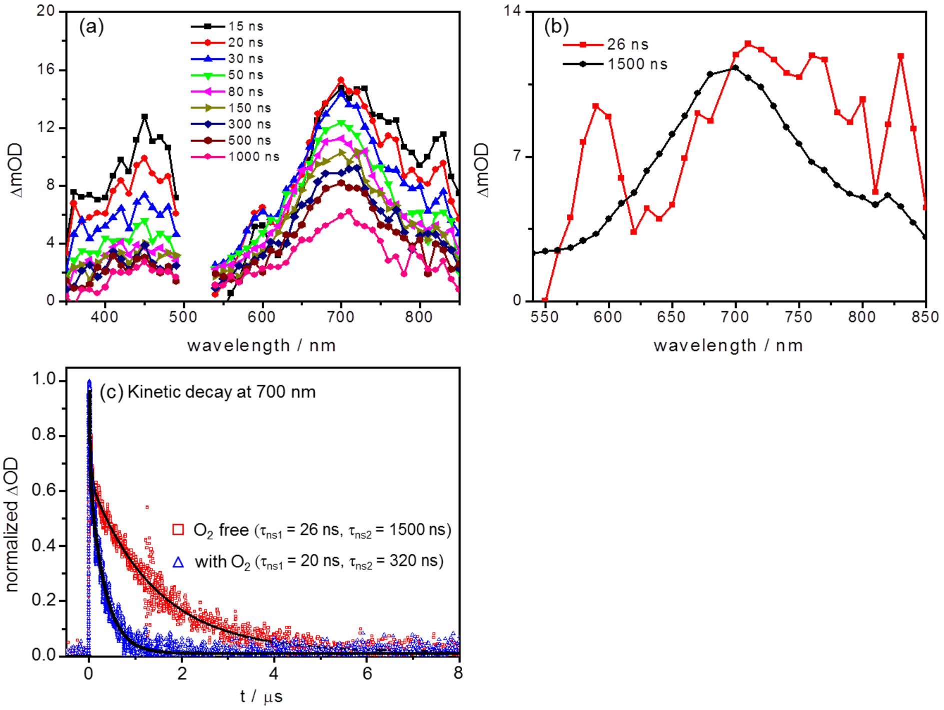

Figure S6. (a) Nanosecond transient absorption spectra of **PTRuC$_{60}$** at selected times upon excitation at 520 nm in deaerated DCM. (b) Corresponding global fit result of the ns transient absorption data which only shows the spectra above 540 nm where displays significant characteristics. (c) Decay kinetics with respective fit curves at 700 nm where $^3C_{60}{}^*$ has the maximum absorption in the presence (blue, triangle) and absence (red, square) of oxygen.

Excitation-wavelength dependent RR spectra of **PTRu**

Similar to triad **PTRuC$_{60}$**, all RR spectra of dyad **PTRu** display PTZ (blue dotted line) and tpy (red dashed line) associated bands. Clearly the relative signal intensities of PTZ and tpy associated bands change with excitation wavelengths (see inset in Figure S7). Decreasing excitation wavelengths (from 515 to 458 nm) results in decreased RR signals of PTZ associated bands ($\tilde{\nu}$ = 1596, 1575, 1352 and 1046 cm^{-1}). Additionally the mode ($\tilde{\nu}$ = 848 cm^{-1}) which belongs to PTZ becomes less prominent when changing the excitation from 515 to 458 nm. It indicates that the electron density of the excited state mainly dominates at the free tpy ligand by decreasing excitation wavelengths. Thus the energy of ^{1}MLCT$_{\text{tpy-PTZ}}$ excited state is lower than that of ^{1}MLCT$_{\text{tpy}}$ excited state.

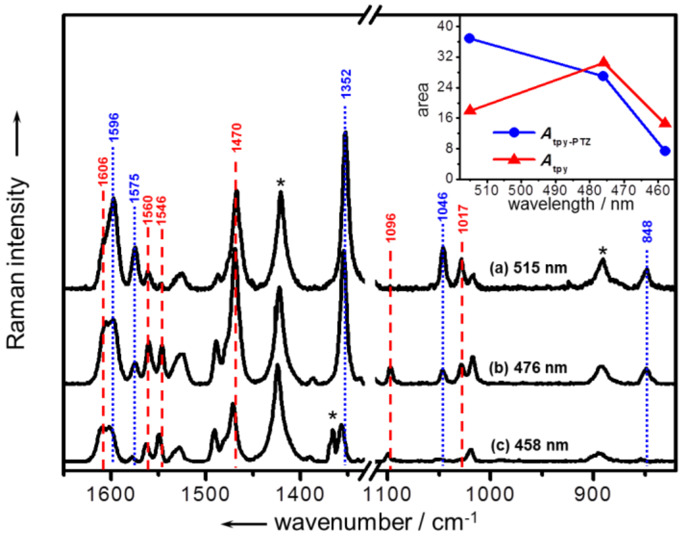

Figure S7. Resonance Raman spectra of **PTRu** in DCM with excitation wavelengths at (a) 515, (b) 476 and (c) 458 nm. The spectra were normalized to the solvent band (asterisks) at 1420 cm^{-1} and only modes showing distinct differences were marked. Color code: PTZ associated bands in blue dotted line, tpy associated bands in red dashed line. Inset: band areas of the PTZ ($A_{\text{tpy-PTZ}}$, blue) and tpy (A_{tpy}, red) associated bands as a function of excitation wavelengths.

Raman data of **PTRuC$_{60}$** and **PTRu**

Table S1. Assignment of the Raman data of triad **PTRuC$_{60}$** and dyad **PTRu**. Only the modes showing distinct difference in signal intensities of the RR spectra upon varying the excitation wavelength were listed in the table. These values are in cm^{-1}. The assignment was based on the unsubstituted [Ru(tpy)$_2$](PF$_6$)$_2$ and *N*-methylphenothiazine (*N*-MePTZ) reported in literature. Note that *N*-MePTZ was measured in solid state and it would show +5 cm^{-1} shift upon dissolution.

Assignment	**PTRuC$_{60}$** [a] $\tilde{\nu}$ / cm^{-1} λ$_{ex}$= 515 nm, 476 nm, 458 nm	**PTRu** $\tilde{\nu}$ / cm^{-1} λ$_{ex}$= 515 nm, 476 nm, 458 nm	[Ru(tpy)$_2$](PF$_6$)$_2$ [b] $\tilde{\nu}$ / cm^{-1}	*N*-MePTZ [c] $\tilde{\nu}$ / cm^{-1}
tpy	1606, 1604, 1607	1607 (sh), 1606,1609	1602	
PTZ	1596, 1595 (sh), -	1597, 1598, 1600		1591
PTZ	1574, 1574, 1578	1575, 1575, 1578		1569
tpy	1559, 1559, 1562	1560, 1560, 1562	1559	
tpy	-	1547, 1547, 1549	1549	
tpy	1469, 1470, 1470	1468, 1469, 1470	1470	
PTZ	1464 (sh), -, -	-		1458
PTZ	1352, 1354, 1356	1352, 1354, 1356		1361
PTZ	1337 (sh), 1337 (sh), -	-		1333
tpy	-	-, 1096, 1096	1094	
PTZ		1046, 1046, -		1038
tpy		1017, 1017, 1018	1018	
PTZ		848, 848, -		841

[a] for triad **PTRuC$_{60}$**, only shows the data in the 1640-1320 cm^{-1} ranges. (sh) = shoulder. For triad **PTRuC$_{60}$** and dyad **PTRu**, the RR data were collected in dichloromethane. [b] taken from reference (reference [13] in main text) which was measured in acetonitrile. [c] taken from reference (reference [14] in main text) which was measured in solid phase. It would show + 5 cm^{-1} shift upon dissolution.

References

[1] J. E. McGarrah, R. Eisenberg, *Inorg. Chem.* **2003**, *42*, 4355-4365; b) C. V. Suneesh, K. R. Gopidas, *J. Phys. Chem. C* **2009**, *113*, 1606-1614.

[2] a) J. Daub, R. Engl, J. Kurzawa, S. E. Miller, S. Schneider, A. Stockmann, M. R. Wasielewski, *J. Phys. Chem. A* **2001**,*105*, 5655-5665; b) R. Sugimura, S. Suzuki, M. Kozaki, K. Keyaki, K. Nozaki, H. Matsushita, N. Ikeda, K. Okada, *Res. Chem. Intermed.* **2013**, *39*,185-204; c) S.-H. Lee, C. T.-L. Chan, K. M.-C. Wong, W. H. Lam, W.-M. Kwok, V. W.-W. Yam, *J. Am. Chem. Soc.* **2014**, *136*, 10041-10052.

[3] K. Barthelmes, J. Kübel, A. Winter, M. Wächtler, C. Friebe, B. Dietzek, U. S. Schubert, *Inorg. Chem.* **2015**, *54*, 3159-3171.

[P2] Direct Detection of the Photoinduced Charge-Separated State in a Ru(II) Bis(terpyridine) – Polyoxometalate Molecular Dyad

Reproduced with permission from: Y. Luo, M. Wächtler, K. Barthelmes, A. Winter, U. S. Schubert and B. Dietzek, "Direct Detection of the Photoinduced Charge-Separated State in a Ru(II) Bis(terpyridine) –Polyoxometalate Molecular Dyad", *Chem. Commun.*, **2018**, *54*, 2970–2973, with permission from the Royal Society of Chemistry.

Volume 54 | Number 24 | 25 March 2018 | Pages 2933–3066

ChemComm

Chemical Communications

rsc.li/chemcomm

ISSN 1359-7345

ROYAL SOCIETY
OF **CHEMISTRY**

COMMUNICATION

Benjamin Dietzek *et al.*

Direct detection of the photoinduced charge-separated state in a Ru(II) bis(terpyridine)–polyoxometalate molecular dyad

Published on 29 January 2018. Downloaded by Thueringer Universitats Landesbibliothek Jena on 3/28/2019 8:58:49 AM.

ChemComm

COMMUNICATION

View Article Online
View Journal | View Issue

Check for updates

Cite this: *Chem. Commun.*, 2018, 54, 2970

Received 29th November 2017,
Accepted 29th January 2018

DOI: 10.1039/c7cc09181h

rsc.li/chemcomm

Direct detection of the photoinduced charge-separated state in a Ru(II) bis(terpyridine)–polyoxometalate molecular dyad†

Yusen Luo,[ab] Maria Wächtler,[b] Kevin Barthelmes,[cd] Andreas Winter,[cd] Ulrich S. Schubert[cd] and Benjamin Dietzek*[abd]

Observation of photoinduced intramolecular charge-separation is difficult for photosensitizer–POM dyads because of rapid backward electron transfer. We report here for the first time on a long-lived charge-separated state (τ = 470 ns) observed in a Ru(II) bis(terpyridine)-based dyad. Charge-separation occurs despite virtually no driving force and the short intrinsic excited-state lifetime of the photosensitizer.

To convert solar radiation to solar fuels, multi-functional intramolecular photocatalytic systems have attracted much attention in the past few decades.[1–4] The photo-populated charge-separated states (CSS), which are essential intermediates in artificial photosynthesis, should exhibit sufficient lifetimes to react with external redox reactants, *e.g.* light-driven water-splitting.[5–9] Polyoxometalates (POMs),[10,11] which can store several electrons with very small structural change, emerged as promising model compounds, in particular due to the fact that reduced POMs are efficient photo-/electro-catalysts for proton reduction.[12–16] Since POMs barely absorb visible light, the incorporation of photosensitizers is necessary to improve the absorption of solar irradiation.[17] Thus, by virtue of proper surface functionalization several covalent photosensitizer–POM dyads have been fabricated.[15–18]

Despite the remarkable electrochemical and electrocatalytic properties of POMs, there are only few examples in the literature on photoinduced electron transfer in covalent photosensitizer–POM dyads.[19–23] For example, Hill and coworkers reported the direct observation of a short-lived CSS in a Re(I)–POM (Dawson-type; lifetime of 1.4 ps) using time-resolved absorption spectroscopy.[19] Proust and coworkers showed the quenching of photosensitizer emission in heteroleptic Ru(II) tris(bipyridine)–POM systems (either Keggin- or Dawson-type).[20] However, no long-lived CSS was observed in either of these dyads, which was rationalized by either fast charge recombination or very low yields of the CSS.[20] In order to improve the photophysical properties of the photosensitizer, the same group replaced the covalently linked Ru(II) photosensitizer by an Ir(III) one. This led to the observation of spectral evidence for intramolecular CSS involving the POM as an acceptor unit. The lifetimes of the CSS (ranging from 2 to 480 ns) represent the longest values reported to date.[21] Fukuzumi and coworkers investigated Sn(IV) porphyrins as photosensitizers in covalently linked photosensitizer–POM dyads (Keggin-type). These authors observed a partial quenching of the emission from the Sn(IV) porphyrins in the dyad. However, no spectroscopic signature of the CSS itself was found, which was interpreted as back electron transfer occurring with a higher rate than the forward electron transfer.[22] Thus, based on the literature the general picture seems to emerge that CSS in molecular dyads containing POMs as acceptor units are rather short lived[19,23] and, in some cases, elude direct detection at all.[20,22]

Some of us recently reported the synthesis of the photosensitizer–POM dyad **Ru–POM**, which contains a Ru(II)–bis(terpyridine) photosensitizer and a Keggin-type POM ($[PW_{11}O_{39}Ge]^{4-}$) (Scheme 1b).[24] The utilization of the Ru(II)–bis(terpyridine) unit as a photosensitizer is motivated by its ability to construct linear structures without inducing geometric or optical isomers.[25,26] In this contribution we will show that despite the relatively short excited-state lifetime inherent to the Ru(II)–bis(terpyridine) complex (*e.g.* 124 ps in acetonitrile[27] and 250 ps in water[28] for $Ru(tpy)_2^{2+}$, while the lifetime, of course, can be affected by the substituents on the tpy ligands[29,30]), photoinduced electron transfer to the POM takes place in **Ru–POM**. To the best of our knowledge, it is the first time to spectroscopically detect a long-lived CSS in photosensitizer–POM dyads when Ru(II)–bis(terpyridine) acts as the photosensitizer.

First insight into the interactions of the individual functional units in the dyad has been gained from steady-state emission spectroscopy (see Fig. S1b, ESI†): upon excitation of the ^{1}MLCT

---

[a] *Institute of Physical Chemistry and Abbe Center of Photonics, Friedrich Schiller University Jena, Helmholtzweg 4, Jena 07743, Germany*
[b] *Leibniz Institute of Photonic Technology (IPHT), Albert-Einstein-Straße 9, Jena 07745, Germany. E-mail: benjamin.dietzek@leibniz-ipht.de*
[c] *Laboratory of Organic and Macromolecular Chemistry (IOMC), Friedrich Schiller University Jena, Humboldtstraße 10, Jena 07743, Germany*
[d] *Center for Energy and Environmental Chemistry Jena (CEEC Jena), Friedrich Schiller University Jena, Philosophenweg 7a, Jena 07743, Germany*

† Electronic supplementary information (ESI) available. See DOI: 10.1039/c7cc09181h

This journal is © The Royal Society of Chemistry 2018

Published on 29 January 2018. Downloaded by Thueringer Universitats Landesbibliothek Jena on 3/28/2019 8:58:49 AM.

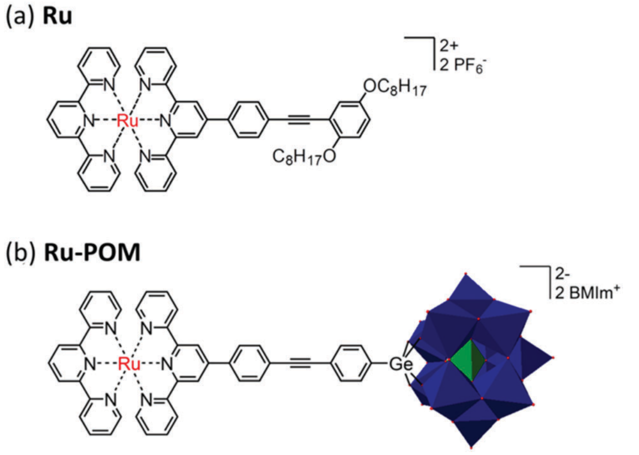

Scheme 1 Schematic representation of the molecular structures of (a) the reference **Ru** and (b) the **Ru–POM** dyad studied in this work. POM is $[PW_{11}O_{39}Ge]^{4-}$ and BMIm$^+$ stands for the 1-butyl-3-methyl-1*H*-imidazol-3-ium cation. Colour code: WO_6 octahedron, blue; PO_4 tetrahedron, green.

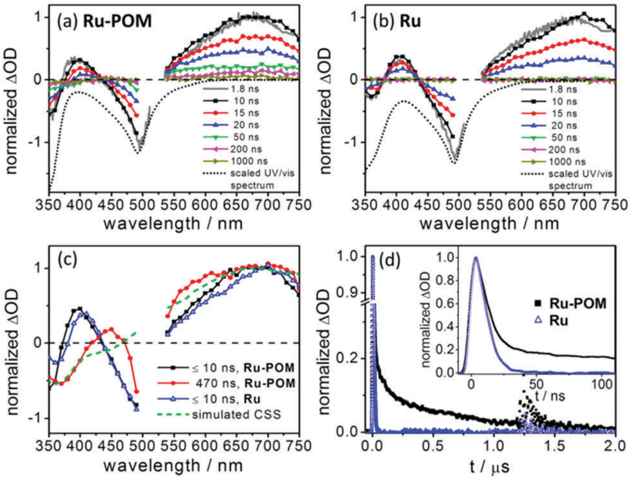

Fig. 1 ns transient absorption spectra at selected times of (a) **Ru–POM** and (b) **Ru** upon excitation at 520 nm in aerated DMSO. For comparison the fs TA spectrum at 1.8 ns was added (grey solid line). The fs TA spectrum (1.8 ns) and ns TA spectrum (at 10 ns) were normalized at 680 nm. The black dotted line represents the inverted ground state absorption spectrum of (a) **Ru–POM** and (b) **Ru**. (c) Global fit results of the ns TA data. The green dashed line shows the simulated absorption spectrum of $Ru^{III}(tpy)_2$–POM$^{\bullet-}$ according to the spectroelectrochemical results (see Fig. S6, ESI†). All spectra were normalized at 680 nm and the simulated absorption spectrum calculated as the $Ru^{III}(tpy)_2$–POM$^{\bullet-}$ was smoothed (for raw data, see Fig. S7, ESI†). (d) Normalized integrated kinetic trace of **Ru–POM** (black) and **Ru** (blue). The pump–probe data were spectrally integrated in the probe-wavelengths range between 540 and 750 nm. Inset: The enlargement of the time region up to 110 ns.

transition (λ_{ex} = 520 nm) the reference compound **Ru** and the dyad **Ru–POM** were found to emit at *ca.* 674 nm, which is slightly red-shifted as compared to a dinuclear Ru–Ru-complex with a related linker structure.[31] When the length of the extended ligand in **Ru** is reduced, as in **Ru–ph** having no additional substituted phenyl ring, the emission becomes slightly blue-shifted (see data of **Ru–ph** shown in the ESI,† for molecular structure of **Ru–ph** see the inset in Fig. S2a).[24] This is attributed to the increased π-conjugation on the tpy ligand in **Ru** and **Ru–POM.**[26,31] In **Ru–POM** the emission decreases by 15% compared to **Ru,** which indicates the existence of additional non-radiative decay pathways of the emissive excited state.

The ns transient absorption (TA) spectra in Fig. 1 provide direct evidence that the decay of the ^{3}MLCT state in **Ru–POM** qualitatively differs from the situation in **Ru**, *i.e.* it involves two kinetically distinct processes: between 10 and 50 ns after excitation the positive excited-state absorption (ESA) band at 400 nm decays completely while the band at 680 nm decreases by only *ca.* 80%. The remaining signal amplitude decays on a sub-μs timescale. This behaviour is fundamentally different from the ns kinetics of the structurally more simple complex **Ru**, for which the ^{3}MLCT state completely decays within 50 ns (Fig. 1b). This observation indicates that the introduction of the POM causes a secondary long-lived state to become available after photoexcitation of the **Ru–POM** dyad. The decay of this state is reflected in the ns transient absorption kinetics shown in Fig. 1d. The integrated kinetics clearly demonstrates that the ESA of **Ru–POM** decays bi-exponentially while the decay of the reference complex **Ru** is mono-exponential (Fig. 1d). A global fit (Fig. 1c and Fig. S3b, ESI†) of the ns TA data of **Ru–POM** yields a short-lived component, $\tau_{ns1} \leq 10$ ns, which has a much stronger absorption intensity (91% of the overall ns decay amplitude, see Fig. S3b, ESI†) than the long-lived one (τ_{ns2} = 470 ns, 9% of the overall ns decay amplitude). The short-lived species (τ_{ns1}) in **Ru–POM** resembles the ns decay kinetics and spectral features of the reference **Ru** (Fig. 1c, see Fig. S2 for more information, ESI†). Thus, the process reflected in τ_{ns1} is attributed to the decay of the ^{3}MLCT state in **Ru–POM.** (We would like to point out that the value of τ_{ns1} is close to the time resolution of the ns transient absorption setup. Thus this ns rate is more reliably determined *via* fs resolved transient absorption spectroscopy with a long optical delay line, see Fig. S4, ESI†.) However, the relaxation of the ^{3}MLCT state in **Ru–POM** does not exclusively repopulate the ground state but a small fraction decays *via* the POM-associated intermediate state whose decay is associated with τ_{ns2}. The presence of oxygen changes the lifetime of this intermediate state (τ_{ns2}) only slightly: τ_{ns2} = 470 ns in aerated solution *vs.* 570 ns in deaerated solution (Fig. S3c, d and Fig. S5, ESI†). This 20% increase of the lifetime in oxygen-free solution is minute compared to the effect of oxygen on the lifetime of triplet states in organic molecules, *e.g.* in C_{60} the triplet state lifetime increases from 800 ns to 13 μs upon removal of oxygen;[29] the lifetime of the ^{3}MLCT state in $Ru(bpy)_3^{2+}$ is 200 and 870 ns with and without oxygen, respectively.[32] This indicates that the species related to τ_{ns2} is not a triplet state, *e.g.* a secondary ^{3}MLCT, whose lifetime will be increased significantly in the absence of oxygen.[33] Hence, we assign the long-lived POM-induced state to a charge-separated state, *i.e.* $Ru^{III}(tpy)_2$–POM$^{\bullet-}$.

The additional quenching pathway of the excited ^{3}MLCT state in **Ru–POM** is further supported by the slightly shortened lifetime of the ^{3}MLCT state in **Ru–POM** (τ = 5.4 ns, Fig. S4b, ESI†) compared to the reference **Ru** (τ = 6.5 ns, Fig. S4d, ESI†).

Published on 29 January 2018. Downloaded by Thueringer Universitats Landesbibliothek Jena on 3/28/2019 8:58:49 AM.

This additional deactivation pathway is assumed to be associated with the electron transfer from the ^{3}MLCT state to establish the charge-separated state Ru$^{\text{III}}$(tpy)$_2$–POM$^{\bullet-}$. Thus, the electron-transfer rate constant k_{CS} in **Ru–POM** can be estimated by $k_{\text{CS}} = 1/\tau - k_0$, where k_0 is 1/6.5 ns^{-1}. This estimation yields $k_{\text{CS}} = 3.13 \times 10^7$ s^{-1} (*i.e.* $\tau_{\text{CS}} = k_{\text{CS}}{}^{-1} = 32$ ns). As a result, a roughly 16% yield of Ru$^{\text{III}}$(tpy)$_2$–POM$^{\bullet-}$ was obtained according to the fs TA data ($k_{\text{CS}}/(k_{\text{CS}} + k_0)$), which is consistent with the slightly quenched emission intensity of **Ru–POM** (15%, Fig. S1b, ESI†) as well as the small contribution to the overall ns decay amplitude observed in the ns TA data of **Ru–POM** (9%, Fig. 1d and Fig. S3b, ESI†).

In order to corroborate this assignment, UV/vis spectroelectrochemistry (SEC) was performed (Fig. S6, ESI†) on the individual molecular fragments **POM** (for molecular structure, see Fig. S6c, ESI†) and **Ru**: upon one-electron reduction of the POM (*i.e.* formation of POM$^{\bullet-}$), a broad absorption band above 450 nm arises (Fig. S6a, ESI†). The peak of this reduction-induced band is at *ca.* 670 nm and is accompanied by an absorption decrease below 450 nm (Fig. S6a, ESI†). The oxidation of **Ru** shows the growth of a new absorption band centred at 406 nm, a decrease of the absorption band at 370 nm along with a loss of ^{1}MLCT intensity (Fig. S6b, ESI†). Based on the SEC data, the spectrum of Ru$^{\text{III}}$(tpy)$_2$–POM$^{\bullet-}$ can be approximated (Fig. 1c, and see Fig. S7 for details, ESI†). This approximation yields a good agreement with the TA spectrum of the long-lived ns species (τ_{ns2}, Fig. 1c), which further adds to the conclusion that upon introduction of the POM unit to the Ru core the charge-separated state Ru$^{\text{III}}$(tpy)$_2$–POM$^{\bullet-}$ becomes accessible upon MLCT excitation. We ascribe the formation of the spectral features of the reduced POM to the charge transfer from the photoexcited Ru-center and exclude a previously suggested mechanism that involves reductive quenching of a POM centered electronically excited state by radical-ion-pair formation.[34] This is due to the fact that the $[\text{PW}_{11}\text{O}_{39}\text{Ge}]^{4-}$ cluster does not absorb at the excitation wavelength (Fig. S1a, ESI†) and the spectral features observed in the transient absorption experiment point to the presence of intramolecular electron transfer instead of energy transfer.

Notably, the calculations of the driving force (details for the calculation can be found in the ESI†) based on the Rehm–Weller equation show that the electron transfer from the photoexcited Ru(II) complex to the POM is a slight uphill process $\left(-\Delta G^\circ_{\text{CS}} = -0.12 \text{ eV in DMF and } -\Delta G^\circ_{\text{CS}} = -0.11 \text{ eV in DMSO}\right)$ – or, given the uncertainties that are associated with the estimation of the driving force based on the Rehm–Weller equation, electron transfer is at best when occurring with virtually no driving force. Nevertheless this process is observed experimentally (see above). This finding is reminiscent of Campagna's observation of a photoinduced electron transfer in an Os(II)–bis(terpyridine)-pyridinium molecular dyad occurring with a positive driving force of similar magnitude $\left(-\Delta G^\circ_{\text{CS}} = -0.12 \text{ eV}\right)$.[35] However, for another dyad with a larger positive driving force $\left(-\Delta G^\circ_{\text{CS}} = -0.22 \text{ eV}\right)$, no CSS was detected.[35] It was thus concluded that "photoinduced electron transfer can occur within multicomponent systems in spite of driving forces virtually approaching zero."[35] To the best of our knowledge, the data shown here present the first observation of an intramolecular electron transfer in a Ru(tpy)$_2$–POM dyad – even taking place with virtually no driving force and in spite of the relative short excited-state lifetime of the Ru–tpy photosensitizer (*e.g.* 6.5 ns for the reference **Ru** in DMSO). The slow charge separation ($\tau_{\text{CS}} = k_{\text{CS}}{}^{-1} = 32$ ns) and the even slower charge recombination ($\tau_{\text{CR}} = 470$ ns) point to the fact that the slightly endergonic electron transfer is thermally activated.

To shed light on the details of the light-induced excited-state pathways, fs TA spectroscopy was employed. In Fig. 2 the data collected by a short (up to 1.8 ns) and a long optical delay line (up to 9.5 ns) are merged (see ESI,† Fig. S4a, for the normalization procedure). The differential absorption spectra (Fig. 2a) are dominated by the ground state bleach (GSB) centred at 487 nm accompanied by ESA from 360 to 430 nm and from 550 to 750 nm. The spectra show the typical TA features of a $[\text{Ru(tpy)}_2]^{2+}$-^{3}MLCT state, including the ligand-centred band at *ca.* 385 nm.[27,36] This band is due to π–π* transitions localized on the reduced ligands.[27] The ESA maximum at early times (*i.e.* at 0.3 ps) appears at 690 nm and subsequently shifts to a shorter probe-wavelength, *i.e.* to 675 nm at 10 ps, while the overall band intensity increases. Subsequently, the spectral shape of the excited state absorption signal remains unchanged within the experimental window (9.5 ns). The fast shift of the ESA maximum is reflected in the decay-associated spectra (τ_1 = 1.3 ns in Fig. 2b) and is assigned to contributions of vibrational cooling and interligand electron transfer within the ^{3}MLCT manifold.[26] As a result of this initial relaxation, a thermalized ^{3}MLCT state is formed, for which the excess electron density is localized on the ligand with the lowest accepting orbitals,[37] *i.e.* the extended tpy-ligand (^{3}MLCT$_{\text{tpy–POM}}$). Hence, the structural changes, *e.g.* photoinduced planarization of the extended terpyridine ligand in a related system,[29] are not involved (it is not indicated by Fig. 2b). The second species (τ_2 = 5400 ps) (Fig. 2b) in the fs TA data is assigned to the decay of the thermalized ^{3}MLCT state as discussed before. Furthermore, a small offset is required in order to account quantitatively for the data (τ_{inf} in Fig. 2b). As has been discussed in the ns TA data, it represents Ru$^{\text{III}}$(tpy)$_2$–POM$^{\bullet-}$. The relaxation processes in photoexcited **Ru–POM** are summarized in Scheme 2.

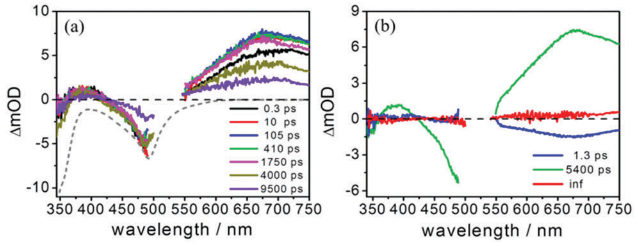

Fig. 2 fs transient absorption spectra (a) at selected delay times and decay-associated spectra (b) resulting from the global fit upon excitation at 520 nm in aerated DMSO for **Ru–POM**. The last two spectra were taken from the fs TA data collected by a longer optical delay line (Fig. S4a, ESI†) and were scaled according to the absorption spectrum at 1750 ps at 680 nm for **Ru–POM**. The grey dashed line represents the shape of the corresponding inverted ground state absorption spectrum. The ground state absorption spectrum is arbitrarily scaled to fit the scale of the respective figure.

Published on 29 January 2018. Downloaded by Thueringer Universitats Landesbibliothek Jena on 3/28/2019 8:58:49 AM.

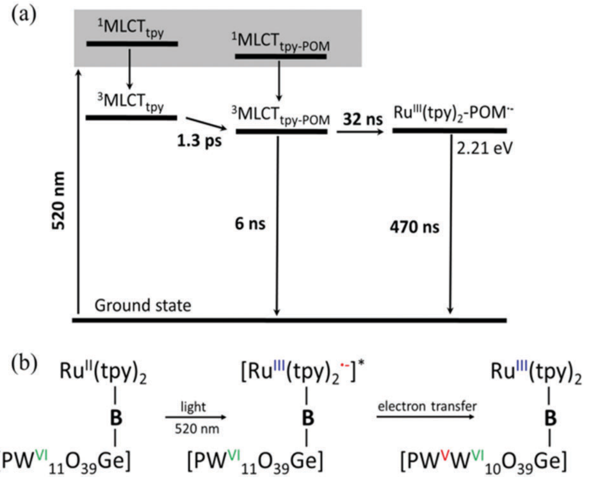

Scheme 2 (a) Energy-level diagrams of **Ru–POM** were developed using electrochemical and fs/ns TA data. (b) Chemical formula for the electron transfer process in **Ru–POM**. The oxidation and reduction states were assigned. B represents the molecular bridge between the Ru complex and POM.

In summary, we have successfully detected the formation of Ru^{III}(tpy)$_2$–POM$^{•-}$ in a molecular dyad **Ru–POM** containing the Ru(II)–bis(terpyridine) photosensitizer using time-resolved spectroscopy. **Ru–POM** is the first photosensitizer–POM dyad in which intramolecular electron transfer was identified even though the driving force is close to zero $\left(\Delta G^{\circ}_{\mathrm{CS}} = -0.12\ \mathrm{eV}\right)$ and despite the fact that the intrinsic excited-state lifetime of the photosensitizer, *i.e.* the Ru(tpy)$_2$ unit, is relatively short. The lifetime (τ = 470 ns) of Ru^{III}(tpy)$_2$–POM$^{•-}$ is comparable to the longest lifetime of such a state reported in the literature for covalently bonded photosensitizer–POM dyads (τ = 482 ± 13 ns). To further understand this process, temperature-dependent time-resolved spectroscopy will be performed to study how the electron-transfer rate and the quantum yields of Ru^{III}(tpy)$_2$–POM$^{•-}$ depend on temperature.

Conflicts of interest

There are no conflicts to declare.

Notes and references

1 M. Rudolf, S. V. Kirner and D. M. Guldi, *Chem. Soc. Rev.*, 2016, **45**, 612–630.
2 N. S. Lewis, *Science*, 2016, **351**, aad1920.
3 S. Chabi, K. M. Papadantonakis, N. S. Lewis and M. S. Freund, *Energy Environ. Sci.*, 2017, **10**, 1320–1338.
4 L. Hammarström, *Faraday Discuss.*, 2017, **198**, 549–560.
5 S. Fukuzumi, K. Ohkubo and T. Suenobu, *Acc. Chem. Res.*, 2014, **47**, 1455–1464.
6 S. Fukuzumi, Y. Yamada, T. Suenobu, K. Ohkubo and H. Kotani, *Energy Environ. Sci.*, 2011, **4**, 2754–2766.
7 B. Matt, J. Fize, J. Moussa, H. Amouri, A. Pereira, V. Artero, G. Izzet and A. Proust, *Energy Environ. Sci.*, 2013, **6**, 1504–1508.
8 S. Tschierlei, M. Presselt, C. Kuhnt, A. Yartsev, T. Pascher, V. Sundström, M. Karnahl, M. Schwalbe, B. Schäfer, S. Rau, M. Schmitt, B. Dietzek and J. Popp, *Chem. – Eur. J.*, 2009, **15**, 7678–7688.
9 L. A. Fredin and P. Persson, *J. Chem. Phys.*, 2016, **145**, 104310.
10 A. Dolbecq, E. Dumas, C. R. Mayer and P. Mialane, *Chem. Rev.*, 2010, **110**, 6009–6048.
11 J. J. Walsh, A. M. Bond, R. J. Forster and T. E. Keyes, *Coord. Chem. Rev.*, 2016, **306**, 217–234.
12 B. Keita, U. Kortz, L. R. B. Holzle, S. Brown and L. Nadjo, *Langmuir*, 2007, **23**, 9531–9534.
13 J. M. Sumliner, H. Lv, J. Fielden, Y. V. Geletii and C. L. Hill, *Eur. J. Inorg. Chem.*, 2014, 635–644.
14 W. Guo, H. Lv, J. Bacsa, Y. Gao, J. S. Lee and C. L. Hill, *Inorg. Chem.*, 2016, **55**, 461–466.
15 G. Izzet, F. Volatron and A. Proust, *Chem. Rec.*, 2017, **17**, 250–266.
16 S. Schönweiz, S. A. Rommel, J. Kübel, M. Micheel, B. Dietzek, S. Rau and C. Streb, *Chem. – Eur. J.*, 2016, **22**, 12002–12005.
17 C. Streb, *Dalton Trans.*, 2012, **41**, 1651–1659.
18 A. Proust, B. Matt, R. Villanneau, G. Guillemot, P. Gouzerh and G. Izzet, *Chem. Soc. Rev.*, 2012, **41**, 7605–7622.
19 C. Zhao, Z. Huang, W. Rodríguez-Córdoba, C. S. Kambara, K. P. O'Halloran, K. I. Hardcastle, D. G. Musaev, T. Lian and C. L. Hill, *J. Am. Chem. Soc.*, 2011, **133**, 20134–20137.
20 B. Matt, C. Coudret, C. Viala, D. Jouvenot, F. Loiseau, G. Izzet and A. Proust, *Inorg. Chem.*, 2011, **50**, 7761–7768.
21 B. Matt, X. Xiang, A. L. Kaledin, N. Han, J. Moussa, H. Amouri, S. Alves, C. L. Hill, T. Lian, D. G. Musaev, G. Izzeta and A. Proust, *Chem. Sci.*, 2013, **4**, 1737–1745.
22 A. Yokoyama, T. Kojima, K. Ohkubo, M. Shiro and S. Fukuzumi, *J. Phys. Chem. A*, 2011, **115**, 986–997.
23 C. Allain, D. Schaming, N. Karakostas, M. Erard, J.-P. Gisselbrecht, S. Sorgues, I. Lampre, L. Ruhlmann and B. Hasenknopf, *Dalton Trans.*, 2013, **42**, 2745–2754.
24 K. Barthelmes, M. Sittig, A. Winter and U. S. Schubert, *Eur. J. Inorg. Chem.*, 2017, 3698–3706.
25 E. Baranoff, J. P. Collin, L. Flamigni and J. P. Sauvage, *Chem. Soc. Rev.*, 2004, **33**, 147–155.
26 M. Wächtler, J. Kübel, K. Barthelmes, A. Winter, A. Schmiedel, T. Pascher, C. Lambert, U. S. Schubert and B. Dietzek, *Phys. Chem. Chem. Phys.*, 2016, **18**, 2350–2360.
27 J. T. Hewitt, P. J. Vallett and N. H. Damrauer, *J. Phys. Chem. A*, 2012, **116**, 11536–11547.
28 J. R. Winkler, T. L. Netzel, C. Creutz and N. Sutin, *J. Am. Chem. Soc.*, 1987, **109**, 2381–2392.
29 K. Barthelmes, J. Kübel, A. Winter, M. Wächtler, C. Friebe, B. Dietzek and U. S. Schubert, *Inorg. Chem.*, 2015, **54**, 3159–3171.
30 J.-P. Sauvage, J.-P. Collin, J.-C. Chambron, S. Guillerez, C. Coudret, V. Baltani, F. Barigelletti, L. D. Cola and L. Flamigni, *Chem. Rev.*, 1994, **94**, 993–1019.
31 R. Siebert, C. Hunger, J. Guthmuller, F. Schlütter, A. Winter, U. S. Schubert, L. González, B. Dietzek and J. Popp, *J. Phys. Chem. C*, 2011, **115**, 12677–12688.
32 A. A. Abdel-Shafi, D. R. Worrall and A. Y. Ershov, *Dalton Trans.*, 2004, 30–36.
33 K. Kawaoka, A. U. Khan and D. R. Kearns, *J. Chem. Phys.*, 1967, **46**, 1842–1853.
34 J. Tucher, K. Peuntinger, J. T. Margraf, T. Clark, D. M. Guldi and C. Streb, *Chem. – Eur. J.*, 2015, **21**, 8716–8719.
35 J. Fortage, G. Dupeyre, F. Tuyèras, V. Marvaud, P. Ochsenbein, I. Ciofini, M. Hromadová, L. Pospísil, A. Arrigo, E. Trovato, F. Puntoriero, P. P. Lainé and S. Campagna, *Inorg. Chem.*, 2013, **52**, 11944–11955.
36 A. M. Brown, C. E. McCusker and J. K. McCusker, *Dalton Trans.*, 2014, **43**, 17635–17646.
37 M. Schwalbe, M. Karnahl, S. Tschierlei, U. Uhlemann, M. Schmitt, B. Dietzek, J. Popp, R. Groake, J. G. Vos and S. Rau, *Dalton Trans.*, 2010, **39**, 2768–2771.

Electronic Supplementary Material (ESI) for ChemComm.
This journal is © The Royal Society of Chemistry 2018

Supporting Information

Direct detection of the photoinduced charge-separated state in a Ru(II) bis(terpyridine)-polyoxometalate molecular dyad

Yusen Luo,[1,2] Maria Wächtler,[2] Kevin Barthelmes,[3,4] Andreas Winter,[3,4] Ulrich S. Schubert,[3,4] and Benjamin Dietzek*[1,2,4]

[1]*Institute of Physical Chemistry and Abbe Center of Photonics, Friedrich-Schiller-University Jena, Helmholtzweg 4, 07743 Jena, Germany*

[2]*Leibniz Institute of Photonic Technology (IPHT), Albert-Einstein-Straße 9, 07745 Jena, Germany*

[3]*Laboratory of Organic and Macromolecular Chemistry (IOMC), Friedrich-Schiller-University Jena, Humboldtstraße 10, 07743 Jena, Germany*

[4]*Center for Energy and Environmental Chemistry Jena (CEEC Jena), Philosophenweg 7a, 07743 Jena, Germany*

**Corresponding author: benjamin.dietzek@leibniz-ipht.de*

Table of contents

General methods

The synthesis, electrochemistry and steady-state absorption and emission spectra of the dyad and the Ru complexes have been reported previously.[1,2] Steady-state UV/Vis absorption spectra (Figure S1a) and emission spectra (Figure S1b) collected in dimethyl sulfoxide (DMSO) are summarized for convenience. Steady-state UV/Vis absorption spectra were recorded with a JASCO V-670 spectrophotometer in a quartz cell with 1 mm path length. Steady-state emission spectra (λ_{ex} = 520 nm, optical density of each sample was adjusted to 0.1 at 520 nm) were recorded with a fluorescence spectrometer (Fluorolog, Horiba group) in a 1 cm quartz cell. For the time-resolved experiments the stability of samples was ensured by recording the steady-state UV/Vis absorption spectra before and after every measurement.

Electrochemistry. UV/Vis spectroelectrochemistry (SEC) measurements were performed in a home-built three-electrode thin-layer cell with an optical path length of 1 mm (Bioanalytical System, USA).[3] The three-electrode setup consists of a transparent platinum mesh working electrode, a platinum wire counter electrode, and an Ag/AgCl reference electrode. All potentials given in the manuscript refer to ferrocene as standard. The corresponding UV/Vis spectra were recorded on a single-beam spectrometer (Avantes, Avalight-DH-S-BAL) at room temperature. Because of the limited electrochemical window of DMSO, the electrochemistry[1] and SEC spectra were collected in dimethylformamide (DMF).

Time-Resolved Transient Absorption Spectroscopy. Femtosecond (fs) transient absorption spectra were collected by two different home-built pump-probe setups. Each setup is based on an amplified Ti: Sapphire oscillator (1 kHz, 800 nm).[4] The compounds were excited by pump pulses centered at 520 nm (TOPAS-C, Lightconversion Ltd.) with a duration of 80 fs. The power of the pump beam at the sample was kept at 0.45 mW, corresponding to an energy of 0.9 μJ per pump pulse. For measurements with a longer delay time range (up to 9.5 ns) the compounds were excited at 520 nm (TOPASwhite, Lightconversion Ltd.) with a duration of 110 fs. The power of the pump beam at the sample was kept at 0.3 mW, corresponding to an energy of 0.6 μJ per pump pulse. For both setups, a white light supercontinuum generated by focusing a fraction of the fundamental in a CaF_2 plate is used to probe the absorbance of the sample between 340 to 800 nm. The pump beam is delayed in time with respect to the probe beam by means of an optical delay line and the polarization between probe and pump is set at the magic angle (54.7°). Each sample solution (adjusted to yield an optical density of 0.2 at 520 nm) was kept in a 1 mm quartz cuvette. Transient absorption data were corrected for the chirp of the probe light and analyzed by a global multi-exponential fit after exclusion of a temporal window of 200 fs around time-zero in order to avoid contributions of the coherent-artifact region[5] to the data analysis.

Nanosecond (ns) transient absorption spectra[2] were collected to study the lifetime of the long-lived species, which are visible in the fs transient absorption data. The pump pulses centered at 520 nm were produced by a Continuum OPO Plus which is pumped by a continuum surelite Nd:YAG laser system (pulse duration 5 ns, repetition rate 10 Hz). The probe light is provided by a 75 W xenon arc lamp. Spherical concave mirrors are used to focus the probe beam into the samples and then to send the beam to the monochromator (Acton, Princeton Instruments). The spectrally selected probe light is detected by a Hamamatsu R928 photomultiplier. The signal is amplified and processed by a commercially available detection system (Pascher Instruments AB). Each sample was freshly prepared for the ns transient absorption measurements yielding an optical density of about 0.37 at the excitation wavelength, i.e. at 520 nm. All measurements were performed in 1 cm path length fluorescence cuvettes. For all measurements, the energy of the pump pulses was kept at 0.25 mJ. Oxygen-free solutions were realized by at least five freeze-pump-thaw cycles.

Considering the limited solubility of compounds studied in this manuscript, all spectroscopic experiments were performed upon dissolving the POM containing samples in DMSO.

UV/Vis absorption spectra and steady-state emission spectra

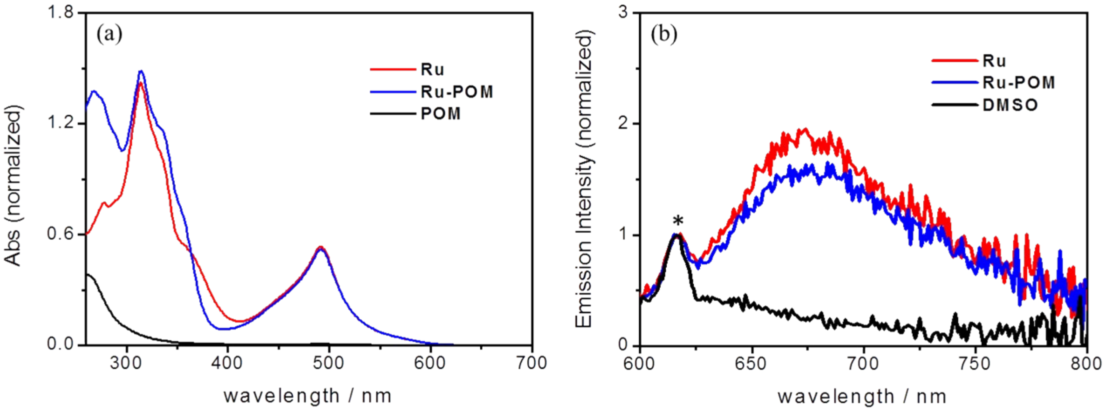

Figure S1. (a) UV-vis absorption spectra ($OD_{520\ nm}$ = 0.2 for fs transient absorption measurement) and (b) normalized steady-state emission spectra (λ_{ex} = 520 nm, $OD_{520\ nm}$ = 0.1) of the compounds collected in aerated DMSO. The emission spectra were normalized to the Raman band (asterisk) of the solvent DMSO. The extinction coefficients of **Ru** (in dichloromethane, λ_{max} = 487 nm, $\varepsilon = 3.54 \times 10^4\ M^{-1}\cdot cm^{-1}$) and **Ru-POM** (in DMSO, λ_{max} = 493 nm, $\varepsilon = 2.68 \times 10^4\ M^{-1}\cdot cm^{-1}$) have been reported.[1, 2]

ns TA spectra of reference Ru-ph and Ru

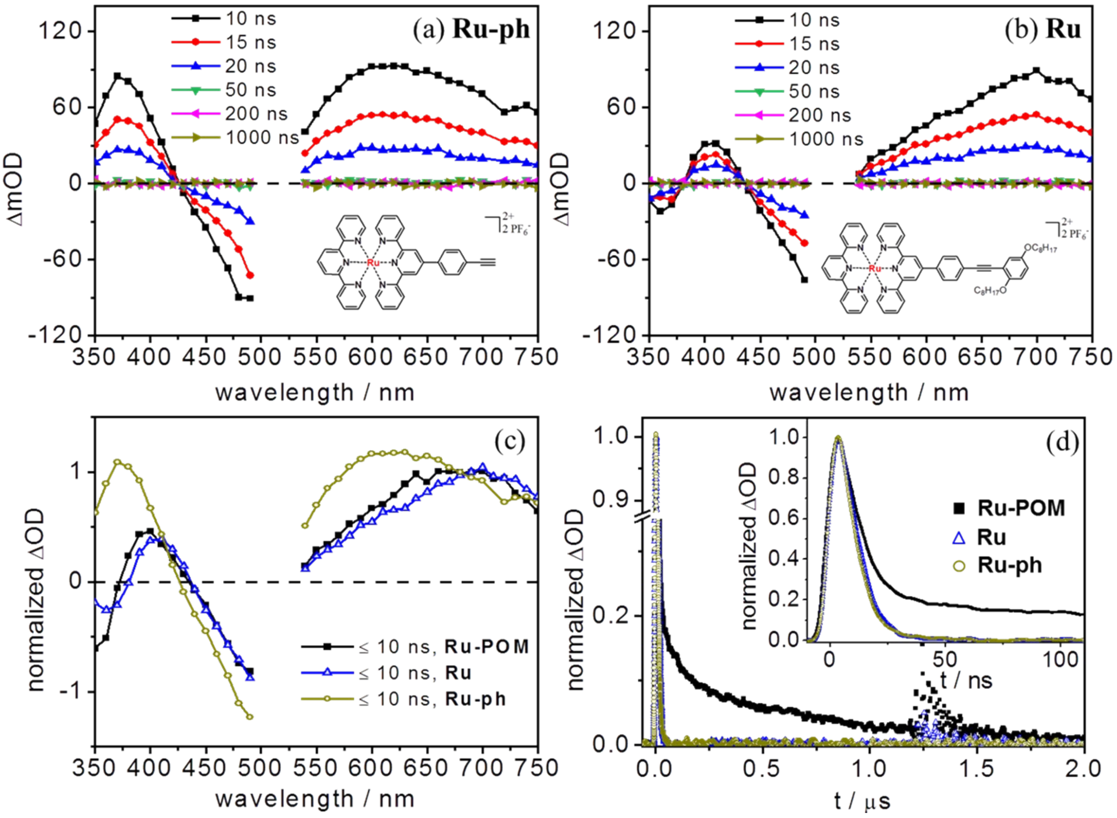

Figure S2. Nanosecond (ns) transient absorption (TA) spectra at selected times of (a) **Ru-ph** and (b) **Ru** upon excitation at 520 nm in aerated DMSO. (c) Normalized (at 680 nm) global fit results of the ns TA data. For comparison the fast component in global fit results of dyad **Ru-POM** was added. (d) Normalized integrated kinetic trace of **Ru-POM** (black), **Ru** (blue) and **Ru-ph** (dark yellow). The pump-probe data were spectrally integrated in the probe-wavelengths range between 540 and 750 nm. Inset: The enlargement of the time region up to 110 ns.

The lifetime of the short-lived species ($\tau_{ns1} \leq 10$ ns) in **Ru-POM** resembles the ns decay kinetics of the reference complexes **Ru** and **Ru-ph** (Fig. S2c). The comparison of the ns TA spectra of **Ru** and **Ru-ph** reveals that the excited-state absorption of ^{3}MLCT shifts bathochromically upon increasing the conjugated chromophore (680 nm for **Ru** vs. 620 nm for **Ru-ph**, see Fig. S2a, b). Since the short-lived species (τ_{ns1}) in **Ru-POM** shows quite similar spectral features to reference **Ru** (Fig. S2c), thus **Ru** is considered to be a more appropriate reference for studying the impact of the POM on the light-induced processes.

ns TA spectra of Ru-POM

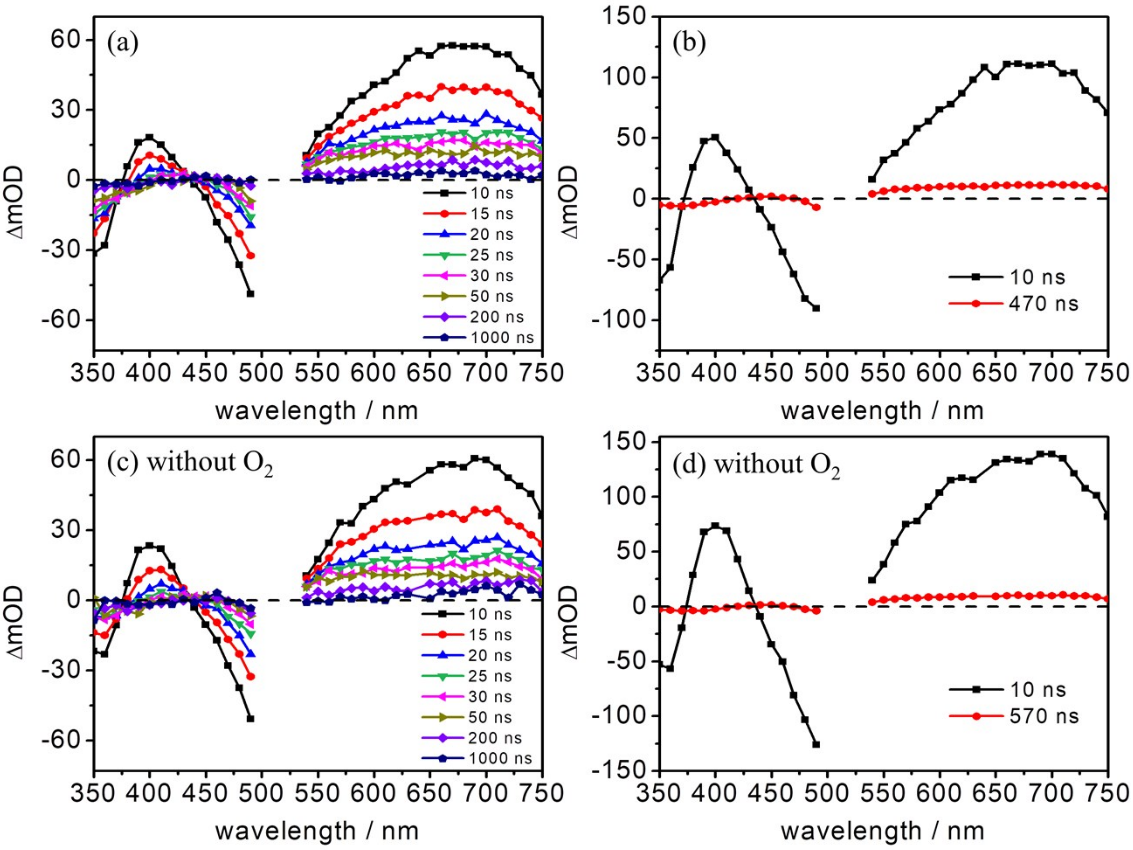

Figure S3. Nanosecond (ns) transient absorption (TA) spectra at selected times of **Ru-POM** upon excitation at 520 nm in (a) aerated and (c) deaerated DMSO. (b and d): Corresponding global fit results of the ns TA data. Note: The time constant for the first species (10 ns) obtained from the global fit is close to the time resolution of our setup. In order to obtain a more reliable value of this process fs TA spectra with a longer delay line (~9.5 ns) was used (see Figure S4a).

fs TA spectra of Ru-POM and Ru at longer time scale

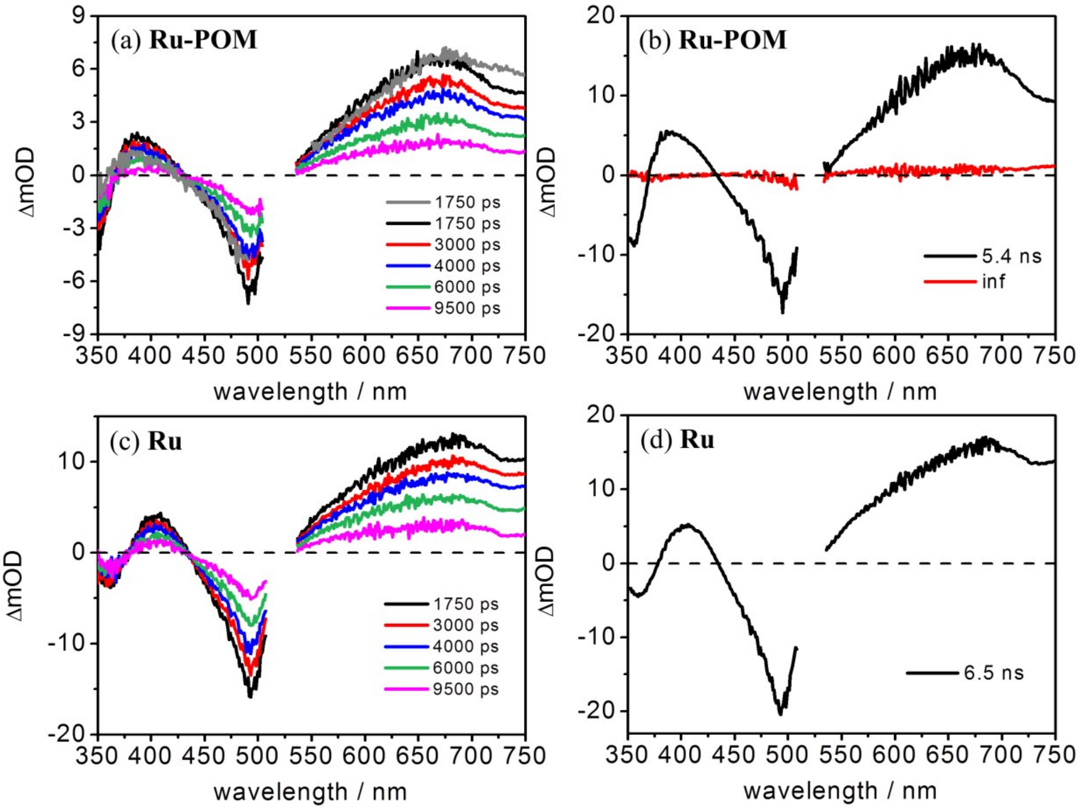

Figure S4. Femtosecond (fs) transient absorption (TA) spectra at selected times of (a) **Ru-POM** and (c) **Ru** upon excitation at 520 nm in aerated DMSO in the time range of 1750 to 9500 ps. For **Ru-POM**, to combine the fs TA data collected by a short (see text) and a long optical delay line, the spectra were scaled according to the spectrum obtained by the short delay line at 1750 ps at 680 nm (grey solid line). Decay-associated spectra of (b) **Ru-POM** and (d) **Ru**.

Integrated kinetic trace of the ns TA data of Ru-POM

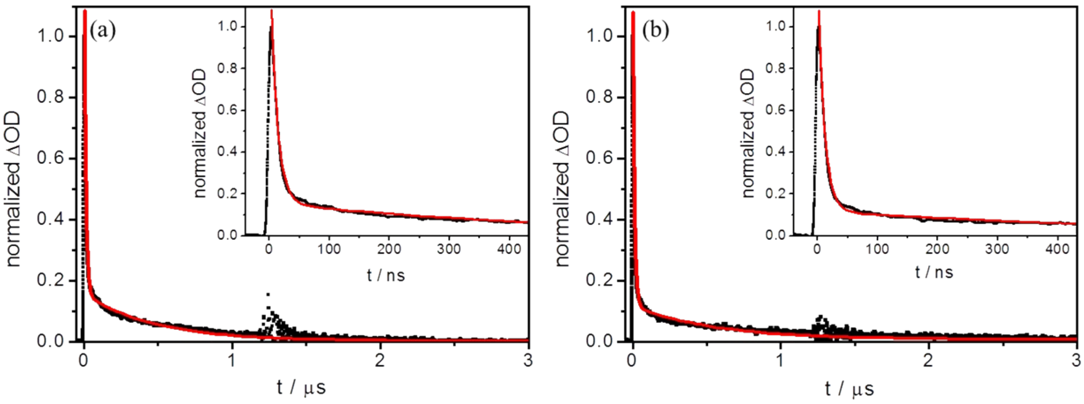

Figure S5. Normalized integrated kinetic trace at the spectral region between 540 and 750 nm where shows significant absorption signals of both species in ns TA data of **Ru-POM** collected upon excitation at 520 nm in (a) aerated and (b) deaerated DMSO. Inset: The enlargement of the time region up to 425 ns.

SEC absorption difference spectra

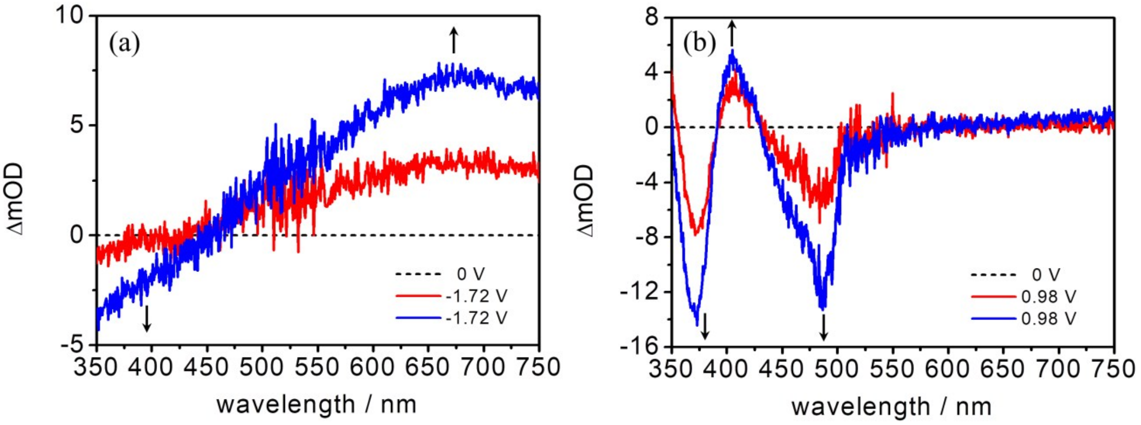

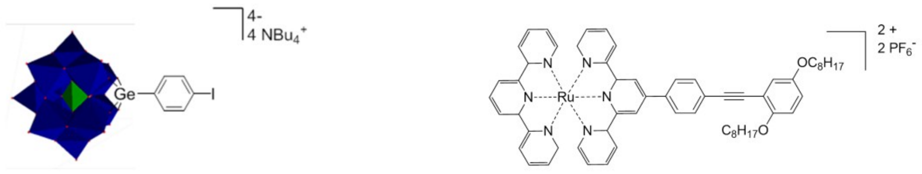
(c) **POM**

(d) **Ru**

Figure S6. Spectroelectrochemical UV/Vis absorption difference spectra of (a) POM$^{\cdot-}$ and (b) Ru^{III} collected in DMF by reduction of **POM** (c) and oxidation of **Ru** (d), respectively. Potentials are given *vs.* Fc$^{+/0}$.

Comparison of the sub-μs species ns TA data with the SEC results

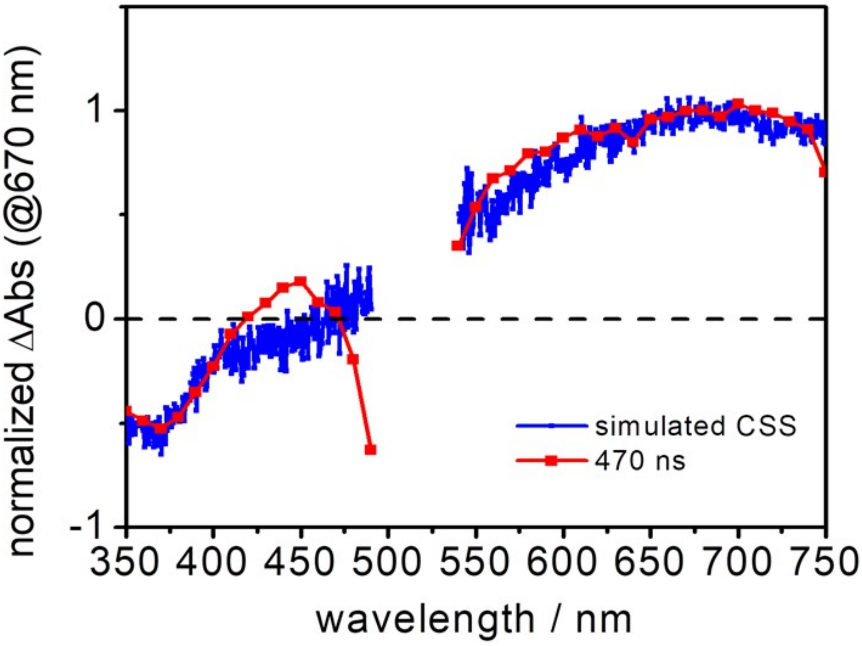

Figure S7. Comparison of the long-lived species in global fit results of the ns TA data with the simulated spectrum of Ru^{III}-$POM^{\cdot -}$ obtained from the SEC.

The simulation is done by considering that only reduced POM dominates at the wavelength region above 550 nm (Figure S6a, b). By normalizing at 670 nm and then comparing the absorbance at 370 nm where both $POM^{\cdot -}$ and Ru^{III} absorb the contribution of Ru^{III} can be calculated.

Driving forces in DMF and DMSO

According to the literature report,[6,7] the driving forces in DMF can be calculated by the following equation:

$$\Delta G^{\circ}_{CS} = e\,(E_{D^+/D} - E_{A/A^-}) - E_{00} - \frac{e^2}{4\pi\varepsilon_0\varepsilon R_{DA}}$$

R_{DA} represents the distance between donor and acceptor which was estimated by the optimized molecular structure (see Figure S8); ε_0 is the vacuum permittivity (8.85×10^{-12} F/m) and ε is the dielectric constant for DMF ($\varepsilon = 38.25$)[8]. E_{00} is the energy difference between the thermalized, lowest ^{3}MLCT excited state and ground state of the Ru(II) complex. As different ^{3}MLCT states are close in energy E_{00} is taken to be 2.07 eV as estimated from the emission spectrum of $[\mathrm{Ru(tpy)_2}]^{2+}$ at 77 K (in butyronitrile glass).[9] The electrochemical data for oxidation ($E_{D^+/D} = 0.75$ V vs. Fc$^+$/Fc) of the Ru(II) and reduction ($E_{A/A^-} = -1.46$ V vs. Fc$^+$/Fc) of the POM were taken from ref. 1.

To calculate the driving force in DMSO, the difference of solvation free enthalpies in different solvents used in electrochemistry (i.e. DMF, $\varepsilon_{ref} = 38.25$[8]) and photo-physical measurement (i.e. DMSO, $\varepsilon = 47.24$[10]) needs to be concerned (the last term):

$$\Delta G^{\circ}_{CS} = e\,(E_{D^+/D} - E_{A/A^-}) - E_{00} - \frac{e^2}{4\pi\varepsilon_0\varepsilon R_{DA}} - \frac{e^2}{8\pi\varepsilon_0}\left(\frac{1}{r_{D^+}} + \frac{1}{r_{A^-}}\right)\left(\frac{1}{\varepsilon_{ref}} - \frac{1}{\varepsilon}\right)$$

where r_{D^+} and r_{A^-} represent the radius of the oxidized donor and reduced acceptor, respectively (see Table S1).

Table S1. Estimated radii of neutral electron donors and acceptors.

unit	radius / Å[a]	radius / Å[b]
PTZ	3.7	3.6[c]
exTTF	4.6	4.2[d]
Ru complex	4.7	4.7[e]
POM	6.2	5.3[f]

[a] radii of electron donors and acceptors were obtained from the optimized molecular structures shown in Figure S7 which were measured without considering the outside hydrogens. [b] shows the comparison to the radii obtained from the crystal structures (without hydrogens). [c-f] were taken from ref. 11-14.

Optimized molecular structure of Ru-POM

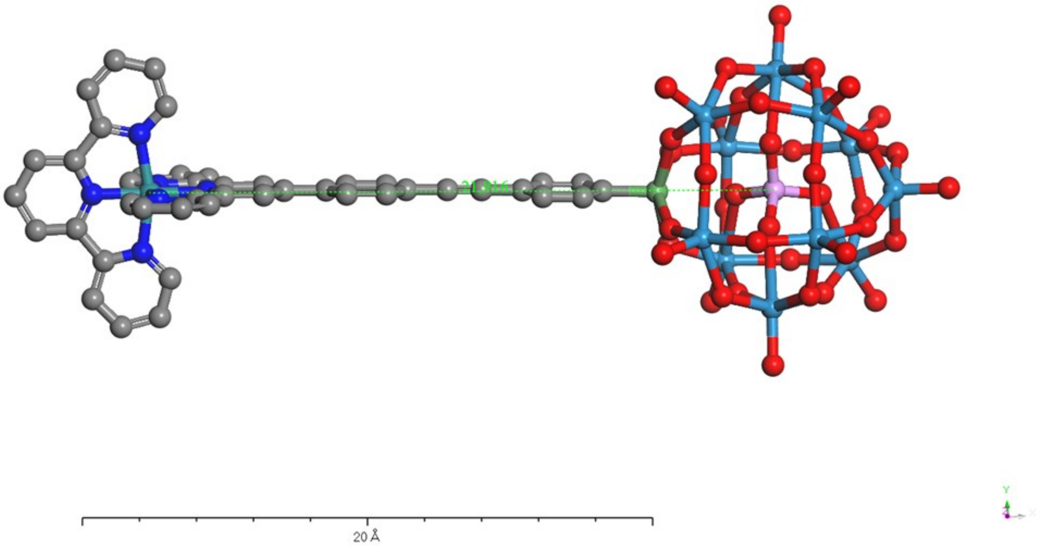

Figure S8. Optimized molecular structure of **Ru-POM**. For measuring the center-to-center distance the ruthenium atom in Ru(II) complex and the central phosphorus atom in POM were used. The center-to-center distance between the Ru(II) complex and the POM is 21.9 Å.

References

1 K. Barthelmes, M. Sittig, A. Winter, U. S. Schubert, *Eur. J. Inorg. Chem.*, 2017, **2017**, 3698–3706.

2 K. Barthelmes, J. Kübel, A. Winter, M. Wächtler, C. Friebe, B. Dietzek, U. S. Schubert, *Inorg. Chem.*, 2015, **54**, 3159–3171.

3 L. Zedler, J. Guthmuller, I. Rabelo de Moraes, S. Krieck, M. Schmitt, J. Popp, B. Dietzek, *J. Phys. Chem. C*, 2013, **117**, 6669–6677.

4 J. Kübel, R. Schroot, M. Wächtler, U. S. Schubert, B. Dietzek, M. Jäger, *J. Phys. Chem. C*, 2015, **119**, 4742–4751.

5 B. Dietzek, T. Pascher, V. Sundström, A. Yartsev, *Laser Phys. Lett.*, 2007, **4**, 38–43.

6 D. Rehm, A. Weller, *Isr. J. Chem.*, 1970, **8**, 259–271.

7 A. Weller, *Zeitschrift fuer Physikalische Chemie*, 1982, **133**, 93–98.

8 J. Wiberg, L. Guo, K. Pettersson, D. Nilsson, T. Ljungdahl, J. Mårtensson, B. Albinsson, *J. Am. Chem. Soc.*, 2007, **129**, 155–163.

9 J.-P. Sauvage, J.-P. Collin, J.-C. Chambron, S. Guillerez, C. Coudret, V. Baltani, F. Barigelletti, L. D. Cola, L. Flamigni, *Chem. Rev.*, 1994, **94**, 993–1019.

10 R. L. David, *Handbook of Chemistry and Physics*, 84th edition, 2003-2004.

11 S. S.C. Chu, D. V. D. Helm, *Acta Cryst.*, 1974, **B30**, 2489–2490.

12 Y. Ren, S. Lee, J. A. Bertke, J. S. Moore, *Acta Cryst. Sect. E*, 2015, **71**, 1475–1479.

13 E. C. Constable, C. E. Housecroft, E. A. Medlycott, M. Neuburger, F. Reinders, S. Reymann, S. *Inorg. Chem. Commun.*, 2008, **11**, 805–808.

14 E. V. Radkov, R. H. Beer, *Inorg. Chim. Acta*, 2000, **297**, 191–198.

[P3] Coexistence of Distinct Intramolecular Electron Transfer Pathways in Polyoxometalate Based Molecular Triads

Reproduced with permission from: Y. Luo, M. Wächtler, K. Barthelmes, A. Winter, U. S. Schubert and B. Dietzek, "Coexistence of Distinct Intramolecular Electron Transfer Pathways in Polyoxometalate Based Molecular Triads", *Phys. Chem. Chem. Phys.*, **2018**, *20*, 11740–11748, with permission of the PCCP Owner Societies.

Published on 26 March 2018. Downloaded by Thueringer Universitats Landesbibliothek Jena on 3/28/2019 8:57:22 AM.

PCCP

ROYAL SOCIETY OF CHEMISTRY

PAPER

View Article Online
View Journal | View Issue

Cite this: *Phys. Chem. Chem. Phys.*, 2018, **20**, 11740

Coexistence of distinct intramolecular electron transfer pathways in polyoxometalate based molecular triads†

Yusen Luo,[ab] Maria Wächtler,[b] Kevin Barthelmes,[cd] Andreas Winter,[cd] Ulrich S. Schubert[cd] and Benjamin Dietzek *[abd]

Polyoxometalate (POM)-associated charge-separated states, formed by the photoinduced oxidation of a covalently attached photosensitizer and reduction of the POM, have attracted much attention due to the remarkable catalytic properties of the reduced POMs. However, short lifetimes of the POM-associated charge-separated state, which in some cases lead to the backward electron transfer being more rapid than the formation of the charge-separated state itself, are generally observed. Recently, we reported on the first example of a relative long-lived (τ = 470 ns) charge-separated state in a Ru(II) bis(terpyridine)-POM molecular dyad. In this manuscript, further studies on extended molecular structures – two molecular triads – which contain an additional electron donor, phenothiazine (PTZ) or π-extended tetrathiafulvalene (exTTF), are discussed. We show that the excitation of the photosensitizer leads to the population of two distinct MLCT states, which differ in the distribution of excess electron density on the two distinct tpy ligands. These two MLCT states decay separately and, thus, constitute the starting points for distinct intramolecular electron-transfer pathways leading to the simultaneous population of two partially charge-separated states, *i.e.* $PTZ^{\bullet+}$-$Ru(tpy)_2^{\bullet-}$-POM and PTZ-$Ru^{III}(tpy)_2$-$POM^{\bullet-}$. These independent decay pathways are unaffected by the choice of the electron donor. Thus, the initial charge distribution within the coordination environment of the photocenter determines the nature of the subsequent (partially) charge separated state that is formed in the triads. These results might open new avenues to design molecular interfaces, in which the directionality of electron transfer can be tuned by the choice of initial excitation.

Received 13th February 2018,
Accepted 24th March 2018

DOI: 10.1039/c8cp01007b

rsc.li/pccp

Introduction

Facing an increasing renewable energy demand and climate change artificial photosynthesis has been intensively studied.[1–6] In order to convert solar radiation to chemical energy, multifunctional systems which can execute light harvesting, electron transfer and catalysis have drawn much attention in the past few decades.[1–11] In this respect, artificial models which contain electron donors, photosensitizers and electron acceptors connected by molecular bridges have been constructed. In these artificial models the structure-dynamics relationship that governs the formation and stability of the intramolecular charge-separated states were explored.[3,12–15] The charge-separated states should have sufficient lifetimes to react with external reactants (*e.g.* in light-driven water-splitting)[15–19] or to be transported into an external circuit (*e.g.* in photovoltaics).[20–24] Photoinduced dynamics in artificial models containing electron donors, such as triarylamine,[25–27] porphyrin,[28–30] ferrocene,[31–33] π-extended tetrathiafulvalene (exTTF)[34,35] and phenothiazine (PTZ),[36–40] covalently linked to electron acceptors such as porphyrins,[41,42] perylene[43–45] and fullerene,[3,40,41,46–48] have been extensively studied in the past and significant improvements in controlling the charge-separation and charge-recombination dynamics have been achieved.[49–51] Apart from the aforementioned acceptors, polyoxometalates (POMs),[52–54] which are discrete anionic metal-oxygen clusters, have emerged as electron acceptors. Studies have demonstrated that POMs can store several electrons with very small structural change and that the reduced POMs represent efficient photo-/electro-catalysts.[55–60] Although POM functionalization is still

---

[a] *Institute of Physical Chemistry and Abbe Center of Photonics, Friedrich Schiller University Jena, Helmholtzweg 4, 07743, Jena, Germany*
[b] *Department Functional Interfaces, Leibniz Institute of Photonic Technology (IPHT), Albert-Einstein-Straße 9, 07745 Jena, Germany. E-mail: benjamin.dietzek@leibniz-ipht.de*
[c] *Laboratory of Organic and Macromolecular Chemistry (IOMC), Friedrich Schiller University Jena, Humboldtstraße 10, 07743 Jena, Germany*
[d] *Center for Energy and Environmental Chemistry Jena (CEEC Jena), Friedrich Schiller University Jena, Philosophenweg 7a, Jena, 07743, Germany*

† Electronic supplementary information (ESI) available. See DOI: 10.1039/c8cp01007b

This journal is © the Owner Societies 2018

Published on 26 March 2018. Downloaded by Thueringer Universitats Landesbibliothek Jena on 3/28/2019 8:57:22 AM.

perceived as non-trivial, several organic moieties anchored onto specific POMs have been reported.[59–62]

Despite the remarkable properties of POMs, the photophysical properties of the developed photosensitizer-POM dyads are generally disappointing:[63–66] either short-lived[65,66] (*e.g.* with a lifetime of 1.4 ps) or no charge-separated states[63,64] at all were detected upon excitation of the photosensitizers. Recently, we have presented the first example of a spectroscopically detectable charge-separated state in a Ru(II) bis(terpyridine)-based molecular dyad **Ru-POM** (Keggin-type POM, $[PW_{11}O_{39}Ge]^{4-}$, Scheme 1).[67] The lifetime of the charge-separated state $Ru^{III}(tpy)_2$-$POM^{\bullet-}$ (τ = 470 ns) is comparable to the longest lifetime reported in the literature so far for a covalently connected heteroleptic Ir^{III} phenylpyridyl-POM dyad (Dawson-type POM, τ = 482 ± 13 ns).[68] Nevertheless, for the dyad **Ru-POM** the oxidative quenching (32 ns) of the ^{3}MLCT state is much slower than the radiative decay (6.5 ns) of the ^{3}MLCT state itself, which results in a low yield of $Ru^{III}(tpy)_2$-$POM^{\bullet-}$.[67]

This finding motivated us to further investigate the molecular triads built on the dyad architecture, which incorporate an additional electron donor, either a well-studied PTZ or exTTF, into the structure (Scheme 1, for details on the synthesis see ref. 69). As a result the driving forces for charge separation are increased in these molecular triads. The energy of the fully charge-separated state, *i.e.* $PTZ^{\bullet+}$-$Ru(tpy)_2$-$POM^{\bullet-}$ and $exTTF^{\bullet+}$-$Ru(tpy)_2$-$POM^{\bullet-}$ are 1.74 and 1.16 eV, respectively. These values are obtained based on the electrochemical data by adding the energy necessary to oxidize and reduce the donor and acceptor, respectively.[77] Hence, the energy is significantly decreased (by *ca.* 0.6 to 1.0 eV) compared to that of $Ru^{III}(tpy)_2$-$POM^{\bullet-}$ (2.21 eV). This is expected to cause more efficient charge separation and longer lifetimes of the fully charge-separated state. However, in this manuscript, we will show that the intramolecular distribution of the initial MLCT state in the unsymmetrical Ru(II) center results in two partially charge-separated states, *e.g.* $PTZ^{\bullet+}$-$Ru(tpy)_2{}^{\bullet-}$-POM and PTZ-$Ru^{III}(tpy)_2$-$POM^{\bullet-}$ being observed simultaneously, instead of generating the fully charge-separated state $PTZ^{\bullet+}$-$Ru(tpy)_2$-$POM^{\bullet-}$.

Experimental section

The synthesis and electrochemical properties of the reference dyads and triads have been reported elsewhere.[69,70] To study the photoinduced dynamics and excited-state properties of the triads, femtosecond (fs)/nanosecond (ns) transient absorption[70–72] and resonance Raman spectroscopy[73] were performed. Note: electrochemistry was performed in DMF because of its wider electrochemical window compared to DMSO.[67,69] All spectroscopic measurements were recorded in DMSO. Detailed experimental information is given in the ESI.†

Results and discussion

The first insight into the interactions of the individual functional units in the dyads and triads is gained from steady-state emission spectroscopy (see Fig. S1, ESI†): upon excitation of the ^{1}MLCT transition (λ_{ex} = 520 nm) the emission of the photosensitizer-acceptor, **Ru-POM**, decreases by 15% compared to the mono-ruthenium complex **Ru**.[67] This is assigned to the oxidative quenching of the emissive excited state.[67] The incorporation of PTZ as an additional electron donor, *i.e.* **PTZ-Ru-POM**, leads to further quenching of the emission from the MLCT excited state (*i.e.* the emission intensity is reduced by 40% compared to **Ru**). The compounds with the stronger electron donor exTTF, namely **exTTF-Ruph** and **exTTF-Ru-POM**, display a fully quenched emission from the excited $Ru(tpy)_2$ photocenter. This points to a reductive quenching pathway of the photoexcited Ru-center, Ru*, being operative in the triads containing the donor moieties.

Driving forces for charge-separation and charge-recombination

The feasibility of photo-driven charge separation can be estimated by calculating the driving forces for charge separation (CS) and charge recombination (CR) through the redox potentials of $D^{\bullet+}/D$ (D referring to the electron donor, *i.e.* PTZ or exTTF),

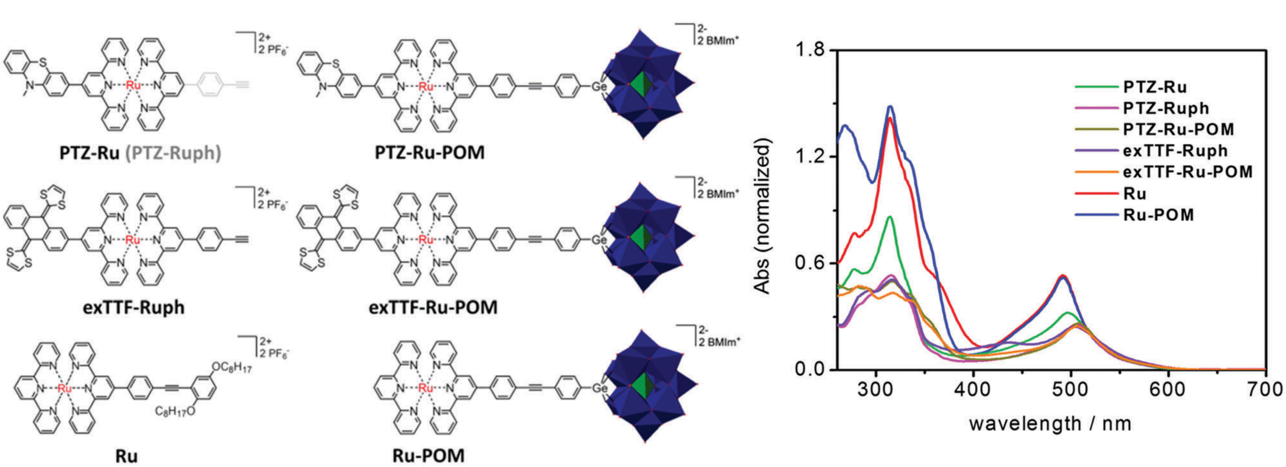

Scheme 1 Left: Schematic representation of the molecular structures of the dyads and triads studied in this work. POM is $[PW_{11}O_{39}Ge]^{4-}$ and $BMIm^+$ stands for the 1-butyl-3-methyl-1*H*-imidazol-3-ium cation. Colour code: WO_6 octahedron, blue; PO_4 tetrahedron, green. Right: UV/Vis absorption spectra collected in isoabsorbing (optical density is 0.2 at 520 nm) DMSO solutions. The extinction coefficients for the compounds were reported in ref. 69.

Published on 26 March 2018. Downloaded by Thueringer Universitats Landesbibliothek Jena on 3/28/2019 8:57:22 AM.

Table 1 Center-to-center distances R, electrochemical data and reaction free-energy changes ($-\Delta G^\circ$) for charge separation (CS) and charge recombination (CR) in dimethylformamide (DMF)

	Center-to-center/Å		$E^{\circ\,d}$/V (*vs.* Fc^+/Fc)				$-\Delta G^{\circ\,e}$/eV			
	$R_{(D\text{-}Ru)}$[a]	$R_{(D\text{-}POM)}$[a]	D^+/D	Ru^{3+}/Ru^{2+}	POM/POM^-	tpy/tpy^-	CS1	CR1	CS2	CR2
PTZ-Ru	9.5	—	0.37	0.78	—	−1.65	0.09	1.98	—	—
PTZ-Ru-POM	9.5	31.1	0.29	0.75	−1.45	−1.69	0.13	1.94	0.21	1.73
exTTF-Ruph	8.3[b] (13.2)[c]	—	−0.16	0.84	—	−1.55	0.72[b] (0.70)[c]	1.35[b] (1.37)[c]	—	—
exTTF-Ru-POM	8.3[b] (13.2)[c]	29.5[b] (35.0)[c]	−0.30	0.84	−1.46	−1.63	0.78[b] (0.76)[c]	1.29[b] (1.31)[c]	0.14[b] (0.16)[c]	1.15[b] (1.15)[c]

[a] Center-to-center distances (Fig. S2, ESI) between the electron donor (D = PTZ or exTTF) and the Ru^{II} complex ($R_{D\text{-}Ru}$) or POM ($R_{D\text{-}POM}$). [b] Shortest distance between exTTF and the Ru^{II} complex since the exTTF unit has a butterfly-like shape and consists of four sulphur atoms (Fig. S2b, ESI). [c] Longest distance between exTTF and the Ru^{II} complex since the exTTF unit has a butterfly-like shape and consists of four sulphur atoms (Fig. S2b, ESI). [d] Except for **PTZ-Ru** (CV curve in Fig. S3, ESI), redox potentials were taken from ref. 69. [e] $\Delta G^\circ_{CR} = e\left(E_{A/A^-} - E_{D^+/D}\right) + e^2/4\pi R\varepsilon_0\varepsilon_s$ is the driving force for charge recombination in DMF.[37] ε_0 is the vacuum permittivity (8.85×10^{-12} F m^{-1}) and ε_s is the dielectric constant for DMF ($\varepsilon_s = 38.25$).[42] For the first charge separation the radical pairs are $tpy^{\bullet-}/PTZ^{\bullet+}$ or $tpy^{\bullet-}/exTTF^{\bullet+}$. For the second charge separation the radical pairs are $POM^{\bullet-}/PTZ^{\bullet+}$ or $POM^{\bullet-}/exTTF^{\bullet+}$. $\Delta G^\circ_{CS1} = -\Delta G^\circ_{CR1} - E_{00}$ is the driving force for the first charge separation. E_{00} is the energy difference between the thermalized, lowest ^{3}MLCT excited state and the ground state of the Ru complex. As the different ^{3}MLCT states are relatively close in energy E_{00} is taken to be 2.07 eV as estimated from the emission spectrum of $[Ru(tpy)_2]^{2+}$ at 77 K (in butyronitrile glass).[74] The driving force for the second charge separation is calculated by $\Delta G^\circ_{CS2} = \Delta G^\circ_{CR1} - \Delta G^\circ_{CR2}$ (this is schematically illustrated in Scheme S1, ESI). Note that the entropy term in Rehm–Weller equation is often neglected for calculating the free-energy changes associated with charge separation. To get the free-energy changes for charge separation and charge recombination in DMSO a correction term should be included (see Tables S1 and S2, ESI for details).

$POM/POM^{\bullet-}$ and $tpy/tpy^{\bullet-}$ by using the Rehm–Weller equation.[75–77] The resultant free-energy changes related to charge separation ($-\Delta G^\circ_{CS}$) and charge recombination ($-\Delta G^\circ_{CR}$) are listed in Table 1.

The extensively studied dyad **PTZ-Ru** (in dichloromethane and acetonitrile)[39,40] was chosen as the reference to triad **PTZ-Ru-POM**. For comparison, the electrochemical data of **PTZ-Ru** were also collected in DMF (Table 1). When comparing the driving forces ($-\Delta G^\circ_{CS1}$) for electron transfer from the PTZ unit to the photoexcited Ru-center in **PTZ-Ru** and **PTZ-Ru-POM** very similar values are found, *i.e.* 0.09 eV for **PTZ-Ru** *vs.* 0.13 eV for **PTZ-Ru-POM**. The small difference in the driving forces ($-\Delta G^\circ_{CS1}$) results from the slightly cathodically-shifted oxidation and reduction potential of the PTZ and tpy unit in **PTZ-Ru-POM**, respectively.[69] This is due to the anionic effect of the POM.[69] The similar values for $-\Delta G^\circ_{CS1}$ hint to the fact that similar rate constants for the photoinduced charge-transfer processes might be expected in both the PTZ-containing dyad and triad. The situation also holds true when comparing **exTTF-Ruph** to **exTTF-Ru-POM**: both systems display very similar driving forces for electron transfer from exTTF to the photoexcited Ru-center, *i.e.* 0.72 *vs.* 0.78 eV. Due to the stronger electron-donating property of exTTF (oxidation potential of −0.16 V in the POM-free dyad **exTTF-Ruph**) compared to PTZ (oxidation potential of 0.37 V in the POM-free dyad **PTZ-Ru**) the driving force for the first electron transfer in **exTTF-Ru-POM** is about 0.6 V more negative than that in **PTZ-Ru-POM**. This implies that a faster kinetics for charge separation might be expected upon changing the donor moiety from PTZ to exTTF. Furthermore, for both **PTZ-Ru-POM** and **exTTF-Ru-POM**, electron transfer from the reductively quenched photosensitizer to the POM is energetically feasible with $-\Delta G^\circ_{CS2}$ of 0.21 and 0.14 eV, respectively. The estimation of the ΔG° values is based on the oxidation and reduction potentials, which were experimentally determined by electrochemical measurements in DMF. In order to account for the fact that DMSO was used in the spectroscopic experiments, the values listed and discussed above will have to be corrected by about 0.01 to 0.02 eV according to literature reported correction procedures[75,76] (also see Tables S1 and S2, ESI† for details).

Time-resolved spectroscopic characterization of the dyad PTZ-Ru and triad PTZ-Ru-POM

To shed light on the photoinduced excited-state relaxation pathways, fs and ns transient absorption (TA) spectroscopy upon optical excitation of the ^{1}MLCT transition of the Ru-photosensitizer (λ_{ex} = 520 nm) was employed. The fs TA spectra of the donor-photosensitizer dyad, *i.e.* **PTZ-Ru**, and the donor-photosensitizer-acceptor triad, *i.e.* **PTZ-Ru-POM**, measured in DMSO, are shown in Fig. 1. In the figure the data collected by a short (up to 1.8 ns) and a long optical delay line (up to 9.5 ns) are merged (see Fig. S4, ESI† for normalization procedure). The differential absorption spectra (Fig. 1a and c) are dominated by ground state bleach (GSB) centred at around 500 nm. GSB is accompanied by excited-state absorption (ESA) from 350 to 425 nm and from 550 to 750 nm. The spectra recorded at short delay times (*e.g.* at 0.3 ps) reveal the characteristic absorption of a $[Ru(tpy)_2]^{2+}$-based ^{3}MLCT state, including a ligand-centred band at *ca.* 380 nm[78,79] and a broad band at *ca.* 625 nm for **PTZ-Ru**. In **PTZ-Ru-POM** both bands undergo a red shift (with a ligand-centred band at *ca.* 400 nm and a broad band at *ca.* 675 nm) which is owing to the ^{3}MLCT state being more delocalized over the extended tpy ligand.[70,80] For **PTZ-Ru**, at long delay times (*e.g.* at 1750 ps) the ESA bands appear blue-shifted to 360 and 596 nm, respectively. This indicates the formation of the one-electron oxidized PTZ ($PTZ^{\bullet+}$) according to spectro-electrochemical results revealing three distinct absorption bands in the absorption spectrum of $PTZ^{\bullet+}$ (in dichloromethane and acetonitrile) at 365, 473 and 580 nm.[39,40]

For quantitative analysis of the fs TA data of **PTZ-Ru** recorded in DMSO, a three exponential fit is required (Fig. 1b). The assignment of the kinetic components is done by referring to previous studies on **PTZ-Ru** in two different solvents – dichloromethane and acetonitrile – which have demonstrated that two different ^{3}MLCT states are populated upon excitation at

This journal is © the Owner Societies 2018

Published on 26 March 2018. Downloaded by Thueringer Universitats Landesbibliothek Jena on 3/28/2019 8:57:22 AM.

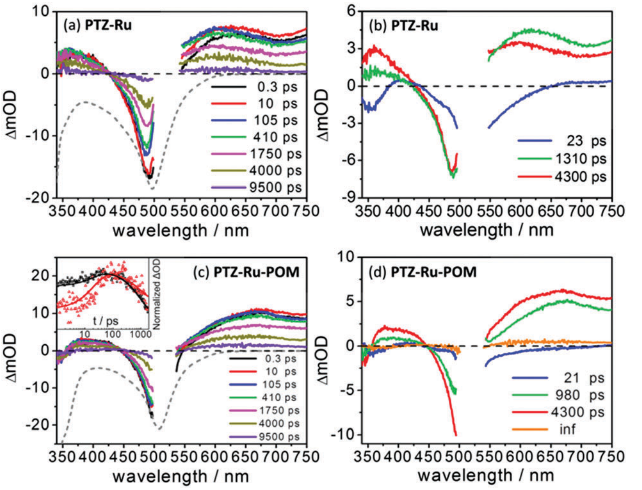

Fig. 1 fs transient absorption spectra (a and c) at selected delay times and decay-associated spectra (b and d) resulting from the global fit upon excitation at 520 nm in aerated DMSO for **PTZ-Ru** (a and b) and **PTZ-Ru-POM** (c and d). The last two spectra in (a) and (c) were taken from the fs TA data collected by means of a longer optical delay line (Fig. S4a and c, ESI†) and were scaled according to the absorption spectrum at 1750 ps at 590 nm and 680 nm for **PTZ-Ru** and **PTZ-Ru-POM**, respectively. The grey dashed line represents the shape of the corresponding inverted ground state absorption spectrum which is arbitrarily scaled to fit the scale of the respective figure. Inset in (c): Normalized integrated kinetics at the spectral region of 360–370 nm (red) and 580–590 nm (black). The kinetics were normalized to the ΔOD-value recorded at a delay time of 105 ps.

520 nm:[39] the ^{3}MLCT$_{\text{PTZ-tpy}}$ state, which is characterized by an initial excess charge-density shift towards the PTZ unit populates PTZ$^{\bullet+}$-Ru(tpy)$_2$$^{\bullet-}$. In contrast, the ^{3}MLCT$_{\text{tpy}}$ state, which is characterized by excess charge-density localized on the terminal tpy ligand, decays radiatively to the ground state.[39] Following this photophysical model,[39] the first component (τ_1 = 23 ps, Fig. 1b) is assigned to charge separation, *i.e.* population of PTZ$^{\bullet+}$-Ru(tpy)$_2$$^{\bullet-}$. This process is characterized by an increase of the positive signal amplitude at 360 and 590 nm, corresponding to the absorption of PTZ$^{\bullet+}$.[39] The third component (τ_3 = 4300 ps) represents the charge recombination of PTZ$^{\bullet+}$-Ru(tpy)$_2$$^{\bullet-}$ showing a decay of the absorption bands associated with PTZ$^{\bullet+}$. The charge-recombination process has also been studied in DMSO by ns TA spectroscopy (Fig. S5a, ESI†) revealing a mono-exponential decay of PTZ$^{\bullet+}$-Ru(tpy)$_2$$^{\bullet-}$ (Fig. S5c, ESI†). The spectral shape of the second component (τ_2 = 1310 ps) resembles the typical features of ^{3}MLCT states in Ru(tpy)$_2$-based complexes[70,78,80] and, thus, is attributed to the decay of the ^{3}MLCT$_{\text{tpy}}$ state to the ground state. The relaxation processes after photoexcitation are summarized in Scheme S2 (ESI†). Additionally, it is found that extension of the terminal tpy ligand of **PTZ-Ru**, *i.e.* yielding **PTZ-Ruph**, only slightly affects the features of the ns TA spectra (a slight red shift compared to **PTZ-Ru**) and basically does not affect the kinetics of the charge-recombination process (Fig. S5c, ESI†). Thus, it is reasonable to use **PTZ-Ru** as the reference to study the triad **PTZ-Ru-POM** (*vide infra*).

For **PTZ-Ru-POM**, between 0.3 and 105 ps, slight signal increases at around 366 and 590 nm are observed, which are attributed to the formation of PTZ$^{\bullet+}$. Both PTZ$^{\bullet+}$-associated bands do not appear as distinctly as in the fs TA spectra of **PTZ-Ru**, likely due to the significant spectral overlap with the ^{3}MLCT-absorption of **PTZ-Ru-POM**. However, the spectral changes associated with the formation of PTZ$^{\bullet+}$ can be observed in the integrated kinetics recorded at 360 to 370 nm and at 580 to 590 nm where the PTZ$^{\bullet+}$ dominates (displayed in the inset in Fig. 1c): this clearly shows the build-up of PTZ$^{\bullet+}$ within the first 100 ps highlighting the population of a charge-separated state. Then, after 100 ps, a decay of the TA signal is observed. Moreover, the DAS of the first kinetic component (τ_1 = 21 ps) resembles the features of the first component (τ_1 = 23 ps) observed for **PTZ-Ru** (Fig. 1b). Hence, it reflects the formation of PTZ$^{\bullet+}$-Ru(tpy)$_2$$^{\bullet-}$-POM. The τ_3 = 4300 ps reveals an absorption shoulder at 590 nm which is indicative of the decay of the charge-separated state PTZ$^{\bullet+}$-Ru(tpy)$_2$$^{\bullet-}$-POM (Fig. 1d). Thus, both **PTZ-Ru-POM** and **PTZ-Ru** show very similar rate constants for charge-separation and charge-recombination (see Fig. 1b and d). The second component (τ_2 = 980 ps) reveals a spectral shape similar to that of the ^{3}MLCT state observed for **Ru-POM**, *i.e.* ^{3}MLCT$_{\text{tpy-POM}}$, with an absorption maximum at about 675 nm (see Fig. S6c, ESI†).[67] Thus, τ_2 is assigned to the decay of the ^{3}MLCT$_{\text{tpy-POM}}$ state. Notably, the decay kinetics of the ^{3}MLCT$_{\text{tpy-POM}}$ state in **PTZ-Ru-POM** (τ_2 = 980 ps) is faster than that in **Ru-POM** (τ_2 = 5400 ps, Fig. S6, ESI†). It should be noted that the decay of the TA signal as observed in the fs TA data is not complete. Thus, ns TA spectroscopy was performed to study the small long-lived signal in the fs TA signal (see Fig. 2).

A global fit of the corresponding ns TA data (Fig. 2a) yields two species (Fig. 2b and Fig. S7, ESI†): the short-lived species (τ_{ns1}) apparent in the global fit results of the ns TA data has a much stronger contribution to the overall fit (90%) and shows the absorption of PTZ$^{\bullet+}$ at 590 nm. Hence, it is assigned to the charge recombination of PTZ$^{\bullet+}$-Ru(tpy)$_2$$^{\bullet-}$-POM with a lifetime of 4300 ps as determined by fs TA spectroscopy (Fig. 1d). The long-lived species (τ_{ns2} = 574) has a relatively small contribution to the overall fit (10%, see Fig. S7b and S8a, ESI†). It shows a broad positive absorption band centered at *ca.* 670 nm along with a negative band at 370 nm which might indicate the formation of reduced POM (see Fig. S10a, ESI†) and oxidized Ru$^{\text{II}}$ (Fig. S10b, ESI†), respectively. Furthermore, it is found that the presence of oxygen in solution only slightly affects its lifetime (τ_{ns2} = 574 ns, aerated solution *vs.* 630 ns, deaerated solution, Fig. S7 and S8, ESI†) which indicates the generation of a charge-separated state.[67,81] Notably, in the spectrum associated with τ_{ns2} there are no peaks discernible at 365, 470 or 590 nm which would be indicative of PTZ$^{\bullet+}$ (Fig. S9, ESI†).[39,40] Finally, the spectral features associated with τ_{ns2} in **PTZ-Ru-POM** are quite similar to the long-lived component in **Ru-POM** (Fig. 2b; also see Fig. S10c, ESI†). This implies that instead of the fully charge-separated state, *i.e.* PTZ$^{\bullet+}$-Ru(tpy)$_2$-POM$^{\bullet-}$, τ_{ns2} refers to the decay of a partially charge-separated state, *i.e.* PTZ-Ru$^{\text{III}}$(tpy)$_2$-POM$^{\bullet-}$. Combined with the fs TA data, which reveal the formation of PTZ$^{\bullet+}$-Ru(tpy)$_2$$^{\bullet-}$-POM ($\tau_1$ = 23 ps) and the separate decay of a ^{3}MLCT$_{\text{tpy-POM}}$ state, we conclude that there are two distinct decay pathways available for PTZ-Ru*-POM: the

Published on 26 March 2018. Downloaded by Thueringer Universitats Landesbibliothek Jena on 3/28/2019 8:57:22 AM.

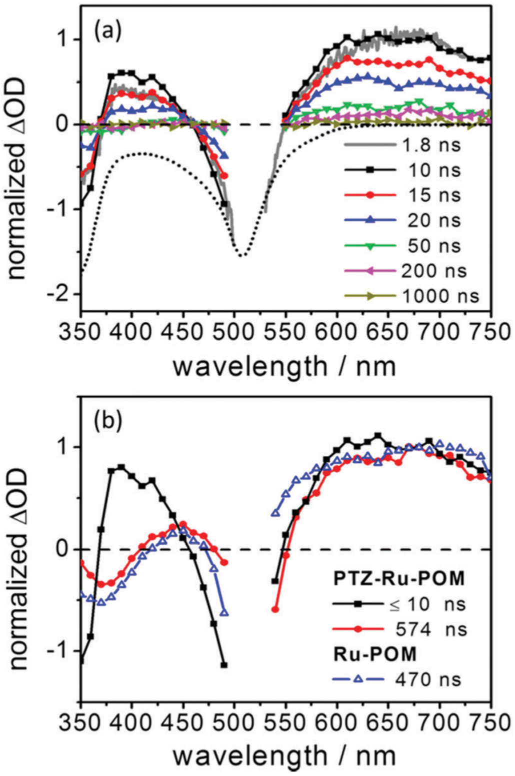

Fig. 2 (a) ns transient absorption spectra at selected times of **PTZ-Ru-POM** upon excitation at 520 nm in aerated DMSO. For comparison the fs TA spectrum at 1.8 ns was added (grey solid line). The fs TA spectrum (1.8 ns) and ns TA spectrum (at 10 ns) were normalized at 680 nm. The black dotted line represents the inverted ground state absorption spectrum of **PTZ-Ru-POM**. (b) Global fit results of the ns TA data. The spectrum of the long-lived species (τ_{ns2}) in **Ru-POM** was added for comparison. All spectra were normalized at 680 nm.

first decay pathway proceeds *via* PTZ$^{\bullet+}$-Ru(tpy)$_2^{\bullet-}$-POM while the second pathway yields PTZ-Ru^{III}(tpy)$_2$-POM$^{\bullet-}$.

The presence of two distinct (partially) charge-separated states in **PTZ-Ru-POM** is reminiscent of a branching of ^{3}MLCT states previously observed in PTZ-Ru-C$_{60}$ triads:[40] the initially populated ^{3}MLCT states, *i.e.* (i) partially distributed on the PTZ-tpy ligand (^{3}MLCT$_{\text{PTZ-tpy}}$) and (ii) partially delocalized on the tpy-POM ligand (^{3}MLCT$_{\text{tpy-POM}}$), decay separately. The ^{3}MLCT$_{\text{PTZ-tpy}}$ state generates PTZ$^{\bullet+}$-Ru(tpy)$_2^{\bullet-}$-POM while the ^{3}MLCT$_{\text{tpy-POM}}$ state decays *via* PTZ-Ru^{III}(tpy)$_2$-POM$^{\bullet-}$. In other words, the ^{3}MLCT$_{\text{PTZ-tpy}}$ and ^{3}MLCT$_{\text{tpy-POM}}$ state decay separately *via* reductive and oxidative quenching, respectively. The electron-transfer rate constant k_{CS}, *i.e.* from the ^{3}MLCT$_{\text{tpy-POM}}$ state to PTZ-Ru^{III}(tpy)$_2$-POM$^{\bullet-}$, can thus be estimated by $k_{\text{CS}} = 1/\tau - k_0$, with $k_0 = 1/\tau_0$ (τ_0 = 6.5 ns in the reference **Ru**, taken from ref. 67; τ = 980 ps, see Fig. 1d). This yields a POM reduction rate of $k_{\text{CS}} = 8.7 \times 10^7\ \text{s}^{-1}$ ($\tau_{\text{CS}} = k_{\text{CS}}^{-1}$ = 1.2 ns).

The relaxation diagram of **PTZ-Ru-POM** (Scheme 2) upon excitation is proposed by referring to the photophysical model developed for **PTZ-Ru.**[39] The similarity of the initially populated MLCT states in **PTZ-Ru-POM** and **PTZ-Ru**[39] is demonstrated by the excitation-wavelength dependent resonance Raman (rR) spectra which can provide insights into the distribution of ^{1}MLCT states over individual ligands:[82] increasing the excitation wavelength from 458 to 515 nm leads to increased rR signals of PTZ-associated bands both in **PTZ-Ru-POM** (see Fig. S11, ESI† for details) and **PTZ-Ru.**[39] This indicates an increased excess-electron density shift towards the PTZ-tpy ligand during ^{1}MLCT transition. Thus, for **PTZ-Ru-POM**, the ^{1}MLCT$_{\text{PTZ-tpy}}$ state is energetically lower than the ^{1}MLCT$_{\text{tpy-POM}}$ state (Scheme 2). However, the energetic ordering of the MLCT states is considered to be inverted in the triplet manifold as already deduced for **PTZ-Ru.**[39] Otherwise the slow process, *i.e.* oxidative quenching of ^{3}MLCT$_{\text{tpy-POM}}$ state (1.2 ns), could kinetically not compete with the interligand electron transfer (which is typically observed on a characteristic time scale of several ps for Ru–polypyridyl complexes;[78,83] the actual value depends on the relative energies of ligands and solvents[39]) which would result in the lowest thermalized ^{3}MLCT state. As a result, no PTZ-Ru^{III}(tpy)$_2$-POM$^{\bullet-}$ would be detected.

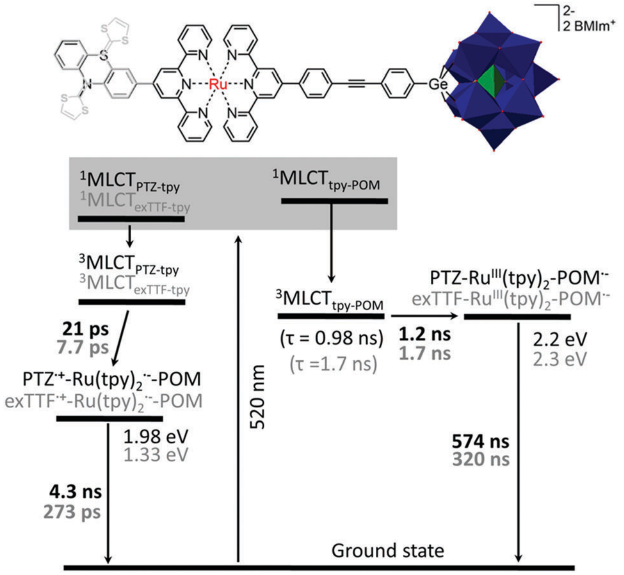

Scheme 2 Energy-level diagrams of **PTZ-Ru-POM** and **exTTF-Ru-POM** (in grey colour) were developed by using electrochemical, resonance Raman (see Fig. S11, ESI†) and fs/ns TA data. For a recompilation of the photophysics of the dyad **PTZ-Ru**, which was published in ref. 39, the reader is referred to the ESI,† Scheme S2.

The results present here show that the fully charge-separated state PTZ$^{\bullet+}$-Ru(tpy)$_2$-POM$^{\bullet-}$ is not formed in **PTZ-Ru-POM** although this process, *i.e.* electron transfer from PTZ$^{\bullet+}$-Ru(tpy)$_2^{\bullet-}$-POM to PTZ$^{\bullet+}$-Ru(tpy)$_2$-POM$^{\bullet-}$, is energetically downhill with a free Gibbs energy change of $-\Delta G_{\text{CS2}}$ = 0.21 eV (Table 1). Instead two partially charge-separated states PTZ$^{\bullet+}$-Ru(tpy)$_2^{\bullet-}$-POM and PTZ-Ru^{III}(tpy)$_2$-POM$^{\bullet-}$ are populated, which are populated independently by the decay of two distinct ^{3}MLCT states. One speculation is that for the second electron-transfer step, *i.e.* from PTZ$^{\bullet+}$-Ru(tpy)$_2^{\bullet-}$-POM to PTZ$^{\bullet+}$-Ru(tpy)$_2$-POM$^{\bullet-}$, the activation barrier is still too high for the electron to overcome.

Excited state processes in the dyad exTTF-Ruph and triad exTTF-Ru-POM

To further increase the driving force for electron transfer in the molecular triad with the Ru(tpy)$_2$ photosensitizer and the

This journal is © the Owner Societies 2018

Published on 26 March 2018. Downloaded by Thueringer Universitats Landesbibliothek Jena on 3/28/2019 8:57:22 AM.

POM-based acceptor, the donor unit was changed from PTZ to exTTF. The oxidation potential of exTTF is about 560 mV more negative than that of PTZ and, hence, more rapid formation of charge-separated states in the resulting molecular dyad **exTTF-Ruph** and triad **exTTF-Ru-POM** may be expected. The resultant fs TA results for the dyad and triad containing exTTF as donor are summarized in Fig. 3. The fs TA spectrum of **exTTF-Ruph** recorded at 0.3 ps after photoexcitation shows GSB in the wavelength region of the ^{1}MLCT absorption band. In addition GSB is visible at 427 nm which is associated with the absorption of the exTTF unit. The absorption features of GSB match the inverted ground-state absorption of the triad quite well (Fig. 3a). The GSB is accompanied by a broad absorption band above 550 nm (at *ca.* 640 nm) and a small band at 370 nm which are quite similar to the ESA of the ^{3}MLCT state in **Ruph** (details see Fig. S12, for the molecular structure see Fig. S12d, ESI†). Hence, upon photoexcitation of **exTTF-Ruph** a mixed MLCT and exTTF-involved excited state is populated. 10 ps after photoexcitation the ESA increases between 550 and 620 nm peaking at *ca.* 600 nm, while the ESA band decreases between 620 and 750 nm. Additionally, the band at 427 nm becomes more negative. Subsequently, the overall spectral shape remains constant and the TA signal decays back to zero within the experimentally accessible range of delay times. In order to quantitatively analyse the experimental data, two kinetic components, τ_1 = 6.2 ps and τ_2 = 230 ps are necessary. The DAS(τ_1) (Fig. 3b) reflects three decaying ESA bands at 365, 427 and 690 nm as well as an increase of the signal at 590 nm. To understand the observed spectra, the absorption features of one-electron oxidized exTTF (*i.e.* exTTF$^{\bullet+}$) are considered as reported by Guldi and coworkers, who performed the pulse radiolysis of unsubstituted exTTF.[84] The authors report the appearance of two absorption bleaches, *i.e.* reduced absorption of the oxidized exTTF compared to the neutral molecule, at *ca.* 360 and 430 nm accompanied by a broad absorption band peaking at *ca.* 610 and 660 nm.[84] From the similarity of DAS(τ_1) with the results presented by Guldi and coworkers[84] it is concluded that the process associated with τ_1 represents the formation of the charge-separated state exTTF$^{\bullet+}$-Ru(tpy)$_2^{\bullet-}$. The second component (τ_2 = 230 ps) is consequently attributed to the recombination of exTTF$^{\bullet+}$-Ru(tpy)$_2^{\bullet-}$. This recombination is complete within the experimental delay time window of 1.8 ns.

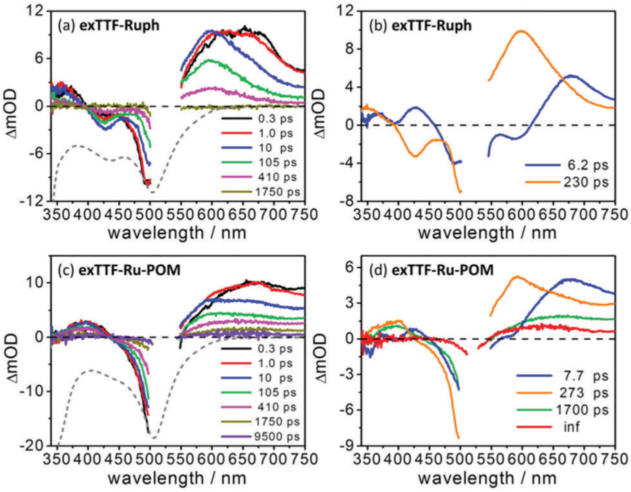

Fig. 3 fs transient absorption spectra (a and c) at selected delay times and decay-associated spectra (b and d) resulting from the global fit upon excitation at 520 nm in aerated DMSO for **exTTF-Ruph** (a and b) and **exTTF-Ru-POM** (c and d). The grey dashed line represents the inverted ground state absorption spectrum of **exTTF-Ruph** (a) and **exTTF-Ru-POM** (c). For **exTTF-Ru-POM** the fs TA data obtained by a longer delay line were added (see Fig. S13, ESI†).

Upon expanding the dyad into the respective triad **exTTF-Ru-POM**, the DAS associated with τ_1 = 7.7 ps and τ_2 = 273 ps resemble the central features of the respective DAS observed for the dyad **exTTF-Ruph**. The less prominent exTTF-related bleach between 400 and 450 nm in the τ_2-associated spectrum of **exTTF-Ru-POM** (which is also reflected in the TA spectra in Fig. 3c) might be rationalized by the relative strong ESA of the reduced extended-tpy ligand in **exTTF-Ru-POM** in the same spectral region. Furthermore, also the ground state absorption of **exTTF-Ru-POM** reveals minor exTTF features as compared to the reference dyad **exTTF-Ruph** (see Fig. 3c). The spectral similarity (as well as the similarity of the characteristic decay times) indicates that the same molecular processes are observed in **exTTF-Ru-POM** and in **exTTF-Ruph** (see Scheme 2): with a characteristic time of 7.7 ps the partially charge-separated state exTTF$^{\bullet+}$-Ru(tpy)$_2^{\bullet-}$-POM is formed, which decays on a sub-ns time scale, *i.e.* with τ_2 = 273 ps. However, different to **exTTF-Ruph** an additional slow process (τ_3 = 1700 ps) and an infinite component (on a 10 ns timescale) become apparent. τ_3 is associated with a positive differential absorption at 390 nm reflecting the reduced tpy ligand, and a broad absorption at a wavelength longer than 550 nm, indicative of a ^{3}MLCT absorption of Ru(II)–polypyridyl complexes. Hence, the process is attributed to the decay of the ^{3}MLCT$_{\text{tpy-POM}}$ state.

The nature of the long-lived species observed in the fs TA data has been studied by ns TA spectroscopy which yields two processes contributing to the ns decay of the signal (Fig. 4b and Fig. S14, S15, ESI†). The relative short-lived species is assigned to the decay of a ^{3}MLCT state delocalized on the extended tpy ligand (^{3}MLCT$_{\text{tpy-POM}}$). The long-lived species (τ_{ns2} = 320 ns) is attributed to the decay of the partially charge-separated state exTTF-Ru$^{\text{III}}$(tpy)$_2$-POM$^{\bullet-}$, which is corroborated by experiments performed in the absence of oxygen showing a weak dependence on oxygen (τ_{ns2} = 320 ns (aerated solution) *vs.* 450 ns (deaerated solution), Fig. S14 and S15, ESI†).[67,81] The spectrum associated with τ_{ns2} in **exTTF-Ru-POM** lines up well with the spectral features of Ru$^{\text{III}}$(tpy)$_2$-POM$^{\bullet-}$ in **Ru-POM** in the wavelength region above 450 nm (Fig. 4b). The spectral deviations below 450 nm are attributed to stronger contributions of Ru$^{\text{III}}$(tpy)$_2$, yielding ΔOD $>$ 0 values, than from the POM$^{\bullet-}$, yielding ΔOD $<$ 0 values (Fig. S10a, ESI†). Thus, the spectral features indicate that τ_{ns2} reflects the decay of the partially charge-separated state exTTF-Ru$^{\text{III}}$(tpy)$_2$-POM$^{\bullet-}$. Due to the emission of **exTTF-Ru-POM** being totally quenched (Fig. S1, ESI†), the electron transfer in **exTTF-Ru-POM** from the ^{3}MLCT$_{\text{tpy-POM}}$ to exTTF-Ru$^{\text{III}}$(tpy)$_2$-POM$^{\bullet-}$ is characterized by the time constant τ_3 = 1700 ps (Fig. 3d). Thus, this process occurs on a similar time scale as in **PTZ-Ru-POM** (τ = 1200 ps). It should be

Published on 26 March 2018. Downloaded by Thueringer Universitats Landesbibliothek Jena on 3/28/2019 8:57:22 AM.

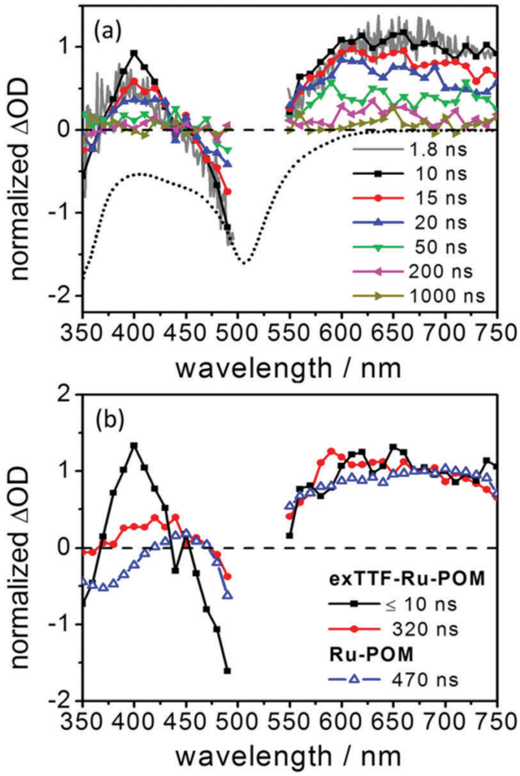

Fig. 4 (a) ns transient absorption spectra at selected times of **exTTF-Ru-POM** upon excitation at 520 nm in aerated DMSO. For comparison the fs TA spectrum at 1.8 ns was added (grey solid line). The fs TA spectrum (1.8 ns) and ns TA spectrum (at 10 ns) were normalized at 670 nm. The black dotted line represents the inverted ground state absorption spectrum of **exTTF-Ru-POM**. (b) Global fit results of the ns TA data. The spectrum of the long-lived species (τ_{ns2}) in **Ru-POM** was added for comparison. All spectra were normalized at 670 nm.

noted that the oxidative quenching of ^{3}MLCT$_{\text{tpy-POM}}$ state is a little slower in **exTTF-Ru-POM** (τ = 1700 ps) than that in **PTZ-Ru-POM** (τ = 1200 ps). This can be rationalized by the different driving forces obtained for the electron transfer from oxidized Ru(tpy)$_2$ to POM and that a more favorable driving force in **PTZ-Ru-POM** ($\Delta G^\circ_{\text{CS}} = 0.1$ eV in DMF) than **exTTF-Ru-POM** ($\Delta G^\circ_{\text{CS}} = 0.2$ eV in DMF) is observed (the driving forces for the oxidative quenching are calculated by the Rehm–Weller equation as shown in the caption of Table 1. For both triads, $D^{\bullet+}/D$ and $A/A^{\bullet-}$ refer to Ru^{3+}/Ru^{2+} and $POM/POM^{\bullet-}$, respectively. The entropy term is also neglected). Thus, similar to **PTZ-Ru-POM**, the ^{3}MLCT states localized on the exTTF-tpy ligand and delocalized on the tpy-POM ligand undergo reductive and oxidative quenching, respectively (Scheme 2).

Conclusions

The photoinduced electron transfer in two molecular triads containing either a phenothiazine (PTZ) or a π-extended tetrathiafulvalene (exTTF) electron donor, a Ru(II)-bis(terpyridine) photosensitizer and a Keggin-type polyoxometalate (POM) electron acceptor (*i.e.* **PTZ-Ru-POM** and **exTTF-Ru-POM**, POM is $[PW_{11}O_{39}Ge]^{4-}$) is investigated spectroscopically. Molecular dyads comprising the electron donor and the photosensitizer (*i.e.* **PTZ-Ru** and **exTTF-Ruph**) or the photosensitizer and the POM (*i.e.* **Ru-POM**[67]) were studied for comparison. The driving forces for charge separation indicate that the two sequential electron-transfer processes are energetically accessible in both triads.

For **PTZ-Ru-POM** (or **exTTF-Ru-POM**), electron transfer from PTZ (or exTTF) to the photoexcited Ru-center was observed by fs transient absorption spectroscopy, *i.e.* the formation of PTZ$^{\bullet+}$-Ru(tpy)$_2$$^{\bullet-}$-POM (or exTTF$^{\bullet+}$-Ru(tpy)$_2$$^{\bullet-}$-POM). However, the formation of the fully charge-separated states PTZ$^{\bullet+}$-Ru(tpy)$_2$-POM$^{\bullet-}$ (or exTTF$^{\bullet+}$-Ru(tpy)$_2$-POM$^{\bullet-}$), is not observed though the process is energetically feasible. Instead, in **PTZ-Ru-POM** (or **exTTF-Ru-POM**) the initially populated MLCT states, *i.e.* MLCT$_{\text{PTZ-tpy}}$ (or MLCT$_{\text{exTTF-tpy}}$) and MLCT$_{\text{tpy-POM}}$, decay separately *via* distinct and independent decay channels. Hence, for the -tpy-Ru-tpy- photosensitizer, photoexcitation would lead to differently distributed charges within the coordination sphere of the Ru(II) and the resultant MLCT states decay *via* different channels. In **PTZ-Ru-POM** (or **exTTF-Ru-POM**) the distribution of the initial MLCT states determines the direction of the electron transfer within the molecular frame. A similar observation was made in a supramolecular photocatalyst for hydrogen evolution, in which the initially excited state of the $[Ru(bpy)_3]^{2+}$ derived photocenter determines the ultrafast excited state dynamics[85] and the photocatalytic efficiency.[86]

Furthermore, based on the fact that no fully charge-separated state is detected no matter which electron donor is used, it might be more useful to increase the driving forces between the photosensitizer and the POM than tuning the electron donors. For this purpose, either different photosensitizers which have better photophysical properties, *e.g.* an iridium(III)–polypyridyl complex,[61,68,87] or different POMs which are easier to be reduced than the POM studied in this work,[68] would be a promising choice.

Conflicts of interest

There are no conflicts to declare.

Acknowledgements

This research is funded by the Deutsche Forschungsgemeinschaft (DFG, Grant No. SCHU1229-16/1 and DI1517-3/1) and the China Scholarship Council (CSC, Y. L.).

Notes and references

1 S. Berardi, S. Drouet, L. Francàs, C. Gimbert-Surinach, M. Guttentag, C. Richmond, T. Stoll and A. Llobet, *Chem. Soc. Rev.*, 2014, **43**, 7501–7519.
2 S. A. Bonke, M. Wiechen, D. R. MacFarlane and L. Spiccia, *Energy Environ. Sci.*, 2015, **8**, 2791–2796.
3 M. Rudolf, S. V. Kirner and D. M. Guldi, *Chem. Soc. Rev.*, 2016, **45**, 612–630.

Published on 26 March 2018. Downloaded by Thueringer Universitats Landesbibliothek Jena on 3/28/2019 8:57:22 AM.

4 N. S. Lewis, *Science*, 2016, **351**, aad1920.

5 S. Chabi, K. M. Papadantonakis, N. S. Lewis and M. S. Freund, *Energy Environ. Sci.*, 2017, **10**, 1320–1338.

6 L. Hammarström, *Faraday Discuss.*, 2017, **198**, 549–560.

7 W. J. Youngblood, S.-H. A. Lee, K. Maeda and T. E. Mallouk, *Acc. Chem. Res.*, 2009, **42**, 1966–1973.

8 M. R. Wasielewski, *Acc. Chem. Res.*, 2009, **42**, 1910–1921.

9 M. D. Kärkäs, O. Verho, E. V. Johnston and B. Åkermark, *Chem. Rev.*, 2014, **114**, 11863–12001.

10 M. G. Pfeffer, B. Schäfer, G. Smolentsev, J. Uhlig, E. Nazarenko, J. Guthmuller, C. Kuhnt, M. Wächtler, B. Dietzek, V. Sundström and S. Rau, *Angew. Chem., Int. Ed.*, 2015, **54**, 5044–5048.

11 S. Tschierlei, M. Karnahl, M. Presselt, B. Dietzek, J. Guthmuller, L. Gonzalez, M. Schmitt, S. Rau and J. Popp, *Angew. Chem., Int. Ed.*, 2010, **49**, 3981–3984.

12 O. S. Wenger, *Acc. Chem. Res.*, 2011, **44**, 25–35.

13 G. Bottari, O. Trukhina, M. Ince and T. Torres, *Coord. Chem. Rev.*, 2012, **256**, 2453–2477.

14 M. Gilbert and B. Albinsson, *Chem. Soc. Rev.*, 2015, **44**, 845–862.

15 S. Fukuzumi, K. Ohkubo and T. Suenobu, *Acc. Chem. Res.*, 2014, **47**, 1455–1464.

16 S. Fukuzumi, Y. Yamada, T. Suenobu, K. Ohkubo and H. Kotani, *Energy Environ. Sci.*, 2011, **4**, 2754–2766.

17 B. Matt, J. Fize, J. Moussa, H. Amouri, A. Pereira, V. Artero, G. Izzet and A. Proust, *Energy Environ. Sci.*, 2013, **6**, 1504–1508.

18 S. Tschierlei, M. Presselt, C. Kuhnt, A. Yartsev, T. Pascher, V. Sundström, M. Karnahl, M. Schwalbe, B. Schäfer, S. Rau, M. Schmitt, B. Dietzek and J. Popp, *Chem. – Eur. J.*, 2009, **15**, 7678–7688.

19 L. A. Fredin and P. Persson, *J. Chem. Phys.*, 2016, **145**, 104310.

20 J. R. Pinzon, D. C. Gasca, S. G. Sankaranarayanan, G. Bottari, T. Torres, D. M. Guldi and L. Echegoyen, *J. Am. Chem. Soc.*, 2009, **131**, 7727–7734.

21 N. Queyriaux, R. A. Wahyuono, J. Fize, C. Gablin, M. Wächtler, E. Martinez, D. Léonard, B. Dietzek, V. Artero and M. Chavarot-Kerlidou, *J. Phys. Chem. C*, 2017, **121**, 5891–5904.

22 V. L. Gunderson, A. L. Smeigh, C. H. Kim, D. T. Co and M. R. Wasielewski, *J. Am. Chem. Soc.*, 2012, **134**, 4363–4372.

23 A. Petrone, D. B. Lingerfelt, N. Rega and X. Li, *Phys. Chem. Chem. Phys.*, 2014, **16**, 24457–24465.

24 B. R. Gautam, R. Younts, W. T. Li, L. Yan, E. Danilov, E. Klump, I. Constantinou, F. So, W. You, H. Ade and K. Gundogdu, *Adv. Energy Mater.*, 2016, **6**, 1501032.

25 K. Lancaster, S. A. Odom, S. C. Jones, S. Thayumanavan, S. R. Marder, J.-L. Brédas, V. Coropceanu and S. Barlow, *J. Am. Chem. Soc.*, 2009, **131**, 1717–1723.

26 M. Orazietti, M. Kuss-Petermann, P. Hamm and O. S. Wenger, *Angew. Chem., Int. Ed.*, 2016, **55**, 9407–9410.

27 J. H. Klein, D. Schmidt, U. E. Steiner and C. Lambert, *J. Am. Chem. Soc.*, 2015, **137**, 11011–11021.

28 J. Petersson, M. Eklund, J. Davidsson and L. Hammarström, *J. Am. Chem. Soc.*, 2009, **131**, 7940–7941.

29 M. Wielopolski, G. M. Rojas, C. Pol, L. Brinkhaus, G. Katsukis, M. R. Bryce, T. Clark and D. M. Guldi, *ACS Nano*, 2010, **4**, 6449–6462.

30 J. Sukegawa, C. Schubert, X. Z. Zhu, H. Tsuji, D. M. Guldi and E. Nakamura, *Nat. Chem.*, 2014, **6**, 899–905.

31 S.-H. Lee, A. G. Larsen, K. Ohkubo, Z.-L. Cai, J. R. Reimers, S. Fukuzumi and M. J. Crossley, *Chem. Sci.*, 2012, **3**, 257–269.

32 M. Natali, M. Ravaglia, F. Scandola, J. Boixel, Y. Pellegrin, E. Blart and F. Odobel, *J. Phys. Chem. C*, 2013, **117**, 19334–19345.

33 A. Tanushi, T. Kusamoto, Y. Hattori, K. Takada and H. Nishihara, *J. Am. Chem. Soc.*, 2015, **137**, 6448–6451.

34 S. Wenger, P.-A. Bouit, Q. Chen, J. Teuscher, D. D. Censo, R. Humphry-Baker, J.-E. Moser, J. L. Delgado, N. Martín, S. M. Zakeeruddin and M. Grätzel, *J. Am. Chem. Soc.*, 2010, **132**, 5164–5169.

35 Y. Takano, M. A. Herranz, N. Martín, S. G. Radhakrishnan, D. M. Guldi, T. Tsuchiya, S. Nagase and T. Akasaka, *J. Am. Chem. Soc.*, 2010, **132**, 8048–8055.

36 J. Daub, R. Engl, J. Kurzawa, S. E. Miller, S. Schneider, A. Stockmann and M. R. Wasielewski, *J. Phys. Chem. A*, 2001, **105**, 5655–5665.

37 S.-H. Lee, C. T.-L. Chan, K. M.-C. Wong, W. H. Lam, W.-M. Kwok and V. W.-W. Yam, *J. Am. Chem. Soc.*, 2014, **136**, 10041–10052.

38 T. Kamimura, K. Ohkubo, Y. Kawashima, S. Ozako, K. Sakaguchi, S. Fukuzumi and F. Tani, *J. Phys. Chem. C*, 2015, **119**, 25634–25650.

39 Y. Luo, K. Barthelmes, M. Wächtler, A. Winter, U. S. Schubert and B. Dietzek, *Chem. – Eur. J.*, 2017, **23**, 4917–4922.

40 Y. Luo, K. Barthelmes, M. Wächtler, A. Winter, U. S. Schubert and B. Dietzek, *J. Phys. Chem. C*, 2017, **121**, 9220–9229.

41 J. Wiberg, L. Guo, K. Pettersson, D. Nilsson, T. Ljungdahl, J. Mårtensson and B. Albinsson, *J. Am. Chem. Soc.*, 2007, **129**, 155–163.

42 E. Göransson, J. Boixel, J. Fortage, D. Jacquemin, H.-C. Becker, E. Blart, L. Hammarström and F. Odobel, *Inorg. Chem.*, 2012, **51**, 11500–11512.

43 I. A. Howard, F. Laquai, P. E. Keivanidis, R. H. Friend and N. C. Greenham, *J. Phys. Chem. C*, 2009, **113**, 21225–21232.

44 S. T. J. Ryan, R. M. Young, J. J. Henkelis, N. Hafezi, N. A. Vermeulen, A. Hennig, E. J. Dale, Y. Wu, M. D. Krzyaniak, A. Fox, W. M. Nau, M. R. Wasielewski, J. F. Stoddart and O. A. Scherman, *J. Am. Chem. Soc.*, 2015, **137**, 15299–15307.

45 P. E. Hartnett, C. M. Mauck, M. A. Harris, R. M. Young, Y.-L. Wu, T. J. Marks and M. R. Wasielewski, *J. Am. Chem. Soc.*, 2017, **139**, 749–756.

46 S. V. Kirner, C. Henkel, D. M. Guldi, J. D. Megiatto Jr and D. I. Schuster, *Chem. Sci.*, 2015, **6**, 7293–7304.

47 D. M. Stoltzfus, J. E. Donaghey, A. Armin, P. E. Shaw, P. L. Burn and P. Meredith, *Chem. Rev.*, 2016, **116**, 12920–12955.

48 M. Yamamoto, J. Fohlinger, J. Petersson, L. Hammarström and H. Imahori, *Angew. Chem., Int. Ed.*, 2017, **56**, 3329–3333.

49 O. S. Wenger, *Chem. Soc. Rev.*, 2011, **40**, 3538–3550.

50 M. Natali, S. Campagna and F. Scandola, *Chem. Soc. Rev.*, 2014, **43**, 4005–4018.

Published on 26 March 2018. Downloaded by Thueringer Universitats Landesbibliothek Jena on 3/28/2019 8:57:22 AM.

51 M. Gilbert and B. Albinsson, *Chem. Soc. Rev.*, 2015, **44**, 845–862.

52 A. Dolbecq, E. Dumas, C. R. Mayer and P. Mialane, *Chem. Rev.*, 2010, **110**, 6009–6048.

53 J. J. Walsh, A. M. Bond, R. J. Forster and T. E. Keyes, *Coord. Chem. Rev.*, 2016, **306**, 217–234.

54 J. Tucher, K. Peuntinger, J. T. Margraf, T. Clark, D. M. Guldi and C. Streb, *Chem. – Eur. J.*, 2015, **21**, 8716–8719.

55 B. Keita, U. Kortz, L. R. B. Holzle, S. Brown and L. Nadjo, *Langmuir*, 2007, **23**, 9531–9534.

56 C. Streb, *Dalton Trans.*, 2012, **41**, 1651–1659.

57 J. M. Sumliner, H. Lv, J. Fielden, Y. V. Geletii and C. L. Hill, *Eur. J. Inorg. Chem.*, 2014, 635–644.

58 W. Guo, H. Lv, J. Bacsa, Y. Gao, J. S. Lee and C. L. Hill, *Inorg. Chem.*, 2016, **55**, 461–466.

59 J. J. Walsh, A. M. Bond, R. J. Forster and T. E. Keyes, *Coord. Chem. Rev.*, 2016, **306**, 217–234.

60 G. Izzet, F. Volatron and A. Proust, *Chem. Rec.*, 2017, **17**, 250–266.

61 S. Schönweiz, S. A. Rommel, J. Kübel, M. Micheel, B. Dietzek, S. Rau and C. Streb, *Chem. – Eur. J.*, 2016, **22**, 12002–12005.

62 A. Proust, B. Matt, R. Villanneau, G. Guillemot, P. Gouzerh and G. Izzet, *Chem. Soc. Rev.*, 2012, **41**, 7605–7622.

63 B. Matt, C. Coudret, C. Viala, D. Jouvenot, F. Loiseau, G. Izzet and A. Proust, *Inorg. Chem.*, 2011, **50**, 7761–7768.

64 A. Yokoyama, T. Kojima, K. Ohkubo, M. Shiro and S. Fukuzumi, *J. Phys. Chem. A*, 2011, **115**, 986–997.

65 C. Zhao, Z. Huang, W. Rodríguez-Córdoba, C. S. Kambara, K. P. O'Halloran, K. I. Hardcastle, D. G. Musaev, T. Lian and C. L. Hill, *J. Am. Chem. Soc.*, 2011, **133**, 20134–20137.

66 C. Allain, D. Schaming, N. Karakostas, M. Erard, J.-P. Gisselbrecht, S. Sorgues, I. Lampre, L. Ruhlmann and B. Hasenknopf, *Dalton Trans.*, 2013, **42**, 2745–2754.

67 Y. Luo, M. Wächtler, K. Barthelmes, A. Winter, U. S. Schubert and B. Dietzek, *Chem. Commun.*, 2018, **54**, 2970–2973.

68 B. Matt, X. Xiang, A. L. Kaledin, N. Han, J. Moussa, H. Amouri, S. Alves, C. L. Hill, T. Lian, D. G. Musaev, G. Izzeta and A. Proust, *Chem. Sci.*, 2013, **4**, 1737–1745.

69 K. Barthelmes, M. Sittig, A. Winter and U. S. Schubert, *Eur. J. Inorg. Chem.*, 2017, 3698–3706.

70 K. Barthelmes, J. Kübel, A. Winter, M. Wächtler, C. Friebe, B. Dietzek and U. S. Schubert, *Inorg. Chem.*, 2015, **54**, 3159–3171.

71 J. Kübel, R. Schroot, M. Wächtler, U. S. Schubert, B. Dietzek and M. Jäger, *J. Phys. Chem. C*, 2015, **119**, 4742–4751.

72 B. Dietzek, T. Pascher, V. Sundström and A. Yartsev, *Laser Phys. Lett.*, 2007, **4**, 38–43.

73 L. Zedler, J. Guthmuller, I. R. Moraes, S. Kupfer, S. Krieck, M. Schmitt, J. Popp, S. Rau and B. Dietzek, *Chem. Commun.*, 2014, **50**, 5227–5229.

74 J.-P. Sauvage, J.-P. Collin, J.-C. Chambron, S. Guillerez, C. Coudret, V. Baltani, F. Barigelletti, L. D. Cola and L. Flamigni, *Chem. Rev.*, 1994, **94**, 993–1019.

75 D. Rehm and A. Weller, *Isr. J. Chem.*, 1970, **8**, 259–271.

76 A. Weller, *Z. Phys. Chem.*, 1982, **133**, 93–98.

77 J. Hankache and O. S. Wenger, *Phys. Chem. Chem. Phys.*, 2012, **14**, 2685–2692.

78 J. T. Hewitt, P. J. Vallett and N. H. Damrauer, *J. Phys. Chem. A*, 2012, **116**, 11536–11547.

79 A. M. Brown, C. E. McCusker and J. K. McCusker, *Dalton Trans.*, 2014, **43**, 17635–17646.

80 R. Siebert, C. Hunger, J. Guthmuller, F. Schlütter, A. Winter, U. S. Schubert, L. González, B. Dietzek and J. Popp, *J. Phys. Chem. C*, 2011, **115**, 12677–12688.

81 L. Flamigni, E. Baranoff, J.-P. Collin and J.-P. Sauvage, *Chem. – Eur. J.*, 2006, **12**, 6592–6606.

82 M. Wächtler, J. Guthmuller, L. Gonzálezd and B. Dietzek, *Coord. Chem. Rev.*, 2012, **256**, 1479–1508.

83 M. T. Indelli, M. Orlandi, C. Chiorboli, M. Ravaglia, F. Scandola, F. Lafolet, S. Welter and L. De Cola, *J. Phys. Chem. A*, 2012, **116**, 119–131.

84 D. M. Guldi, L. Sánchez and N. MartÍn, *J. Phys. Chem. B*, 2001, **105**, 7139–7144.

85 M. Wächtler, J. Guthmuller, S. Kupfer, M. Maiuri, D. Brida, J. Popp, S. Rau, G. Cerullo and B. Dietzek, *Chem. – Eur. J.*, 2015, **21**, 7668–7674.

86 S. Tschierlei, M. Karnahl, M. Presselt, B. Dietzek, J. Guthmuller, L. González, M. Schmitt, S. Rau and J. Popp, *Angew. Chem., Int. Ed.*, 2010, **49**, 3981–3984.

87 S. A. Rommel, D. Sorsche, N. Rockstroh, F. W. Heinemann, J. Kübel, M. Wächtler, B. Dietzek and S. Rau, *Eur. J. Inorg. Chem.*, 2015, 3730–3739.

Electronic Supplementary Material (ESI) for Physical Chemistry Chemical Physics.
This journal is © the Owner Societies 2018

Supporting Information

Coexistence of distinct intramolecular electron transfer pathways in polyoxometalate based molecular triads

Yusen Luo[1,2], Maria Wächtler[2], Kevin Barthelmes[3,4], Andreas Winter[3,4], Ulrich S. Schubert[3,4] and Benjamin Dietzek*[1,2,4]

[1]*Institute of Physical Chemistry and Abbe Center of Photonics, Friedrich Schiller University Jena, Helmholtzweg 4, 07743 Jena, Germany*

[2]*Department Functional Interfaces, Leibniz Institute of Photonic Technology (IPHT), Albert-Einstein-Str. 9, 07745 Jena, Germany*

[3]*Laboratory of Organic and Macromolecular Chemistry (IOMC), Friedrich Schiller University Jena, Humboldtstr. 10, 07743 Jena, Germany*

[4]*Center for Energy and Environmental Chemistry Jena (CEEC Jena), Friedrich Schiller University Jena, Philosophenweg 7a, 07743 Jena, Germany*

**Corresponding author: benjamin.dietzek@leibniz-ipht.de*

Table of contents

General methods

The synthesis, electrochemistry and steady-state absorption and emission spectra of the mono-ruthenium complex, dyads and triads have been reported.[1-3] Steady-state UV/Vis absorption spectra (Figure S1a) and emission spectra (Figure S1b) collected in dimethyl sulfoxide (DMSO) are summarized for convenience. Steady-state UV/Vis absorption spectra were recorded with a JASCO V-670 spectrophotometer in a quartz cell with 1 mm path length. Steady-state emission spectra (λ_{ex} = 520 nm, optical density of each sample was adjusted to 0.1 at 520 nm) were recorded with a fluorescence spectrometer (Fluorolog, Horiba group) in a 1 cm quartz cell. For the time-resolved experiments and resonance Raman measurements the stability of samples was ensured by recording the steady-state UV/Vis absorption spectra before and after every measurement.

Electrochemistry. CV measurement for **PTZ-Ru** was carried out with PC-controlled potentiostat (VersaSTAT 3) with a standard three-electrode system by using a glassy-carbon-disk working electrode, a platinum wire counter electrode and an Ag/AgCl reference electrode. The scan rate is 200 mV/s. All potentials given in the manuscript refer to ferrocene as standard. Because of the limited electrochemical window of DMSO, the electrochemistry[1] was collected in dimethylformamide (DMF).

Time-Resolved Transient Absorption Spectroscopy. Femtosecond (fs) transient absorption (TA) spectra were collected by two different home-built pump-probe setups. Each setup is based on an amplified Ti: Sapphire oscillator (1 kHz, 800 nm).[4] The compounds were excited by pump pulses centered at 520 nm (TOPAS-C, Lightconversion Ltd.) with a duration of 80 fs. The power of the pump beam at the sample was kept at 0.45 mW, corresponding to an energy of 0.9 µJ per pump pulse. For measurements with a longer delay time range (up to 9.5 ns) the compounds were excited at 520 nm (TOPASwhite, Lightconversion Ltd.) with a duration of 110 fs. The power of the pump beam at the sample was kept at 0.3 mW, corresponding to an energy of 0.6 µJ per pump pulse. For both setups, a white light supercontinuum generated by focusing a fraction of the fundamental in a CaF_2 plate is used to probe the absorbance of the sample between 340 to 800 nm. The pump beam is delayed in time with respect to the probe beam by means of an optical delay line and the polarization between probe and pump is set at the magic angle (54.7°). Each sample solution (adjusted to yield an optical density of 0.2 at 520 nm) was kept in a 1 mm quartz cuvette. Transient absorption data were corrected for the chirp of the probe light and analyzed by a global multi-exponential fit after exclusion of a temporal window of 200 fs around time-zero in order to avoid contributions of the coherent-artifact region[5] to the data analysis.

Nanosecond (ns) TA spectra[2] were collected to study the lifetime of the long-lived species, which are visible in the fs TA data. The pump pulses centered at 520 nm were produced by a Continuum OPO Plus which is pumped by a continuum surelite Nd:YAG laser system (pulse duration 5 ns, repetition rate 10 Hz). The probe light is provided by a 75 W xenon arc lamp. Spherical concave mirrors are used to focus the probe beam into the samples and then to send the beam to the monochromator (Acton, Princeton Instruments). The spectrally selected probe light is detected by a Hamamatsu R928 photomultiplier. The signal is amplified and processed by a commercially available detection system (Pascher Instruments AB). Each sample was freshly prepared for the ns transient absorption measurements yielding an optical density of about 0.37 at the excitation wavelength, i.e. at 520 nm. All measurements were performed in 1 cm path length fluorescence cuvettes. For all measurements, the energy of the pump pulses was kept at 0.25 mJ. Oxygen-free solutions were realized by at least five freeze-pump-thaw cycles.

Resonance Raman Spectra. Excitation-wavelength dependent resonance Raman (rR) spectra were recorded in a conventional 90° scattering arrangement.[6] RR spectra were recorded upon excitation at 458, 476, 496 and 515 nm (delivered by a Coherent Innova300C MotoFreD Ion Laser). A rotating cell was utilized to prevent sample decomposition. In order to check for sample integrity, absorption spectra of the samples were recorded before and after each rR measurement. No changes in the absorption spectra were observed.

Considering the limited solubility of compounds studied in this manuscript, all spectroscopic experiments were performed upon dissolving the POM containing samples in DMSO.

Steady-state emission spectra

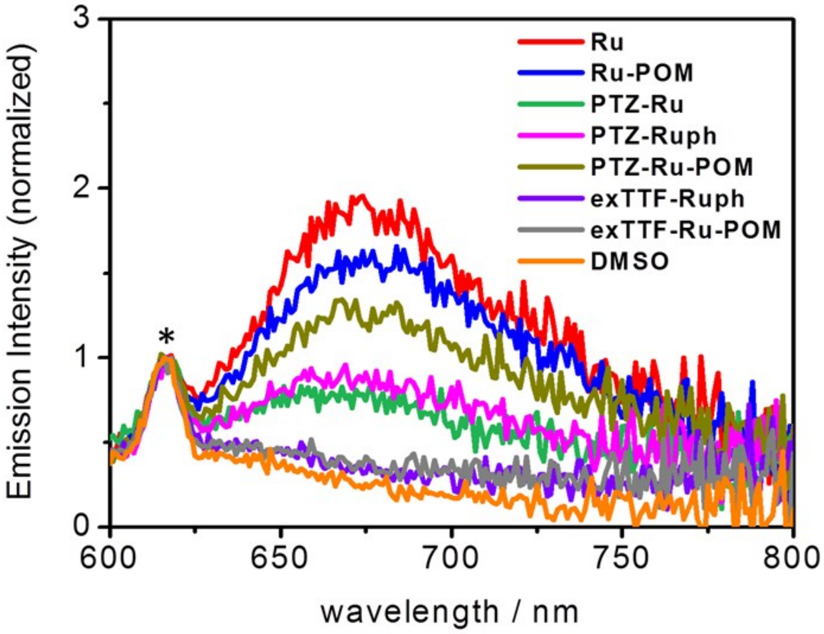

Figure S1. Normalized steady-state emission spectra (λ_{ex} = 520 nm, $OD_{520\ nm}$ = 0.1) of the compounds collected in aerated dimethyl sulfoxide (DMSO).[1,3] The emission spectra were normalized to the Raman band (asterisk) of the solvent DMSO.

Optimized molecular structure of PTZ-Ru-POM and exTTF-Ru-POM

The structures were optimized by molecular modelling (MM) with *BIOVIA* Material Studio v8.0 using the Forcite module with default settings (algorithm = smart; convergence tolerance: energy = 0.001 kcal/mol, force = 0.5 kcal/mol/Å; maximum number of iterations = 2000; motion groups rigid = NO). The start structure of the POM unit was the geometry optimized structure of a similar POM reported by Matt *et al.*.[7]

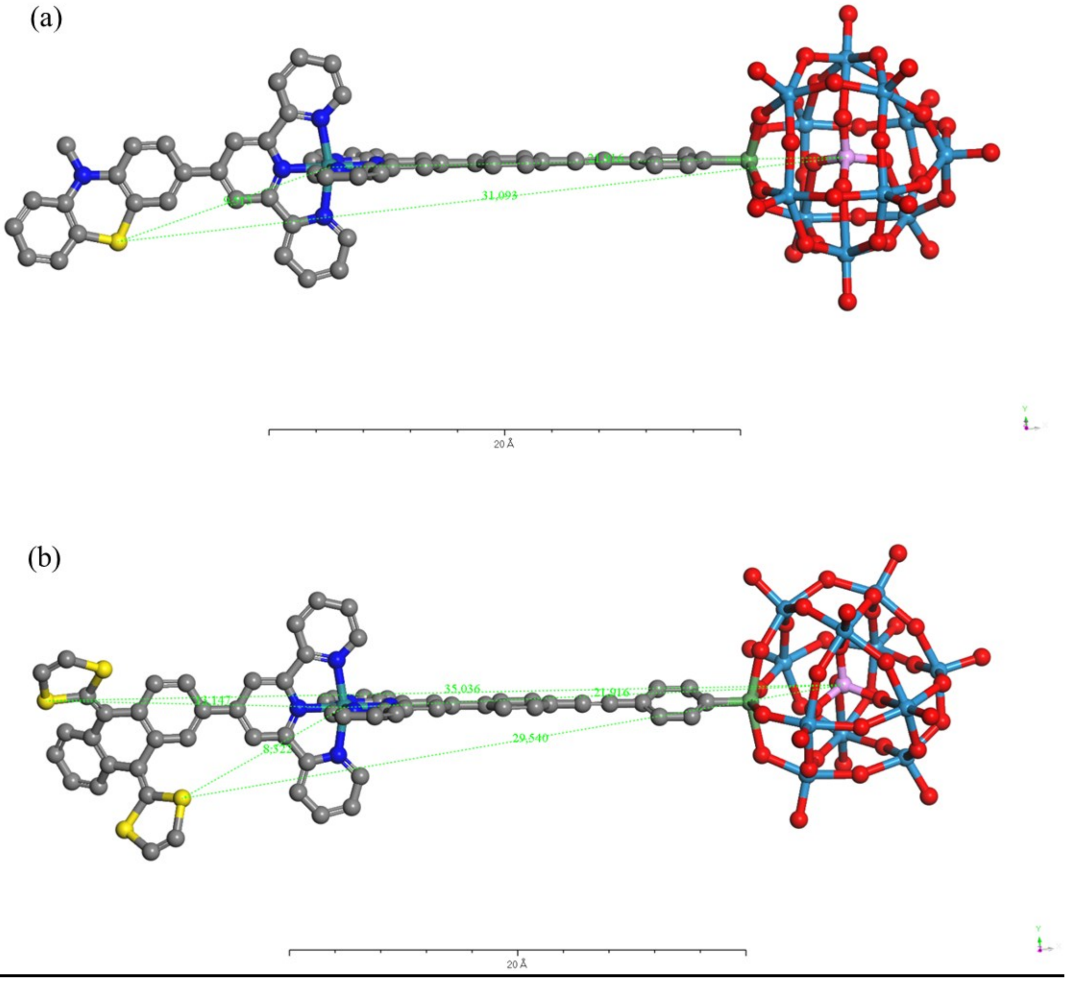

Figure S2. Optimized molecular structure of (a) **PTZ-Ru-POM** and (b) **exTTF-Ru-POM**. For measuring the center-to-center distance, the sulfur atom in PTZ and exTTF units, the ruthenium atom in Ru^{II} complex and the central phosphorus atom in POM were used. Since the exTTF unit has a butterfly-like shape and consists of four sulfur atoms, there are different distances from each sulfur atom. Only the shortest and longest distance were displayed and used.

Cyclic voltammetry curve of PTZ-Ru

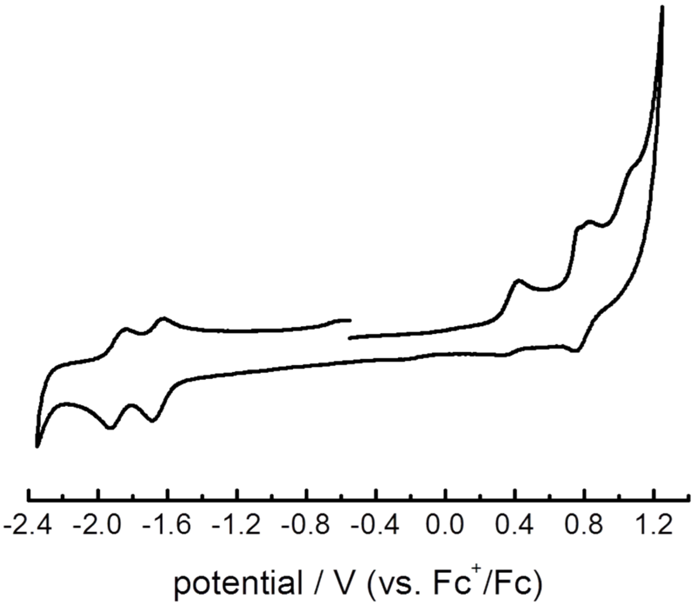

Figure S3. Cyclic voltammetry curve (scan rate 200 mV/s) for dyad **PTZ-Ru** in DMF/0.1 M Bu_4NPF_6.

Schematic illustration for the calculation of driving forces

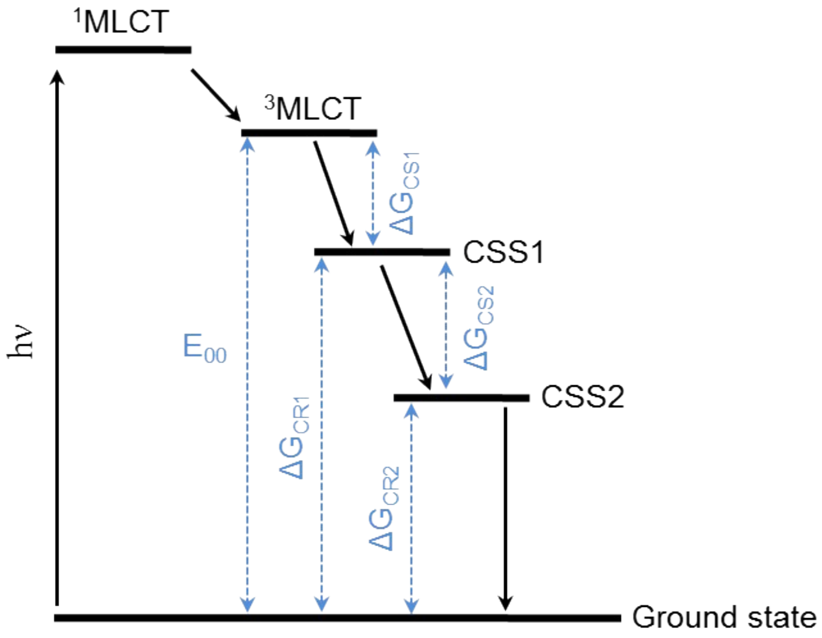

Scheme S1. The possible relaxation processes of the triads upon photoexcitation.

Here is an anticipated scheme for the two sequential electron-transfer processes of the triads after photoexcitation of the Ru-center. For the first charge separation (CSS1) the radical pairs are $tpy^{\cdot -}$ / $PTZ^{\cdot +}$ or $tpy^{\cdot -}$ / $exTTF^{\cdot +}$; for the second charge separation (CSS2) the radical pairs are $POM^{\cdot -}$ / $PTZ^{\cdot +}$ or $POM^{\cdot -}$ / $exTTF^{\cdot +}$, and $\Delta G^\circ_{CR} = e\,(E_{A/A^-} - E_{D^+/D}) + e^2 / 4\pi R\varepsilon_0\varepsilon_s$. $\Delta G^\circ_{CS1} = -\Delta G^\circ_{CR1} - E_{00}$ is the driving force for the first charge separation. E_{00} is the energy difference between the thermalized, lowest ^{3}MLCT excited state and ground state of Ru complex. Thus, the driving force for the second charge separation (*i.e.* from CSS1 to CSS2 state) can be calculated by $\Delta G^\circ_{CS2} = \Delta G^\circ_{CR1} - \Delta G^\circ_{CR2}$.

Driving forces in DMSO

According to the literature report,[8,9] the driving forces in DMSO can be calculated by the following equation:

$$\Delta G^{\circ}_{CS} = e\,(E_{D^+/D} - E_{A/A^-}) - E_{00} - \frac{e^2}{4\pi\varepsilon_0\varepsilon R_{DA}} - \frac{e^2}{8\pi\varepsilon_0}\left(\frac{1}{r_{D^+}} + \frac{1}{r_{A^-}}\right)\left(\frac{1}{\varepsilon_{ref}} - \frac{1}{\varepsilon}\right)$$

the last term concerning the difference of solvation free enthalpies in different solvents used in electrochemistry (ε_{ref}) and photo-physical measurement (ε). R_{DA} is the distance between donor and acceptor. r_D^+ and r_A^- represent the radius of the oxidized donor and reduced acceptor, respectively.

Table S1. Estimated radii of neutral electron donors and acceptors.

unit	radius / Å[a]	radius / Å[b]
PTZ	3.7	3.6[c]
exTTF	4.6	4.2[d]
Ru complex	4.7	4.7[e]
POM	6.2	5.3[f]

[a] Radii of electron donors and acceptors were obtained from the optimized molecular structures shown in Figure S2 which were measured without considering the outside hydrogens. [b] Shows the comparison to the radii obtained from the crystal structures (without hydrogens). [c-f] Were taken from ref. 10-13.

Table S2. Center-to-center distances R, electrochemical data and reaction free-energy changes (–ΔG°) for charge separation (CS) and charge recombination (CR) in DMSO.

	center-to-center / Å		E° / V (vs Fc⁺/Fc)[e]				- ΔG° / eV[f]			
	$R_{(D\text{-}Ru)}$[a]	$R_{(D\text{-}POM)}$[b]	D^+/D	Ru^{3+}/Ru^{2+}	POM/POM^-	tpy/tpy^-	CS1	CR1	CS2	CR2
PTZ-Ru	9.5	-	0.37	0.78	-	-1.65	0.10	1.97	-	-
PTZ-Ru-POM	9.5	31.1	0.29	0.75	-1.45	-1.69	0.14	1.93	0.22	1.71
exTTF-Ruph	8.3[c] (13.2)[d]	-	-0.16	0.84	-	-1.55	0.73[c] (0.72)[d]	1.34[c] (1.35)[d]	-	-
exTTF-Ru-POM	8.3[c] (13.2)[d]	29.5[c] (35.0)[d]	-0.30	0.84	-1.46	-1.63	0.79[c] (0.78)[d]	1.28[c] (1.29)[d]	0.14[c] (0.15)[d]	1.14[c] (1.14)[d]

[a,b] Center-to-center distances (Figure S2) between the electron donor (PTZ or exTTF) and Ru^{II} complex ($R_{D\text{-}Ru}$) or POM ($R_{D\text{-}POM}$). [c] Shortest and [d] longest distance between exTTF and Ru^{II} complex since the exTTF unit has a butterfly-like shape and consists of four sulphur atoms (Figure S2b). [e] Except **PTZ-Ru** (Figure S3), redox potentials were taken from ref. 1. [f] driving forces for charge-separation and charge-recombination in DMSO were calculated by the equation shown above which concerning the different solvents used in electrochemistry and photo-physical measurement. For calculation, the radii of neutral electron donors and acceptors obtained from the optimized molecular structures were used (Table S1).

fs TA spectra of PTZ-Ru and PTZ-Ru-POM at longer time scale

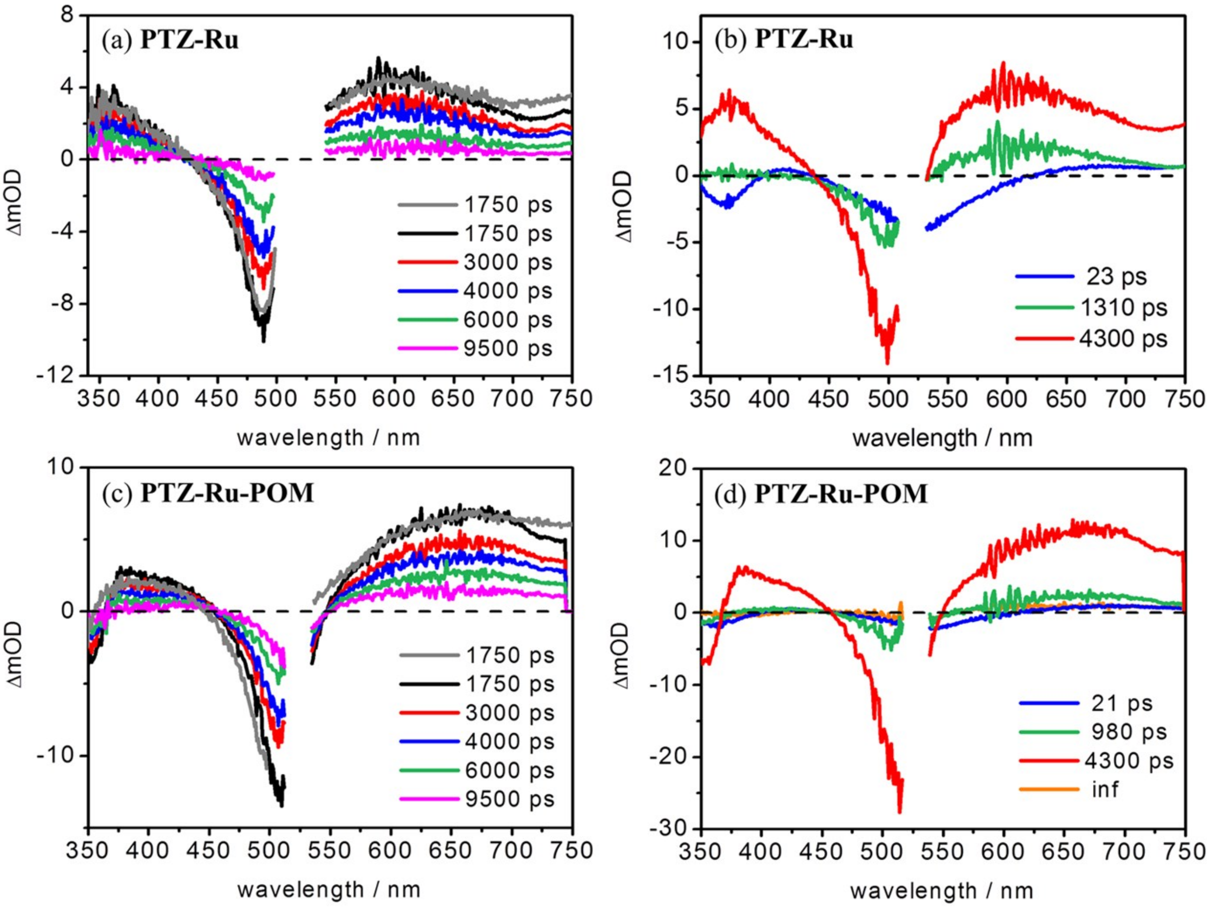

Figure S4. Femtosecond (fs) transient absorption (TA) spectra at selected times of (a) **PTZ-Ru** and (c) **PTZ-Ru-POM** upon excitation at 520 nm in aerated DMSO in the time range of 1750 to 9500 ps. To combine the fs TA data collected by a short and a long optical delay line, the spectra were scaled according to the spectrum obtained by the short delay line at 1750 ps at 590 and 680 nm (grey solid line) for **PTZ-Ru** and **PTZ-Ru-POM**, respectively. (b) and (d) Corresponding decay-associated spectra which were obtained by fixing the first two time constants obtained from the fs TA data measured with a short optical delay line.

ns TA spectra of PTZ-Ru and PTZ-Ruph

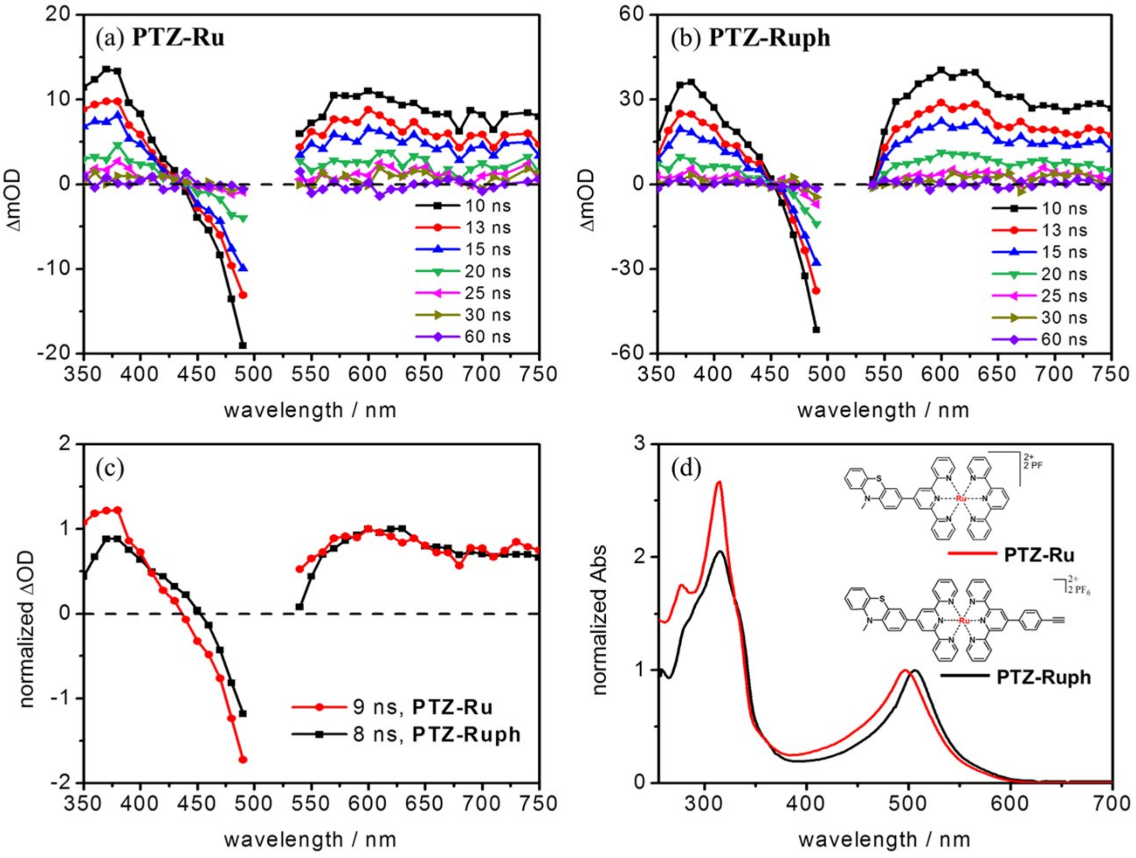

Figure S5. Nanosecond (ns) transient absorption (TA) spectra at selected times of (a) **PTZ-Ru** and (b) **PTZ-Ruph** upon excitation at 520 nm in aerated DMSO. (c) Normalized (at 600 nm) global fit result of the ns TA. (d) Normalized (at absorption maximum for each compound) UV/Vis absorption spectra in DMSO.

fs TA spectra of Ru-POM

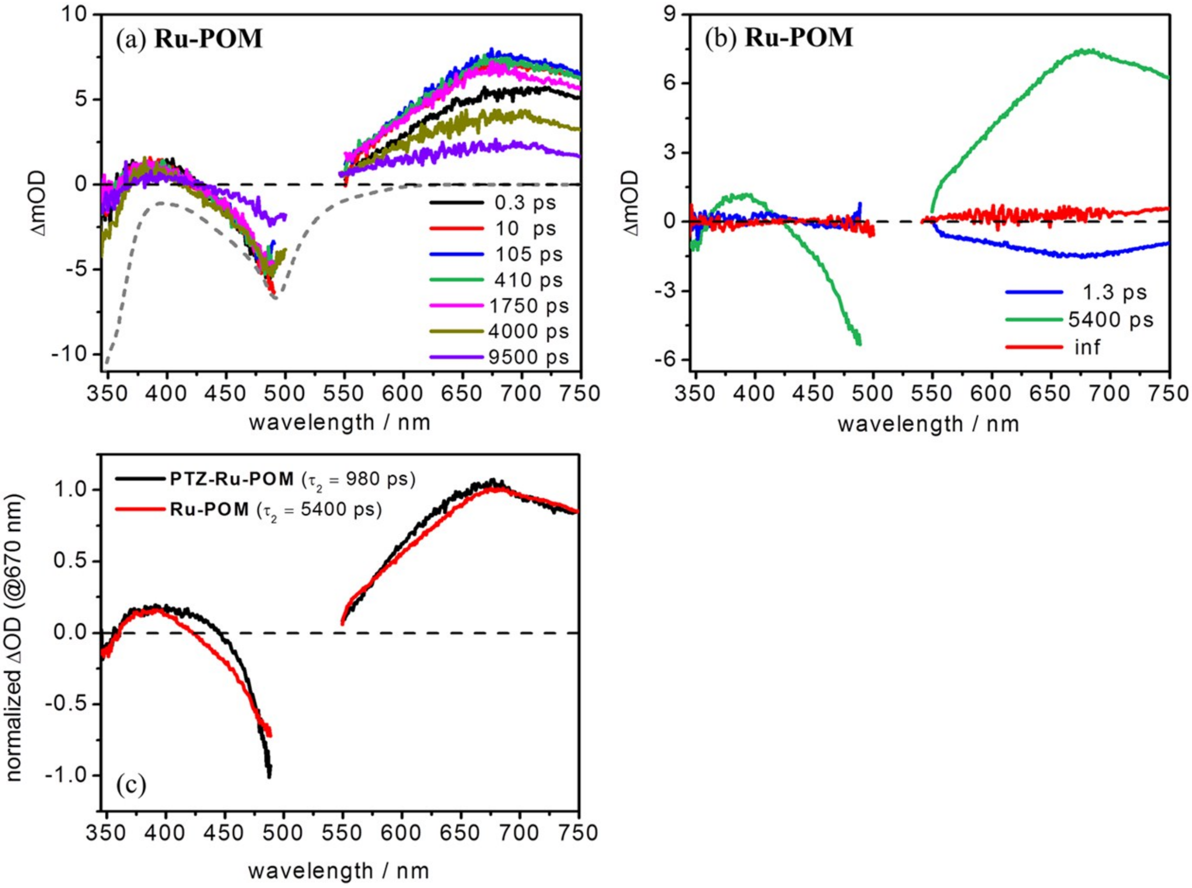

Figure S6. (a) Femtosecond transient absorption spectra at selected times of (a) **Ru-POM** upon excitation at 520 nm in aerated DMSO and (b) decay-associated spectra.[3] (c) Comparison of the second species (normalized at 670 nm) in decay-associated spectra of **PTZ-Ru-POM** (see the main text) and **Ru-POM**.

ns TA spectra of PTZ-Ru-POM

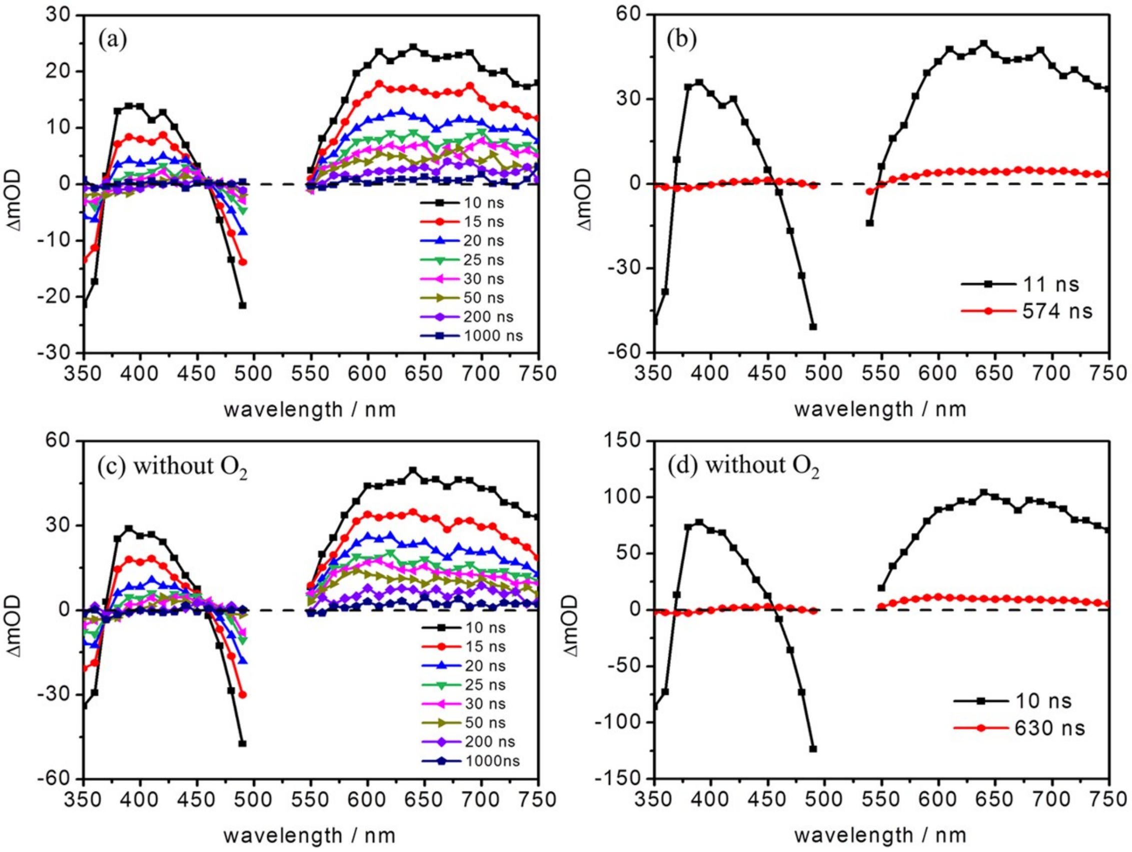

Figure S7. Nanosecond (ns) transient absorption (TA) spectra at selected times of **PTZ-Ru-POM** upon excitation at 520 nm in (a) aerated and (c) deaerated DMSO. (b) and (d) Corresponding global fit results of the ns TA data. Note: the time constant for the first species (~10 ns) obtained from the global fit is close to the time resolution of our setup. In order to get a more reliable value for this process fs TA spectra with a longer delay line (~9.5 ns) was used (see Figure S4).

Integrated kinetic trace of the ns TA data of PTZ-Ru-POM

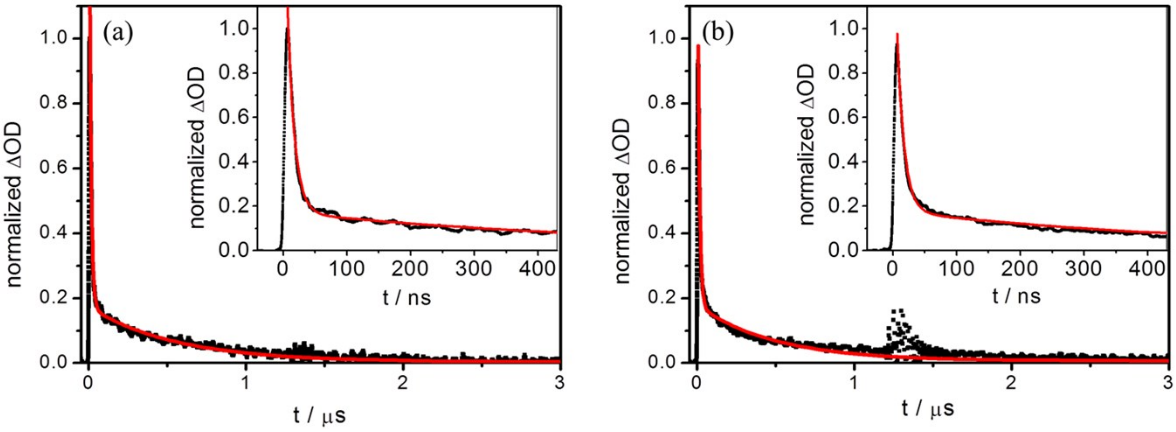

Figure S8. Normalized integrated kinetic trace at the spectral region between 540 and 750 nm where shows significant absorption signals of both species in ns TA data of **PTZ-Ru-POM** collected upon excitation at 520 nm in (a) aerated and (b) deaerated DMSO. Inset: the enlargement of the time region up to 425 ns. The decay was fitted by a bi-exponential function: $I(x) = A_1 \cdot \exp(-x/\tau_1) + A_2 \cdot \exp(-x/\tau_2) + I_0$.

Simulation of the absorption spectra of the oxidized donor in PTZ-Ru-POM

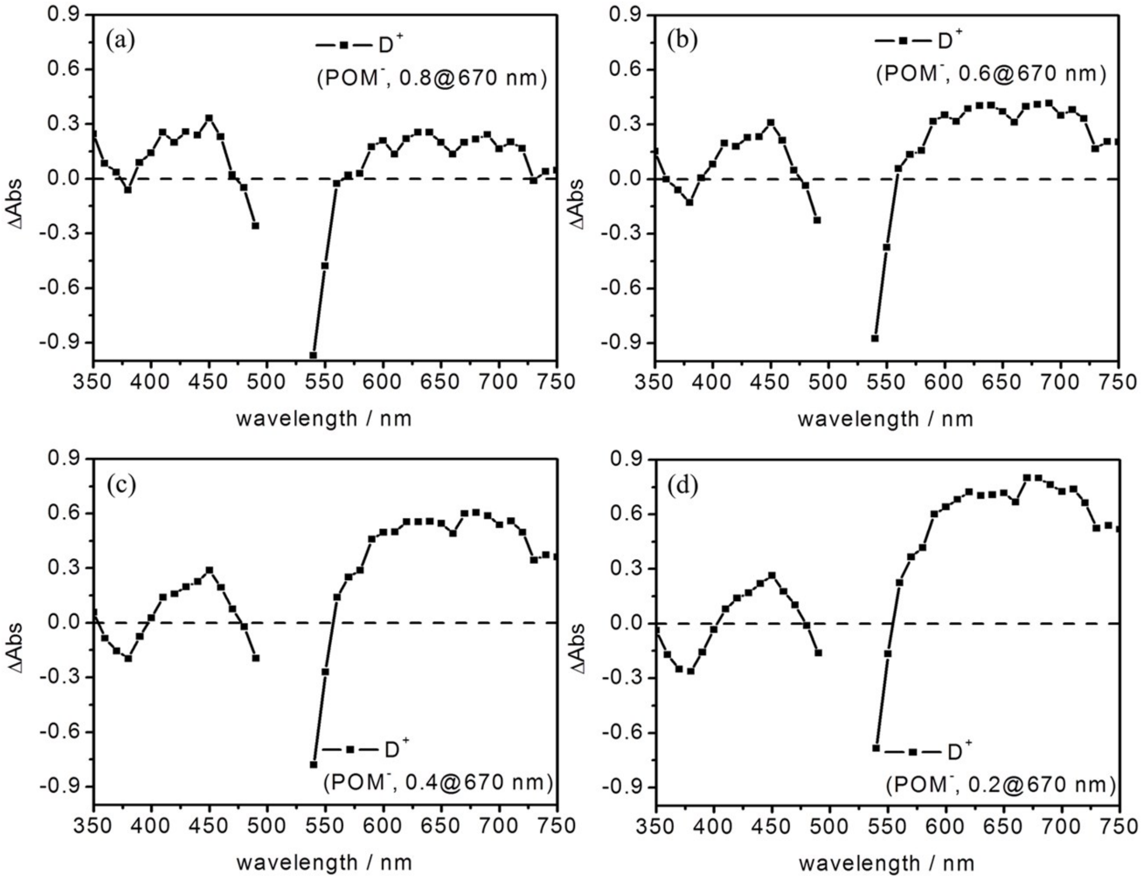

Figure S9. In order to exclude the formation of PTZ$^{\cdot+}$-Ru(tpy)$_2$-POM$^{\cdot-}$, the absorption spectra of the oxidized donor (D$^+$) were simulated: from the normalized (at 670 nm) spectrum of the long-lived species in global fit of the ns TA data (Figure S7b) different contributions of the reduced POM were subtracted. The POM$^{\cdot-}$ has a contribution at 670 nm of (a) 0.8, (b) 0.6, (c) 0.4 and (d) 0.2. All the resulting spectra do not display the significant positive absorption bands of PTZ$^{\cdot+}$ at 365, 470 and 590 nm.[14,15] Thus the long-lived species in **PTZ-Ru-POM** is not the PTZ$^{\cdot+}$-Ru(tpy)$_2$-POM$^{\cdot-}$. See Figure S10a for the spectrum of reduced POM.

Comparison of the sub-μs species ns TA data with the SEC results

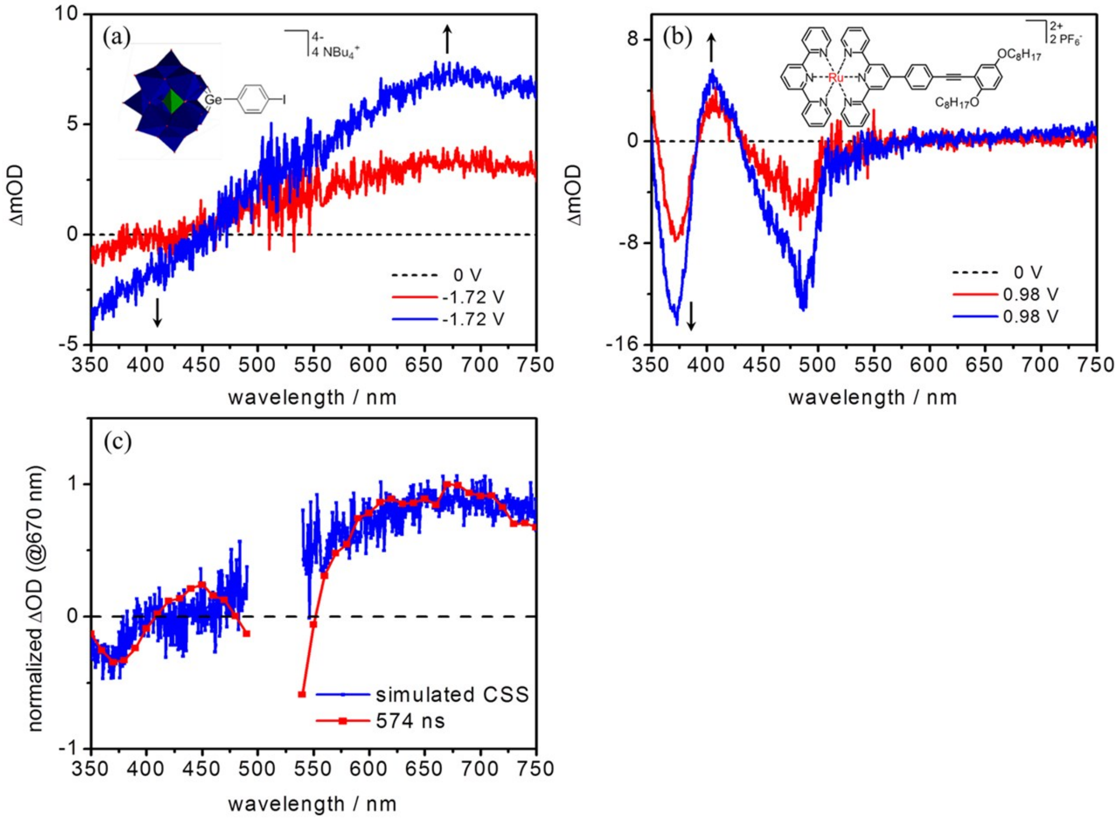

Figure S10. (a) Reductive and (b) oxidative spectroelectrochemistry-UV/Vis absorption difference spectra of POM and Ru, respectively.[3] Inset: molecular structure of the POM and Ru complex studied. (c) Comparison of the long-lived species in global fit results of the ns TA data of **PTZ-Ru-POM** with the simulated spectrum of $\mathrm{Ru^{III}}$-$\mathrm{POM^{\cdot -}}$ taken from ref. 3.

Resonance Raman spectra of PTZ-Ru-POM

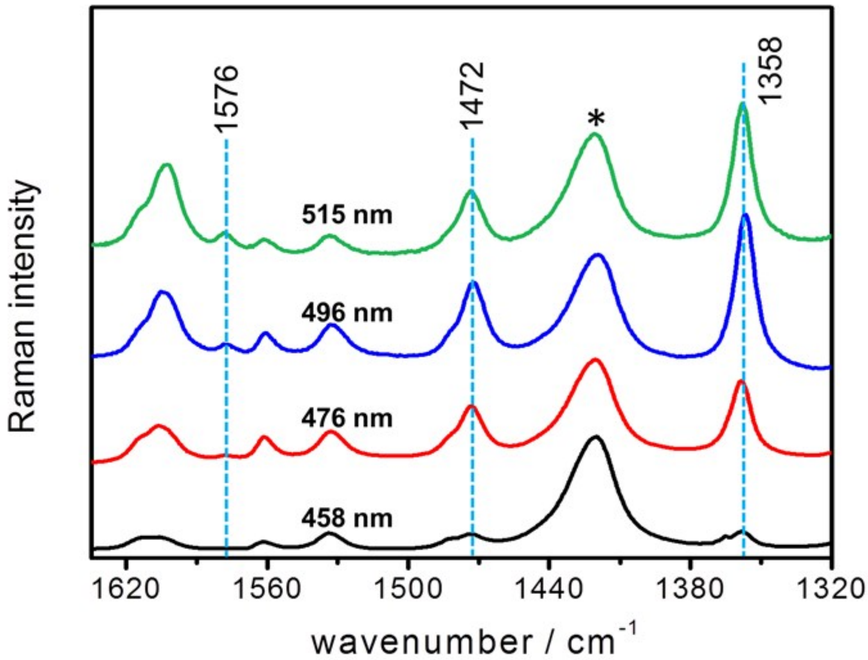

Figure S11. Resonance Raman spectra of **PTZ-Ru-POM** recorded in DMSO with excitation wavelengths at 515, 496, 476 and 458 nm. For comparison the spectra were normalized to the solvent band (asterisks) at 1420 cm^{-1} and only the modes (associated with PTZ) showing distinct differences in signal intensities upon variation of the excitation wavelengths were marked.

The excitation-wavelength dependent resonance Raman of triad **PTZ-Ru-POM** shows similar results to that of **PTZ-Ru**.[14] Thus the Jablonski scheme for **PTZ-Ru-POM** was made by referring to **PTZ-Ru**.[14]

Comparison of the fs TA spectra of exTTF-Ruph and Ruph

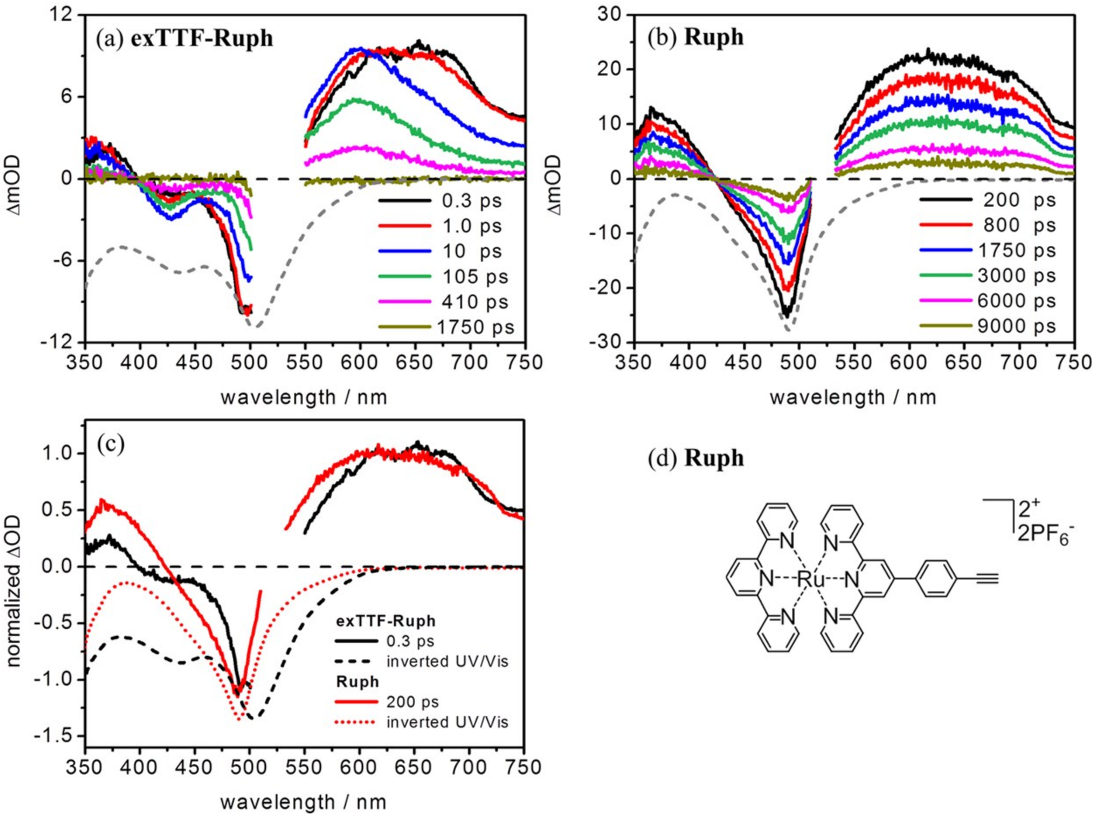

Figure S12. Femtosecond (fs) transient absorption (TA) spectra at selected times of (a) **exTTF-Ruph** (short optical delay line) and (b) **Ruph** (long optical delay line) upon excitation at 520 nm in aerated DMSO. The grey dashed line in a and b represents the inverted ground state absorption spectrum respectively. (c) Comparison of the spectrum of **exTTF-Ruph** collected at 0.3 ps and **Ruph** collected at 200 ps. (d) Molecular structure of **Ruph** studied.

For the mono-ruthenium complex **Ruph**, the transient absorption spectra collected at long delay times, e.g. 200 ps, shows the decay of the ^{3}MLCT state. The spectral features of **exTTF-Ruph** collected at early times, i.e. 0.3 ps, resemble the spectrum of the ^{3}MLCT state in **Ruph** but with a slight red-shift which is already indicated in the inverted UV/Vis absorption spectra (Figure S12c).

fs TA spectra of exTTF-Ru-POM at longer time scale

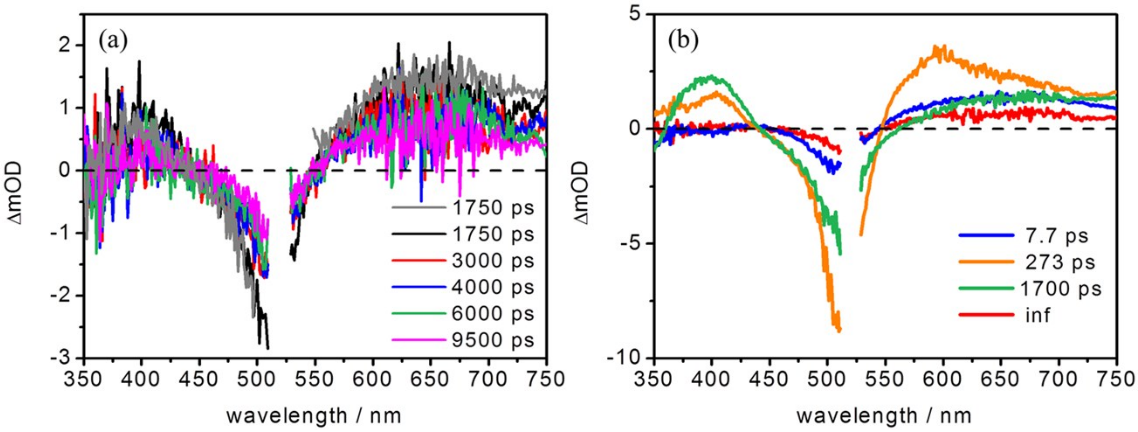

Figure S13. (a) Femtosecond (fs) transient absorption (TA) spectra at selected times of **exTTF-Ru-POM** upon excitation at 520 nm in aerated DMSO in the time range of 1750 to 9500 ps. To combine the fs TA data collected by a short and a long optical delay line, the spectra were scaled according to the spectrum obtained by the short delay line at 1750 ps at 630 nm (grey solid line). (b) Corresponding decay-associated spectra which were obtained by fixing the first two time constants obtained from the fs TA data measured with a short optical delay line.

ns TA spectra of exTTF-Ru-POM

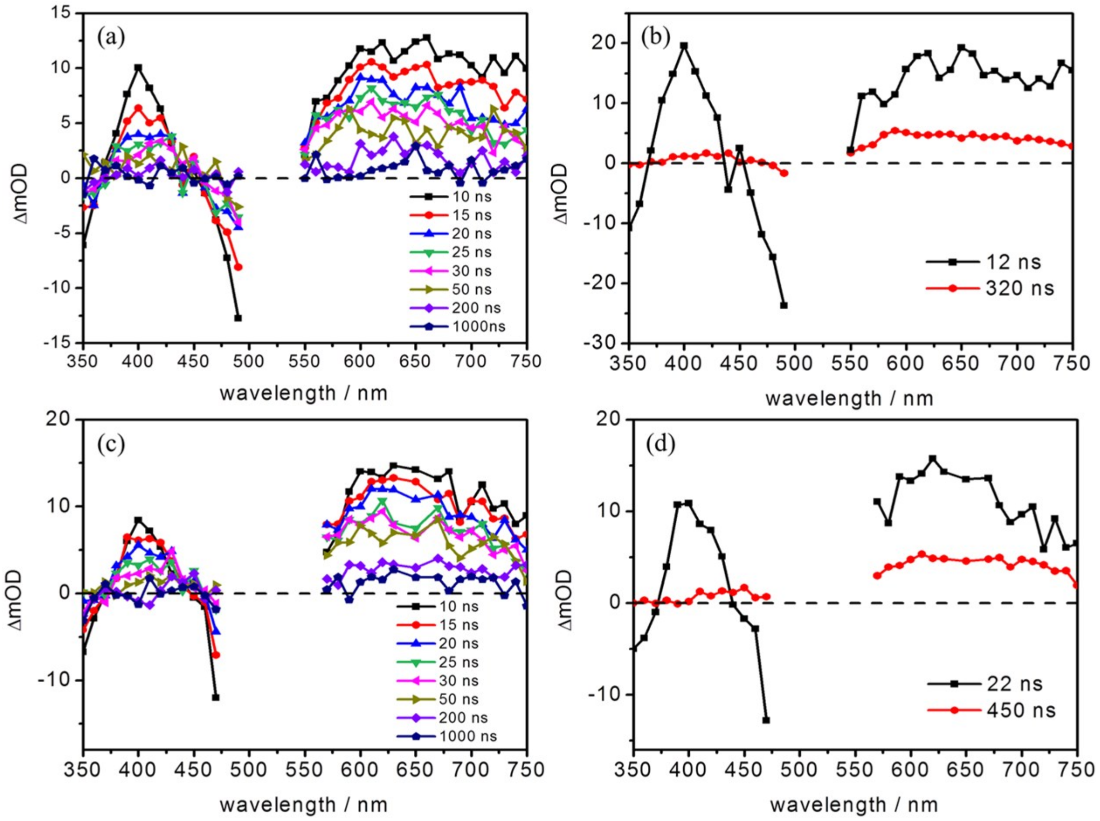

Figure S14. Nanosecond (ns) transient absorption (TA) spectra at selected times of **exTTF-Ru-POM** upon excitation at 520 nm in (a) aerated and (c) deaerated DMSO. (b) and (d) Corresponding global fit results of the ns TA data. Note: the time constant for the first species obtained from the global fit is close to the time resolution of our setup. In order to get the accurate value for this process fs TA spectra with a longer delay line (~9.5 ns) was used (see Figure S13).

Integrated kinetic trace of the ns TA data of exTTF-Ru-POM

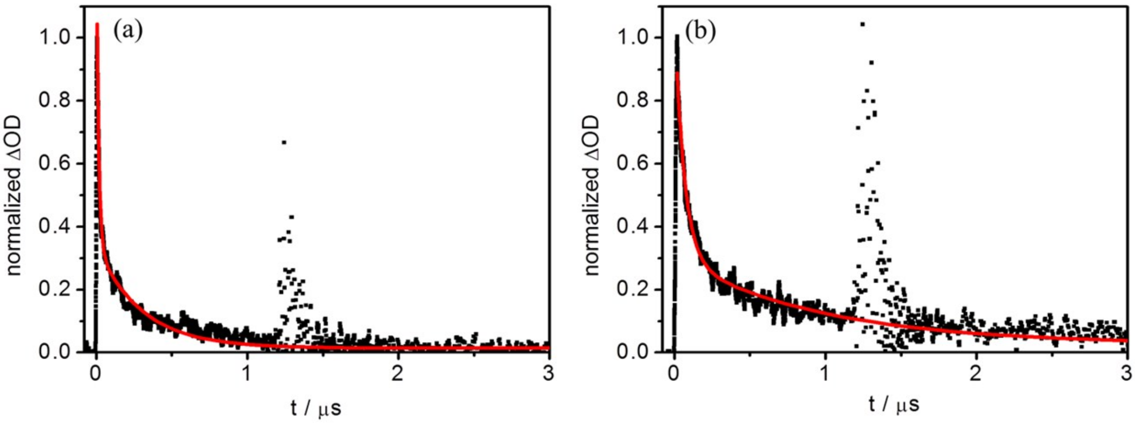

Figure S15. Normalized integrated kinetic trace at the spectral region between 540 and 750 nm of **exTTF-Ru-POM** collected upon excitation at 520 nm in (a) aerated and (b) deaerated DMSO.

Jablonski scheme for PTZ-Ru

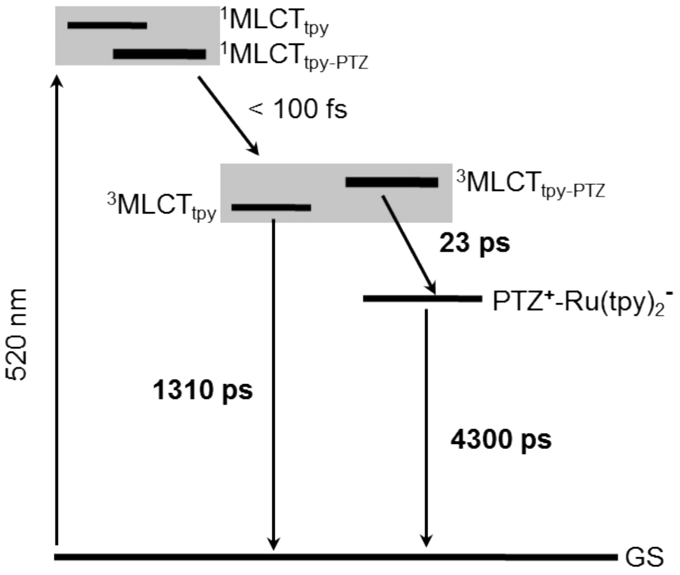

Scheme S2. Photoinduced relaxation processes for **PTZ-Ru**.

References

1 K. Barthelmes, M. Sittig, A. Winter, U. S. Schubert, *Eur. J. Inorg. Chem.* 2017, **2017**, 3698–3706.

2 K. Barthelmes, J. Kübel, A. Winter, M. Wächtler, C. Friebe, B. Dietzek, U. S. Schubert, *Inorg. Chem.* 2015, **54**, 3159–3171.

3 Y. Luo, M. Wächtler, K. Barthelmes, A. Winter, U. S. Schubert, B. Dietzek, *Chem. Commun.* 2018, DOI: 10.1039/c7cc09181h.

4 J. Kübel, R. Schroot, M. Wächtler, U. S. Schubert, B. Dietzek, M. Jäger, *J. Phys. Chem. C* 2015, **119**, 4742–4751.

5 B. Dietzek, T. Pascher, V. Sundström, A. Yartsev, *Laser Phys. Lett.* 2007, **4**, 38–43.

6 L. Zedler, J. Guthmuller, I. R. Moraes, S. Kupfer, S. Krieck, M. Schmitt, J. Popp, S. Rau, B. Dietzek, *Chem. Commun.* 2014, **50**, 5227–5229.

7 B. Matt, X. Xiang, A. L. Kaledin, N. Han, J. Moussa, H. Amouri, S. Alves, C. L. Hill, T. Lian, D. G. Musaev, G. Izzeta, A. Proust, *Chem. Sci.* 2013, **4**, 1737–1745.

8 D. Rehm, A. Weller, *Isr. J. Chem.* 1970, **8**, 259–271.

9 A. Weller, *Z. Phys. Chem.* 1982, **133**, 93–98.

10 S. S.C. Chu, D. V. D. Helm, *Acta Cryst.* 1974, **B30**, 2489–2490.

11 Y. Ren, S. Lee, J. A. Bertke, J. S. Moore, *Acta Crys. Sect. E* 20[15], **71**, 1475–1479.

12 E. C. Constable, C. E. Housecroft, E. A. Medlycott, M. Neuburger, F. Reinders, S. Reymann, S. *Inorg. Chem. Commun.* 2008, **11**, 805–808.

13 E. V. Radkov, R. H. Beer, *Inorg. Chim. Acta* 2000, **297**, 191–198.

14 Y. Luo, K. Barthelmes, M. Wächtler, A. Winter, U. S. Schubert, B. Dietzek, *Chem. Eur. J.* 2017, **23**, 4917–4922.

15 Y. Luo, K. Barthelmes, M. Wächtler, A. Winter, U. S. Schubert, B. Dietzek, *J. Phys. Chem. C* 2017, **121**, 9220–9229.

[P4] Increased Charge Separation Rates with Increasing Donor-Acceptor Distance in Molecular Triads: The Effect of Solvent Polarity

Reproduced with permission from: Y. Luo, K. Barthelmes, M. Wächtler, A. Winter, U. S. Schubert and B. Dietzek, “Increased Charge Separation Rates with Increasing Donor-Acceptor Distance in Molecular Triads: The Effect of Solvent Polarity”, *J. Phys. Chem. C*, **2017**, *121*, 9220−9229. Copyright © 2017, American Chemical Society.

THE JOURNAL OF
PHYSICAL CHEMISTRY C

Article

pubs.acs.org/JPCC

Downloaded via THURINGER UNIV LANDESBIBLIOTHEK on March 28, 2019 at 09:00:09 (UTC).
See https://pubs.acs.org/sharingguidelines for options on how to legitimately share published articles.

Increased Charge Separation Rates with Increasing Donor−Acceptor Distance in Molecular Triads: The Effect of Solvent Polarity

Yusen Luo,[†,‡] Kevin Barthelmes,[§,∥] Maria Wächtler,[‡] Andreas Winter,[§,∥] Ulrich S. Schubert,[§,∥] and Benjamin Dietzek*[,†,‡,∥]

[†]Institute of Physical Chemistry and Abbe Center of Photonics, Friedrich Schiller University Jena, Helmholtzweg 4, 07743 Jena, Germany

[‡]Leibniz Institute of Photonic Technology (IPHT), Albert-Einstein-Straβe 9, 07745 Jena, Germany

[§]Laboratory of Organic and Macromolecular Chemistry (IOMC), Friedrich Schiller University Jena, Humboldtstraβe 10, 07743 Jena, Germany

[∥]Jena Center for Soft Matter (JCSM), Friedrich Schiller University Jena, Philosophenweg 7, 07743 Jena, Germany

S *Supporting Information*

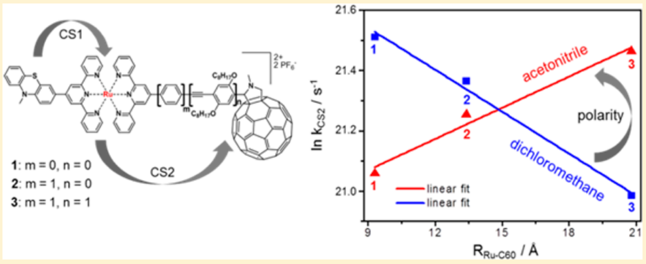

ABSTRACT: Distance-dependent electron transfer in donor−spacer−acceptor systems is accepted to occur via two distinct mechanisms, that is, by coherent superexchange or incoherent hopping. In general, the rate of electron transfer (k_{ET}) decreases with increasing donor−acceptor distances, irrespective of the actual mechanism being responsible for the process. However, recently Wenger and his group showed that in the frame of the superexchange mechanism electron-transfer rates can pass a maximum when increasing the transfer distance. This manuscript presents an investigation of the forward electron transfer in a series of donor (*N*-methylphenothiazine)−photocenter (Ru(II) bis(terpyridine) complex)−acceptor (*N*-methylfulleropyrrolidine) triads that reveals the control of the electron-transfer rates by solvent variation to an extent that in acetonitrile an increasing electron-transfer rate is observed with increasing donor−acceptor distance, while in dichloromethane an increase in the separation causes the electron transfer rate to drop. This behavior is qualitatively rationalized based on a recently introduced model. Nonetheless, the quantitative mismatch between the results presented here and the theory indicates that nonexponential distance-dependent couplings will have to be considered in extending the theory.

■ INTRODUCTION

Light-driven electron transfer represents a fundamental step in natural and artificial photosynthesis.[1,2] The resultant long-lived charge-separated states (CSS) are important for the production of solar electricity[3,4] and solar fuels.[5,6] Over the past decades many studies have focused on the electron-transfer processes taking place in molecular models, for example, for artificial photosynthetic systems, involving electron donors and electron acceptors which are connected by various spacers.[7−10] Through tuning the lengths of the spacers, distance-dependent electron-transfer dynamics have been extensively evaluated.[11−16] These studies manifested that electron transfer can occur via either coherent superexchange or incoherent hopping in the donor−spacer−acceptor systems; the specific transfer mode in action depends on the energy barriers between the donor and spacer states.[16−21] The superexchange mechanism requires the virtual spacer states to be higher in energy than the donor state. Hopping, on the contrary, takes place when the spacer states are energetically similar or lower than the donor states.[13,20] The two mechanisms show distinct distance dependences: In superexchange a drastic decrease in electron-transfer rates upon increasing donor−acceptor distance is observed, while an only weak distance dependence of the electron transfer rates is observed if the hopping mechanism is active.[17−26] The specific mechanism for intramolecular electron transfer generally can be inferred from the attenuation factor β in the McConnell's relation (eq 1),[17−32] which is established to be a quantitative tool to assess the capability of a spacer to transport electrons in donor−spacer−acceptor systems.[7−10,17−26] Here k_{ET} is the electron-transfer rate, k_0 represents the electron-transfer rate when the donor and acceptor are connected directly, and R_{DA} is the donor−acceptor distance. It should be pointed out that eq 1 is derived from the superexchange mechanism, and for the incoherent hopping the observed small β values are strictly phenomenological.[13] To get an efficient electron transfer over long distances, low β values are required.[22−26] In this respect, π-conjugated oligomers are frequently selected as spacers in molecular electron-transfer units owing to their relative weak distance-dependent electron-transfer properties (i.e., low β value) compared with saturated σ spacers.[9,17−21]

Received: March 17, 2017
Revised: April 6, 2017
Published: April 12, 2017

© 2017 American Chemical Society

Scheme 1. Schematic Representation of the Molecular Structures of (a) Reference Dyad and (b) Triads 1−3

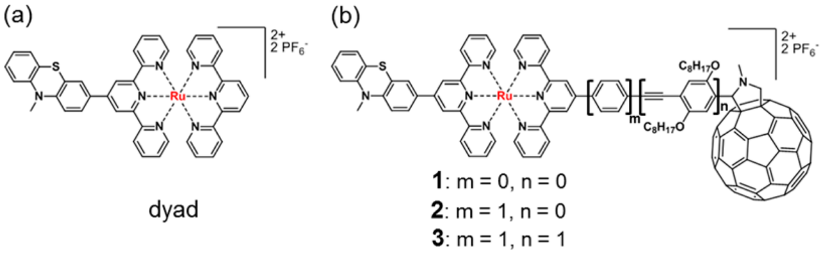

$$k_{\mathrm{ET}} = k_0 \cdot \mathrm{e}^{-\beta \cdot R_{\mathrm{DA}}} \qquad (1)$$

Apart from the nature of the spacers and the specific choice of donors and acceptors, the surrounding environment, for example, the solvent polarity, influences the electron-transfer properties and hence the β values. However, investigations of the solvent dependence of β values are still sparse;[33−37] for example, Otsubo and coworkers reported for porphyrin−oligothiophere−C_{60} systems the β value for charge-separation process to be pronouncedly solvent polarity-dependent (0.03 and 0.11 $Å^{-1}$ in solvent with higher and lower polarity, respectively).[33] Langa and coworkers reported the same trend for zinc porphyrin−oligo(thienylenevinylene)−C_{60} systems with β values for charge separation in different solvents (0.016 and 0.03 $Å^{-1}$ in solvent with higher and lower polarity, respectively).[34] Albinsson and coworkers observed nearly identical β values for charge separation in a range of solvents for a zinc porphyrin−oligo(*p*-phenyleneethynylene)−gold porphyrin system,[35] while Guldi obtained identical β values in two different solvents when studying the charge recombination process in tetrathiafulvalenes−oligo(*p*-phenylenevinylenes)−C_{60} systems.[36] Thus the studies available in literature do not show a universal trend. While some investigations indicated a lower β value in more polar solvents,[33,34] other authors observe solvent polarity-independent β values.[35−37]

This attracted our interest in studying the possible effects of solvent polarity on the forward and backward electron-transfer processes in a donor−spacer−acceptor system based on a recently reported molecular triad[38,39] (Scheme 1b, **1**) with donor−acceptor distances (center-to-center) ranging from 18.3 to 37.1 Å (see Scheme 1). The triads combine a *N*-methylphenothiazine (PTZ) electron donor, a Ru(II) bis(terpyridine) photocenter (P), and a *N*-methylfulleropyrrolidine (C_{60}) acceptor. Photoinduced electron transfer is mediated by π-conjugated spacers of various lengths. The photoinduced processes in the reference dyad and triad **1** have been reported previously,[38] so this contribution will focus on triads **2** and **3** and the resultant discussion of distance- and solvent polarity-dependent electron-transfer dynamics in the triad series **1**−**3**.

■ EXPERIMENTAL SECTION

The synthesis, electrochemical, and photophysical properties of the reference dyad and triads **1**−**3** have been reported previously.[39] Steady-state UV−vis absorption spectra (Figure S1) and emission spectra (Figure S2) collected in dichloromethane and acetonitrile are summarized for convenience. Steady-state UV−vis absorption spectra were recorded with a JASCO V-670 spectrophotometer in a quartz cell with 1 mm path length. Steady-state emission spectra were recorded with a JASCO FP-6200 spectrofluorometer in a 1 cm quartz cell. For all of the time-resolved experiments the stability of samples was ensured by recording the steady-state UV−vis absorption spectra before and after every measurement.

Spectroelectrochemistry. Spectroelectrochemistry (SEC) measurements were performed in a home-built three-electrode thin-layer cell with a path length of 1 mm (Bioanalytical System, USA).[40] The three-electrode setup consists of a transparent platinum mesh working electrode, a platinum wire counter electrode, and a Ag/AgCl reference electrode. Potentials were tuned using a PC-controlled potentiostat. All potentials given in the manuscript refer to ferrocene as standard. The corresponding UV−vis spectra were recorded on a double-beam Cary 5000 UV−vis spectrometer (Varian, USA) at room temperature. Both the oxidative and reductive SEC were reversible by obtaining the recovered initial sample absorption when a zero voltage cycle was applied to the working electrode.

Time-Resolved Spectroscopy. Femtosecond (fs) transient absorption spectra were collected by using a previously reported home-built pump−probe laser system that is based on an amplified Ti:sapphire oscillator (Libra, Coherent)[41] All compounds were excited by pump pulse centered at 520 nm (TOPASwhite, Lightconversion) with a duration of 110 fs. The power of the pump beam was kept at 0.3 mW before samples, and the beam diameter of the pump was 0.38 mm inside the sample volume. A white-light supercontinuum generated by focusing a fraction of the fundamental in a rotating CaF_2 plate is used to probe the samples in a wide spectral range (340 to 800 nm). The probe beam is delayed in time with respect to the pump beam by means of an optical delay line and the polarization between probe and pump is set at the magic angle (54.7°). Each solution (optical density ca. 0.2 at the excitation wavelength) was kept in a 1 mm quartz cuvette. Transient absorption data were displayed after chirp correction. The transient absorption data were analyzed by a global multi-exponential fit after exclusion of a temporal window of 200 fs around time zero to avoid contributions of the coherent-artifact region to the data analysis. Furthermore, a spectral band of 20 nm around the pump wavelength is omitted from the data analysis due to pump-scatter in this spectral range.

Nanosecond (ns) transient absorption spectra[42] were collected to study the long-lived species appearing in fs transient absorption data. The pump pulses centered at 520 nm were produced by a Continuum Surelite OPO Plus apparatus that is pumped by an Nd:YAG laser system (pulse duration 5 ns, repetition rate 10 Hz). The probe light is provided by a 75 W xenon arc lamp. Spherical concave mirrors are used to focus the probe beam into the samples and then send the beam to the monochromator (Acton, Princeton Instruments). The probe light is detected by a Hamamatsu R928 photomultiplier. The signal is amplified and processed by a commercially available detection system (Pascher Instruments AB). Each sample was freshly prepared, and the optical density (ca. 0.37) at the

DOI: 10.1021/acs.jpcc.7b02513
J. Phys. Chem. C 2017, 121, 9220−9229

Table 1. Center-to-Center Distances *R*, Electrochemical Data and Reaction Free-Energy Changes ($-\Delta G°$) for Charge Separation and Charge Recombination in Dichloromethane and Acetonitrile (in Brackets)

	center-to-center/Å[a]		$E°$/V (vs Fc^+/Fc)[b]			$-\Delta G°$/eV[c]			
	$R_{(PTZ\text{-}C60)}$	$R_{(Ru-C60)}$	PTZ^+/PTZ	C_{60}/C_{60}^-	tpy/tpy^-	CS1	CR1	CS2	CR2
dyad	9.6[d]		0.35		−1.60	0.29	1.78		
			(0.39)		(−1.57)	(0.15)	(1.92)		
1	18.3	9.3	0.34	−1.03	−1.67	0.23	1.84	0.56	1.28
			(0.40)	(−0.80)	(−1.54)	(0.17)	(1.90)	(0.72)	(1.18)
2	22.9	13.4	0.34	−1.11	−1.64	0.26	1.81	0.43	1.38
			(0.40)	(−0.86)	(−1.54)	(0.17)	(1.90)	(0.66)	(1.24)
3	30.1	20.8	0.35	−1.13	−1.65	0.24	1.83	0.40	1.43
			(0.39)	(−0.94)	(−1.52)	(0.20)	(1.87)	(0.55)	(1.32)

[a] Center-to-center distances, *R*, were obtained from the optimized molecular structures and taken from ref 39. [b] Redox potentials were taken from ref 39. [c] $\Delta G°_{CR} = e(E_{A/A^-} - E_{D^+/D}) + e^2/4\pi R\varepsilon_0\varepsilon_s$ is the driving force for charge recombination.[45] For the first and second charge recombination the radical pairs are $tpy^{\bullet-}/PTZ^{\bullet+}$ and $C_{60}{}^{\bullet-}/PTZ^{\bullet+}$, respectively. ε_0 is the vacuum permittivity (8.85×10^{-12} F/m) and ε_s is the dielectric constant of the solvent (8.93 for dichloromethane and 35.9 for acetonitrile).[44] $\Delta G°_{CS1} = -\Delta G°_{CR1} - E_{00}$ is the driving force for the first charge separation. E_{00} is the energy difference between the thermalized, lowest ^{3}MLCT excited state and ground state. Electron transfer in the shortest triad **1** occurs from an upper-lying ^{3}MLCT state.[38] As different ^{3}MLCT states are relatively close in energy, E_{00} is taken to be 2.07 eV, as estimated from the emission spectrum of $[Ru(tpy)_2]^{2+}$ at 77 K (in butyronitrile glass).[47,48] The driving force for the second charge separation is calculated by $\Delta G°_{CS2} = \Delta G°_{CR1} - \Delta G°_{CR2}$. [d] For the reference dyad it is the distance between PTZ and Ru-center.

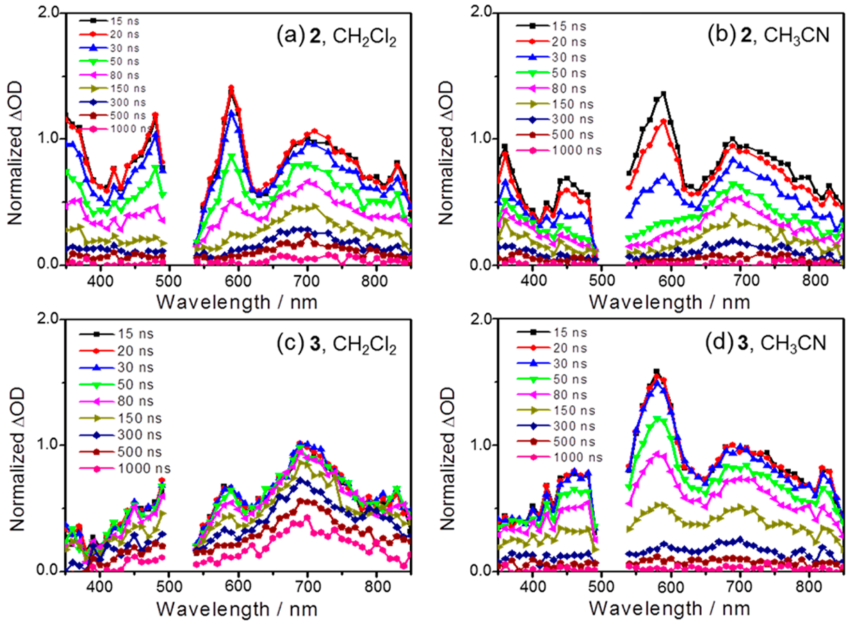

Figure 1. Nanosecond transient absorption spectra at selected times of **2** (a,b) and **3** (c,d) upon excitation at 520 nm in dichloromethane (CH_2Cl_2, panels a and c) and acetonitrile (CH_3CN, panels b and d). For comparison the ns TA spectra were normalized by the absorption maxima of $^3C_{60}*$ (at 700 nm at 15 ns).

excitation wavelengths 520 nm was kept the same. For all measurements, the power of the pump beam was kept at 0.35 mJ. All measurements were performed in 1 cm path length fluorescence cuvettes. A spectral band of 20 nm around the pump wavelength is omitted from the data analysis due to pump-scatter in this spectral range.

■ RESULTS AND DISCUSSION

Upon excitation of the ^{1}MLCT transition (λ_{ex} = 495 nm) the reference dyad shows very weak MLCT state emission, while all triads are found to be basically nonemissive (Figure S2); that is, no emission from the Ru-tpy photocenter is observed. In the following, ultrafast time-resolved spectroscopy will be employed to provide detailed information about the intramolecular electron-transfer mechanism.

Driving Forces for Charge Separation and Recombination. Before considering the actual time-resolved spectroscopic data, an estimation of the driving forces for the possible charge separation and recombination processes according to the model developed for **1**[38] can be made based on the redox potentials of $PTZ^{\bullet+}$/PTZ, tpy/$tpy^{\bullet-}$, and $C_{60}/C_{60}{}^{\bullet-}$ couples by using the Rehm−Weller equation, which is used for calculating the "Gibbs free energy change of photoinduced electron transfer".[43−46] The respective values of the center-to-center distances between donor and acceptor, the free energy changes related to charge separation ($-\Delta G°_{CS}$), and charge recombination ($-\Delta G°_{CR}$) are summarized in Table 1.

As discussed for **1**,[38] the $PTZ^{\bullet+}$ and $C_{60}{}^{\bullet-}$ radical ion pair formation involves two sequential electron-transfer steps with the intermediate state $PTZ^{\bullet+}$-$P^{\bullet-}$-C_{60} being spectroscopically visible

$$\begin{tikzcd}
\mathrm{PTZ{-}^{3}P^{*}{-}C_{60}} \arrow[r, "\mathrm{CS1}"] & \mathrm{PTZ^{\cdot+}{-}P^{\cdot-}{-}C_{60}} \arrow[rr, "\mathrm{CS2}"] \arrow[dr, "\mathrm{CR1}"'] & & \mathrm{PTZ^{\cdot+}{-}P{-}C_{60}^{\cdot-}} \arrow[dl, "\mathrm{CR2}"] \\
& & \mathrm{PTZ{-}P{-}C_{60}} &
\end{tikzcd} \tag{2}$$

For triads, the solvent polarity has little influence on the driving forces for the first charge separation reactions ($-\Delta G^{\circ}_{\mathrm{CS1}}$), that is, reductive quenching of the photoexcited photocenter by electron transfer from the PTZ donor (eq 2, CS1). However, the driving forces for the formation of PTZ$^{\bullet+}$-P-C$_{60}$$^{\bullet-}$, electron transfer from the reduced Ru-photocenter to C$_{60}$, are notably influenced by solvent polarity: In acetonitrile the driving force ($-\Delta G^{\circ}_{\mathrm{CS2}}$) for this process is estimated to be 0.2 eV higher (i.e., more negative) than that in dichloromethane. This implies that solvent-dependent electron-transfer rates might be observed for the formation of PTZ$^{\bullet+}$-P-C$_{60}$$^{\bullet-}$, while the kinetics describing the oxidation of PTZ are expected to be solvent polarity-independent. Additionally solvent polarity distinctly influences the recombination of PTZ$^{\bullet+}$-P-C$_{60}$$^{\bullet-}$, with the driving forces ($-\Delta G^{\circ}_{\mathrm{CR2}}$) being 0.1 eV lower in acetonitrile than in dichloromethane. Considering the molecular architectures of **1**−**3**, the driving forces for the formation ($-\Delta G^{\circ}_{\mathrm{CS2}}$) and recombination ($-\Delta G^{\circ}_{\mathrm{CR2}}$) of PTZ$^{\bullet+}$-P-C$_{60}$$^{\bullet-}$ change with the donor−acceptor distance.

Ultrafast Time-Resolved Spectroscopy. To study the impact of donor−acceptor distance and solvent polarity on the photoinduced electron-transfer processes in the series **1**−**3**, fs and ns transient absorption (TA) spectroscopy were performed in dichloromethane and acetonitrile. Thus the triads were excited at 520 nm in the red edge of the ^{1}MLCT band of the photocenter. The ns TA spectra of **2** and **3** (Figure 1) are quite similar and exhibit the same spectral characteristics as the previously reported triad **1** (Figure S4a),[38] that is, two distinct long-lived excited-state absorption bands centered at 590 and 700 nm. The latter band indicates the formation of ^{3}C$_{60}$*, while the former one is attributed to the absorption of the PTZ$^{\bullet+}$ radical cation. This assignment is based on the results of oxidative UV−vis spectroelectrochemistry (Figure S3a), which manifests the appearance of three new absorption bands at 365, 473, and 580 nm for the one-electron oxidized PTZ unity (PTZ$^{\bullet+}$).[38] We point out that the nonpronounced PTZ$^{\bullet+}$ absorption at 365 nm in the ns TA spectra of **2** and **3** is considered as the formation of PTZ$^{\bullet+}$-P-C$_{60}$$^{\bullet-}$ owing to the spectral overlap with the negative absorption of C$_{60}$$^{\bullet-}$ below 380 nm (Figure S3b), which has been discussed in detail for **1** in our previous work.[38] The very similar ns TA features observed for **1**−**3** indicates that identical excited-state electron-transfer pathways are active in these triads; that is, the relaxation pathway can be described (as shown in Scheme S1) as an electron-transfer (indicated by the PTZ$^{\bullet+}$ absorption at 590 nm) and an energy-transfer path (indicated by the formation of ^{3}C$_{60}$* absorption at 700 nm), as previously reported for **1**.[38]

Figure 1 reveals that the relative intensities of the two bands representing the products of electron and energy transfer, respectively, change with the donor−acceptor distance and solvent polarity. For example, in dichloromethane the transient absorption spectrum recorded at 15 ns (Figure 1a,c) shows a reduced relative intensity of the PTZ$^{\bullet+}$ absorption at 590 nm from 1.4 in **2** to 0.7 in **3** relative to the intensity of the absorption band of ^{3}C$_{60}$* at 700 nm. Upon changing the solvent from dichloromethane to acetonitrile (Figure 1c,d) the 590 nm absorption band of **3** increases significantly, indicating a more preferential population of PTZ$^{\bullet+}$-P-C$_{60}$$^{\bullet-}$. As far as the stability (lifetime) of PTZ$^{\bullet+}$-P-C$_{60}$$^{\bullet-}$ is concerned, dissolution of **3** in acetonitrile leads to a decrease in the lifetime of PTZ$^{\bullet+}$-P-C$_{60}$$^{\bullet-}$ compared with dichloromethane. For **2** the ns TA spectra reveal a drop of the band at 590 nm from 15 to 20 ns in acetonitrile (Figure 1b), while the spectra are quite stable during the same period in dichloromethane (Figure 1a). A direct comparison of the PTZ$^{\bullet+}$-P-C$_{60}$$^{\bullet-}$ lifetimes is facilitated by considering the integrated TA kinetics (integrated over the probe-range from 540 to 630 nm), which is characteristic for PTZ$^{\bullet+}$-P-C$_{60}$$^{\bullet-}$ (see Figure 2): PTZ$^{\bullet+}$-P-C$_{60}$$^{\bullet-}$ in **2** decays faster than that in **3**. This reflects a faster backward electron-transfer rate with shorter donor−acceptor distance. PTZ$^{\bullet+}$-P-C$_{60}$$^{\bullet-}$ in both **2** and **3** decays more rapidly in acetonitrile than in dichloromethane.

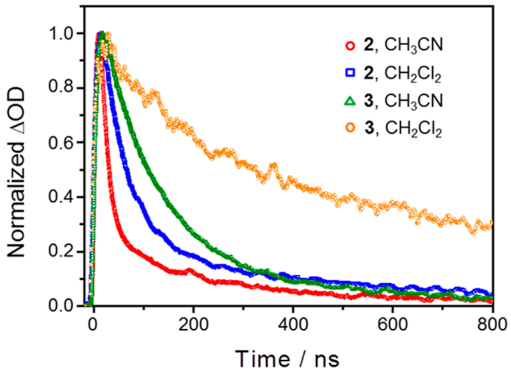

Figure 2. Normalized integrated kinetic traces at the spectral region of PTZ$^{\bullet+}$-P-C$_{60}$$^{\bullet-}$ (540 to 630 nm) of the ns TA data upon excitation at 520 nm of **2** and **3** in dichloromethane (CH$_2$Cl$_2$) and acetonitrile (CH$_3$CN).

Quantitative analysis of the temporal development (Figures S5 and S6 and Table 2) reveals that the PTZ$^{\bullet+}$ feature at 590 nm decays much faster than ^{3}C$_{60}$* (feature at 700 nm). Increasing the distance of donor−acceptor from **1** over **2** to **3**, the lifetime of PTZ$^{\bullet+}$-P-C$_{60}$$^{\bullet-}$ increases from 20 ns (18.3 Å in **1**),[38] 52 ns (22.9 Å in **2**), to 180 ns (30.1 Å in **3**) in dichloromethane (see Table 2). The data summarized in Table 2 reveal: (i) the charge recombination rate (k_{CR2}) decreases with increasing donor−acceptor distance in both solvents and (ii) charge recombination is faster in acetonitrile than in dichloromethane. Considering that the driving forces for charge recombination, that is, $-\Delta G^{\circ}_{\mathrm{CR2}}$ are always lower (i.e., less negative) in acetonitrile than in dichloromethane, it is concluded that charge recombination in **1**, **2**, and **3** occurs in the Marcus-inverted region;[43−46,49] (iii) The yield of PTZ$^{\bullet+}$-P-C$_{60}$$^{\bullet-}$ in **2** is the highest and is barely influenced by solvent polarity. For **3**, the yield of PTZ$^{\bullet+}$-P-C$_{60}$$^{\bullet-}$ increases by a factor of 3 in acetonitrile compared with dichloromethane.

On the basis of the data presented in Table 2, the attenuation factor β was calculated according to McConnell's relation (eq 1).[17−32] A logarithmic plot of the backward electron-transfer rates as a function of the PTZ-C$_{60}$ distance is shown in Figure 3. The logarithm of k_{CR2} decreases linearly with increasing donor−acceptor distance, yielding a phenomenological β_{CR2} = 0.18 and 0.19 Å^{-1} in dichloromethane and acetonitrile, respectively. The spacer in this triad system is very similar to the well-studied oligo(*p*-phenyleneethynylene) (OPE) structures, and the obtained β_{CR2} values are consistent with the literature results that report β to be in the range of 0.1 to 0.4 Å^{-1} for electron transfer, albeit with different donor and

DOI: 10.1021/acs.jpcc.7b02513
J. Phys. Chem. C 2017, 121, 9220−9229

Table 2. Global Fit Results of the ns TA Data of 1−3 in Dichloromethane (CH_2Cl_2) and Acetonitrile (CH_3CN)[a]

		τ_{CR2}/ns		k_{CR2}/s^{-1}		$I_{CSS}/I^3_{C_{60}}$ [b]	
	$R_{PTZ\text{-}C60}$/Å[c]	CH_2Cl_2	CH_3CN	CH_2Cl_2	CH_3CN	CH_2Cl_2	CH_3CN
1	18.3	20[d]	<10[e]	5.0×10^7	$>10 \times 10^7$	2.5	
2	22.9	52	19	1.9×10^7	5.3×10^7	3.1	3.3
3	30.1	180	94	0.6×10^7	1.1×10^7	0.6	2.1

[a] τ_{CR2} represents the time constants for charge recombination of $PTZ^{\bullet+}$-P-$C_{60}^{\bullet-}$ and k_{CR2} is the corresponding charge recombination rate. I_{CSS}/I^3_{C60*} is the comparison of absorption intensities of $PTZ^{\bullet+}$-P-$C_{60}^{\bullet-}$ and $^3C_{60}$*. [b] Calculated by comparing the absorption maxima of the component spectra which are characteristic for $PTZ^{\bullet+}$-P-$C_{60}^{\bullet-}$ (at 590 nm) and $^3C_{60}$* (at 700 nm) in global fit results (Figures S5 and S6). [c] Center-to-center distances, R.[39] [d] Lifetime of $PTZ^{\bullet+}$-P-$C_{60}^{\bullet-}$ in **1** in dichloromethane was taken from ref 38. [e] Because of the fast charge recombination of $PTZ^{\bullet+}$-P-$C_{60}^{\bullet-}$ in **1** in acetonitrile (Figure S4b), the real value cannot be obtained under the time resolution (~10 ns) of our setup.

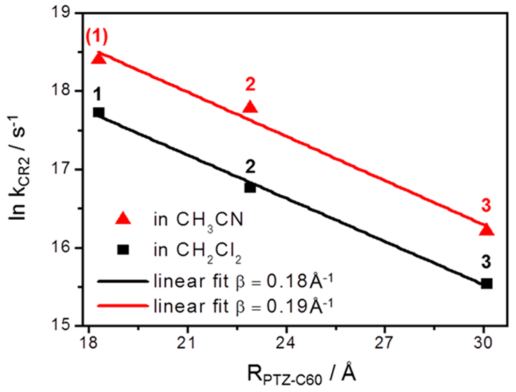

Figure 3. Distance dependence of the backward electron transfer ln(k_{CR2}) in **1**, **2**, and **3** in dichloromethane (CH_2Cl_2, black squares) and acetonitrile (CH_3CN, red triangles). Note: In acetonitrile, charge recombination in **1** is within the time resolution of the setup (~10 ns) and the value is an estimate.

acceptor combinations.[18,35,37,50−53] β_{CR2} is thus relatively insensitive to the solvent, and the absolute value (in either solvent) indicates that charge recombination in **1**−**3** takes place in the superexchange regime, for which β values of 0.2 to 0.3 $Å^{-1}$ have been identified before, while incoherent hopping is characterized by significant lower β values.[13,16]

The mechanistic details of forward electron transfer in the triads are revealed by fs TA spectroscopy (see Figures 4 and 5). The transient spectra of **2** and **3** show ground-state bleach around 500 nm and two regions of excited state absorption (ESA), that is, from 340 to 460 nm and from 530 to 735 nm. The spectra recorded at short delay times are typical for a ^{3}MLCT absorption of the $[Ru(tpy)_2]^{2+}$ center, that is, featuring a broad ESA above 550 nm with the maximum at ca. 600 nm.[42,54−56] The ESA band in the UV region is assigned to the absorption of $tpy^{\bullet-}$.[42,54−56] For **3** this band appears at 415 nm and hence is red-shifted compared with **2** (band at ca. 380 nm). This is due to the extended π−π conjugation at the 4′ position of the tpy ligand.[54−57] At long delay times the spectra of **2** match the respective ns TA data, with the $PTZ^{\bullet+}$ being visible at 473 and 590 nm and $^3C_{60}$* at 700 nm. For **3** the fs TA spectra (Figure 4b) are relatively unstructured at probe wavelengths larger than 530 nm at long delay times, while the corresponding ns TA data (Figure 1c) already indicate the final excited states in **3**, that is, $PTZ^{\bullet+}$-P-$C_{60}^{\bullet-}$ and $^3C_{60}$*.

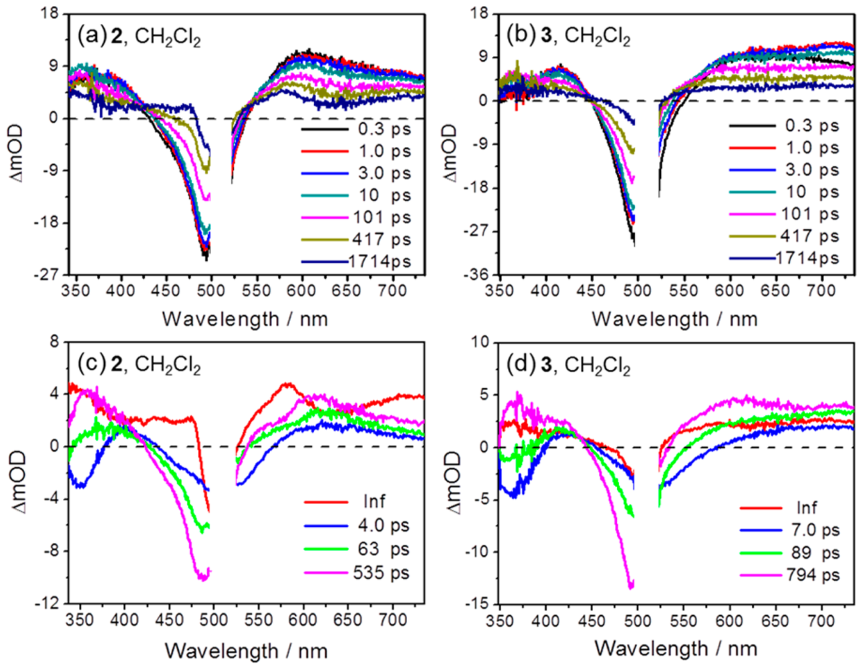

Figure 4. Transient absorption spectra (up) at selected delay times and decay-associated spectra (down) resulting from the global fit upon excitation at 520 nm in dichloromethane (CH_2Cl_2) for **2** (a,c) and **3** (b,d).

DOI: 10.1021/acs.jpcc.7b02513
J. Phys. Chem. C 2017, 121, 9220−9229

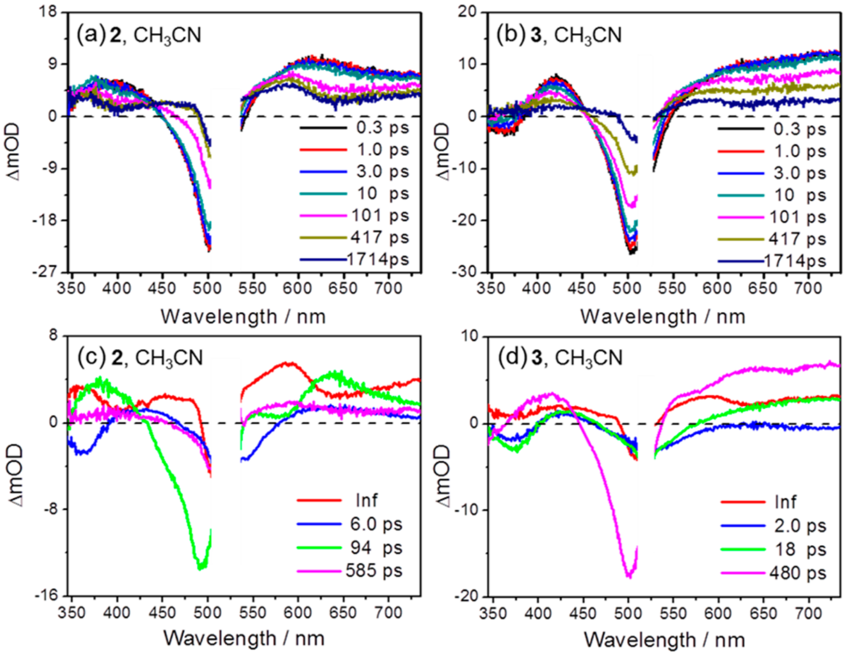

Figure 5. Transient absorption spectra (up) at selected delay times and decay-associated spectra (down) resulting from the global fit upon excitation at 520 nm in acetonitrile (CH_3CN) for **2** (a,c) and **3** (b,d).

Table 3. Summary of the Time Constants for the Second Charge Separation (τ_{CS2}) and Energy Transfer (τ_{EnT}) Processes in Triads in Dichloromethane (CH_2Cl_2) and Acetonitrile (CH_3CN)[a]

		τ_{CS2}/ps		k_{CS2}/s^{-1}		τ_{EnT}/ps		k_{EnT}/s^{-1}	
	R_{Ru-C60}/Å[b]	CH_2Cl_2	CH_3CN	CH_2Cl_2	CH_3CN	CH_2Cl_2	CH_3CN	CH_2Cl_2	CH_3CN
1	9.3	457	716	2.2×10^9	1.4×10^9	20	23	5.0×10^{10}	4.3×10^{10}
2	13.4	535	585	1.9×10^9	1.7×10^9	63	94	1.6×10^{10}	1.1×10^{10}
3	20.8	794	480	1.3×10^9	2.1×10^9	89	18	1.1×10^{10}	5.6×10^{10}

[a] k_{CS2} and k_{EnT} represent the electron-transfer and energy-transfer rates. [b] Center-to-center distances, *R*.[39]

The quantitative interpretation of the fs TA data[38,58,59] yields three kinetic components and a long-lived species for both **2** (Figure 4c) and **3** (Figure 4d). The interpretation of the kinetic components follows the previously reported study on **1** (Figure S8c) and the reference dyad (Figure S7c):[38] The long-lived species in decay-associated spectra (DAS, Figure 4c,d) reveal spectral features indicative of a mixture of PTZ$^{\bullet+}$-P-$C_{60}^{\bullet-}$ and $^3C_{60}$* states. The fastest component (τ_1 = 4 and 7 ps in dichloromethane for **2** and **3**, respectively) in DAS is assigned to the formation of the charge-transfer intermediate PTZ$^{\bullet+}$-P$^{\bullet-}$-C_{60} state, which describes an increase in positive signal amplitude at the position (i.e., at 365 nm) of the absorption of oxidized PTZ. τ_2 = 63 and 89 ps in dichloromethane for **2** (Figure 4c) and **3** (Figure 4d), respectively, is attributed to energy transfer from the excited Ru-photocenter to the C_{60} acceptor. This assignment is based on the similarity of the spectral characteristics observed in **1** (associated with τ_2 = 20 ps; Figure S8c), which reveals a spectral shape similar to the ESA of ^{3}MLCT state. We would like to clarify that the electron transfer (τ_1) and energy transfer (τ_2) occur from the differently distributed ^{3}MLCT states (instead of the lowest ^{3}MLCT state, see Scheme S1), which has been proven by excited-wavelength-dependent resonance Raman and nanosecond TA spectroscopy.[38] Hence the two decay pathways can have different time constants because they do not compete with each other kinetically. Finally, the third process (τ_3 = 535 and 794 ps in dichloromethane for triad **2** and **3**, respectively) is assigned to the formation of PTZ$^{\bullet+}$-P-$C_{60}^{\bullet-}$.

Changing the solvent from dichloromethane to acetonitrile (higher polarity, Figure 5) causes the absorption bands of **3** at 473 and 580 nm (the absorption of PTZ$^{\bullet+}$) to become more pronounced. This is also reflected in the ns TA data (Figure 1d). The results of the quantitative analysis of the photoinduced kinetics in both acetonitrile and dichloromethane are listed in Table 3, and the excited-state relaxation diagrams of **1**−**3** are graphically depicted in Scheme S1.

The rates for the first charge separation, that is, the formation of PTZ$^{\bullet+}$-P$^{\bullet-}$-C_{60}, in **1**−**3** are rather similar, which can be rationalized by invoking the fixed distance between the PTZ donor and the photoactive Ru center as well as the similar driving forces $-\Delta G°_{CS1}$ (see Table 1). However, the rates for the formation of PTZ$^{\bullet+}$-P-$C_{60}^{\bullet-}$ significantly depend on the donor−acceptor distance and the solvent polarity (see Table 3). The data show that k_{CS2} displays qualitatively different distance dependence in different solvents. In dichloromethane k_{CS2} decreases with increasing donor−acceptor distance, while in acetonitrile k_{CS2} increases by a factor of 1.5 from the shortest triad **1** to the longest triad **3**. This is graphically reflected in Figure 6, which depicts the logarithm of k_{CS2} versus the Ru−C_{60} distance, R_{Ru-C60}. This behavior leads to a positive slope (+0.034 Å^{-1}) in acetonitrile and a negative slope (−0.046 Å^{-1}) in dichloromethane (Figure 6). If we refer to the McConnell's relation (eq 1) a phenomenological negative β (−0.034 Å^{-1}) in

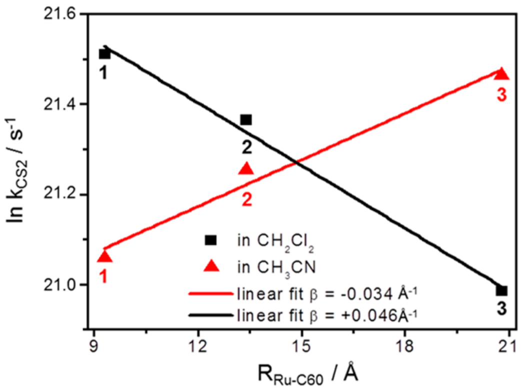

Figure 6. Distance dependence of the second electron transfer $\ln(k_{CS2})$ in **1**, **2**, and **3** in dichloromethane (CH_2Cl_2, black squares) and acetonitrile (CH_3CN, red triangles).

acetonitrile and positive β (+0.046 Å^{-1}) in dichloromethane are obtained. Thus, to the best of our knowledge, this study presents the first report revealing that the distance dependences of electron-transfer rates (thus the sign of the phenomenological β values) can be switched by varying the solvents. The absolute values of the phenomenological β for the forward electron transfer are rather low compared with other β values reported for OPE spacers (0.1 to 0.4 Å^{-1}).[18,35,37,50−53]

To rationalize this finding of changing the sign of the phenomenological β value by changing the solvent, one might resort to eq 3, which relates β to the spacer length, r_0, the energy gap between donor states and the spacer subunits, Δ, and the electronic coupling between different subunits of the spacer, ν[13,17−21,25,50,60,61]

$$\beta = \frac{2}{r_0}\ln\left|\frac{\Delta}{\nu}\right| \qquad (3)$$

Many studies indicated that changing Δ notably impacts the electron-transfer rates and, hence, the β values obtained for the same spacer.[18−20,50,62,63] Because both donor and spacer states, in principle, are solvent-dependent one might argue that slight changes in Δ could lead to a change in the sign of $\ln\left|\frac{\Delta}{\nu}\right|$ if the magnitude of Δ was close to the magnitude of ν. However, Albinsson and coworkers specified $\Delta/\nu \gg 1$ for OPE-based spacers.[63] Albeit the fact that Δ/ν is a function of both the donor and the spacer, a quantitative comparison between the electrochemical properties of the triads reported here and the donor groups reported by Albinsson[63] makes it highly unlikely that the change in sign of the β values reported here can be explained based on eq 3. Another possibility is that eq 3 is not valid anymore because for our triad system the spacer cannot be treated as identical spacer subunits according to the superexchange model. Furthermore, Albinsson suggested a *local β value* based on a modified tunneling theory that regards the spacers as a single tunneling barrier of width and height to account for untypical, nonexponential distance dependence of donor−acceptor electronic coupling. This model indicates that if the variation of the energy of the spacer states with distance is large then the *local β value* is negative, which can explain the unusual nonexponential increased donor−acceptor electronic coupling with increasing distance.[63] Deviating from the generally expected trend, that is, decreasing electron-transfer rates with increasing donor−acceptor distances (irrespective of the actual transfer mechanism[11−16,28,46,64−66]), theory has predicated a regime in which the electron-transfer rates increase with increasing donor−acceptor distances.[67] Experimentally such a regime has been observed when studying the distance dependence of photoinduced electron transfer in a given solvent. For example, Wasielewski and coworkers reported on a donor−spacer−acceptor (PTZ-B$_n$-PDI) system for which a significant decrease in charge recombination rate was observed from PTZ-B$_1$-PDI to PTZ-B$_3$-PDI (β = 0.67 Å^{-1}); then, upon further elongation of the bridge, a slight increase in rate was observed from PTZ-B$_3$-PDI to PTZ-B$_5$-PDI. This result was explained based on the interplay between a reduced energy gap (eq 3) and a decreasing internal reorganization energy.[68] Very recently, in an related approach, the Wenger group attributed this unusual distance dependence of the backward electron transfer rates to the interplay between reorganization energy and electronic coupling based on the Marcus theory (eq 4) and a superexchange model (eq 5).[69−71] The authors presented extended numerical simulations invoking the distance dependencies of the reorganization energy (λ), the donor−acceptor electronic coupling (H_{DA}), and the driving forces ($-\Delta G_{ET}°$) to illustrate the complex distance dependency of the electron-transfer rates.[71]

$$k_{ET} = \sqrt{\frac{\pi}{\hbar^2\cdot\lambda\cdot k_B\cdot T}}\cdot H_{DA}{}^2\cdot\exp\left(-\frac{(\lambda + \Delta G^0_{ET})^2}{4\cdot\lambda\cdot k_B\cdot T}\right) \qquad (4)$$

$$H_{DA} = H_0\cdot\exp\left(-\frac{\beta}{2}\cdot R_{DA}\right) \qquad (5)$$

$$\lambda = \lambda_i + \lambda_o \qquad (6)$$

$$\lambda_o = \frac{e^2}{4\cdot\pi\cdot\varepsilon_0}\cdot\left(\frac{1}{2a_1} + \frac{1}{2a_2} - \frac{1}{R_{DA}}\right)\cdot\left(\frac{1}{\eta^2} - \frac{1}{\varepsilon_s}\right) \qquad (7)$$

On the basis of the theory provided by Wenger,[71] the distance dependence of k_{ET} as a function of different parameters (i.e., the attenuation factor β, the driving force, the reorganization energy, and solvent polarity) in our system were simulated. Figure 7 is one example that qualitatively describes the different distance dependences of k_{ET} in two solvents and shows that in certain donor−acceptor distance (R_{DA}) regions k_{ET} increases/decreases with increasing R_{DA} in acetonitrile/dichloromethane, which would result in different slopes with opposite sign, and thus the opposite sign of β values determined according to the McConnell's relation would be obtained. However, during the simulations only positive β values were employed according to the model.[71] This indicates that the frequently used relation (eq 1) might be questioned in some cases because the relation (eq 1) is simplified and derived from the assumption ($k_{ET} \propto H^2_{DA}$) assuming that the distance dependences of the reorganization energy and driving force are weak,[71] but according to the estimated reorganization energy (Table S1) and driving forces (Table 1) for the second charge-separation process the effects of donor−acceptor distances cannot be ignored, which means that eq 1 is oversimplified for our system. Hence, the simulation combined with the Marcus theory (eq 4) and superexchange model (eq 5)[71] qualitatively reproduce our observation and indicate the presence of a range of donor−acceptor distances for which a variation of the solvent will experimentally yield the slopes of opposite sign. However, the simulation cannot quantitatively describe our experimental results within a reasonable breadth of parameters (see Figure 7 and Figure S9). Thus it seems that the widely

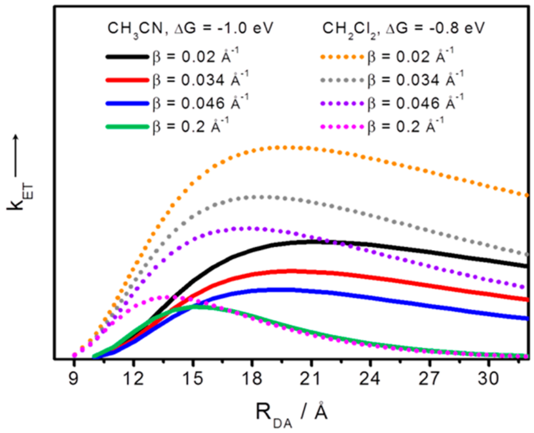

Figure 7. Distance dependences of k_{ET} resulting from the Marcus theory and superexchange model. The parameters used for simulation are as follows: (i) the outer reorganization energy λ_o was estimated by eq 7: CH_3CN, $\eta = 1.3416$,[72] $\varepsilon_s = 35.9$[44] and CH_2Cl_2, $\eta = 1.4212$,[72] $\varepsilon_s = 8.93$.[44] $a_1 = 9.6$ Å and $a_2 = 4.5$ Å: The second electron-transfer process occurs from an intermediate state $PTZ^{\bullet+}$-$P^{\bullet-}$-C_{60}, the electron density is thought to be delocalized over the conjugated PTZ and Ru complex unities, and thus the radius of the donor (a_1) was estimated to be 9.6 Å according to the optical molecular structure.[39] The inner reorganization energy $\lambda_i = 0.1$ eV.[71] (ii) $H_0 = 100\ \mathrm{cm}^{-1}$ is taken from ref 71 and the variations of β values are shown in Figure 7. (iii) Driving forces $\Delta G°_{ET}$, CH_3CN, $\Delta G°_{ET} = -1.0$ eV and CH_2Cl_2, $\Delta G°_{ET} = -0.8$ eV. The values of the driving forces $\Delta G°_{ET}$ are based on the fact that the absolute values of $\Delta G°_{ET}$ in dichloromethane are ~80% that in acetonitrile according to Table 1 (i.e., $-\Delta G°_{CS2}$). It should be pointed out that in practice $\Delta G°_{ET}$ is also distance-dependent, but in this simulation we assumed $\Delta G°_{ET}$ is constant in a certain solvent.[71]

used superexchange model (eqs 1, 3, and 5) cannot be used to quantitatively account for the experimental data discussed here. This indicates that the model seminally put forward by Wenger needs to be extended to account for nonexponential distance-dependent couplings, an approach that was introduced by Albinsson[63] to account for electron-transfer rates in a tunneling model without explicit consideration of the solvent polarity.

CONCLUSIONS

The photoinduced ultrafast electron transfer (forward and backward) in a series of molecular triads has been studied by ultrafast time-resolved spectroscopy. It is found that the phenomenological β, which is frequently utilized to describe the exponential change of electron-transfer rates (k_{ET}) with spacer elongation, (i) varies for the different electron (forward- or back-) transfer steps and (ii) can be tuned by solvent polarity in a previously unreported manner; that is, a negative β value was obtained in acetonitrile, while β was positive in dichloromethane. The numerical simulation based on the Marcus theory and the superexchange model theoretically qualitatively accounts for the different distance dependences of k_{ET} observed in this study. However, the theories currently discussed in the literature seem to fail to quantitatively account for the data, indicating that a model extension, for example, toward including nonexponential distance dependencies of the coupling or alternative parametrization of the reorganization energies, will have to be considered in the future.

ASSOCIATED CONTENT

Supporting Information

The Supporting Information is available free of charge on the ACS Publications website at DOI: 10.1021/acs.jpcc.7b02513.

> UV−vis absorption spectra, emission spectra, UV−vis-spectroelectrochemistry (SEC) absorption difference spectra, nanosecond (ns) transient absorption (TA) spectra of **1**, global fit results of the ns TA data, femtosecond (fs) TA spectra of reference dyad, fs TA spectra of **1**, relaxation diagrams, numerical simulations of the distance-dependent electron transfer rates and estimation of the reorganization energy. (PDF)

AUTHOR INFORMATION

Corresponding Author

*E-mail: benjamin.dietzek@leibniz-ipht.de.

ORCID

Ulrich S. Schubert: 0000-0003-4978-4670

Benjamin Dietzek: 0000-0002-2842-3537

Notes

The authors declare no competing financial interest.

ACKNOWLEDGMENTS

This research is funded by the Deutsche Forschungsgemeinschaft (DFG, Grant Nos. SCHU1229-16/1 and DI1517-3/1) and the China Scholarship Council (CSC, Y.L.).

REFERENCES

(1) Kärkäs, M. D.; Verho, O.; Johnston, E. V.; Åkermark, B. Artificial Photosynthesis: Molecular Systems for Catalytic Water Oxidation. *Chem. Rev.* **2014**, *114*, 11863−12001.

(2) Rudolf, M.; Kirner, S. V.; Guldi, D. M. A Multicomponent Molecular Approach to Artificial Photosynthesis − The Role of Fullerenes and Endohedral Metallofullerenes. *Chem. Soc. Rev.* **2016**, *45*, 612−630.

(3) Wasielewski, M. R. Self-Assembly Strategies for Integrating Light Harvesting and Charge Separation in Artificial Photosynthetic Systems. *Acc. Chem. Res.* **2009**, *42*, 1910−1921.

(4) Clarke, T. M.; Durrant, J. R. Charge Photogeneration in Organic Solar Cells. *Chem. Rev.* **2010**, *110*, 6736−6767.

(5) Poddutoori, P.; Co, D. T.; Samuel, A. P. S.; Kim, C. H.; Vagnini, M. T.; Wasielewski, M. R. Photoinitiated Multistep Charge Separation in Ferrocene−Zinc porphyrin−Diiron Hydrogenase Model Complex Triads. *Energy Environ. Sci.* **2011**, *4*, 2441−2450.

(6) Yuhas, B. D.; Smeigh, A. L.; Samuel, A. P. S.; Shim, Y.; Bag, S.; Douvalis, A. P.; Wasielewski, M. R.; Kanatzidis, M. G. Biomimetic Multifunctional Porous Chalcogels as Solar Fuel Catalysts. *J. Am. Chem. Soc.* **2011**, *133*, 7252−7255.

(7) Ricks, A. B.; Solomon, G. C.; Colvin, M. T.; Scott, A. M.; Chen, K.; Ratner, M. A.; Wasielewski, M. R. Controlling Electron Transfer in Donor-Bridge-Acceptor Molecules Using Cross-Conjugated Bridges. *J. Am. Chem. Soc.* **2010**, *132*, 15427−15434.

(8) Wenger, O. S. How Donor-Bridge-Acceptor Energetics Influence Electron Tunneling Dynamics and Their Distance Dependences. *Acc. Chem. Res.* **2011**, *44*, 25−35.

(9) Gilbert, M.; Albinsson, B. Photoinduced Charge and Energy Transfer in Molecular Wires. *Chem. Soc. Rev.* **2015**, *44*, 845−862.

(10) Gorczak, N.; Renaud, N.; Galan, E.; Eelkema, R.; Siebbeles, L. D. A.; Grozema, F. C. Computational Design of Donor-Bridge-Acceptor Systems Exhibiting Pronounced Quantum Interference Effects. *Phys. Chem. Chem. Phys.* **2016**, *18*, 6773−6779.

(11) Wolfrum, S.; Pinzón, J. R.; Molina-Ontoria, A.; Gouloumis, A.; Martín, N.; Echegoyen, L.; Guldi, D. M. Utilization of Sc3N@C80 in

Long-Range Charge Transfer Reactions. *Chem. Commun.* **2011**, *47*, 2270−2272.

(12) Lloveras, V.; Vidal-Gancedo, J.; Figueira-Duarte, T. M. F.; Nierengarten, J.-F.; Novoa, J. J.; Mota, F.; Ventosa, N.; Rovira, C.; Veciana, J. Tunneling versus Hopping in Mixed-Valence Oligo-p-Phenylenevinylene Polychlorinated Bis(triphenylmethyl) Radical Anions. *J. Am. Chem. Soc.* **2011**, *133*, 5818−5833.

(13) Ricks, A. B.; Brown, K. E.; Wenninger, M.; Karlen, S. D.; Berlin, Y. A.; Co, D. T.; Wasielewski, M. R. Exponential Distance Dependence of Photoinitiated Stepwise Electron Transfer in Donor−Bridge−Acceptor Molecules: Implications for Wirelike Behavior. *J. Am. Chem. Soc.* **2012**, *134*, 4581−4588.

(14) Kuss-Petermann, M.; Wolf, H.; Stalke, D.; Wenger, O. S. Influence of Donor-Acceptor Distance Variation on Photoinduced Electron and Proton Transfer in Rhenium(I)-Phenol Dyads. *J. Am. Chem. Soc.* **2012**, *134*, 12844−12854.

(15) Winkler, J. R.; Gray, H. B. Long-Range Electron Tunnelling. *J. Am. Chem. Soc.* **2014**, *136*, 2930−2939.

(16) Gilbert Gatty, M.; Kahnt, A.; Esdaile, L. J.; Hutin, M.; Anderson, H. L.; Albinsson, B. Hopping versus Tunneling Mechanism for Long-Range Electron Transfer in Porphyrin Oligomer Bridged Donor-Acceptor Systems. *J. Phys. Chem. B* **2015**, *119*, 7598−7611.

(17) Walther, M. E.; Wenger, O. S. Hole Tunneling and Hopping in a $Ru(bpy)_3^{(2+)}$-Phenothiazine Dyad with a Bridge Derived from Oligo-p-Phenylene. *Inorg. Chem.* **2011**, *50*, 10901−10907.

(18) Albinsson, B.; Eng, M. P.; Pettersson, K.; Winters, M. U. Electron and Energy Transfer in Donor-Acceptor Systems with Conjugated Molecular Bridges. *Phys. Chem. Chem. Phys.* **2007**, *9*, 5847−5864.

(19) Wenger, O. S. Photoinduced Electron and Energy Transfer in Phenylene Oligomers. *Chem. Soc. Rev.* **2011**, *40*, 3538−3550.

(20) Natali, M.; Campagna, S.; Scandola, F. Photoinduced Electron Transfer across Molecular Bridges: Electron- and Hole-Transfer Superexchange Pathways. *Chem. Soc. Rev.* **2014**, *43*, 4005−4018.

(21) Li, G.; Govind, N.; Ratner, M. A.; Cramer, C. J.; Gagliardi, L. Influence of Coherent Tunneling and Incoherent Hopping on the Charge Transfer Mechanism in Linear Donor-Bridge-Acceptor Systems. *J. Phys. Chem. Lett.* **2015**, *6*, 4889−4897.

(22) Atienza-Castellanos, C.; Wielopolski, M.; Guldi, D. M.; van der Pol, C.; Bryce, M. R.; Filippone, S.; Martín, N. Determination of the Attenuation Factor in Fluorene-Based Molecular Wires. *Chem. Commun.* **2007**, *48*, 5164−5166.

(23) Albinsson, B.; Mårtensson, J. Long-Range Electron and Excitation Energy Transfer in Donor-Bridge-Acceptor Systems. *J. Photochem. Photobiol., C* **2008**, *9*, 138−155.

(24) Brunetti, F. G.; López, J. L.; Atienza, C.; Martín, N. pi-Extended TTF: A Versatile Molecule for Organic Electronics. *J. Mater. Chem.* **2012**, *22*, 4188−4205.

(25) Kirk, M. L.; Shultz, D. A.; Stasiw, D. E.; Lewis, G. F.; Wang, G.; Brannen, C. L.; Sommer, R. D.; Boyle, P. D. Superexchange Contributions to Distance Dependence of Electron Transfer/Transport: Exchange and Electronic Coupling in Oligo(para-phenylene)- and Oligo(2,5-thiophene)-Bridged Donor-Bridge-Acceptor Biradical Complexes. *J. Am. Chem. Soc.* **2013**, *135*, 17144−17154.

(26) Vela, S.; Bauroth, S.; Atienza, C.; Molina-Ontoria, A.; Guldi, D. M.; Martín, N. Determining the Attenuation Factor in Molecular Wires Featuring Covalent and Noncovalent Tectons. *Angew. Chem., Int. Ed.* **2016**, *55*, 15076−15080.

(27) Meier, H. High Electrical Conductance of Single Molecules: A Challenge in the Series of Conjugated Oligomers. *Angew. Chem., Int. Ed.* **2009**, *48*, 3911−3913.

(28) Wielopolski, M.; de Miguel Rojas, G.; van der Pol, C.; Brinkhaus, L.; Katsukis, G.; Bryce, M. R.; Clark, T.; Guldi, D. M. Control Over Charge Transfer through Molecular Wires by Temperature and Chemical Structure Modifications. *ACS Nano* **2010**, *4*, 6449−6462.

(29) Arrigo, A.; Santoro, A.; Indelli, M. T.; Natali, M.; Scandola, F.; Campagna, S. On the Effect of the Nature of the Bridge on Oxidative or Reductive Photoinduced Electron Transfer in Donor-Bridge-Acceptor Systems. *Phys. Chem. Chem. Phys.* **2014**, *16*, 818−826.

(30) Proppe, J.; Herrmann, C. Communication through Molecular Bridges: Different Bridge Orbital Trends Result in Common Property Trends. *J. Comput. Chem.* **2015**, *36*, 201−209.

(31) McConnell, H. M. Intramolecular Charge Transfer in Aromatic Free Radicals. *J. Chem. Phys.* **1961**, *35*, 508−515.

(32) Jortner, J.; Bixon, M.; Langenbacher, T.; Michel-Beyerle, M. E. Charge Transfer and Transport in DNA. *Proc. Natl. Acad. Sci. U. S. A.* **1998**, *95*, 12759−12765.

(33) Nakamura, T.; Fujitsuka, M.; Araki, Y.; Ito, O.; Ikemoto, J.; Takimiya, K.; Aso, Y.; Otsubo, T. Photoinduced Electron Transfer in Porphyrin-Oligothiophene-Fullerene Linked Triads by Excitation of a Porphyrin Moiety. *J. Phys. Chem. B* **2004**, *108*, 10700−10710.

(34) Oswald, F.; Shafiqul Islam, D.-M.; El-Khouly, M. E.; Araki, Y.; Caballero, R.; de la Cruz, P.; Ito, O.; Langa, F. Photoinduced Electron Transfer of Zinc Porphyrin−Oligo(thienylenevinylene)−Fullerene[60] Triads; Thienylenevinylenes as Efficient Molecular Wires. *Phys. Chem. Chem. Phys.* **2014**, *16*, 2443−2451.

(35) Pettersson, K.; Wiberg, J.; Ljungdahl, T.; Mårtensson, J.; Albinsson, B. Interplay between Barrier Width and Height in Electron Tunneling: Photoinduced Electron Transfer in Porphyrin-Based Donor-Bridge-Acceptor Systems. *J. Phys. Chem. A* **2006**, *110*, 319−326.

(36) Giacalone, F.; Segura, J. L.; Martín, N.; Guldi, D. M. Exceptionally Small Attenuation Factors in Molecular Wires. *J. Am. Chem. Soc.* **2004**, *126*, 5340−5341.

(37) Linton, K. E.; Fox, M. A.; Pålsson, L.-O.; Bryce, M. R. Oligo(p-phenyleneethynylene) (OPE) Molecular Wires: Synthesis and Length Dependence of Photoinduced Charge Transfer in OPEs with Triarylamine and Diaryloxadiazole End Groups. *Chem. - Eur. J.* **2015**, *21*, 3997−4007.

(38) Luo, Y.; Barthelmes, K.; Wächtler, M.; Winter, A.; Schubert, U. S.; Dietzek, B. Energy vs. Electron Transfer − Controlling the Excitation Transfer in Molecular Triads. *Chem. - Eur. J.* **2017**, *23*, 4917−4922.

(39) Barthelmes, K.; Winter, A.; Schubert, U. S. Dyads and Triads Based on Phenothiazine, Bis(terpyridine)ruthenium(II) Complexes, and Fullerene. *Eur. J. Inorg. Chem.* **2016**, *2016*, 5132−5142.

(40) Zedler, L.; Guthmuller, J.; Rabelo de Moraes, I.; Krieck, S.; Schmitt, M.; Popp, J.; Dietzek, B. Redox State Sensitive Spectroscopy of the Model Compound $[(H\text{-dcbpy})_2Ru^{II}(NCS)_2]^{2-}$ (dcbpy = 2,2′-Bipyridine-4,4 ′-dicarboxylato). *J. Phys. Chem. C* **2013**, *117*, 6669−6677.

(41) Kübel, J.; Schroot, R.; Wächtler, M.; Schubert, U. S.; Dietzek, B.; Jäger, M. Photoredox-Active Dyads Based on a Ru(II) Photosensitizer Equipped with Electron Donor or Acceptor Polymer Chains: A Spectroscopic Study of Light-Induced Processes Toward Efficient Charge Separation. *J. Phys. Chem. C* **2015**, *119*, 4742−4751.

(42) Barthelmes, K.; Kübel, J.; Winter, A.; Wächtler, M.; Friebe, C.; Dietzek, B.; Schubert, U. S. New Ruthenium Bis(terpyridine) Methanofullerene and Pyrrolidinofullerene Complexes: Synthesis and Electrochemical and Photophysical Properties. *Inorg. Chem.* **2015**, *54*, 3159−3171.

(43) Göransson, E.; Boixel, J.; Fortage, J.; Jacquemin, D.; Becker, H.-C.; Blart, E.; Hammarström, L.; Odobel, F. Long-Range Electron Transfer in Zinc-Phthalocyanine-Oligo(phenylene-ethynylene)-Based Donor-Bridge-Acceptor Dyads. *Inorg. Chem.* **2012**, *51*, 11500−11512.

(44) Hankache, J.; Wenger, O. S. Photoinduced Electron Transfer in Covalent Ruthenium-Anthraquinone Dyads: Relative Importance of Driving-Force, Solvent Polarity, and Donor-Bridge Energy Gap. *Phys. Chem. Chem. Phys.* **2012**, *14*, 2685−2692.

(45) Lee, S.-H.; Chan, C. T.-L.; Wong, K. M.-C.; Lam, W. H.; Kwok, W.-M.; Yam, V. W.-W. Design and Synthesis of Bipyridine Platinum(II) Bisalkynyl Fullerene Donor-Chromophore-Acceptor Triads with Ultrafast Charge Separation. *J. Am. Chem. Soc.* **2014**, *136*, 10041−10052.

(46) Sukegawa, J.; Schubert, C.; Zhu, X. Z.; Tsuji, H.; Guldi, D. M.; Nakamura, E. Electron Transfer through Rigid Organic Molecular

DOI: 10.1021/acs.jpcc.7b02513
J. Phys. Chem. C 2017, 121, 9220−9229

Wires Enhanced by Electronic and Electron-Vibration Coupling. *Nat. Chem.* **2014**, *6*, 899−905.

(47) Sauvage, J.-P.; Collin, J.-P.; Chambron, J.-C.; Guillerez, S.; Coudret, C.; Balzani, V.; Barigelletti, F.; De Cola, L. D.; Flamigni, L. Ruthenium(II) and Osmium(II) Bis(terpyridine) Complexes in Covalently−Linked Multicomponent Systems: Synthesis, Electrochemical Behavior, Absorption Spectra, and Photochemical and Photophysical Properties. *Chem. Rev.* **1994**, *94*, 993−1019.

(48) Amini, A.; Harriman, A.; Mayeux, A. The Triplet Excited State of Ruthenium(II) Bis(2,2:6′,2″-terpyridine): Comparison between Experiment and Theory. *Phys. Chem. Chem. Phys.* **2004**, *6*, 1157−1164.

(49) Marcus, R. A.; Sutin, N. Electron Transfers in Chemistry and Biology. *Biochim. Biophys. Acta, Rev. Bioenerg.* **1985**, *811*, 265−322.

(50) Wiberg, J.; Guo, L.; Pettersson, K.; Nilsson, D.; Ljungdahl, T.; Mårtensson, J.; Albinsson, B. Charge Recombination versus Charge Separation in Donor-Bridge-Acceptor Systems. *J. Am. Chem. Soc.* **2007**, *129*, 155−163.

(51) Atienza, C.; Martín, N.; Wielopolski, M.; Haworth, N.; Clark, T.; Guldi, D. M. Tuning Electron Transfer through p-Phenyleneethynylene Molecular Wires. *Chem. Commun.* **2006**, *30*, 3202−3204.

(52) Lembo, A.; Tagliatesta, P.; Guldi, D. M.; Wielopolski, M.; Nuccetelli, M. Porphyrin-beta-Oligo-Ethynylenephenylene-[60]-Fullerene Triads: Synthesis and Electrochemical and Photophysical Characterization of the New Porphyrin-Oligo-PPE-[60]Fullerene Systems. *J. Phys. Chem. A* **2009**, *113*, 1779−1793.

(53) Scott, A. M.; Butler Ricks, A.; Colvin, M. T.; Wasielewski, M. R. Comparing Spin-Selective Charge Transport through Donor-Bridge-Acceptor Molecules with Different Oligomeric Aromatic Bridges. *Angew. Chem., Int. Ed.* **2010**, *49*, 2904−2908.

(54) Hewitt, J. T.; Vallett, P. J.; Damrauer, N. H. Dynamics of the ^{3}MLCT in Ru(II) Terpyridyl Complexes Probed by Ultrafast Spectroscopy: Evidence of Excited-State Equilibration and Interligand Electron Transfer. *J. Phys. Chem. A* **2012**, *116*, 11536−11547.

(55) Vallett, P. J.; Damrauer, N. H. Experimental and Computational Exploration of Ground and Excited State Properties of Highly Strained Ruthenium Terpyridine Complexes. *J. Phys. Chem. A* **2013**, *117*, 6489−6507.

(56) Brown, A. M.; McCusker, C. E.; McCusker, J. K. Spectroelectrochemical Identification of Charge-Transfer Excited States in Transition Metal-Based Polypyridyl Complexes. *Dalton Trans.* **2014**, *43*, 17635−17646.

(57) Chaignon, F.; Torroba, J.; Blart, E.; Borgström, M.; Hammarström, L.; Odobel, F. Distance-Independent Photoinduced Energy Transfer over 1.1 to 2.3 nm in Ruthenium Trisbipyridine−Fullerene Assemblies. *New J. Chem.* **2005**, *29*, 1272−1284.

(58) Siebert, R.; Winter, A.; Schubert, U. S.; Dietzek, B.; Popp, J. The Molecular Mechanism of Dual Emission in Terpyridine Transition Metal Complexes − Ultrafast Investigations of Photoinduced Dynamics. *Phys. Chem. Chem. Phys.* **2011**, *13*, 1606−1617.

(59) Reichardt, C.; Sainuddin, T.; Wächtler, M.; Monro, S.; Kupfer, S.; Guthmuller, J.; Gräfe, S.; McFarland, S.; Dietzek, B. Influence of Protonation State on the Excited State Dynamics of a Photobiologically Active Ru(II) Dyad. *J. Phys. Chem. A* **2016**, *120*, 6379−6388.

(60) Eng, M. P.; Albinsson, B. The Dependence of the Electronic Coupling on Energy Gap and Bridge Conformation−Towards Prediction of the Distance Dependence of Electron Transfer Reactions. *Chem. Phys.* **2009**, *357*, 132−139.

(61) Tsuji, Y.; Movassagh, R.; Datta, S.; Hoffmann, R. Exponential Attenuation of Through-Bond Transmission in a Polyene: Theory and Potential Realizations. *ACS Nano* **2015**, *9*, 11109−11120.

(62) Schubert, C.; Wielopolski, M.; Mewes, L.-H.; de Miguel Rojas, G.; van der Pol, C.; Moss, K. C.; Bryce, M. R.; Moser, J. E.; Clark, T.; Guldi, D. M. Precise Control of Intramolecular Charge-Transport: The Interplay of Distance and Conformational Effects. *Chem. - Eur. J.* **2013**, *19*, 7575−7586.

(63) Eng, M. P.; Albinsson, B. Non-Exponential Distance Dependence of Bridge-Mediated Electronic Coupling. *Angew. Chem., Int. Ed.* **2006**, *45*, 5626−5629.

(64) Gray, H. B.; Winkler, J. R. Long-Range Electron Transfer. *Proc. Natl. Acad. Sci. U. S. A.* **2005**, *102*, 3534−3539.

(65) Edwards, P. P.; Gray, H. B.; Lodge, M. T. J.; Williams, R. J. P. Electron Transfer and Electronic Conduction through an Intervening Medium. *Angew. Chem., Int. Ed.* **2008**, *47*, 6758−6765.

(66) Cordes, M.; Giese, B. Electron Transfer in Peptides and Proteins. *Chem. Soc. Rev.* **2009**, *38*, 892−901.

(67) Brunschwig, B. S.; Ehrenson, S.; Sutin, N. Distance Dependence of Electron-Transfer Reactions: Rate Maxima and Rapid Rates at Large Reactant Separations. *J. Am. Chem. Soc.* **1984**, *106*, 6858−6859.

(68) Weiss, E. A.; Ahrens, M. J.; Sinks, L. E.; Gusev, A. V.; Ratner, M. A.; Wasielewski, M. R. Making a Molecular Wire: Charge and Spin Transport Through para-Phenylene Oligomers. *J. Am. Chem. Soc.* **2004**, *126*, 5577−5584.

(69) Kuss-Petermann, M.; Wenger, O. S. Increasing Electron-Transfer Rates with Increasing Donor−Acceptor Distance. *Angew. Chem., Int. Ed.* **2016**, *55*, 815−819.

(70) Kuss-Petermann, M.; Wenger, O. S. Electron Transfer Rate Maxima at Large Donor−Acceptor Distances. *J. Am. Chem. Soc.* **2016**, *138*, 1349−1358.

(71) Kuss-Petermann, M.; Wenger, O. S. Unusual Distance Dependences of Electron Transfer Rates. *Phys. Chem. Chem. Phys.* **2016**, *18*, 18657−18664.

(72) Heitele, H.; Pöllinger, F.; Weeren, S.; Michel-Beyerle, M. E. Influence of Solvent Polarity on Intramolecular Electron-Transfer − A Consistency Test of Free-Energies of Reaction and Solvent Reorganization with Experimental Rates. *Chem. Phys.* **1990**, *143*, 325−332.

Supporting Information

Increased Charge Separation Rates with Increasing Donor-Acceptor Distance in Molecular Triads: the Effect of Solvent Polarity

Yusen Luo[†,‡], Kevin Barthelmes[§,⊥], Maria Wächtler[‡], Andreas Winter[§,⊥], Ulrich S. Schubert[§,⊥] and Benjamin Dietzek[*†,‡,⊥]

[†] *Institute of Physical Chemistry and Abbe Center of Photonics, Friedrich Schiller University Jena, Helmholtzweg 4, 07743 Jena, Germany*

[‡] *Leibniz Institute of Photonic Technology (IPHT), Albert-Einstein-Straße 9, 07745 Jena, Germany*

[§] *Laboratory of Organic and Macromolecular Chemistry (IOMC), Friedrich Schiller University Jena, Humboldtstraße 10, 07743 Jena, Germany*

[⊥] *Jena Center for Soft Matter (JCSM), Friedrich Schiller University Jena, Philosophenweg 7, Jena, 07743, Germany*

[*] E-mail: benjamin.dietzek@leibniz-ipht.de

Table of contents

UV-vis absorption spectra

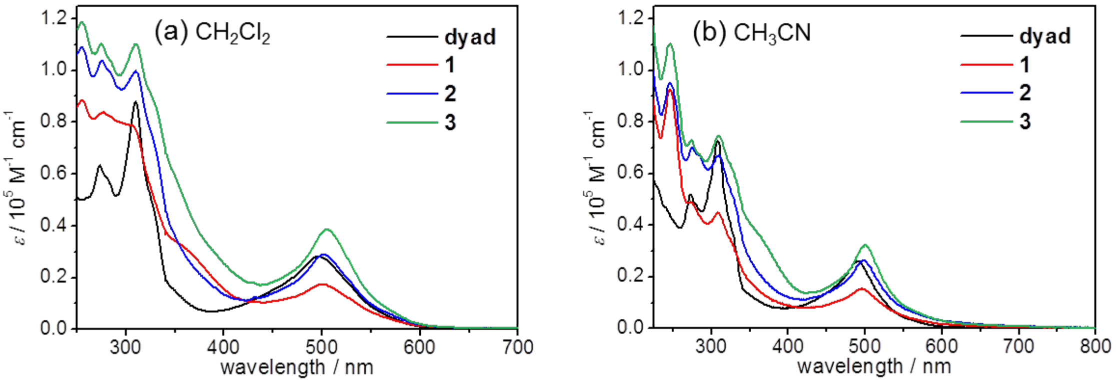

Figure S1. UV-vis absorption spectra of the reference dyad and triads **1-3** collected in (a) aerated dichloromethane (CH_2Cl_2) and (b) aerated acetonitrile (CH_3CN).

Emission spectra

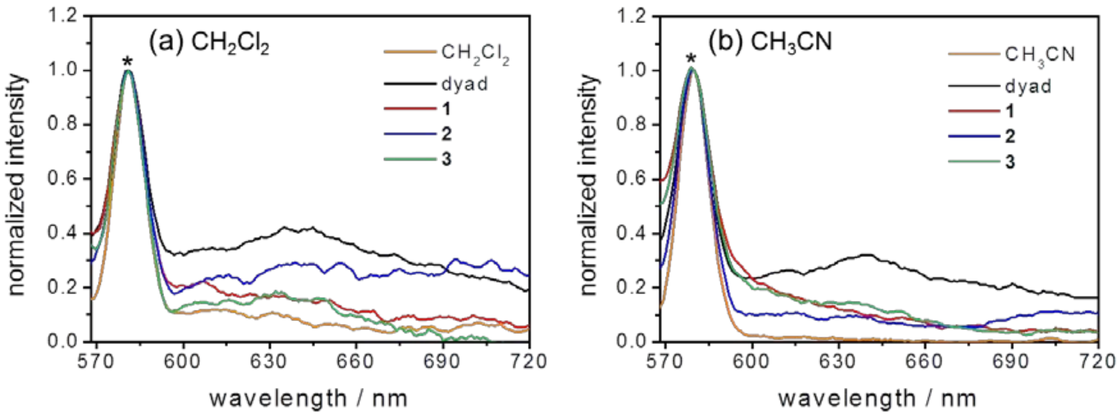

Figure S2. Normalized emission spectra (λ_{ex} = 495 nm) of the reference dyad and triads **1-3** collected in (a) aerated dichloromethane (CH_2Cl_2) and (b) aerated acetonitrile (CH_3CN) at room temperature. The absorption intensity at 495 nm for all compounds is kept the same (ca. 0.2). The emission spectra were normalized to the Raman band (asterisk) of the solvent.

UV-vis-SEC absorption difference spectra

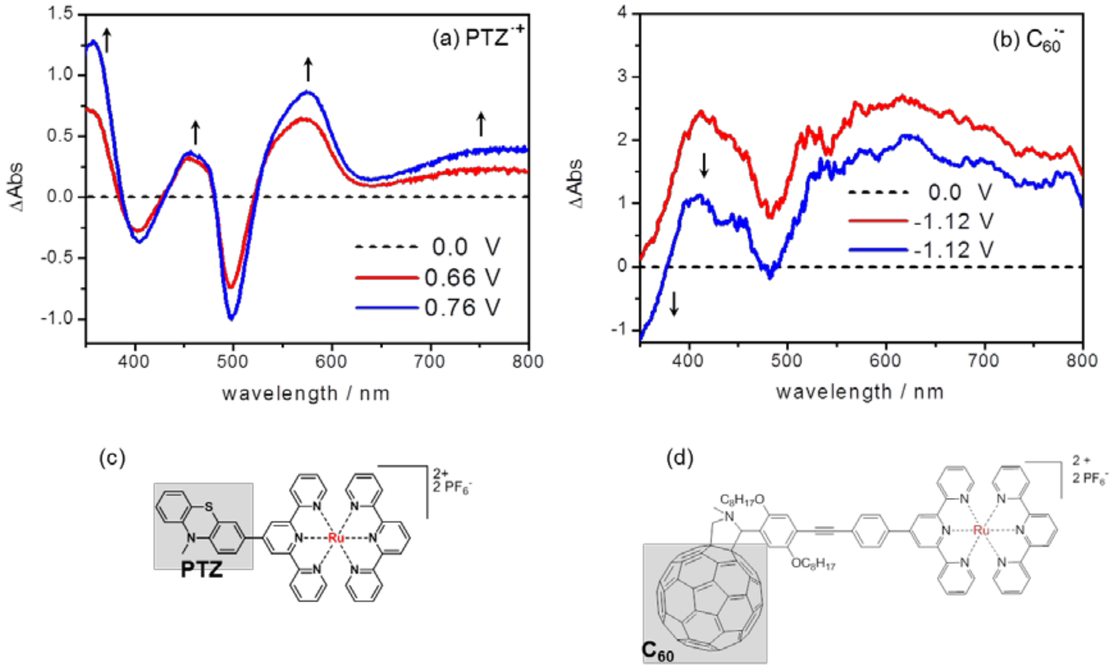

Figure S3. Spectroelectrochemical UV-vis absorption difference spectra of (a) PTZ$^{\cdot+}$ and (b) C$_{60}^{\cdot-}$ collected in aerated acetonitrile by oxidation of the reference dyad (Figure S3c) and reduction of **RuC$_{60}$** (Figure S3d) respectively. Potentials are given vs Fc$^{+/0}$. The reductive UV-vis-SEC spectra of C$_{60}^{\cdot-}$ were smoothed by the method of adjacent-averaging of 50 points of window.

ns TA spectra of **1**

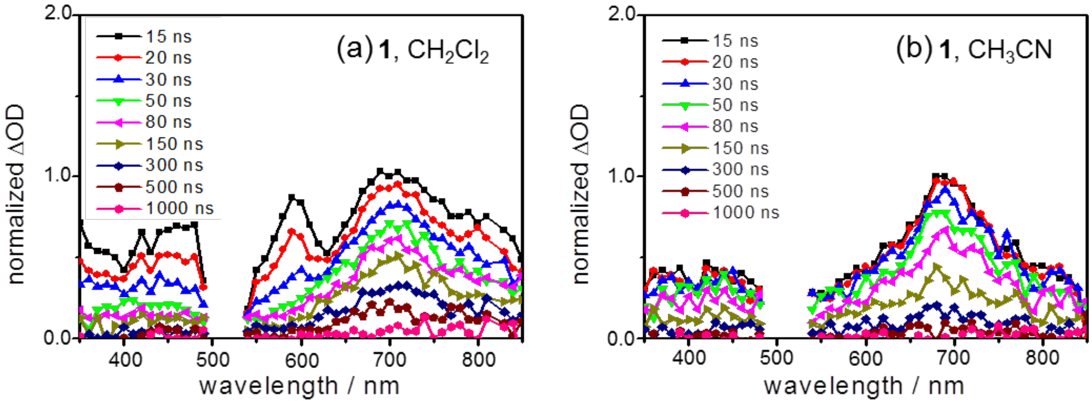

Figure S4. Nanosecond transient absorption spectra at selected times of **1** upon excitation at 520 nm in (a) aerated dichloromethane (CH_2Cl_2) and (b) aerated acetonitrile (CH_3CN). For comparison with other triads the ns TA spectra were normalized by the absorption maxima of $^3C_{60}{}^*$ (at 700 nm at 15 ns).

Global fit results of the ns TA data

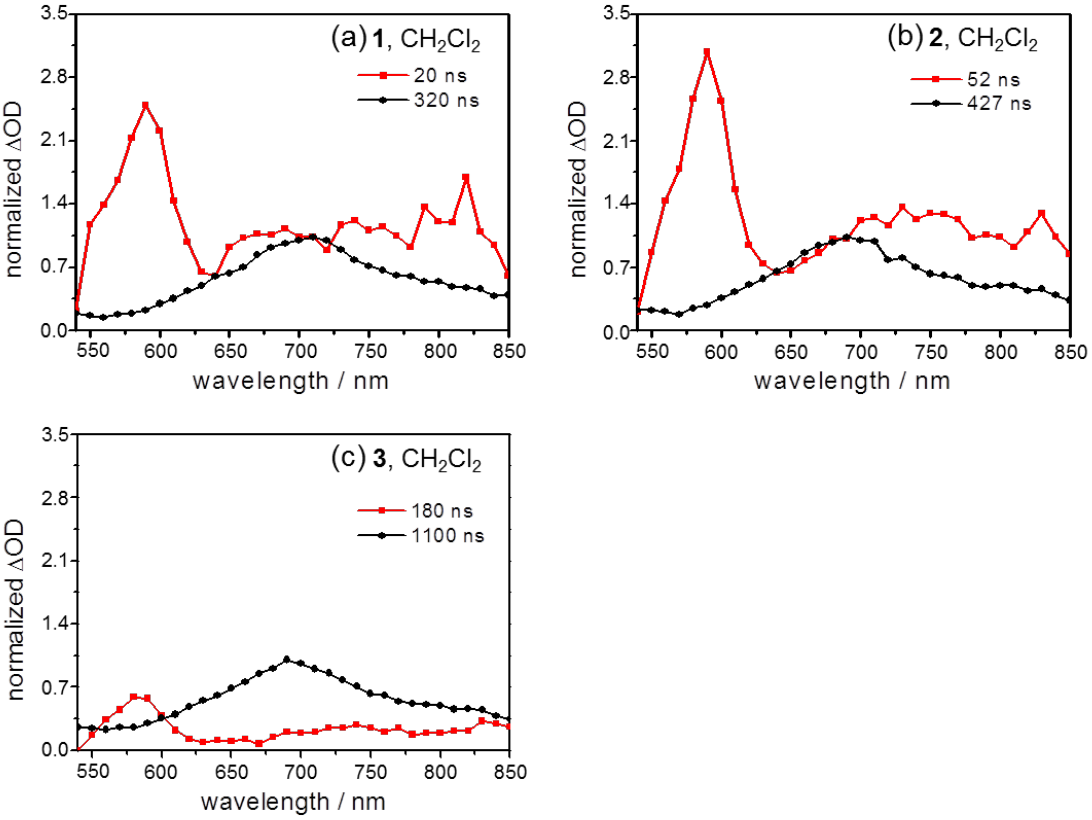

Figure S5. Global fit results of the ns TA data of (a) **1**, (b) **2** and (c) **3** upon excitation at 520 nm in aerated dichloromethane (CH$_2$Cl$_2$). All spectra were normalized by the corresponding absorption maximum of $^3C_{60}{}^*$ (at 700 nm) and only show the spectral region above 540 nm where displays significant characteristics. The relative short one (red squares) mainly dominates at 590 nm (the absorption of PTZ$^{\cdot+}$) and the longer one (black spheres) dominates at 700 nm which is assigned to PTZ$^{\cdot+}$-P-C$_{60}{}^{\cdot-}$ and $^3C_{60}{}^*$ respectively.

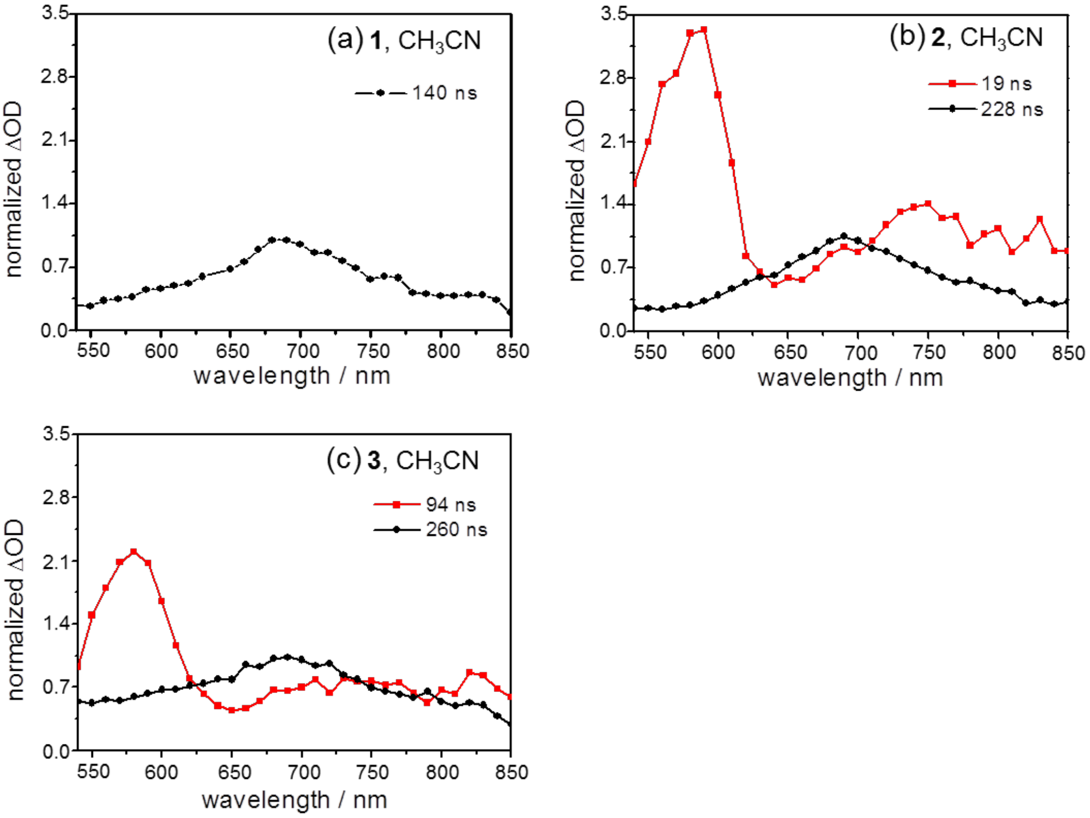

Figure S6. Global fit results of the ns TA data of (a) **1**, (b) **2** and (c) **3** upon excitation at 520 nm in aerated acetonitrile (CH_3CN). All spectra were normalized by the corresponding absorption maximum of $^3C_{60}^*$ (at 700 nm) and only show the spectral region above 540 nm where displays significant characteristics. The relative short one (red squares) mainly dominates at 590 nm (the absorption of $PTZ^{\cdot+}$) and the longer one (black spheres) dominates at 700 nm which is assigned to $PTZ^{\cdot+}$-P-$C_{60}^{\cdot-}$ and $^3C_{60}^*$ respectively.

fs TA spectra of reference dyad

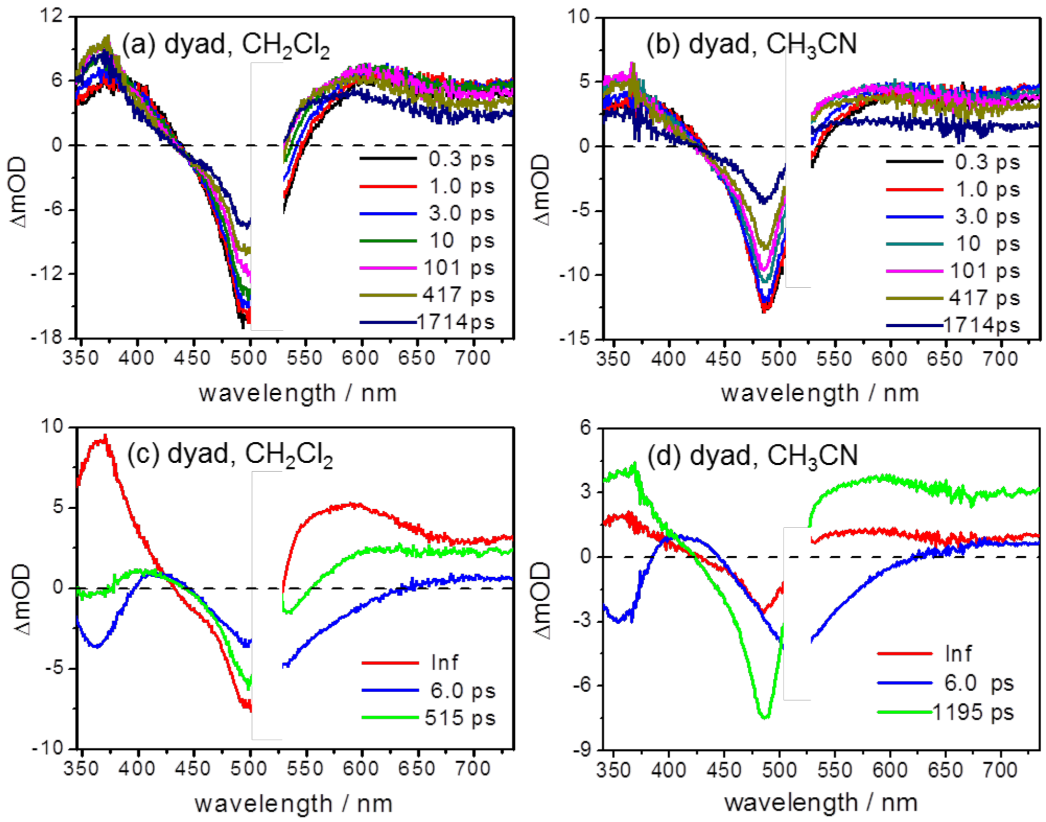

Figure S7. Transient absorption spectra (up) at selected delay times and decay-associated spectra (down) resulting from the global fit upon excitation at 520 nm for the reference dyad in (a, c) aerated dichloromethane and (b, d) aerated acetonitrile.

Interpretation of the fs TA data in dichloromethane has already been reported in the prior work.[1] Changing solvent from dichloromethane to acetonitrile shows notable changes in spectra: In the visible region, the fs TA spectra in acetonitrile are flatter than in dichloromethane. Another distinct difference is located at the UV region where the absorption of PTZ$^{\cdot+}$ displays very fast decay between 417 and 1714 ps in acetonitrile while it shows no significant change after photoexcitation in dichloromethane. It is reasonable to think that charge recombination is faster in acetonitrile than that in dichloromethane. The assignment of time constants in Figure S7d can be done in accordance to Figure S7c. Hence in acetonitrile, the first component (τ_1 = 6 ps) is also attributed to the formation of PTZ$^{\cdot+}$-P$^{\cdot-}$. While the shape of the second component (τ_2 = 1195 ps) is very close to an overall decay, it might be that there is already contribution from the recombination of PTZ$^{\cdot+}$-P$^{\cdot-}$ owing to the fast decay in more polar solvent.

fs TA spectra of **1**

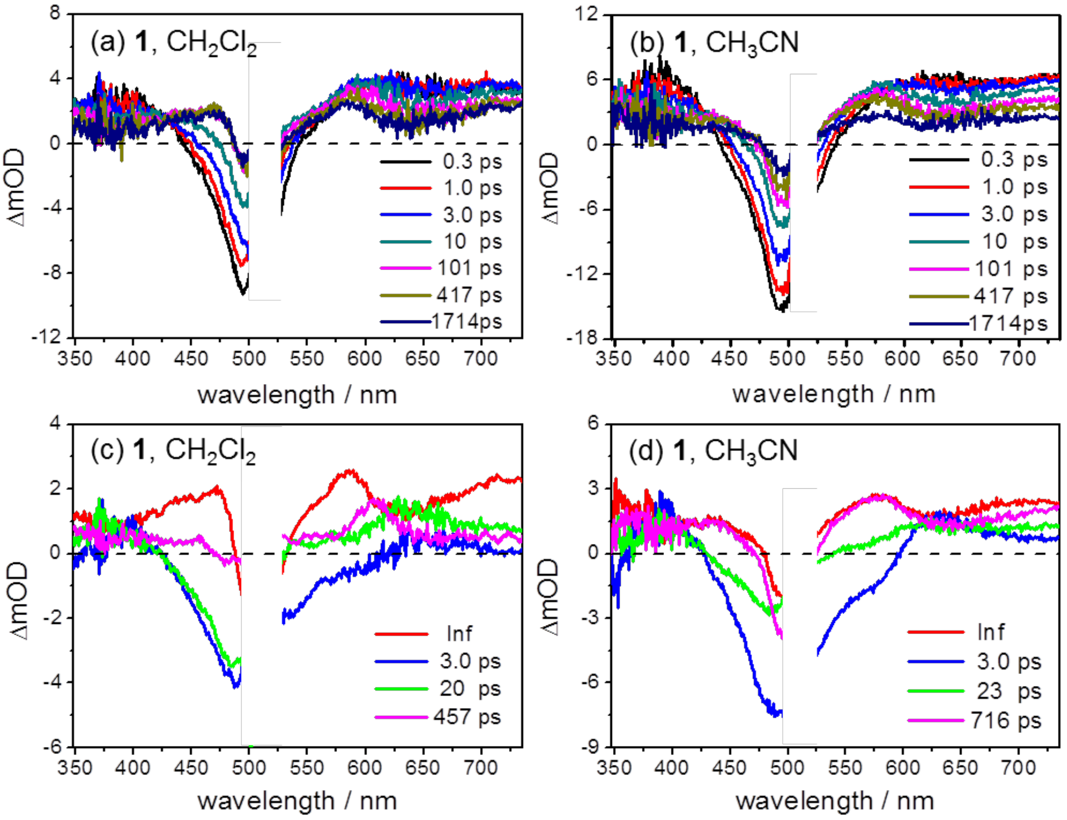

Figure S8. Transient absorption spectra (up) at selected delay times and decay-associated spectra (down) resulting from the global fit upon excitation at 520 nm for the shortest triad **1** in (a, c) aerated dichloromethane and (b, d) aerated acetonitrile.

Interpretation of the fs TA data in dichloromethane has already been reported in the prior work.[1] Changing solvent from dichloromethane to acetonitrile, the most significant difference is that the band at 473 nm in acetonitrile (Figure S8b) is not as pronounced as in dichloromethane (Figure S8a). The assignment of time constants in Figure S8d can be done in accordance to Figure S8c, both of which shows quite similar dynamics for the first charge separation ($\tau_1 = 3$ ps) and energy transfer ($\tau_2 = 20$ ps in dichloromethane, $\tau_2 = 23$ ps in acetonitrile) processes. The third component is attributed to the formation of PTZ$^{\cdot+}$-P-C$_{60}$$^{\cdot-}$ which is slower in acetonitrile ($\tau_3 = 716$ ps) than that in dichloromethane ($\tau_3 = 457$ ps). Moreover, the shape of the third component ($\tau_3 = 716$ ps) is very close to an overall decay, it might be that there is already contribution from the recombination of PTZ$^{\cdot+}$-P-C$_{60}$$^{\cdot-}$ which is indicated by the ns TA data (< 10 ns).

Relaxation diagrams of 1- 3

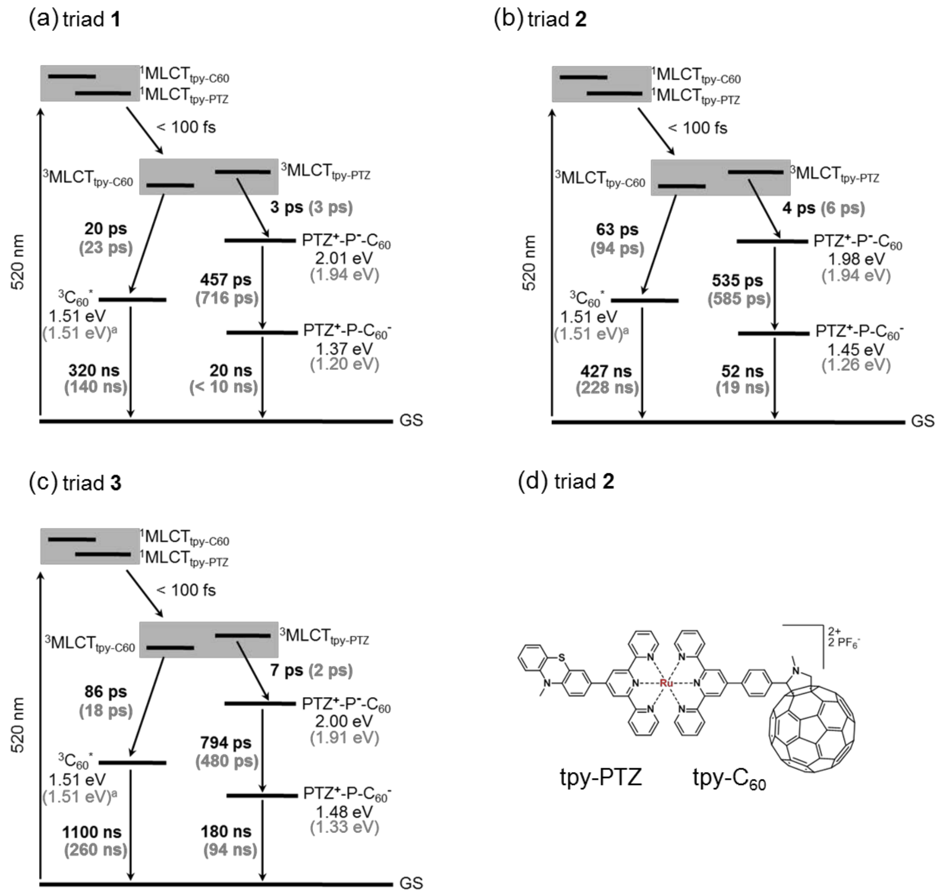

Scheme S1. Energy-level diagrams of **1** (a), **2** (b) and **3** (c) are developed by electrochemical, resonance Raman and fs / ns TA data.[1] (d) Molecular structure of **2** as an example to show the different ligands that the terpyridine (tpy) ligand connecting with *N*-methylphenothiazine (PTZ) is named as tpy-PTZ and another tpy ligand close to C_{60} is named as tpy-C_{60}. [a] The energy of $^{3}C_{60}^{*}$ is 1.51 eV which is polarity independent.[2] Note: for relaxation dynamics in acetonitrile, time constants are marked in grey and listed in brackets.

Numerical Simulations of the distance dependent electron transfer rates

$$\mathrm{k_{ET}} = \sqrt{\frac{\pi}{\hbar^2 \cdot \lambda \cdot \mathrm{k_B} \cdot \mathrm{T}}} \cdot \mathrm{H_{DA}}^2 \cdot \exp\left(-\frac{(\lambda + \Delta \mathrm{G^0_{ET}})^2}{4 \cdot \lambda \cdot \mathrm{k_B} \cdot \mathrm{T}}\right) \tag{1}$$

$$\mathrm{H_{DA}} = \mathrm{H_0} \cdot \exp(-\frac{\beta}{2} \cdot \mathrm{R_{DA}}) \tag{2}$$

$$\lambda = \lambda_\mathrm{i} + \lambda_\mathrm{o} \tag{3}$$

$$\lambda_\mathrm{o} = \frac{e^2}{4 \cdot \pi \cdot \varepsilon_0} \cdot \left(\frac{1}{2\mathrm{a_1}} + \frac{1}{2\mathrm{a_2}} - \frac{1}{\mathrm{R_{DA}}}\right) \cdot \left(\frac{1}{\eta^2} - \frac{1}{\varepsilon_\mathrm{s}}\right) \tag{4}$$

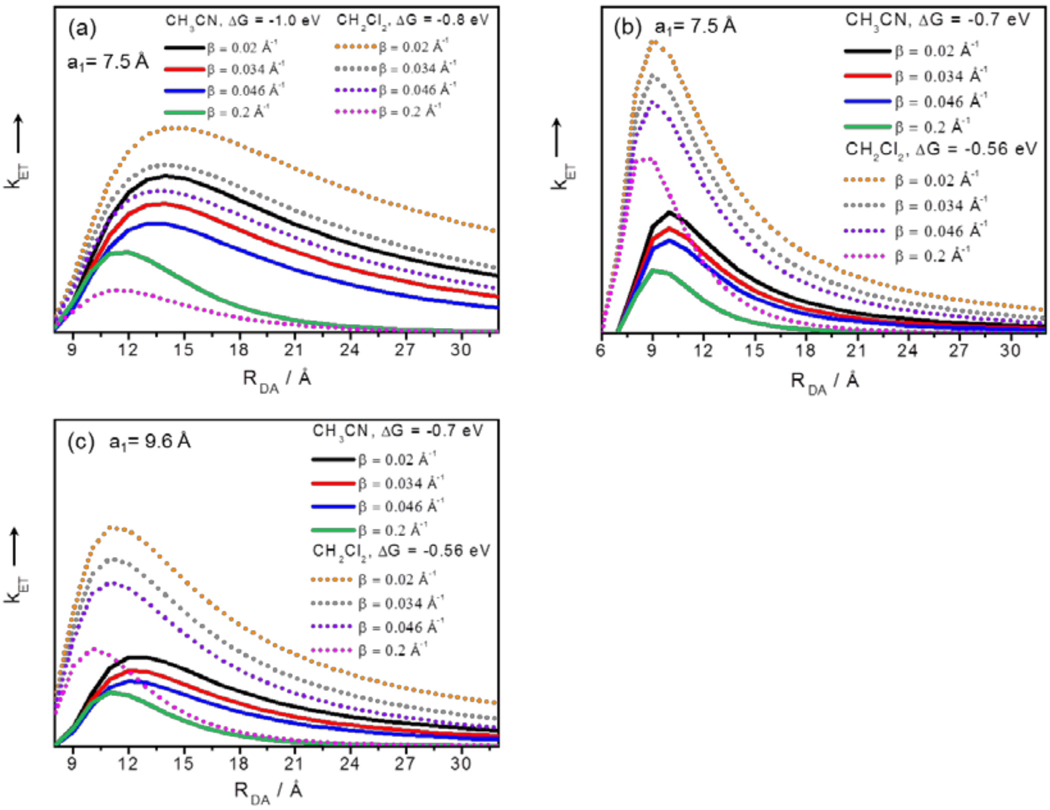

Figure S9. Distance dependences of $\mathrm{k_{ET}}$ resulted from the Marcus theory (eq S1, 3 and 4) and superexchange model (eq S2).[3] The parameters used for simulations are within the reasonable regions based on the experimental results and are displayed in the corresponding figures. Except these parameter variations (*i.e.* the attenuation factor β, the radius of the donor $\mathrm{a_1}$ and driving force) in simulations, for $\mathrm{CH_3CN}$, $\eta = 1.3416$,[4] $\varepsilon_\mathrm{s} = 35.9$[3] and for $\mathrm{CH_2Cl_2}$, $\eta = 1.4212$,[4] $\varepsilon_\mathrm{s} = 8.93$.[3] The radius of the acceptor $\mathrm{C_{60}}$ ($\mathrm{a_2}$) is estimated to be 4.5 Å. The inner reorganization energy (λ_i) is assumed to be 0.1 eV.[3] We would like to pointed out that: i) The values of the driving forces $\Delta \mathrm{G^\circ_{ET}}$ are based on the fact that the absolute values of $\Delta \mathrm{G^\circ_{ET}}$ in dichloromethane are around 80%

of that in acetonitrile according to Table 1 (*i.e.* ΔG°_{CS2}). Two sets of driving forces were used, *i.e.* -1.0 eV in CH_3CN vs. -0.8 eV in CH_2Cl_2 (a), and -0.7 eV in CH_3CN vs. -0.56 eV in CH_2Cl_2 (b, c). It should be noted that in principle ΔG°_{ET} is also distance dependent but in the simulations here we assumed ΔG°_{ET} is constant in a certain solvent.[3] ii) For the values of a_1, the second electron transfer process occurs from an intermediate state $PTZ^{\cdot+}$-$P^{\cdot-}$-C_{60}, the electron density is thought to be delocalized over the conjugated PTZ and Ru complex unities. According to the optimized molecular structure the radius of Ru complex is estimated to be 5 Å.[5] Here two values of a_1 were used, *i.e.* a_1 = 7.5 Å (a, b; 50% of the radius added) and a_1 = 9.6 Å (c; it is the center-to-center distance between PTZ and Ru). iii) The β-values used in simulations were based on the absolute values of the experimental results (0.034 $Å^{-1}$ in acetonitrile and 0.046 $Å^{-1}$ in dichloromethane) and were adjusted around them.

The numerical simulations qualitatively describe the different distance dependences of k_{ET} in two solvents and illustrates that in certain donor-acceptor distance (R_{DA}) regions, the k_{ET} increases / decreases with increasing R_{DA} in acetonitrile / dichloromethane which would result in different slopes with opposite sign (by plotting $\ln k_{ET}$ vs. R_{DA}). Although the simulations here indicate the possibility of observing the inversion of the distance dependence of the electron transfer rates which could be tuned by varying the solvent polarity, compared with the experimental data (in which the second charge separation process in **1**-**3** takes place in a distance (R_{DA}) region of 10 to 21 Å), there are still some deviations. One reason for the deviations might result from the error of parameters estimation, *i.e.* β-values, reorganization energy (a_1, a_2 and λ_i in eq S3, S4) and driving forces used in the simulation. For example, in the simulation only positive β-values were considered.[3] More importantly, we think that the method used here which combines the Marcus theory and the superexchange model[3] should be extended in order to account for non-exponential distance-dependent couplings, an approach that was introduced by Albinsson[6] (see the main text).

Estimation of the reorganization energy

Table S1. The reorganization energies for the charge-separation (λ_{CS1} and λ_{CS2} for the first and second charge-separation step, respectively) and charge-recombination (λ_{CR2} for the recombination of $PTZ^{\cdot+}$-P-$C_{60}^{\cdot-}$) processes were estimated by using eq S3 and S4. The inner reorganization energy (λ_i) is assumed to be 0.1 eV.[3] The radius of PTZ, Ru complex and C_{60} is 4, 5 and 4.5 Å, respectively.[5]

	λ_{CS1} / eV		λ_{CS2} / eV		λ_{CR2} / eV	
	CH_2Cl_2	CH_3CN	CH_2Cl_2	CH_3CN	CH_2Cl_2	CH_3CN
1	0.77	1.02	0.67	0.89	1.09	1.48
2	0.77	1.02	0.85	1.13	1.16	1.56
3	0.77	1.02	1.00	1.34	1.22	1.64

References

(1) Luo, Y.; Barthelmes, K.; Wächtler, M.; Winter, A.; Schubert, U. S.; Dietzek, B. Energy vs. Electron Transfer – Controlling the Excitation Transfer in Molecular Triads. *Chem. Eur. J.* **2017**, *23*, 4917-4922.

(2) Guldi, D. M.; Prato, M. Excited-State Properties of C(60) Fullerene Derivatives. *Acc. Chem. Res.* **2000**, *33*, 695-703.

(3) Kuss-Petermann, M.; Wenger, O. S. Unusual Distance Dependences of Electron Transfer Rates. *Phys. Chem. Chem. Phys.* **2016**, *18*, 18657-18664.

(4) Heitele, H.; Pöllinger, F.; Weeren, S.; Michel-Beyerle, M. E. Influence of Solvent Polarity on Intramolecular Electron-Transfer – A Consistency Test of Free-Energies of Reaction and Solvent Reorganization with Experimental Rates. *Chem. Phys.* **1990**, *143*, 325-332.

(5) Barthelmes, K.; Winter, A.; Schubert, U. S. Dyads and Triads Based on Phenothiazine, Bis(terpyridine)ruthenium(II) Complexes, and Fullerene. *Eur. J. Inorg. Chem.* **2016**, *2016*, 5132-5142.

(6) Eng, M. P.; Albinsson, B. Non-Exponential Distance Dependence of Bridge-Mediated Electronic Coupling. *Angew. Chem. Int. Ed.* **2006**, *45*, 5626-5629.

[P5] Superexchange on the Fast Lane – Intramolecular Electron Transfer in a Molecular Triad Occurs by Conformationally-Gated Superexchange

Reproduced with permission from: Y. Luo, M. Wächtler, K. Barthelmes, A. Winter, U. S. Schubert and B. Dietzek, "Superexchange on the Fast Lane – Intramolecular Electron Transfer in a Molecular Triad Occurs by Conformationally-Gated Superexchange", *Chem. Commun.*, Submitted/not yet published, with permission from the Royal Society of Chemistry.
The manuscript was submitted on March 7th 2019, the decision was made on March 25th 2019 and the revised manuscript was submitted on March 26th 2019.

Updated information:
The manuscript has been already published: *Chem. Commun.*, **2019**, *55*, 5251–5254.

Published on 05 April 2019. Downloaded by Thueringer Universitats Landesbibliothek Jena on 7/11/2019 3:48:35 PM.

ChemComm

COMMUNICATION

View Article Online
View Journal | View Issue

Check for updates

Cite this: *Chem. Commun.*, 2019, **55**, 5251

Received 7th March 2019,
Accepted 5th April 2019

DOI: 10.1039/c9cc01886g

rsc.li/chemcomm

Superexchange in the fast lane – intramolecular electron transfer in a molecular triad occurs by conformationally gated superexchange†

Yusen Luo,[ab] Maria Wächtler,[ab] Kevin Barthelmes,[cd] Andreas Winter,[cd] Ulrich S. Schubert[cd] and Benjamin Dietzek *[abd]

Photoinduced electron transfer *via* hopping is generally considered to have a stronger temperature dependence than electron transfer *via* superexchange. However, in this work, an opposite trend of the temperature dependence is observed. This unexpected result is rationalized by considering the specific geometrical and electronic structure of the Ru-bis(terpyridine) photosensitizer.

Photoinduced electron transfer in donor–spacer–acceptor (D–S–A) molecules is extensively studied both experimentally[1–4] and theoretically[5,6] to understand the underlying mechanism and to correlate it with the molecular structure. Studies have indicated that electron transfer through molecular spacers is mediated by either coherent superexchange or incoherent hopping.[1–4] Also, a combination of both mechanisms was found to be operative in some cases.[7–9] Electron transfer *via* superexchange requires orbital overlap and spacer states higher in energy than the donor states. Consequently, no spacer radicals are formed – not even transiently.[1–3,8,9] This leads to the characteristic exponential dependence of the electron transfer rates (k_{ET}) on the donor–acceptor distances (R_{DA}):[1–4,7,8] $k_{\mathrm{ET}} = k_0 \cdot \mathrm{e}^{-\beta \cdot R_{\mathrm{DA}}}$, β is the attenuation factor. When the spacer states become energetically similar or lower than the donor states, which can be achieved by structural variation of the spacer, *e.g.* lengthening the π-conjugation[10,11] or introduction of proper substituents,[7,10,12] the spacer becomes accessible for accepting an electron. As a result, the spacer-localized intermediate charge-separated states take part in electron transfer.[1–4,9] Such a situation leads to electron transfer *via* the so-called hopping mechanism. $\ln k_{\mathrm{ET}}$ *vs.* R_{DA} is often considered to evaluate the mechanism of electron transfer and small β values (<0.2 Å^{-1}) are attributed to hopping.[1–4,8,10,13] However, recent studies have shown that differentiating the electron transfer mechanisms by the magnitude of the β value only might lead to misconceptions.[8,9] Nevertheless, hopping is generally considered to be more efficient than superexchange at longer donor–acceptor distances. Hence, the appearance of a slope change when studying $\ln k_{\mathrm{ET}}$ *vs.* R_{DA} may indicate a change of the electron-transfer mechanisms.[10,14–16]

Another approach to understand the mechanism of electron transfer is to investigate the temperature dependence of k_{ET}. Consequently, a few studies have employed the reformed Marcus equation:[9,17–21]

$$\ln\left(k_{\mathrm{ET}} \cdot T^{\frac{1}{2}}\right) = \ln\left(\sqrt{\frac{\pi}{\hbar^2 \cdot \lambda \cdot k_{\mathrm{B}}}} \cdot H_{\mathrm{DA}}{}^2\right) - \frac{(\lambda + \Delta G)^2}{4 \cdot \lambda \cdot k_{\mathrm{B}} \cdot T}$$

where λ, H_{DA} and ΔG represent the reorganization energy, electronic coupling and free energy change associated with electron transfer, respectively. By plotting $\ln(k_{\mathrm{ET}} \cdot T^{1/2})$ *vs.* $1/T$, λ and H_{DA} can be extracted from the slope (ΔG is estimated by Rehm–Weller equation[22]) and the intercept, respectively. The activation energy for electron transfer can be obtained as: $\Delta G^{\ddagger} = (\lambda + \Delta G)^2/4\lambda$.[19,20]

A change in electron transfer mechanism upon variation in the temperature will lead to deviations from linearity of the $\ln(k_{\mathrm{ET}} \cdot T^{1/2})$ *vs.* $1/T$ plot.[9,17–21] Following this approach, in literature reports on cases of temperature dependent slopes of $\ln(k_{\mathrm{ET}} \cdot T^{1/2})$ *vs.* $1/T$, most research comes to the conclusion that hopping has a stronger temperature dependence than superexchange.[18–21] However, such analysis has to be conducted with care as temperature-induced changes in the solvent's dielectric properties might cause λ, H_{DA} and ΔG to become temperature-dependent quantities.[3,11,23,24] Considering this, Wasielewski pointed out that positive activation cannot exclusively indicate a hopping mechanism while less activated behavior (*i.e.* flat slopes) alone cannot be conclusively attributed to superexchange.[24] The studies available in the literature rely on organic chromophores as photosensitizers.[9,17–21]

---

[a] *Institute of Physical Chemistry and Abbe Center of Photonics, Friedrich-Schiller-University Jena, Helmholtzweg 4, 07743 Jena, Germany*
[b] *Department Functional Interfaces, Leibniz Institute of Photonic Technology (IPHT), Albert-Einstein-Straße 9, 07745 Jena, Germany. E-mail: benjamin.dietzek@leibniz-ipht.de*
[c] *Laboratory of Organic and Macromolecular Chemistry (IOMC), Friedrich-Schiller-University Jena, Humboldtstraße 10, 07743 Jena, Germany*
[d] *Center for Energy and Environmental Chemistry Jena (CEEC Jena), Philosophenweg 7a, 07743 Jena, Germany*

† Electronic supplementary information (ESI) available. See DOI: 10.1039/c9cc01886g

This journal is © The Royal Society of Chemistry 2019

Published on 05 April 2019. Downloaded by Thueringer Universitats Landesbibliothek Jena on 7/11/2019 3:48:35 PM.

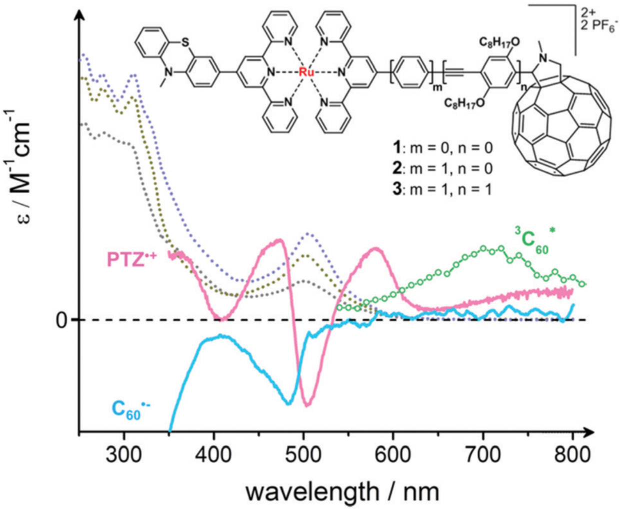

Fig. 1 Schematic representation of the molecular triads **1–3** studied in this work. The UV-vis absorption spectra of **1–3** (dotted line, from bottom to top) were recorded at room temperature.[30] The absorption spectrum of the fullerene triplet state (*i.e.* $^3C_{60}$*) was taken from the ns TA data.[28] The UV-vis absorption difference spectrum of the oxidized PTZ donor (*i.e.* $PTZ^{\bullet+}$) shows three new bands at 365, 473 and 580 nm while the reduced fullerene (*i.e.* $C_{60}^{\bullet-}$) has a negative contribution below 400 nm.[28,29] All the spectra were recorded in dichloromethane. Note: only the spectra of $^3C_{60}$*, $C_{60}^{\bullet-}$ and $PTZ^{\bullet+}$ were arbitrarily scaled and are shown here to facilitate the discussion.

However, the practical applications of photo-driven electron transfer, *e.g.* in artificial photosynthesis, often exploit Ru-polypyridyl complexes as versatile and potent photosensitizers.[25–27]

We have previously reported a triad system (Fig. 1) which contains an *N*-methylphenothiazine (PTZ) electron donor, a Ru(II) bis(terpyridine) photosensitizer (P) and an *N*-methylfullerpyrrolidine (C_{60}) electron acceptor.[28,29] Studies at room temperature indicated that upon excitation of the MLCT transitions, a two-step electron transfer $\left(PTZ{-}^3P^*{-}C_{60} \xrightarrow{ET1} PTZ^{\bullet+}{-}P^{\bullet-}{-}C_{60} \xrightarrow{ET2} PTZ^{\bullet+}{-}P{-}C_{60}^{\bullet-}\right)$ and a triplet–triplet energy transfer take place from two distinct ^{3}MLCT states (see Fig. S1, ESI†).[28,29] In different triads, ET2 takes place between the $Ru(tpy)_2^{\bullet-}$ and C_{60} acceptor at varying distances. To identify the underlying mechanism of ET2, temperature-dependent fs transient absorption (TA) spectroscopy was performed.

In the fs TA measurements, samples were excited at 520 nm, *i.e.* in the red edge of the MLCT band to enable direct comparison with the previously obtained results at room temperature.[28,29] The TA data were collected in the temperature range between 300 and 230 K (for full sets of data see Fig. S2–S7, ESI†). For each compound, the TA spectra do not display significant changes upon changing the temperature. Thus, the model previously developed at room temperature for **1–3** (Fig. S1, ESI†) is applied to analyze the data recorded at different temperatures. Fig. 2 exemplarily depicts the TA spectra recorded at 240 K of the shortest and the longest triad. At short delay times, the typical spectral features of the ^{3}MLCT states of the Ru(II) polypyridyl complexes are displayed: a strong ground state bleach (GSB) at around 500 nm and two excited-state absorption (ESA) bands in

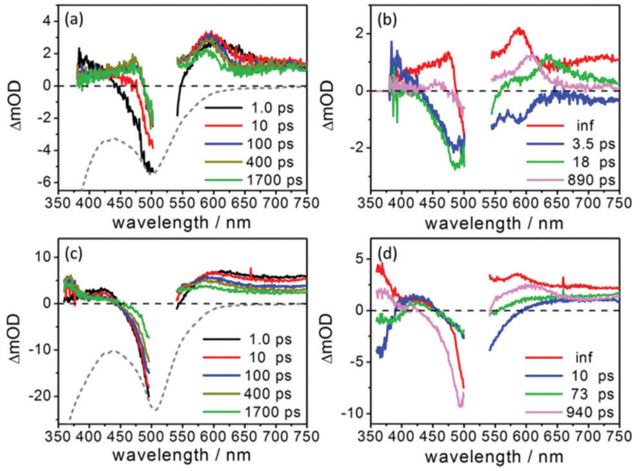

Fig. 2 (a and c) The fs transient absorption spectra at selected delay times and (b and d) decay-associated spectra resulting from the global fit upon excitation at 520 nm in a 1 cm cuvette in dichloromethane for **1** (a and b) and **3** (c and d) at 240 K. The grey dashed line represents the shape of the corresponding inverted ground state absorption spectrum which is scaled to fit the respective figure.

the wavelength region of 350 to 450 nm and 550 to 750 nm.[31] The extended conjugation of the tpy ligands leads to red-shifted ESA bands,[31] *i.e.* from a maximum below 400 nm in **1** to 425 nm in **3** (at 1 ps). At long delay times, *e.g.* at 1700 ps, three distinct ESA bands appear at 475, 590 and around 700 nm for **1** (Fig. 2a and b) as well as for **2** (see Fig. S4, ESI†). The bands at 475 and 590 nm indicate the formation of the oxidized phenothiazine radical ($PTZ^{\bullet+}$, Fig. 1) and the broadband at around 700 nm is attributed to the absorption of fullerene triplet states ($^3C_{60}$*, Fig. 1).[28,29] The spectra of **3** recorded at long delay times (Fig. 2c and d) appear relatively unstructured compared to **1** but the ESA band at around 590 associated with the formation of $PTZ^{\bullet+}$ is still discernible.

The characteristic time constants associated with each process were obtained by globally fitting the data (Fig. 2c, d and Fig. S3, S5, S7, ESI†). For all triads, consistent with the data at room temperature (Fig. S1, ESI†), three kinetic components and a long-lived component are sufficient to account for the data between 300 and 230 K: the first component (τ_1 = 3.5 and 10 ps for **1** and **3**, respectively) is characterized by an increased TA signal at around 365 nm (**3**) and at 590 nm (**1**), and thus, is attributed to the formation of $PTZ^{\bullet+}{-}P^{\bullet-}{-}C_{60}$ (ET1, the different time constants for ET1 in **1** and **3** at the same temperature is due to the distinct H_{DA}.[32] Fig. S1, ESI†).[28,29] The spectral changes associated with τ_2 (18 and 73 ps for **1** and **3**, respectively) revealing a decay of the ^{3}MLCT state without the formation of $PTZ^{\bullet+}$, indicates energy transfer to form $^3C_{60}$* (Fig. S1, ESI†).[28,29] The third component (τ_3 = 890 and 940 ps for **1** and **3**, respectively) is characterized by a decreasing signal both at 350 to 400 nm and at 610 nm. This is associated with the decay of the reduced ligand $tpy^{\bullet-}$[31] in $PTZ^{\bullet+}{-}P^{\bullet-}{-}C_{60}$. Additionally, $C_{60}^{\bullet-}$ has a negative contribution below 400 nm (see Fig. 1). Thus, τ_3 is assigned to ET2, *i.e.* $PTZ^{\bullet+}{-}P^{\bullet-}{-}C_{60} \xrightarrow{ET2} PTZ^{\bullet+}{-}P{-}C_{60}^{\bullet-}$. The long-lived species represents a charge recombination of

Published on 05 April 2019. Downloaded by Thueringer Universitats Landesbibliothek Jena on 7/11/2019 3:48:35 PM.

$PTZ^{\bullet +}$–P–$C_{60}^{\bullet -}$ and relaxation of $^3C_{60}{}^*$ to the ground state. As a result, both the electron and energy transfer are still active in the entire temperature range probed. We would like to point out that the coexistence of both decay channels even at low temperatures, *i.e. via* stepwise electron transfer on the one hand and energy transfer on the other hand, is due to the fact that they originate from the two distinct ^{3}MLCT, whose decays do not compete with each other kinetically (see Fig. S1, ESI†).[28,29]

Regarding the mechanisms underlying ET2, its distance dependence is considered first. The k_{ET2} (summarized in Table S1, ESI†) decreases with increasing donor–acceptor distance at 300 and 280 K consistent with the result observed at room temperature in dichloromethane.[29] However, upon further decreasing the temperature, k_{ET2}(**3**) becomes larger than k_{ET2}(**2**). The distance dependence of k_{ET2} as a function of temperature is depicted in Fig. 3a: at 300 and 280 K ln(k_{ET2}) falls onto a single linear relation with distance $R_{Ru\text{-}C_{60}}$. However, upon decreasing the temperature from 270 to 230 K an increased k_{ET2}(**3**) is observed (Fig. 3a). Or to put it differently: at temperatures lower than 270 K a minimal k_{ET2}(**2**) is observed (Fig. 3a). The electron transfer rates thus do not decay exponentially with increasing distance in the temperature range between 270 and 230 K (Fig. 3a). Such changes in the slope of $\ln k_{ET}$ *vs.* R_{DA} already presented in literature[10,14–16] indicate a switch in the electron-transfer mechanism from superexchange (**1** and **2**) to hopping (**3**). Fig. 3b shows a re-evaluation of the temperature dependent kinetics of ET2. In doing so, the temperature dependence of the solvent's dielectric properties was explicitly taken into account: both λ (estimated based on Marcus's dielectric continuum model, eqn (S1)–(S2), ESI†) and $\Delta G^{\ddagger}$, *i.e.* $(\lambda + \Delta G)^2/4\lambda$, are nearly temperature independent (Tables S2–S4, ESI†). Thus, the solvent properties themselves do not induce significant deviations to the Marcus analysis. Fig. 3b shows that k_{ET2} is well described by the Marcus equation and no slope-changes indicative of different electron-transfer mechanisms in different temperature ranges are apparent.[9,17–21] Consequently, combined with the results obtained from Fig. 3a, we conclude that from 300 to 230 K electron transfer in the two short triads occurs *via* superexchange while incoherent hopping is dominant in **3**. Hopping being operative in **3** can be understood by the rather extended conjugated molecular spacer between the Ru(tpy)$_2$-photosensitizer and C_{60} acceptor.[7,10,12] The structural changes in the electronically excited state of the extended conjugated D–S–A systems might impact the distance and temperature dependence of k_{ET}, *e.g.* ET can be gated by torsional motions in the molecular spacer.[11,33,34] For **3**, this would correlate to the torsional motion in the alkoxy substituted oligo(*p*-phenyleneethynylene)s molecular spacer. However, the experimentally determined activation energy $\Delta G^{\ddagger}$ for ET2 in **3** amounts to only 0.04 eV, *i.e.* it is an order of magnitude smaller than the calculated torsional barrier (0.3–0.6 eV, depending on the actual theoretical method used) for the related oligo(*p*-phenylene-ethynylene)s molecular spacers.[35,36] Hence, ET2 in **3** does not appear to be gated by torsional dynamics of the ligand system.

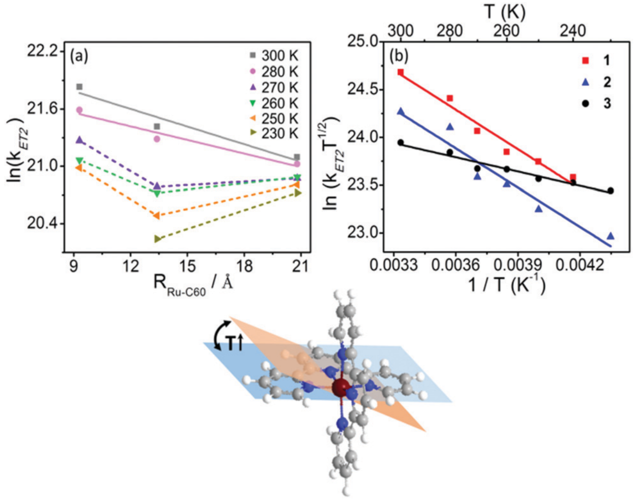

Fig. 3 (a) The plots of ln(k_{ET2}) *versus* the center-to-center distance between the Ru complex and C_{60}, *i.e.* $R_{Ru\text{-}C_{60}}$. $R_{Ru\text{-}C_{60}}$ was obtained from the neutral, optimized molecular structure.[30] The dashed lines are given to show the trend of the electron transfer rates as a function of distance. (b) Plots of ln($k_{ET2}\cdot T^{1/2}$) *vs.* 1/T in **1–3** with the corresponding linear fit. All data were collected in dichloromethane. Bottom: A simplified graphical representation of the temperature-activated geometry of the Ru photosensitizer for superexchange. Color code: red Ru, blue N, grey C.

Notably, however, ET2 in **3**, occurring *via* hopping, has a weaker temperature dependence (*i.e.* a flatter slope) than the superexchange underlying ET2 in **1** and **2** (Fig. 3b). To the best of our knowledge, this is the first observation of superexchange having a stronger temperature dependence than hopping in structurally related systems: literature on the temperature-dependent electron/hole transfer rates, which were investigated in a range of molecular assemblies containing electron donors π-extended tetrathiafulvalenes, phenothiazine, porphyrin and ferrocene, and electron acceptors fullerene and perylene,[9,17–21] points out that incoherent hopping is more sensitive to changes in temperature than coherent superexchange. However, none of the studies reported in the literature are concerned with the Ru-polypyridine derived photosensitizers.

As $\lambda > |-\Delta G|$ (Table 1), ET2 occurs in the Marcus normal region for **1–3**. Thus, the relatively weak temperature-dependence of k_{ET2}(**3**) is not due to the electron transfer in the Marcus inverted region in which ET shows a very weak temperature dependence or is even completely temperature independent.[11,23] We relate the observation of significant thermal activation of the superexchange underlying ET2 in **1** and **2** to the specific structure of the Ru(tpy)$_2$ photosensitizer. In the triads at hand, ET2 occurs from the negatively charged tpy ligand connected to the PTZ donor (*i.e.* PTZ–tpy ligand, Fig. S1, ESI†).[28,29] Nonetheless, the orbitals carrying the excess charge on the PTZ–tpy ligand are spatially orthogonal to

Table 1 Driving force ($-\Delta G$),[29] reorganization energy (λ), electronic coupling (H_{DA}) and activation energy ($\Delta G^{\ddagger}$) for ET2 in **1–3** dissolved in dichloromethane

	1	**2**	**3**
$-\Delta G$/eV	0.56	0.43	0.40
λ/eV	1.36	1.17	0.77
H_{DA}/cm^{-1}	35	28	5
$\Delta G^{\ddagger}$/eV	0.1	0.1	0.04

Published on 05 April 2019. Downloaded by Thueringer Universitats Landesbibliothek Jena on 7/11/2019 3:48:35 PM.

the orbitals on the tpy–C_{60} ligand (see Fig. 3). Superexchange, however, requires (at least fractional) orbital overlap. Hence, ET2 *via* superexchange can only occur in thermally activated geometrical structures, *i.e.* slightly distorted geometries of the photosensitizer. Consequently, stronger temperature dependence for superexchange in **1** and **2** is observed than for hopping in the longest triad **3**. This finding highlights the specific electronic properties of the Ru(tpy)$_2$ photosensitizer in the D–S–A triad. In the literature, which investigated the temperature dependent k_{ET}[9,17–21] electron transfer from (rather) planar organic photosensitizers, *i.e.* excited C_{60}, porphyrin and perylene derivatives, k_{ET} *via* hopping is generally found to be more temperature dependent than the rate of superexchange. In such molecular architectures,[9,17–21] the thermal population of a specific conformation of the photosensitizers is not necessarily required to trigger superexchange.

Photoinduced dynamics in triads containing a PTZ electron donor, a Ru(tpy)$_2$ photosensitizer (P) and a C_{60} electron acceptor were studied by temperature dependent fs transient absorption spectroscopy. Particular focus was put on the mechanism of the second electron transfer $PTZ^{\bullet+}{-}P^{\bullet-}{-}C_{60} \xrightarrow{ET2} PTZ^{\bullet+}{-}P{-}C_{60}{}^{\bullet-}$. Studies on the temperature- and distance-dependent electron transfer rates reveal that ET2 occurs *via* hopping in the longest triad while for the two short triads superexchange is operative. Electron transfer *via* superexchange shows a much more pronounced temperature dependence compared to hopping, which is rationalized by the specific molecular geometry of the Ru(tpy)$_2$ photosensitizer. This finding requires taking the rule of thumb according to which a relatively weak temperature dependence of an electron transfer process indicates superexchange being operative with caution. Instead, the specific nature of the photosensitizer has to be considered. Our previous work conducted at room temperature[29] showed opposing distance dependence of k_{ET2} in different solvents. A simulation based on Marcus theory and a superexchange model failed to quantitatively rationalize the results. Here, we show that this is indeed due to the fact that hopping, instead of superexchange, is operative in the longest triad.

This research is supported by the CSC and the Deutsche Forschungsgeminschaft (DFG, grant no. SCHU1229-16/1).

Conflicts of interest

There are no conflicts to declare.

Notes and references

1 O. S. Wenger, *Chem. Soc. Rev.*, 2011, **40**, 3538–3550.
2 M. Natali, S. Campagna and F. Scandola, *Chem. Soc. Rev.*, 2014, **43**, 4005–4018.
3 M. Gilbert and B. Albinsson, *Chem. Soc. Rev.*, 2015, **44**, 845–862.
4 A. Shah, B. Adhikari, S. Martic, A. Munir, S. Shahzad, K. Ahmad and H.-B. Kraatz, *Chem. Soc. Rev.*, 2015, **44**, 1015–1027.
5 D. D. Powell, M. R. Wasielewski and M. A. Ratner, *J. Phys. Chem. B*, 2017, **121**, 7190–7203.
6 H. Oberhofer, K. Reuter and J. Blumberger, *Chem. Rev.*, 2017, **117**, 10319–10357.
7 M. E. Walther and O. S. Wenger, *Inorg. Chem.*, 2011, **50**, 10901–10907.
8 A. B. Ricks, K. E. Brown, M. Wenninger, S. D. Karlen, Y. A. Berlin, D. T. Co and M. R. Wasielewski, *J. Am. Chem. Soc.*, 2012, **134**, 4581–4588.
9 M. G. Gatty, A. Kahnt, L. J. Esdaile, M. Hutin, H. L. Anderson and B. Albinsson, *J. Phys. Chem. B*, 2015, **119**, 7598–7611.
10 W. B. Davis, W. A. Svec, M. A. Ratner and M. R. Wasielewski, *Nature*, 1998, **396**, 60–63.
11 A. M. Scott and M. R. Wasielewski, *J. Am. Chem. Soc.*, 2011, **133**, 3005–3013.
12 M. E. Walther and O. S. Wenger, *ChemPhysChem*, 2009, **10**, 1203–1206.
13 C. Schubert, J. T. Margraf, T. Clark and D. M. Guldi, *Chem. Soc. Rev.*, 2015, **44**, 988–998.
14 T. Miura, R. Carmieli and M. R. Wasielewski, *J. Phys. Chem. A*, 2010, **114**, 5769–5778.
15 F. D. Lewis, H. Zhu, P. Daublain, B. Cohen and M. R. Wasielewski, *Angew. Chem., Int. Ed.*, 2006, **45**, 7982–7985.
16 D. Bu, Y. Xiong, Y. N. Tan, M. Meng, P. J. Low, D.-B. Kuang and C. Y. Liu, *Chem. Sci.*, 2018, **9**, 3438–3450.
17 A. Kahnt, J. Kärnbratt, L. J. Esdaile, M. Hutin, K. Sawada, H. L. Anderson and B. Albinsson, *J. Am. Chem. Soc.*, 2011, **133**, 9863–9871.
18 V. Lloveras, J. Vidal-Gancedo, T. M. Figueira-Duarte, J.-F. Nierengarten, J. J. Novoa, F. Mota, N. Ventosa, C. Rovira and J. Veciana, *J. Am. Chem. Soc.*, 2011, **133**, 5818–5833.
19 F. Giacalone, J. L. Segura, N. Martín and D. M. Guldi, *J. Am. Chem. Soc.*, 2004, **126**, 5340–5341.
20 M. Wielopolski, G. de Miguel Rojas, C. van der Pol, L. Brinkhaus, G. Katsukis, M. R. Bryce, T. Clark and D. M. Guldi, *ACS Nano*, 2010, **4**, 6449–6462.
21 G. Yzambart, A. Zieleniewska, S. Bauroth, T. Clark, M. R. Bryce and D. M. Guldi, *J. Phys. Chem. C*, 2017, **121**, 13557–13569.
22 A. Weller, *Z. Phys. Chem.*, 1982, **133**, 93–98.
23 J. Kroon, H. Oevering, J. W. Verhoeven, J. M. Warman, A. M. Oliver and M. N. Paddon-Row, *J. Phys. Chem.*, 1993, **97**, 5065–5069.
24 R. H. Goldsmith, O. DeLeon, T. M. Wilson, D. Finkelstein-Shapiro, M. A. Ratner and M. R. Wasielewski, *J. Phys. Chem. A*, 2008, **112**, 4410–4414.
25 D. L. Ashford, C. R. K. Glasson, M. R. Norris, J. J. Concepcion, S. Keinan, M. K. Brennaman, J. L. Templeton and T. J. Meyer, *Inorg. Chem.*, 2014, **53**, 5637–5646.
26 M. Abrahamsson, H.-C. Becker and L. Hammarström, *Dalton Trans.*, 2017, **46**, 13314–13321.
27 A. Pannwitz and O. S. Wenger, *J. Am. Chem. Soc.*, 2017, **139**, 13308–13311.
28 Y. Luo, K. Barthelmes, M. Wächtler, A. Winter, U. S. Schubert and B. Dietzek, *Chem. – Eur. J.*, 2017, **23**, 4917–4922.
29 Y. Luo, K. Barthelmes, M. Wächtler, A. Winter, U. S. Schubert and B. Dietzek, *J. Phys. Chem. C*, 2017, **121**, 9220–9229.
30 K. Barthelmes, A. Winter and U. S. Schubert, *Eur. J. Inorg. Chem.*, 2016, 5132–5142.
31 J. T. Hewitt, P. J. Vallett and N. H. Damrauer, *J. Phys. Chem. A*, 2012, **116**, 11536–11547.
32 Y. Luo, J. H. Tran, M. Wächtler, M. Schulz, K. Barthelmes, A. Winter, S. Rau, U. S. Schubert and B. Dietzek, *Chem. Commun.*, 2019, **55**, 2273–2276.
33 W. B. Davis, M. A. Ratner and M. R. Wasielewski, *J. Am. Chem. Soc.*, 2001, **123**, 7877–7886.
34 E. A. Weiss, M. J. Tauber, R. F. Kelley, M. J. Ahrens, M. A. Ratner and M. R. Wasielewski, *J. Am. Chem. Soc.*, 2005, **127**, 11842–11850.
35 P. V. James, P. K. Sudeep, C. H. Suresh and K. G. Thomas, *J. Phys. Chem. A*, 2006, **110**, 4329–4337.
36 N. Li, K. Jia, S. Wang and A. Xia, *J. Phys. Chem. A*, 2007, **111**, 9393–9398.

Electronic Supplementary Material (ESI) for ChemComm.
This journal is © The Royal Society of Chemistry 2019

Supporting Information

Superexchange on the Fast Lane – Intramolecular electron transfer in a molecular triad occurs by conformationally-gated superexchange

Yusen Luo,[1,2] Maria Wächtler,[1,2] Kevin Barthelmes,[3,4] Andreas Winter,[3,4] Ulrich S. Schubert[3,4] and Benjamin Dietzek*[1,2,4]

[1]Institute of Physical Chemistry and Abbe Center of Photonics, Friedrich Schiller-University Jena, Helmholtzweg 4, 07743 Jena, Germany

[2]Department Functional Interfaces, Leibniz Institute of Photonic Technology (IPHT), Albert-Einstein-Straβe 9, 07745 Jena, Germany

[3]Laboratory of Organic and Macromolecular Chemistry (IOMC), Friedrich Schiller-University Jena, Humboldtstraβe 10, 07743 Jena, Germany

[4]Center for Energy and Environmental Chemistry Jena (CEEC Jena), Friedrich Schiller-University Jena, Philosophenweg 7a, 07743 Jena, Germany

**Corresponding author:* *benjamin.dietzek@leibniz-ipht.de*

Experimental details

The synthesis, steady-state emission spectra, electrochemical properties and photoinduced dynamics of **1–3** at room temperature have been reported elsewhere.[1-3]

Time-Resolved Spectroscopy. Femtosecond (fs) transient absorption (TA) spectra were collected by using a previously reported home-built pump-probe laser system which is based on an amplified Ti: Sapphire oscillator (1 kHz, 800 nm).[4] Samples were excited by pump pulse centered at 520 nm (TOPAS-C, Lightconversion Ltd.) with a duration of 80 fs. The power of the pump beam at the sample position was kept at 0.35 mW, corresponding to an energy of 0.7 μJ per pump pulse. A white light supercontinnum generated by focusing a fraction of the fundamental in a CaF_2 plate is used to probe the samples in a wide spectral range (340 to 750 nm). The pump beam is delayed in time with respect to the probe beam by means of an optical delay line and the polarization between probe and pump is set at the magic angle (54.7°). For TA spectroscopy the samples are placed in a 1 cm cuvette (with an optical density of 0.24 at the excitation wavelength) which is placed in a temperature-controlled cryostat (Optistat DN, Oxford Instrument) cooled with liquid nitrogen. Temperatures were set by a temperature controller (ITC 503S, Oxford Instruments) and the actual temperature inside the cuvette is monitored by a temperature sensor connected to a digital multimeter (Keithley 2000 multimeter). A fresh solution is used for measurement at each temperature. The fs TA spectra are displayed after chirp correction. The fs TA data were analyzed by a global multi-exponential fit after exclusion of a temporal window of 500 fs around time-zero in order to avoid contributions of the coherent-artifact region to the data analysis. Furthermore, a spectral band of ca. 20 nm around the pump-wavelength is omitted from the data analysis due to pump-scatter in this spectral range. During all experiments the sample integrity was ensured by recording UV/Vis absorption spectra at room temperature before and after each fs TA measurement.

Relaxation scheme of triads upon excitation

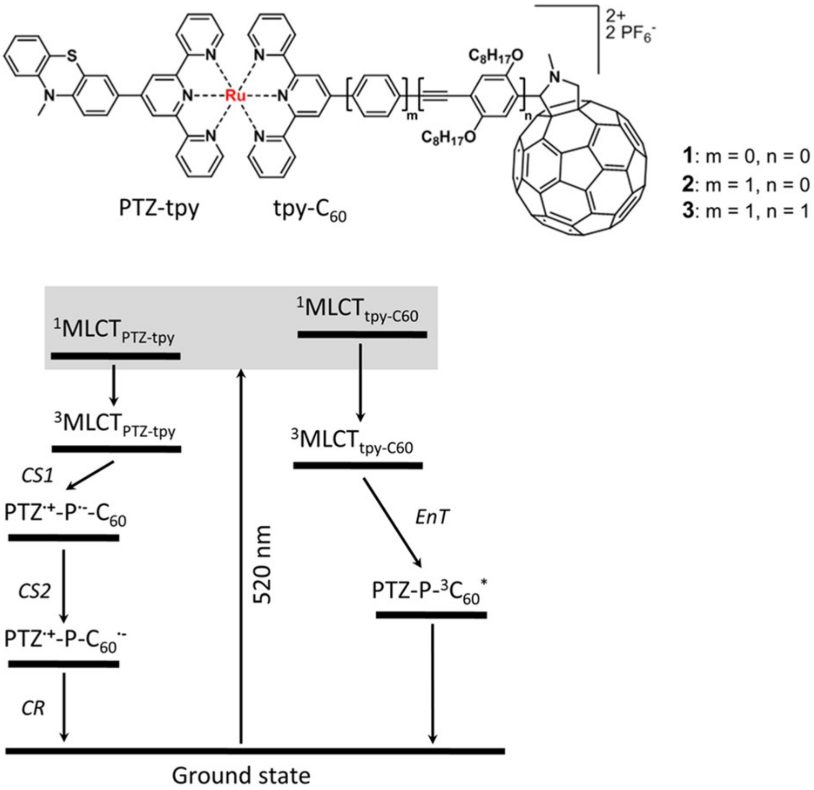

Figure S1. Relaxation processes for **1-3** which refer to the model proposed at room temperature.[1,2] Terpyridine (tpy) ligand connected with *N*-methylphenothiazine (PTZ) and fullerene (C_{60}) are named as PTZ-tpy and tpy-C_{60}, respectively. Excitation of $Ru(tpy)_2$ photosensitizer generates two differently distributed MLCT states, *i.e.* $MLCT_{PTZ\text{-}tpy}$ and $MLCT_{tpy\text{-}C60}$, which decays *via* electron transfer (left side) and energy transfer (right side), respectively.

Temperature dependent fs TA spectra of **1**

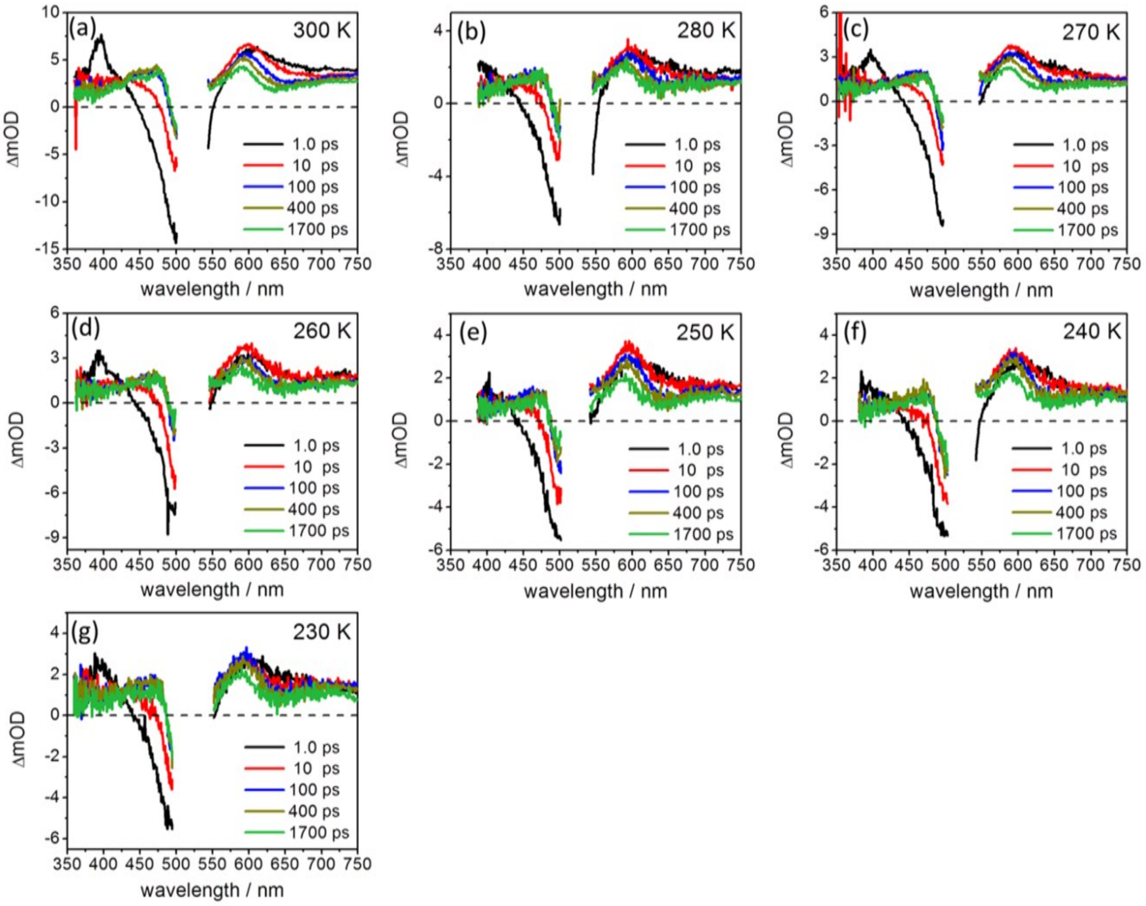

Figure S2. fs transient absorption spectra of **1** upon excitation at 520 nm in dichloromethane at selected delay times at temperature regions from 300 to 230 K.

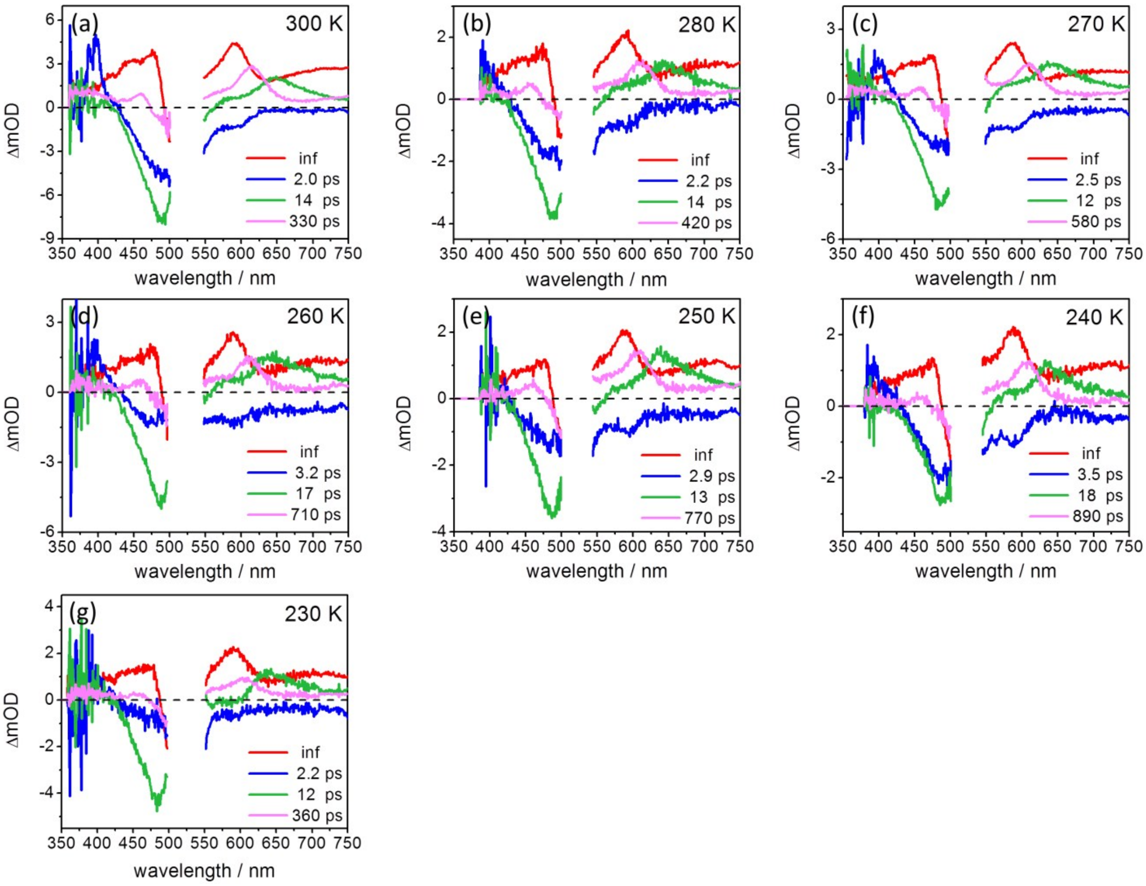

Figure S3. Decay-associated spectra of **1** resulting from the global fit upon excitation at 520 nm in dichloromethane.

We would like to point out that the fs TA data at 230 K (Figure S3g) yields three kinetic processes which are all faster than the corresponding process at higher temperatures. Meanwhile the spectral features of the second and third components in Figure S3g are different to the other data. Thus, the data point of the shortest triad **1** at the lowest temperature 230 K was not included in the Marcus analysis in the main text.

Temperature dependent fs TA spectra of **2**

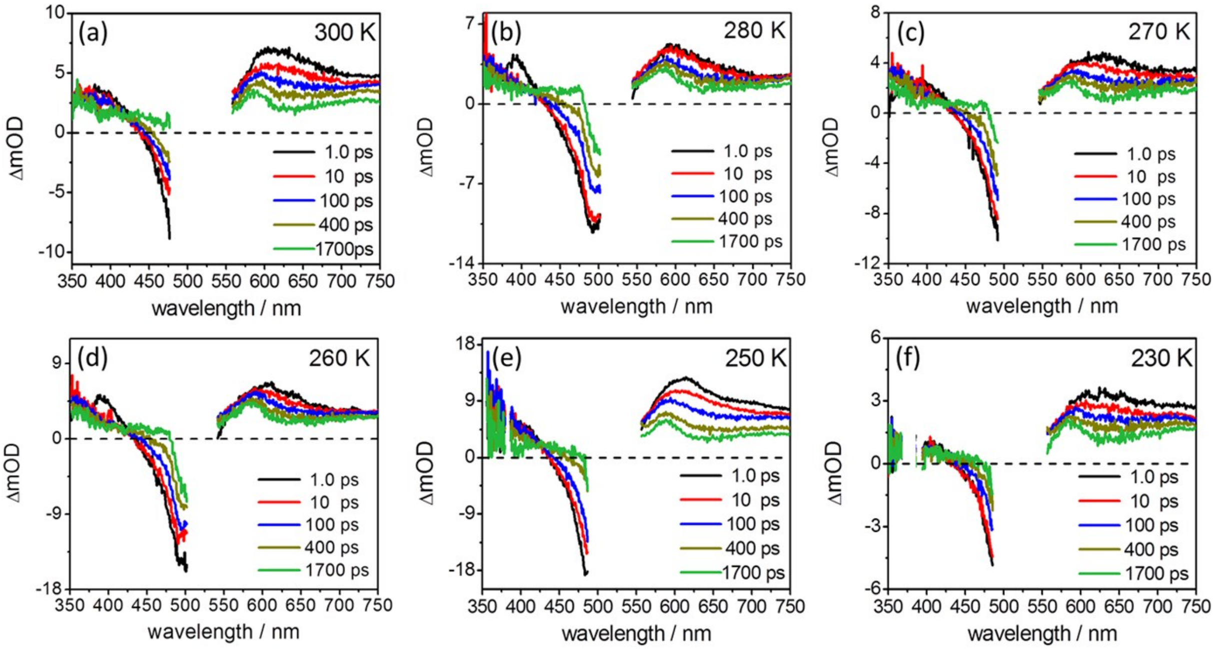

Figure S4. fs transient absorption spectra of **2** upon excitation at 520 nm in dichloromethane at selected delay times at temperature regions from 300 to 230 K.

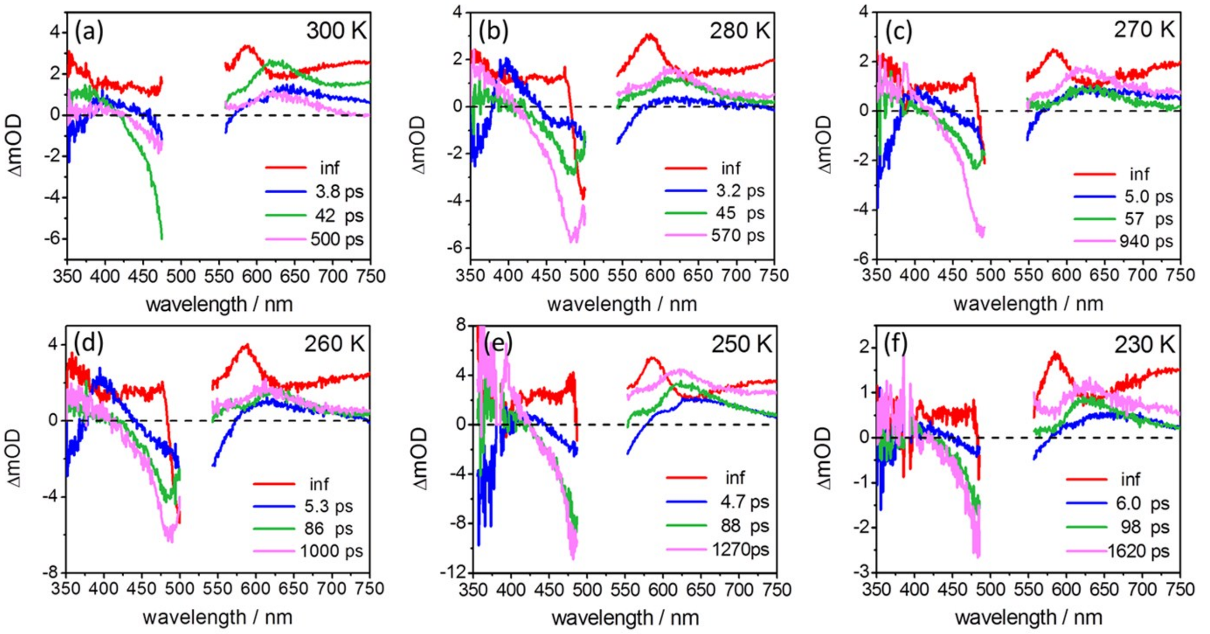

Figure S5. Decay-associated spectra of **2** resulting from the global fit upon excitation at 520 nm in dichloromethane.

Temperature dependent fs TA spectra of **3**

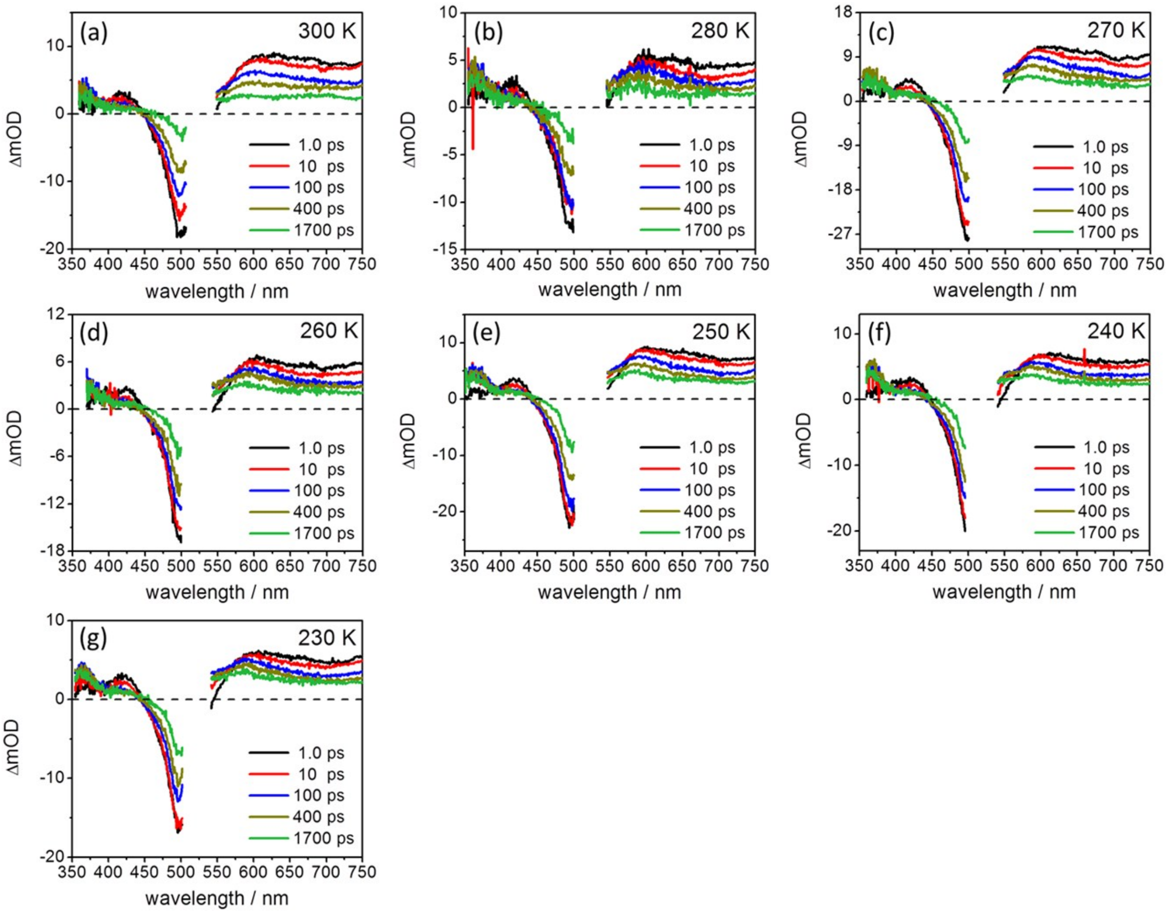

Figure S6. fs transient absorption spectra of **3** upon excitation at 520 nm in dichloromethane at selected delay times at temperature regions from 300 to 230 K.

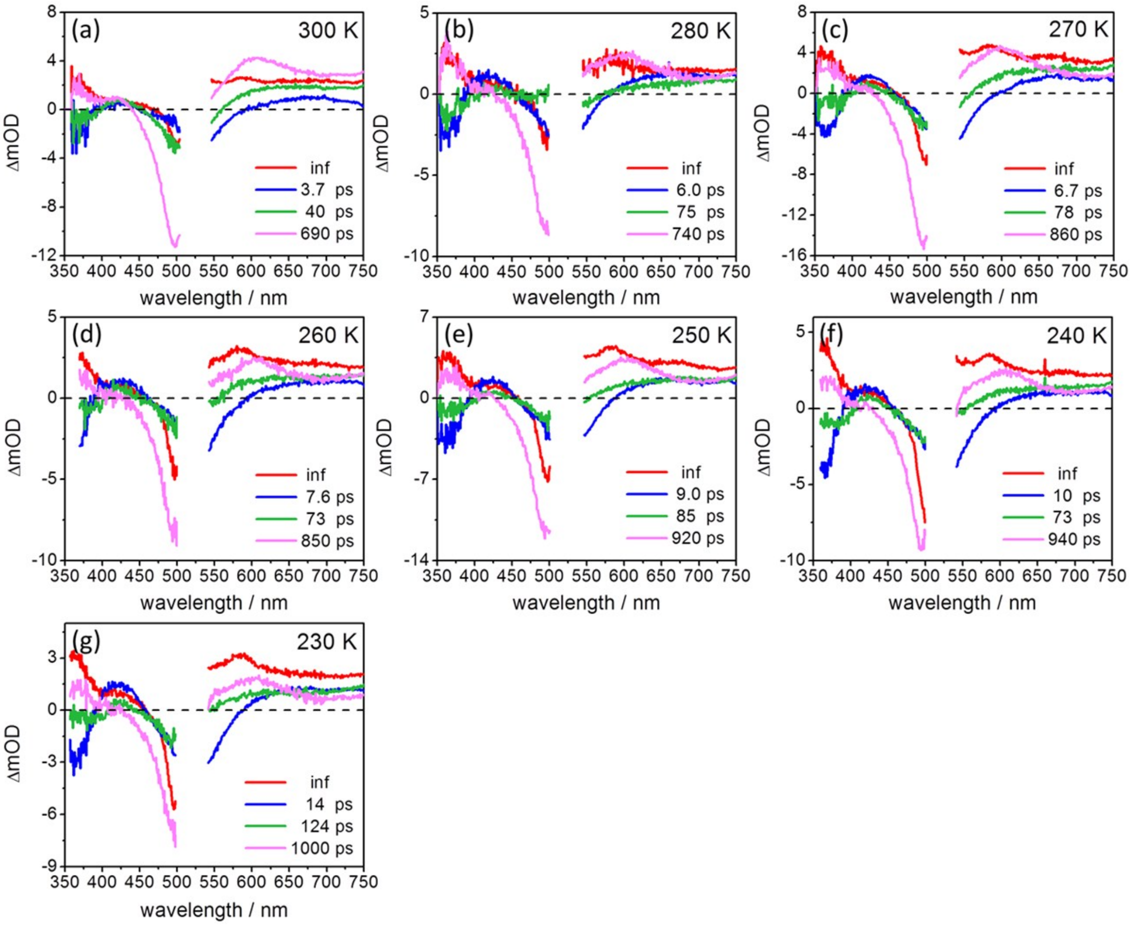

Figure S7. Decay-associated spectra of **3** resulting from the global fit upon excitation at 520 nm in dichloromethane.

Estimation of reorganization energy and the temperature dependence

$$\lambda = \lambda_i + \lambda_o \tag{1}$$

$$\lambda_o = \frac{e^2}{4 \cdot \pi \cdot \varepsilon_0} \cdot \left(\frac{1}{2a_1} + \frac{1}{2a_2} - \frac{1}{R_{DA}} \right) \cdot \left(\frac{1}{n^2} - \frac{1}{\varepsilon_s} \right) \tag{2}$$

where λ_i and λ_o represent the inner and outer reorganization energy, respectively.[5] λ_i reflects the free energy change associated with the nuclear bond length changes within molecules while λ_o accounts for the reorganization of the surrounding chemical environment, *e.g.* solvent molecules. In the simplest model, electron donor and acceptor are treated as spheres with radii a_1 and a_2.[6] R_{DA} is the distance between donor and acceptor. n and ε_s represent refractive index and dielectric constant of the solvent involved during charge transfer, respectively. ε_0 is the vacuum permittivity (8.85×10^{-12} F/m).

For this triad system:

1. λ_i is estimated to be 0.1 eV[6,7] and commonly treated as distance[6] and temperature independent.[8,9]

2. Both n and ε_s are temperature dependent, $\varepsilon_s(T) = a + bT + cT^2 + dT^3$, for dichloromethane, $a = 0.40452 \times 10^2$, $b = -0.17748 \times 10^0$, $c = 0.23942 \times 10^{-3}$, $d = 0$;[10] for dichloromethane $n(T) = 1.59078 - 5.66 \times 10^{-4}\ T$.[11]

3. For the first electron transfer (PTZ-$^3P^*$-C_{60}→$PTZ^{\cdot+}$-$P^{\cdot-}$-C_{60}), PTZ and Ru complex are the electron donor (a_1 = 4 Å) and acceptor (a_2 = 5 Å), respectively. The center-to-center distance R_{DA} is 9.6 Å. For the second electron transfer ($PTZ^{\cdot+}$-$P^{\cdot-}$-C_{60}→$PTZ^{\cdot+}$-P-$C_{60}^{\cdot-}$), reduced Ru complex and C_{60} are the electron donor (a_1 = 5 Å) and acceptor (a_2 = 4.5 Å), respectively. The center-to-center distance R_{DA} is 9.3, 13.4 and 20.8 Å for **1**, **2** and **3**, respectively. Note: the parameters a_1, a_2 and R_{DA} were estimated from the neutral, optimized molecular structures.[2,3]

For *ET1*, due to the same electron donor, electron acceptor and the same donor-acceptor distance, identical reorganization energy will be produced which was already shown in a previous study.[12] The calculated reorganization energy for *ET2* as a function of temperature is summarized in Table S2-4.

Temperature dependence of driving forces

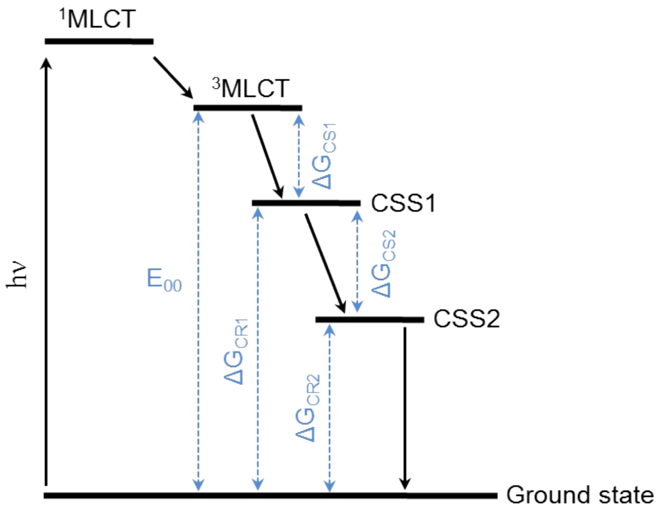

$$\Delta G_{CS1} = e\,(E_{D^+/D} - E_{A/A^-}) - E_{00} - \frac{e^2}{4\pi\varepsilon_0 \varepsilon R_{DA}} \tag{3}$$

$$\Delta G_{CR1} = -\,\Delta G_{CS1} - E_{00} \tag{4}$$

For the first electron transfer step, the radical pairs are $tpy^{\cdot -}$ / $PTZ^{\cdot +}$; E_{00} is the energy difference between the thermalized, lowest ^{3}MLCT excited state and ground state of Ru complex. E_{00} is taken to be 2.07 eV.[2]

For the second electron transfer step the radical pairs are $C_{60}^{\cdot -}$ / $PTZ^{\cdot +}$.

$$\Delta G_{CS2} = \Delta G_{CR1} - \Delta G_{CR2} \tag{5}$$

$$\Delta G_{CR2} = e\,(E_{A/A^-} - E_{D^+/D}) + \frac{e^2}{4\pi\varepsilon_0 \varepsilon R_{DA}} \tag{6}$$

The values of $E_{PTZ+/PTZ}$, $E_{tpy/tpy-}$ and $E_{C60/C60-}$ were taken from ref. 3. The influence of temperature on driving forces is caused by the temperature dependent dielectric constant (ε) of dichloromethane.

Summary of time and rate constants for *ET2*

Table S1. Temperature dependence of time constants and the corresponding rate constants for the second electron transfer process in **1**–**3** obtained from the global fit of fs TA data.

	τ_{ET2} / ps			$k_{ET2} \times 10^9$ / s^{-1}		
T /K	**1**	**2**	**3**	**1**	**2**	**3**
300	330	500	690	3.0	2.0	1.5
280	420	570	740	2.4	1.8	1.4
270	580	940	860	1.7	1.1	1.2
260	710	1000	850	1.4	1.0	1.2
250	770	1270	920	1.3	0.8	1.1
240	890	–[a]	940	1.1	–[a]	1.1
230	–[b]	1620	1000	–[b]	0.6	1.0

[a] fs TA data for **2** at 240 K were not collected. [b] The data for **1** at 230 K is not included here because of the changed TA spectral features, see Figure S3.

Summary of theoretical estimation for *ET2*

Table S2. Summary of the estimated temperature dependent dielectric constant (ε) and refractive index (n) of dichloromethane as well as reorganization energy (λ_{ET2}), driving force ($-\Delta G_{ET2}$), activation energy ($\Delta G^{‡}_{ET2}$) associated with the second electron transfer in triad **1**.

T / K	ε	n	λ_{ET2} / eV	$-\Delta G_{ET2}$ / eV	$\Delta G^{‡}_{ET2}$ / eV
300	8.7558	1.4210	0.668	0.559	0.004
270	9.9861	1.4380	0.672	0.569	0.004
250	11.0458	1.4493	0.675	0.576	0.004
230	12.2969	1.4606	0.678	0.582	0.003

Table S3. Summary of the calculated temperature dependent dielectric constant (ε) and refractive index (n) of solvent dichloromethane as well as reorganization energy (λ_{ET2}), driving force ($-\Delta G_{ET2}$), activation energy ($\Delta G^{‡}_{ET2}$) associated with the second electron transfer in triad **2**.

T / K	ε	n	λ_{ET2} / eV	$-\Delta G_{ET2}$ / eV	$\Delta G^{‡}_{ET2}$ / eV
300	8.7558	1.4210	0.847	0.431	0.051
270	9.9861	1.4380	0.852	0.443	0.049
250	11.0458	1.4493	0.856	0.451	0.048
230	12.2969	1.4606	0.859	0.459	0.047

Table S4. Summary of the calculated temperature dependent dielectric constant (ε) and refractive index (n) of solvent dichloromethane as well as reorganization energy (λ_{ET2}), driving force ($-\Delta G_{ET2}$), activation energy ($\Delta G^{‡}_{ET2}$) associated with the second electron transfer in triad **3**.

T / K	ε	n	λ_{ET2} / eV	$-\Delta G_{ET2}$ / eV	$\Delta G^{‡}_{ET2}$ / eV
300	8.7558	1.4210	0.995	0.403	0.088
270	9.9861	1.4380	1.001	0.418	0.085
250	11.0458	1.4493	1.006	0.428	0.083
230	12.2969	1.4606	1.010	0.437	0.081

The influence of temperature on solvent dielectric properties, *i.e.* dielectric constant ε and refractive index n, which may change λ (eq S1-2) and $-\Delta G_{ET}$ (eq S3-6), is considered in this work. It should be noted that the single linear relation indicated by the Marcus equation in the main text can really be expected when both λ and the term $(\lambda+\Delta G)^2/4\lambda$ (*i.e.* activation energy, $\Delta G_{ET}{}^{\ddagger}$) are temperature independent.[13] Otherwise, deviation from single linear regression would be observed because of the impact of temperature on solvent dielectric properties.[13] The previous study has shown that for the first electron transfer process both λ and $\Delta G_{ET}{}^{\ddagger}$ are insensitive to temperature change.[12] For the second electron transfer, according to Table S2-4, λ and $\Delta G_{ET}{}^{\ddagger}$ are constant with temperature which show maximum changes smaller than 2% and 8%, respectively. Hence, we conclude that the solvent itself would not cause significant deviations due to temperature change.

Temperature dependence of *ET1*

Table S5. Temperature dependence of time constants and the corresponding rate constants for the second electron transfer process (k_{ET1}) in **1**–**3** obtained from the global fit of fs TA data.

	τ_{ET1} / ps			$k_{ET1} \times 10^{11}$ / s^{-1}		
T / K	**1**	**2**	**3**	**1**	**2**	**3**
300	2.0	3.8	3.0	5.0	2.6	2.7
280	2.2	3.2	6.0	4.5	3.1	1.7
270	2.5	5.0	6.7	4.0	2.0	1.5
260	3.2	5.3	7.6	3.1	1.9	1.3
250	2.9	4.7	9.0	3.4	2.1	1.1
240	3.5	–	10	2.9	–	1.0
230	–	6.0	14	–	1.7	0.7

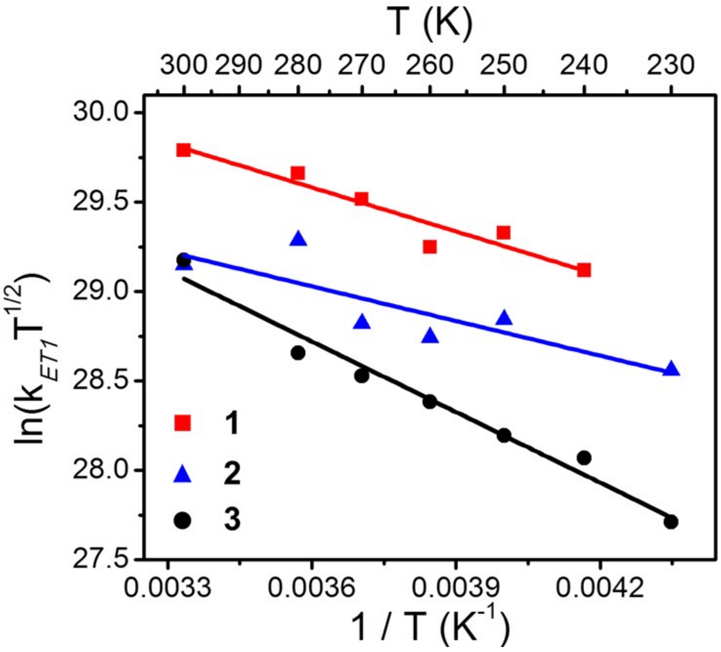

Figure S8. Plots of $\ln(k_{ET1} \cdot T^{1/2})$ *vs.* 1/T for the first electron transfer process *ET1* in **1** (red square), **2** (blue triangle) and **3** (black circle) with the corresponding linear fit according to eqn. (2).

Table S6. Summary of driving force (–ΔG), reorganization energy (λ), electronic coupling (H_{DA}) and activation energy ($\Delta G^{\ddagger}$) obtained from the experimental results for *ET1* in **1**–**3**.

	1	**2**	**3**
$-\Delta G$ / eV	0.23	0.26	0.24
λ / eV	0.67	0.63	0.86
H_{DA} / cm^{-1}	157	86	265
$\Delta G^{\ddagger}$ / eV	0.07	0.05	0.1

Concerning the *ET1* (temperature dependence of k_{ET1} see Figure S8) for which identical PTZ donor, donor-acceptor distance and chemical linkage are involved, Table S6 indicates very similar –ΔG values for **1**–**3** which vary by only 10% from 0.26 (**2**) to 0.23 (**1**). Likewise, λ is rather similar for **1** (0.67 eV) and **2** (0.63 eV). However, for **3** λ is approximately 36% larger (0.86 eV). Noteworthily, H_{DA} values are quite different amongst the investigated triads. H_{DA} decreases in the order **3** (265 cm^{-1}) > **1** (157 cm^{-1}) > **2** (86 cm^{-1}). This observation can be rationalized by the different substitution on the tpy–C_{60} ligand.[12] Similar results have recently been reported in structurally related dyad systems.[12] The variations in λ and H_{DA} amongst the triads can be rationalized by considering the electron-rich $-OC_8H_{17}$ groups in **3**. They indirectly increase the electron density at the photoactive $Ru(tpy)_2$-core and increase λ and H_{DA}.[12] **1** and **2** on the other hand contain pure electron-withdrawing substituents on the tpy-C_{60} ligand, the electronic effect of which apparently decrease the electronic coupling underlying *ET1*.[12]

REFERENCES

1. Y. Luo, K. Barthelmes, M. Wächtler, A. Winter, U. S. Schubert and B. Dietzek, *Chem. Eur. J.*, 2017, **23**, 4917–4922.

2. Y. Luo, K. Barthelmes, M. Wächtler, A. Winter, U. S. Schubert and B. Dietzek, *J. Phys. Chem. C*, 2017, **121**, 9220–9229.

3. K. Barthelmes, A. Winter and U. S. Schubert, *Eur. J. Inorg. Chem.*, 2016, 5132–5142.

4. M. Wächtler, J. Kübel, K. Barthelmes, A. Winter, A. Schmiedel, T. Pascher, C. Lambert, U. S. Schubert and B. Dietzek, *Phys. Chem. Chem. Phys.*, 2016, **18**, 2350–2360.

5. R. A. Marcus and N. Sutin, *Biochim. Biophys. Acta*, 1985, **811**, 265–322.

6. M. Kuss-Petermann and O. S. Wenger, *Phys. Chem. Chem. Phys.*, 2016, **18**, 18657–18664.

7. E. Göransson, J. Boixel, J. Fortage, D. Jacquemin, H.-C. Becker, E. Blart, L. Hammarström and F. Odobel, *Inorg. Chem.*, 2012, **51**, 11500−11512.

8. J. Kroon, H. Oevering, J. W. Verhoeven, J. M. Warman, A. M. Oliver, M. N. Paddon-Row, *J. Phys. Chem.*, 1993, **97**, 5065–5069.

9. P. Vath, M. B. Zimmt, D. V. Matyushov, G. A. Voth, *J. Phys. Chem. B*, 1999, **103**, 9130–9140.

10. D. R. Lide, editor in chief. *Handbook of Chemistry and Physics*, 84th edition.

11. H. Shekaari, A. Bezaatpour and A.Soltanpour, *J. Chem. Eng. Data*, 2010, **55**, 5927–5931.

12. Y. Luo, J. H. Tran, M. Wächtler, M. Schulz, K. Barthelmes, A. Winter, S. Rau, U. S. Schubert and B. Dietzek, *Chem. Commun.*, 2019, **55**, 2273–2276.

13. J. Kroon, H. Oevering, J. W. Verhoeven, J. M. Warman, A. M. Oliver and M. N. Paddon-Row, *J. Phys. Chem.*, 1993, **97**, 5065–5069.

[P6] Remote Control of Electronic Coupling – Modification of Excited-State Electron Transfer Rates in Ru(tpy)$_2$-Based Donor-Acceptor Systems by Remote Ligand Design

Reproduced with permission from: Y. Luo, J. H. Tran, M. Wächtler, M. Schulz, K. Barthelmes, A. Winter, S. Rau, U. S. Schubert and B. Dietzek, "Remote Control of Electronic Coupling – Modification of Excited-State Electron Transfer Rates in Ru(tpy)$_2$-Based Donor-Acceptor Systems by Remote Ligand Design", *Chem. Commun.*, **2019**, *55*, 2273–2276, with permission from the Royal Society of Chemistry.

ChemComm

COMMUNICATION

View Article Online
View Journal | View Issue

Check for updates

Cite this: *Chem. Commun.*, 2019, 55, 2273

Received 20th December 2018,
Accepted 24th January 2019

DOI: 10.1039/c8cc10075f

rsc.li/chemcomm

Published on 24 January 2019. Downloaded on 3/28/2019 8:55:40 AM.

Remote control of electronic coupling – modification of excited-state electron-transfer rates in $Ru(tpy)_2$-based donor–acceptor systems by remote ligand design†

Yusen Luo,[ab] Jens H. Tran,[a] Maria Wächtler,[ab] Martin Schulz,[a]
Kevin Barthelmes,[cd] Andreas Winter,[cd] Sven Rau,[e] Ulrich S. Schubert[cd] and
Benjamin Dietzek*[abd]

A comprehensive understanding of how the molecular structure influences the electronic coupling is crucial in optimizing (supra) molecular assemblies for photoinduced electron transfer. Here, we report that the electronic coupling underlying electron transfer from a phenothiazine donor to a photoexcited $Ru(tpy)_2$ acceptor is modulated by substitution of the second (remote) tpy-ligand.

Photoinduced electron transfer is a fundamental process in natural and artificial photosynthesis.[1–4] Compared to natural photosynthesis where electron transfer proceeds with unity quantum efficiencies and long-lived charge-separated states (CSS) are generated,[4] the artificial (supra)molecular assemblies need to be optimized to achieve efficient electron transfer and to produce long-lived CSS.[4–7] Optimization of such man-made systems requires an in depth understanding of the interplay between molecular structure and key parameters for electron transfer, *i.e.* electronic coupling (H_{DA}), reorganization energy (λ) and driving force ($-\Delta G^\circ$) according to the semi-classical Marcus theory.[1,3–5] While the impact of molecular structure on λ and $-\Delta G^\circ$ is quite well understood[4,5,8,9] and/or can be estimated quite well from *e.g.* electrochemical measurements (see ESI† for a more detailed description), the factors governing H_{DA} are not fully comprehended yet: the nature of electron donor (D) and electron acceptor (A), the structure of molecular spacers (*e.g.* length[1,3,10,11] and substituents[12–17]) separating D and A as well as the molecular conformation[18–21] have significant effects on H_{DA}: H_{DA} generally decreases with increasing D–A distance.[1,3,10,11] Carbonera and coworkers pointed out that substitution of a molecular spacer in structurally related carotenoid–porphyrin–fullerene triads increased H_{DA} and, thus, significantly increased the charge recombination rate.[13] Albinsson and coworkers reported conformer-dependent electron-transfer rates in a (zinc porphyrin)$_2$–fullerene dyad.[20] The significantly different electron-transfer rates for different molecular conformers were ascribed to the significantly different H_{DA} in the two conformers.[20] Despite these and other careful studies on the structural impact on the electron-transfer rates[1,3,4,10–18] it is difficult to isolate the impact of various structural factors on H_{DA} in photoactive transition metal complexes based D–A systems: altering *e.g.* the chemical nature of D or A will impact not only electronic coupling but also the driving force for electron transfer.

In this contribution, we discuss how electronic coupling underlying the photoinduced electron transfer in a phenothiazine donor–$Ru(tpy)_2$ acceptor complex (*i.e.* **D1**, Fig. 1) can be modified without changing the D–A distance or the chemical nature of the linkage. Tuning H_{DA} is simply achieved by modifying the substituents at the 4′-position of the remote terpyridine ligand (*i.e.* –R, Fig. 1). This ligand does not link the photoactive Ru(II) core to the phenothiazine donor, and hence, it presents a convenient handle to tune the electronic coupling within the paradigm D–A dyad. We vary the substituent R from H atom to C_{60}, phenyl and more extended phenylmethyl, phenylmethoxy and show that H_{DA} values in the systems change significantly albeit similar driving forces, fixed chemical nature of D and identical D–A linkage and consequently fixed distance and mutual arrangement of D and A.

To quantify the H_{DA} values temperature-dependent electron-transfer rates were determined between 300 and 240 K by transient absorption spectroscopy (see Fig. S2–S11 for the full sets of data, ESI†): the $Ru(tpy)_2$-core was excited at 520 nm, *i.e.* the red edge of the MLCT band. For each of the compounds, the TA spectra do not change significantly upon decreasing the temperatures. Hence, the previously developed model to account for the photoinduced processes in **D1** and **T1** at room temperature

---

[a] *Institute of Physical Chemistry and Abbe Center of Photonics, Friedrich Schiller University Jena, Helmholtzweg 4, 07743 Jena, Germany*
[b] *Department Functional Interfaces, Leibniz Institute of Photonic Technology (IPHT), Albert-Einstein-Straße 9, 07745 Jena, Germany. E-mail: benjamin.dietzek@leibniz-ipht.de*
[c] *Laboratory of Organic and Macromolecular Chemistry (IOMC), Friedrich Schiller University Jena, Humboldtstraße 10, 07743 Jena, Germany*
[d] *Center for Energy and Environmental Chemistry Jena (CEEC Jena), Friedrich Schiller University Jena, Philosophenweg 7a, 07743 Jena, Germany*
[e] *Institute for Inorganic Chemistry I, Ulm University, Albert-Einstein-Allee 11, 89081 Ulm, Germany*

† Electronic supplementary information (ESI) available. See DOI: 10.1039/c8cc10075f

This journal is © The Royal Society of Chemistry 2019

View Article Online

Published on 24 January 2019. Downloaded on 3/28/2019 8:55:40 AM.

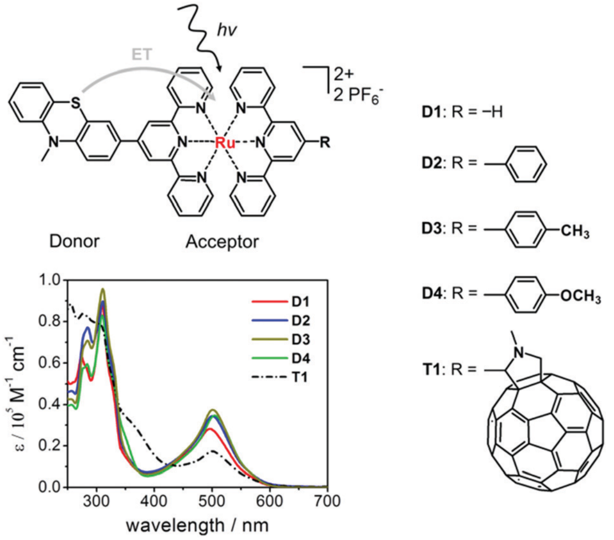

Fig. 1 Molecular dyads **D1–D4** and triad **T1** studied in this work. Upon excitation of $Ru^{II}(tpy)_2$ center, electron transfer (ET) takes place from phenothiazine (PTZ) donor to photo-oxidized Ru(II) in the $Ru(tpy)_2$ center.[23,24] This process is of particular interest and we will focus on it in this work. For detailed decay processes after photoexcitation see Fig. S1 (ESI†). The UV-vis absorption spectra shown here were recorded at room temperature in dichloromethane. For **D1** and **T1** the spectra were taken from ref. 22.

(Fig. S1, ESI†)[23,24] is applied to analyze the temperature-dependent data. Fig. 2 exemplarily show the fs TA spectra of **D1** and **T1** at 270 K: at short delay times, the spectra are dominated by strong ground state bleach (GSB) at around 500 nm and two excited-state absorption (ESA) bands below 450 nm and above 550 nm. At long delay times, *e.g.* at 1700 ps for **D1**, the ESA band shifts from 600 to 580 nm meanwhile a new ESA band appears at 365 nm (Fig. 2a).

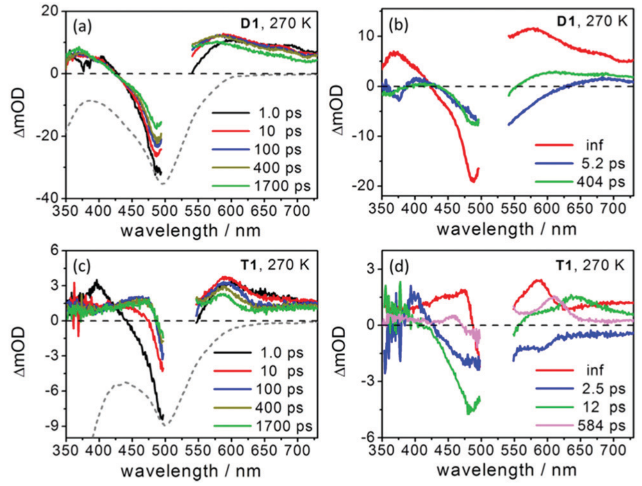

Fig. 2 (a and c) fs TA spectra at selected delay times and (b and d) decay-associated spectra resulting from the global fit of fs TA data collected in a 1 cm cuvette in dichloromethane at 270 K for **D1** (a and b) and **T1** (c and d). The grey dashed line represents the shape of the corresponding inverted ground state absorption spectrum which is scaled to fit the respective figure.

Both features are indicative of the formation of one-electron oxidized phenothiazine ($PTZ^{\bullet+}$) according to spectroelectrochemistry revealing three distinct absorption bands at 365, 473 and 580 nm for $PTZ^{\bullet+}$.[23] The band at 473 nm is not prominent in **D1** (Fig. 2a) which is due to the spectral overlap with the residual GSB. These observations agree with our previous reports on **D1** at room temperature[23] and indicate an electron transfer from the PTZ donor to the excited acceptor $Ru(tpy)_2^*$, *i.e.* the formation of $PTZ^{\bullet+}$–$Ru(tpy)_2^{\bullet-}$. For **T1** at 1700 ps, two distinct ESA bands are observed at 475, 585 and a rather broad feature at around 700 nm (Fig. 2c). The two bands are assigned to the absorption of $PTZ^{\bullet+}$ and the far-red feature is attributed to the absorption of the fullerene triplet state ($^3C_{60}^*$). Different to **D1** (Fig. 2a), the absorption band of $PTZ^{\bullet+}$ at 365 nm is not pronounced in fs TA spectra of **T1** (Fig. 2c) due to the spectral overlap with the negative absorption of reduced fullerene ($C_{60}^{\bullet-}$) below 400 nm.[23] Hence, in **T1** the fully charge-separated state, $PTZ^{\bullet+}$–$Ru(tpy)_2$–$C_{60}^{\bullet-}$, is formed.

Temperature-dependent electron-transfer time constants were obtained by global fits of the fs TA data (see Fig. 2b, d and Fig. S3, S5, S7, S9, S11, ESI†). Previous experiments combining fs/ns transient absorption and resonance Raman spectroscopy showed that the processes associated with τ_1 and τ_2 (Fig. 2b and d) occur from two distinct ^{3}MLCT states (Fig. S1, ESI†).[23] The first kinetic component (τ_1) is characterized by an increased absorption at 365 nm and at 550 to 590 nm corresponding to the absorption of $PTZ^{\bullet+}$.[23] Thus, the respective kinetic component is attributed to the PTZ → $Ru(tpy)_2^*$ electron transfer. It should be noted that the characteristic time constant of the electron transfer is in the same range as previously described rotational motion around the terpyridine-phenyl (tpy-ph) bond (typically also observed on a some-ps timescale for $Ru(tpy)_2$-derived systems[25–27]). This indicates that the PTZ → $Ru(tpy)_2^*$ electron transfer is likely accompanied by planarization of the tpy-ph ligand in **D2–D4**. The second component (τ_2) represents the relaxation of ^{3}MLCT state localized on the terminal tpy ligand, *i.e.* a $^3MLCT_{tpy\text{-}R}$ state: for **D1–D4** it deactivates directly to ground state. For **T1** $^3MLCT_{tpy\text{-}R}$ undergoes an energy transfer yielding a $^3C_{60}^*$ state.[23] The third component in **T1** is attributed to the formation of $PTZ^{\bullet+}$–$Ru(tpy)_2$–$C_{60}^{\bullet-}$.[23,24] To investigate how intramolecular electronic coupling is influenced by substitution of the remote ligand, we focus on the PTZ → $Ru(tpy)_2^*$ electron transfer for which all compounds have the same D and D–A distance.

To obtain H_{DA} values for the photoinduced electron transfer PTZ → $Ru(tpy)_2^*$, the Marcus equation was used:[28–32]

$$\ln\left(k_{ET}\cdot T^{\frac{1}{2}}\right) = \ln\left(\sqrt{\frac{\pi}{\hbar^2\cdot\lambda\cdot k_B}}\cdot H_{DA}{}^2\right) - \frac{(\lambda+\Delta G^\circ)^2}{4\cdot\lambda\cdot k_B\cdot T} \qquad (1)$$

Plotting $\ln(k_{ET}\cdot T^{1/2})$ *vs.* $1/T$ yields a straight line (see Fig. 3b) indicating that both λ and $(\lambda + \Delta G^\circ)^2/4\lambda$ are temperature-independent.[33,34] This is in line with the estimated λ (according to Marcus' dielectric continuum model) and $-\Delta G^\circ$ in the temperature region of 300 to 240 K that λ and the term $(\lambda + \Delta G^\circ)^2/4\lambda$ (*i.e.* the activation energy barrier $\Delta G^\ddagger$) are nearly temperature independent (see Tables S3 and S4, ESI†). Recently, Wenger showed

Published on 24 January 2019. Downloaded on 3/28/2019 8:55:40 AM.

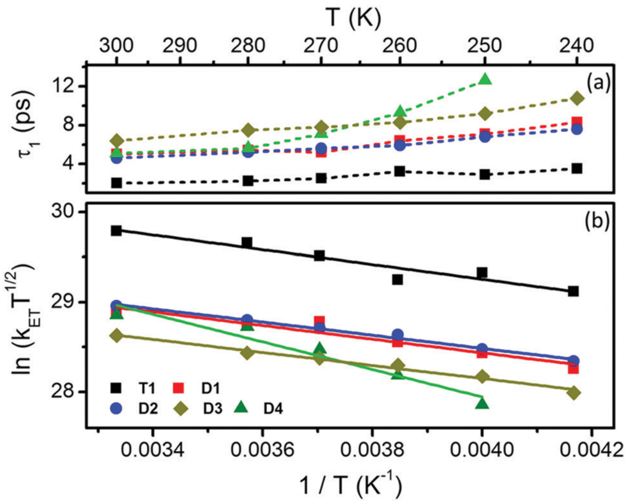

Fig. 3 (a) Temperature dependence of the time constant associated with PTZ → Ru(tpy)$_2$* electron transfer. The dashed lines are only guides to the reader. (b) Plots of ln ($k_{ET}\cdot T^{1/2}$) *vs.* 1/T for **D1–D4** and **T1** with the corresponding linear fit. The adjusted R^2 value of the linear fit is 0.90 (**D1**), 0.99 (**D2**), 0.98 (**D3**), 0.92 (**D4**) and 0.90 (**T1**).

experimentally that $-\Delta G^\circ$ is indeed temperature independent in a related donor–photosensitizer–acceptor system.[35] Under such conditions λ and H_{DA} can be extracted from the slope and the intercept of the linear regression, respectively.[28,29] Experimentally, τ_1 increases with decreasing temperature (Fig. 3a and Table S1, ESI†) indicating reduced electron-transfer rates (k_{ET}) at lower temperatures. The full set of parameters describing electron transfer within Marcus' theory, *i.e.* λ, $-\Delta G^\circ$, H_{DA} and $\Delta G^\ddagger$ extracted from Fig. 3b, is summarized in Table 1.

$-\Delta G^\circ$ for PTZ → Ru(tpy)$_2$* electron transfer varies by only 20% within the investigated series from 0.29 (**D1**) to 0.23 eV (**T1**). Likewise, due to identical D, D–A distance and mutual D–A orientation the reorganization energy (λ) is rather similar for **D1–D3** and **T1** varying from 0.65 (**D3**) to 0.72 eV (**D1**). However, **D4** exhibits a roughly 40% higher λ which indicates that the inner-sphere reorganization energy λ_i must be significantly changed, as the outer-sphere reorganization energy λ_o is not supposed to vary a lot within the assumptions of the dielectric continuum model (eqn (S1) and (S2), ESI†). In contrast to λ and $-\Delta G^\circ$, H_{DA} values are quite different within the series of complexes investigated. They vary by more than 400% from **D3** to **D4** despite of minimal structural differences (see Table 1): **D4**, with the strongly electron-donating substituent –OCH$_3$, shows the strongest coupling (371 cm^{-1}); **T1** with the directly connected strongly electron withdrawing –C$_{60}$ reveals moderate coupling (157 cm^{-1}); for **D1–D3** the H_{DA} values are significantly lower (*i.e.* between 90 and 70 cm^{-1}). Thus, for example, replacing the –H atom at the 4′-position of the terminal tpy ligand in **D1** by –C$_{60}$ (*i.e.* **T1**) causes a roughly 70% increase of H_{DA} between PTZ and Ru(tpy)$_2$* despite the fact that **D1** and **T1** have the same D, D–A linkage and D–A distance. The electron rich –OCH$_3$ group in *para* position of the phenyl ring increases the coupling by a factor of 3 comparing **D2** and **D4**.

Table 1 Summary of driving force ($-\Delta G^\circ$), reorganization energy (λ), electronic coupling (H_{DA}) and activation energy barrier ($\Delta G^\ddagger$) obtained from the experimental results shown in Fig. 3b for the PTZ → Ru(tpy)$_2$* electron-transfer process in **D1–D4** and **T1**

	D1	D2	D3	D4	T1
$-\Delta G^\circ$/eV	0.29[a]	0.26[b]	0.25[b]	0.24[b]	0.23[a]
λ/eV	0.72	0.67	0.65	0.95	0.71
H_{DA}/cm^{-1}	94	90	74	371	157
$\Delta G^\ddagger$/eV	0.064	0.063	0.062	0.13	0.072

[a] Values were taken from ref. 24. [b] Values were obtained from the electrochemical data (Fig. S12, ESI) according to Rehm–Weller equation (eqn (S3) and (S4), ESI).

Similar effects have been reported for mixed-valence Ru^{II}/Ru^{III} complexes.[36,37] Here, the properties of intervalence charge-transfer (IVCT) transitions were altered by design of remote ligands: while this strategy ensured almost identical driving forces in a broad range of substitutions the electronic coupling underlying the IVCT could be altered by 20%. However, this work[36] does not consider photoinduced excited-state electron-transfer reactions in the mixed-valence systems.

To rationalize the control of the donor–acceptor coupling by remote ligand design, we will consider the influence of the substituents –R on the charge densities. Such consideration is based on the fact that H_{DA} will be largely determined by the electronic structure of the molecular fragments involved.[38] Previously published calculations have studied the ground[39] and ^{1}MLCT excited-states[40] of two model Ru(tpy)$_2$ complexes with strongly electron donating (–NH$_2$) and electron withdrawing (–NO$_2$) groups attached to the 4′-position of the tpy ligand *via* a phenyl spacer (ph, see Fig. S13, ESI†).[39,40] Calculations showed an increased π-character and a consequently shortened tpy-ph bond upon introducing the –NH$_2$ substituent. Furthermore, the electron donating group reduces the dihedral angle between ph and tpy in the ground state of the complex.[39] The –NO$_2$ facilitates long-range charge delocalization both in the ground- and excited-state albeit a larger tpy-ph dihedral angle in the ground state.[39,40] Similar effects on the electronic levels of a Ru(II) complex were calculated by Kupfer, who considered the effect of coligand exchange on the electronics of charge-accumulation within a photoactive Ru(II)-complex.[41]

The above discussed literature details the impact of substituents on the electronic situation in related Ru(II) complexes, leaving the question unanswered if such substitutions can be utilized to affect electronic coupling of the photoactive Ru(II) core with an electron donor linked *via* a second non-modified ligand. Comparing the PTZ–Ru(tpy)$_2$* electronic coupling within the series of complexes investigated here, will address this issue (to the best of our knowledge for the first time in a systematic experimental approach). Within the series of the dyads investigated the electron rich –OCH$_3$ substituent drastically increases the PTZ–Ru(tpy)$_2$* coupling as reflected in the H_{DA} value. This is accompanied by a significant increase of λ associated with the PTZ → Ru(tpy)$_2$* electron transfer. This increase in λ is likely associated with a decreased tpy-ph bond length and smaller tpy-ph dihedral angle in **D4** as λ_i can be related to the free energy change associated with bond length changes[42] which upon electron transfer

Published on 24 January 2019. Downloaded on 3/28/2019 8:55:40 AM.

would be different. Thus, the electron rich –OCH_3 substituent in **D4** leads to structural changes within the modified (remote) tpy ligand affecting λ but also to electronic changes altering the electronic coupling underlying PTZ–$Ru(tpy)_2{}^*$ electron transfer. The slight ($\sim$18%) decrease in H_{DA} comparing **D3** to **D2** might stem from the weak electron-donating ability of the $-CH_3$ group. This property causes the tpy-ph unit to be more planar than in **D2**.[39] Consequently, upon photoexcitation of the $Ru(tpy)_2$-photocenter in its MLCT transition, the access charge on the formally reduced ligand(s) becomes somewhat more delocalized, hence, reducing the coupling for the PTZ → $Ru(tpy)_2{}^*$ electron transfer. Alterations of the remote ligand upon introduction of $-C_{60}$, *i.e.* comparing **D1** and **T1**, increase H_{DA} by 70%. The effect of the C_{60}-containing tpy ligand also shifts the Ru^{III}/Ru^{II} oxidation anodically by 120 mV compared to **D1** (Table S2, ESI†). The shifted HOMO apparently impacts the electronic levels on the PTZ-tpy ligand and thus increases the coupling underlying the PTZ → $Ru(tpy)_2{}^*$ electron transfer.

An experimental investigation on the electronic coupling underlying the photoinduced electron transfer in D–A dyads of the form PTZ–(tpy)Ru(tpy–R) is presented. The data reveal the possibility to modulate H_{DA} between the PTZ donor and the Ru(II) acceptor/photosensitizer by a factor of four by changing the remote substituent –R. Altering the electronics in the photoexcited $Ru(tpy)_2{}^*$-photosensitizer, either by delocalization of the relaxed excited-state within the ligand sphere or by modifying the HOMO level of the Ru(II) ion, impacts the electronic coupling for photoinduced electron transfer in the dyad. Thus, the data point towards an additional design parameter for molecular systems, in which realizing efficient and specific electron transfer paths is key to improved function.

This research is supported by the China Scholarship Council.

Conflicts of interest

There are no conflicts to declare.

Notes and references

1 M. Natali, S. Campagna and F. Scandola, *Chem. Soc. Rev.*, 2014, **43**, 4005–4018.
2 M. D. Kärkäs, O. Verho, E. V. Johnston and B. Åkermark, *Chem. Rev.*, 2014, **114**, 11863–12001.
3 M. Gilbert and B. Albinsson, *Chem. Soc. Rev.*, 2015, **44**, 845–862.
4 M. Rudolf, S. V. Kirner and D. M. Guldi, *Chem. Soc. Rev.*, 2016, **45**, 612–630.
5 S. Fukuzumi, K. Ohkubo and T. Suenobu, *Acc. Chem. Res.*, 2014, **47**, 1455–1464.
6 K. A. Mazzio and C. K. Luscombe, *Chem. Soc. Rev.*, 2015, **44**, 78–90.
7 L. Hammarström, *Faraday Discuss.*, 2017, **198**, 549–560.
8 P. Vath and M. B. Zimmt, *J. Phys. Chem. A*, 2000, **104**, 2626–2633.
9 C. Schubert, J. T. Margraf, T. Clark and D. M. Guldi, *Chem. Soc. Rev.*, 2015, **44**, 988–998.
10 M. Kuss-Petermann and O. S. Wenger, *Angew. Chem., Int. Ed.*, 2016, **55**, 815–819.
11 T. Higashino, T. Yamada, M. Yamamoto, A. Furube, N. V. Tkachenko, T. Miura, Y. Kobori, R. Jono, K. Yamashita and H. Imahori, *Angew. Chem., Int. Ed.*, 2016, **55**, 629–633.
12 C. Lambert, G. Nöll and J. Schelter, *Nat. Mater.*, 2002, **1**, 69–73.
13 M. D. Valentin, A. Bisol, G. Agostini and D. Carbonera, *J. Chem. Inf. Model.*, 2005, **45**, 1580–1588.
14 M. P. Eng and B. Albinsson, *Chem. Phys.*, 2009, **357**, 132–139.
15 R. N. Sampaio, E. J. Piechota, L. Troian-Gautier, A. B. Maurer, K. Hu, P. A. Schauer, A. D. Blair, C. P. Berlinguette and G. J. Meyer, *Proc. Natl. Acad. Sci. U. S. A.*, 2018, **115**, 7248–7253.
16 S. E. Miller, A. S. Lukas, E. Marsh, P. Bushard and M. R. Wasielewski, *J. Am. Chem. Soc.*, 2000, **122**, 7802–7810.
17 M. E. Walther and O. S. Wenger, *ChemPhysChem*, 2009, **10**, 1203–1206.
18 Y. Zhao, X. Li, Z. Wang, W. Yang, K. Chen, J. Zhao and G. G. Gurzadyan, *J. Phys. Chem. C*, 2018, **122**, 3756–3772.
19 A. C. Benniston, A. Harriman, P. Li, P. V. Patel and C. A. Sams, *Phys. Chem. Chem. Phys.*, 2005, **7**, 3677–3679.
20 M. U. Winters, J. Kärnbratt, H. E. Blades, C. J. Wilson, M. J. Frampton, H. L. Anderson and B. Albinsson, *Chem. – Eur. J.*, 2007, **13**, 7385–7394.
21 D. M. Guldi, A. Hirsch, M. Scheloske, E. Dietel, A. Troisi, F. Zerbetto and M. Prato, *Chem. – Eur. J.*, 2003, **9**, 4968–4979.
22 K. Barthelmes, A. Winter and U. S. Schubert, *Eur. J. Inorg. Chem.*, 2016, 5132–5142.
23 Y. Luo, K. Barthelmes, M. Wächtler, A. Winter, U. S. Schubert and B. Dietzek, *Chem. – Eur. J.*, 2017, **23**, 4917–4922.
24 Y. Luo, K. Barthelmes, M. Wächtler, A. Winter, U. S. Schubert and B. Dietzek, *J. Phys. Chem. C*, 2017, **121**, 9220–9229.
25 P. P. Laine, F. Bedioui, F. Loiseau, C. Chiorboli and S. Campagna, *J. Am. Chem. Soc.*, 2006, **128**, 7510–7521.
26 K. Barthelmes, J. Kübel, A. Winter, M. Wächtler, C. Friebe, B. Dietzek and U. S. Schubert, *Inorg. Chem.*, 2015, **54**, 3159–3171.
27 R. Siebert, D. Akimov, M. Schmitt, A. Winter, U. S. Schubert, B. Dietzek and J. Popp, *ChemPhysChem*, 2009, **10**, 910–919.
28 M. G. Gatty, A. Kahnt, L. J. Esdaile, M. Hutin, H. L. Anderson and B. Albinsson, *J. Phys. Chem. B*, 2015, **119**, 7598–7611.
29 A. Kahnt, J. Kärnbratt, L. J. Esdaile, M. Hutin, K. Sawada, H. L. Anderson and B. Albinsson, *J. Am. Chem. Soc.*, 2011, **133**, 9863–9871.
30 F. Giacalone, J. L. Segura, N. Martín and D. M. Guldi, *J. Am. Chem. Soc.*, 2004, **126**, 5340–5341.
31 A. M. Scott and M. R. Wasielewski, *J. Am. Chem. Soc.*, 2011, **133**, 3005–3013.
32 M. Kuss-Petermann and O. S. Wenger, *J. Am. Chem. Soc.*, 2016, **138**, 1349–1358.
33 J. Kroon, H. Oevering, J. W. Verhoeven, J. M. Warman, A. M. Oliver and M. N. Paddon-Row, *J. Phys. Chem.*, 1993, **97**, 5065–5069.
34 R. H. Goldsmith, O. DeLeon, T. M. Wilson, D. Finkelstein-Shapiro, M. A. Ratner and M. R. Wasielewski, *J. Phys. Chem. A*, 2008, **112**, 4410–4414.
35 S. Neumann and O. S. Wenger, *Inorg. Chem.*, 2019, **58**, 855–860.
36 J.-Y. Shao and Y.-W. Zhong, *Chem. – Eur. J.*, 2014, **20**, 8702–8713.
37 Y.-W. Zhong, Z.-L. Gong, J.-Y. Shao and J. Yao, *Coord. Chem. Rev.*, 2016, **312**, 22–40.
38 C.-P. Hsu, *Acc. Chem. Res.*, 2009, **42**, 509–518.
39 M. Presselt, B. Dietzek, M. Schmitt, S. Rau, A. Winter, M. Jäger, U. S. Schubert and J. Popp, *J. Phys. Chem. A*, 2010, **114**, 13163–13174.
40 J. Preiß, M. Jäger, S. Rau, B. Dietzek, J. Popp, T. Martínez and M. Presselt, *ChemPhysChem*, 2015, **16**, 1395–1404.
41 S. Kupfer, *Phys. Chem. Chem. Phys.*, 2016, **18**, 13357–13367.
42 G. J. Kavarnos and N. J. Turro, *Chem. Rev.*, 1986, **86**, 401–449.

This journal is © The Royal Society of Chemistry 2019

Electronic Supplementary Material (ESI) for Chemical Communications.
This journal is © The Royal Society of Chemistry 2019

Supporting Information

Remote control of electronic coupling – modification of excited-state electron-transfer rates in Ru(tpy)$_2$-based donor-acceptor systems by remote ligand design

Yusen Luo,[1,2] Jens H. Tran,[1] Maria Wächtler,[1,2] Martin Schulz,[1] Kevin Barthelmes,[3,4] Andreas Winter,[3,4] Sven Rau,[5] Ulrich S. Schubert[3,4] and Benjamin Dietzek*[1,2,4]

[1] *Institute of Physical Chemistry and Abbe Center of Photonics, Friedrich Schiller University Jena, Helmholtzweg 4, 07743 Jena, Germany*

[2] *Department Functional Interfaces, Leibniz Institute of Photonic Technology (IPHT), Albert-Einstein-Straße 9, 07745 Jena, Germany*

[3] *Laboratory of Organic and Macromolecular Chemistry (IOMC), Friedrich Schiller University Jena, Humboldtstraße 10, 07743 Jena, Germany*

[4] *Center for Energy and Environmental Chemistry Jena (CEEC Jena), Friedrich Schiller University Jena, Philosophenweg 7a, 07743 Jena, Germany*

[5] *Institute for Inorganic Chemistry I, Ulm University, Albert-Einstein-Allee 11, 89081 Ulm, Germany*

**Corresponding author: benjamin.dietzek@leibniz-ipht.de*

Experimental details

UV/Vis Spectroscopy. The UV/Vis absorption spectra of **D2**-**D4** were recorded with a Cary 5000 UV/Vis spectrometer (Varian, USA) in a 1 cm cuvette at room temperature.

Time-Resolved Spectroscopy. Femtosecond (fs) transient absorption (TA) spectra were collected by using a previously reported home-built pump-probe laser system which is based on an amplified Ti: Sapphire oscillator (1 kHz, 800 nm).[1] Samples were excited by pump pulse centered at 520 nm (TOPAS-C, Lightconversion Ltd.) with a duration of 80 fs. The power of the pump beam at the sample position was kept at 0.35 mW with a beam diameter of 112 μm, corresponding to 1.86×10^{20} photos m^{-2} per pump pulse. A white light supercontinuum generated by focusing a fraction of the fundamental in a CaF_2 plate is used to probe the samples in a wide spectral range (340 to 750 nm). The pump beam is delayed in time with respect to the probe beam by means of an optical delay line and the polarization between probe and pump is set at the magic angle (54.7°). Temperature-dependent fs TA spectra were recorded by putting the sample in a 1 cm cuvette (optical density 0.24 at 520 nm) which was then placed in a temperature-controlled cryostat (Optistat DN, Oxford Instrument) cooled with liquid nitrogen. Temperatures were set by an intelligent temperature controller (ITC 503S, Oxford Instruments) and the real-time temperature inside the cuvette was monitored by a temperature sensor which was connected to a digital multimeter (Keithley 2000 multimeter). Fresh solution was used for the fs TA measurement at each temperature. All samples have been cooled down until stable before starting the pump-probe experiment. The fs TA spectra were displayed after chirp correction. The fs TA data were analyzed by a global multi-exponential fit after exclusion of a temporal window of 500 fs around time-zero in order to avoid contributions of the coherent-artifact region to the data analysis. Furthermore, a spectral band of ca. 20 nm around the pump-wavelength is omitted from the data analysis due to pump-scatter in this spectral range. For all the time-resolved experiments the stability of samples was ensured by recording the UV/Vis absorption spectra (JASCO V-670 spectrometer) at room temperature before and after fs TA measurement.

Electrochemistry. Cyclic voltammograms (CVs) of **D2**-**D4** were performed in a three-electrode setup consists of a glassy carbon working electrode, a platinum wire counter electrode and an Ag/AgCl reference electrode. CVs were obtained in dichloromethane with a PC-controlled potentiostat (Zahner Zennium Pro). The scan rate was 200 mV/s which kept consistence with the previous electrochemical measurements for **D1** and **T1**.[2] All potentials given in Table S2 refer to ferrocene as standard.

Synthesis and Characterization Data. D1, **T1** and all terpyridine ligands were prepared according to literature procedures.[2] All other chemicals were purchased from commercial suppliers and were used as received. Reactions were monitored by thin-layer chromatography (TLC, silica gel on aluminum sheets with fluorescent marker F254 Merk). ^{1}H-, ^{13}C{H}-NMR were recorded at 20 °C on Bruker Advance AC400 and AC600 spectrometers. Chemical shifts are reported in parts per million relative to tetramethysilane (^{1}H-, ^{13}C{H}-NMR), as external standards. The residual signal of the deuterated solvents [d^3]MeCN, were used as internal standards in ^{1}H- and ^{13}C{H}-NMR experiments. J values are given in Hz. ESI-MS mass spectra were recorded either on a Finnigan MAZ95XL or on a Finnigan MAT SSQ 710. The experimental isotope pattern of the respective compound was compared to the calculated isotope pattern. Presented yields are not optimized.

1) General procedure for [Ru(tpy-Ar)]Cl_3 complexes

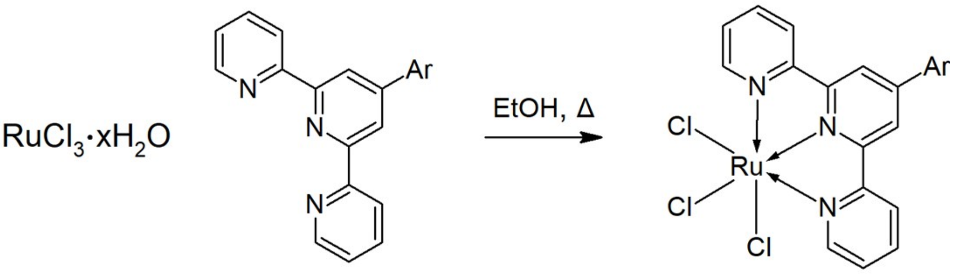

A microwave vial was charged with $RuCl_3$•xH_2O (0.29 mmol), the respective tpy-Ar (0.29 mmol) and EtOH (25 mL). The vial was capped and degassed with nitrogen for 20 min. The suspension was heated to 96 °C for 4h. Subsequently the suspension was filtered and the precipitate was washed with EtOH (30 mL) and diethyl ether (30 mL). After drying *in vacuo* the dark brown crude product was used as received.

[Ru(tpy-Ph)]Cl_3 (124.2 mg, 82%).

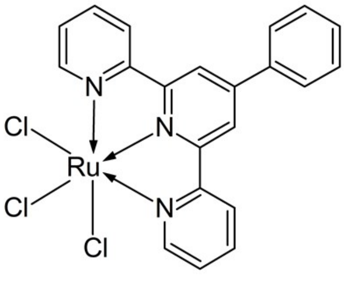

[Ru(tpy-PhMe)]Cl$_3$ (352.9 mg, 89%)

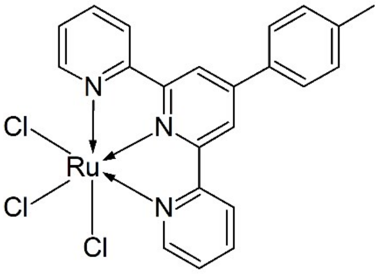

[Ru(tpy-PhOMe)]Cl$_3$ (217.9 mg, 91%)

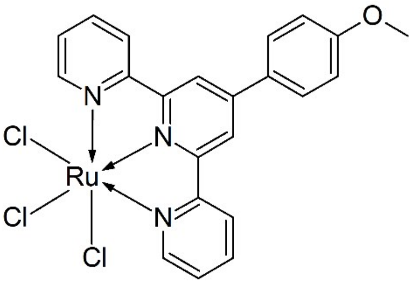

2) General procedure for [Ru(MeCN)$_3$(tpy-Ar)](PF$_6$)$_2$

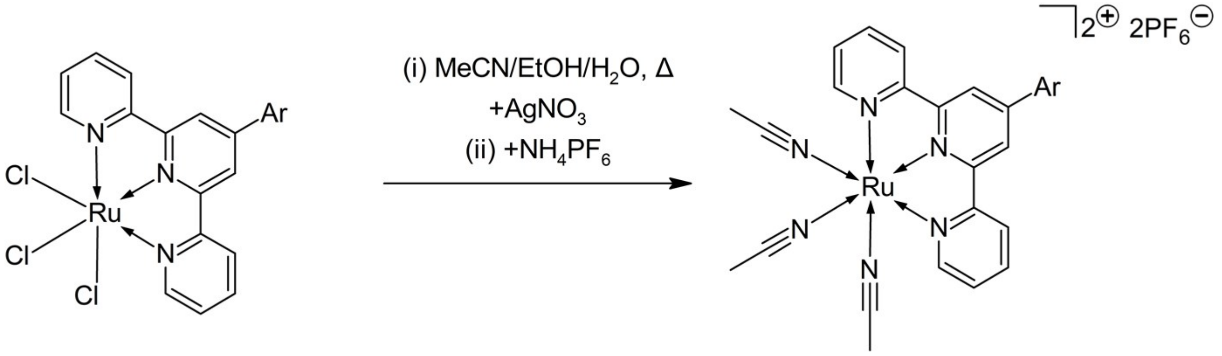

A microwave vial was charged with the respective [Ru(tpy-Ar)]Cl$_3$ (0.17 mmol) AgNO$_3$ (0.17 mmol) and MeCN/EtOH/water (6:1:1, 18 mL). The vial was capped and degassed with nitrogen for 20 min and heated to 80 °C for 4h. Subsequently the solution was filtered to remove the fine AgCl precipitate. Excess NH$_4$PF$_6$ was added to the filtrate and the solution was concentrated *in vacuo*. When precipitation occurred water was added and the suspension was centrifuged. The solid was washed with water (2 × 20 mL). The residue was then dissolved in a minimum of MeCN and the product was precipitated in diethyl ether (30 mL). The suspension was centrifuged and the product was obtained as orange/yellow powder and subsequently dried *in vacuo* and used as received.

$[Ru(MeCN)_3(tpy\text{-}Ph)](PF_6)_2$ (36.6 mg, 26%)

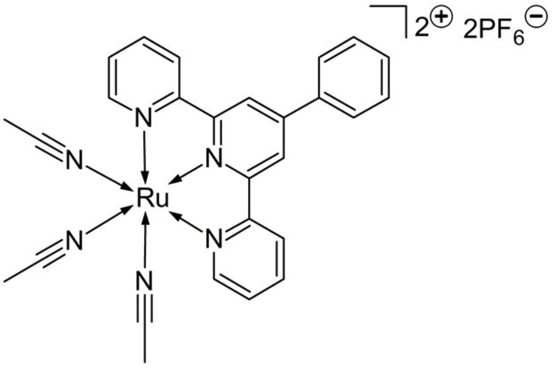

^{1}H NMR (400 MHz, CD_3CN): $\delta = 8.93$ (2H, d, $J = 5.3$ Hz), 8.65 (2H, s), 8.55 (2H, d, $J = 7.9$ Hz), 8.21 (2H, td, $J = 7.9$, 1.5 Hz), 8.01-8.07 (2H, m), 7.73-7.78 (2H, m), 7.66-7.72 (2H, m), 7.64 (1H, d, $J = 7.3$ Hz), 2.75 ppm (3H, s). ^{13}C NMR (101 MHz, CD_3CN): $\delta = 160.0$, 159.6, 155.5, 151.0, 140.1, 137.4, 131.7, 130.6, 129.1, 128.8, 125.2, 121.9 ppm.

$[Ru(MeCN)_3(tpy\text{-}PhMe)](PF_6)_2$ (211.5 mg, 58%)

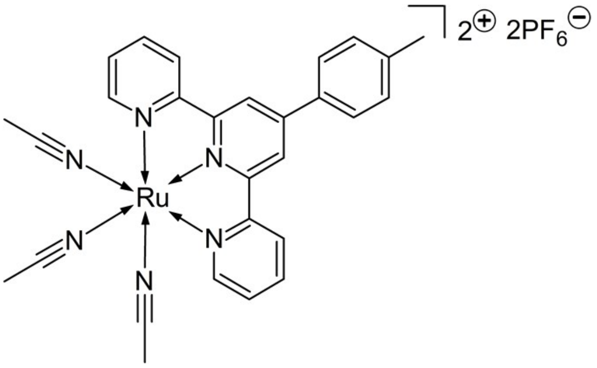

^{1}H NMR (400 MHz, CD_3CN): $\delta = 8.90$-8.96 (2H, m), 8.63 (2H, s), 8.55 (2H, d, $J = 7.9$ Hz), 8.20 (2H, td, $J = 7.9$, 1.8 Hz), 7.94 (2H, d, $J = 8.5$ Hz), 7.75 (2H, ddd, $J = 7.7$, 5.5, 1.2 Hz), 7.50 (2H, d, $J = 7.9$ Hz), 2.75 (3H, s), 2.49 ppm (3H, s). ^{13}C NMR (101 MHz, CD_3CN): $\delta = 159.9$, 159.7, 155.5, 142.4, 140.0, 134.4, 131.4, 131.3, 129.0, 128.6, 125.1, 121.5, 118.4, 118.5, 21.4, 4.3 ppm.

$[Ru(MeCN)_3(tpy\text{-}PhOMe)](PF_6)_2$ (88.1 mg, 34%)

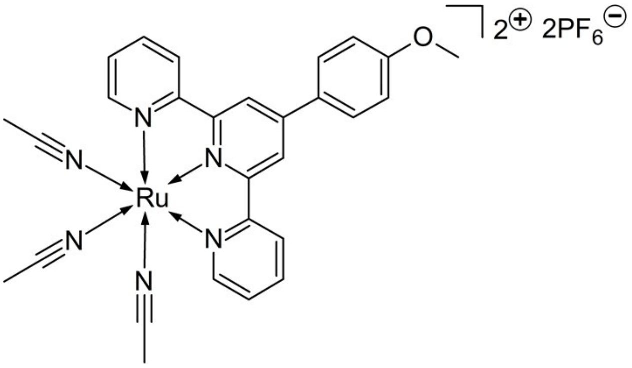

^1H NMR (400 MHz, CD_3CN): $\delta = 8.92$ (2Hd, $J = 5.0$ Hz), 8.61 (2H, s), 8.54 (2H, d, $J = 8.2$ Hz), 8.20 (2H, td, $J = 7.9$, 1.5 Hz), 8.03 (2H, d, $J = 9.1$ Hz), 7.70-7.78 (2H, m), 7.22 (2H, d, $J = 8.8$ Hz), 3.93 (3H, s), 2.74 ppm (3H, s). ^{13}C NMR (101 MHz, CD_3CN): $\delta = 159.8$, 159.8, 155.5, 150.6, 143.8, 140.0, 131.0, 130.3, 129.4, 129.0, 125.1, 121.1, 56.4 ppm.

3) General procedure for $[Ru(tpy\text{-}ptz)(tpy\text{-}Ar)](PF_6)_2$ complexes (**D2**-**D4**)

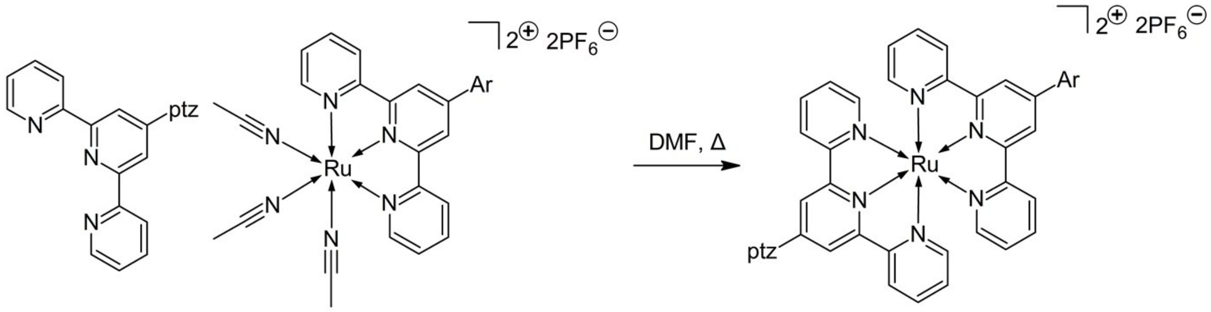

A microwave vial was charge with the respective $[Ru(MeCN)_3(tpy\text{-}Ar)](PF_6)_2$ (0.04 mmol), tpy-ptz (0.04 mmol) and DMF (10 mL). The vial was capped and degassed with nitrogen for 20 min and heated 96 °C for 2-3h. The red crude product was then precipitated in diethyl ether (20 mL) and centrifuged. The red solid was then washed with diethyl ether (5 mL). The crude product was then further purified by column chromatography (silica; MeCN/H_2O/satd. aq. KNO_3 solution; 40:4:1). An excess of NH_4PF_6 was added to the red fraction which was then concentrated *in vacuo*. When precipitation occurred the solution was added to water (30 mL). The formed precipitate was centrifuged and washed with water (2 × 20 mL). After drying *in vacuo* the complex was obtained as dark red powder.

D2: [Ru(tpy-ptz)(tpy-Ph)]$(PF_6)_2$ (16.3 mg, 39%)

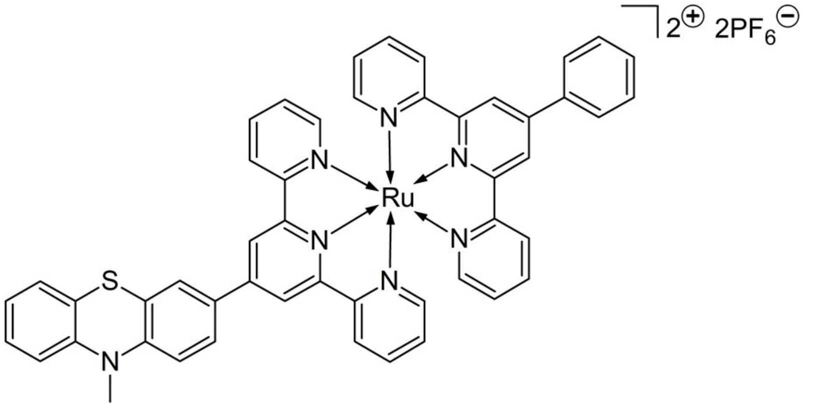

^{1}H NMR (400 MHz, CD_3CN): $\delta = 9.01$ (2H, s), 8.97 (2H, s), 8.64 (4H, d, $J = 7.9$ Hz), 8.17-8.24 (2H, m), 8.03-8.14 (2H, m), 7.94 (4H, td, $J = 7.9$, 1.5 Hz), 7.73-7.81 (2H, m), 7.65-7.72 (1H, m), 7.42 (4H, br d, $J = 5.6$ Hz), 7.28-7.36 (1H, m), 7.22-7.27 (2H, m), 7.13-7.21 (4H, m), 6.99-7.11 (2H, m), 3.52 ppm (3H, s). ^{13}C NMR (101 MHz, CD_3CN): $\delta = 159.4$, 159.3, 156.6, 156.4, 153.5, 153.5, 149.5, 149.4, 148.9, 148.1, 146.0, 139.1, 138.0, 131.5, 130.7, 129.2, 128.9, 128.5, 128.5, 128.3, 128.1, 126.8, 125.6, 125.6, 125.3, 124.3, 123.1, 122.8, 121.6, 116.2, 116.2, 36.3 ppm. Found C, 50.35; H, 3.01; N, 8.57; S, 2.44. Calc. for $C_{49}H_{35}F_{12}N_7P_2RuS$: C, 51.40; H, 3.08; N, 8.56; S, 2.80. HRMS (Micro-ESI pos) calcd. for $C_{49}H_{35}F_6N_7P^{96}RuS$ [M^+] = 994.1402.1549. Found 994.1392.

D3: [Ru(tpy-ptz)(tpy-PhMe)]$(PF_6)_2$ (20.0 mg, 14%)

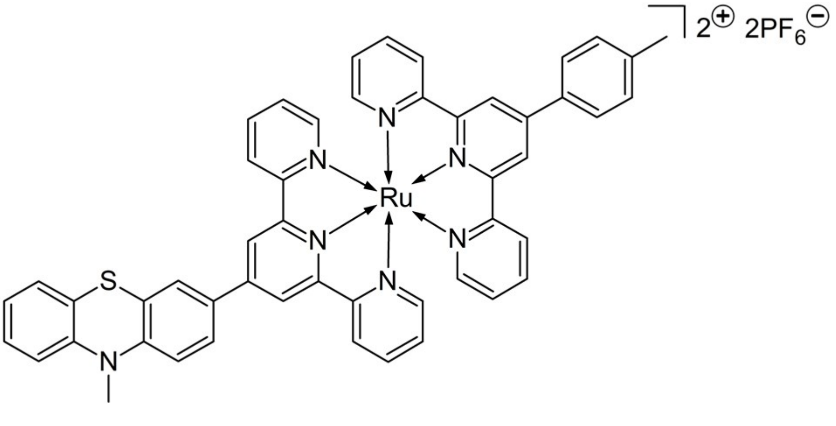

^{1}H NMR (400 MHz, CD_3CN): $\delta = 8.98$ (4H, d, $J = 8.5$ Hz), 8.64 (4H, d, $J = 8.2$ Hz), 8.02-8.15 (4H, m), 7.89-7.98 (4H, m), 7.58 (2H, d, $J = 8.2$ Hz), 7.39-7.47 (4H, m), 7.31 (1H, ddd, $J = 8.3$, 7.5, 1.5 Hz), 7.22-7.27 (2H, m), 7.17 (4H, ddd, $J = 7.3$, 5.8, 1.5 Hz), 7.01-7.11 (2H, m), 3.52 (3H, s), 2.54 ppm (3H, s). ^{13}C NMR (101 MHz, CD_3CN): $\delta = 159.4$, 159.3, 156.5, 156.4, 153.5, 153.5, 149.4, 149.3, 148.9, 148.0, 147.9, 146.0, 142.1, 139.0, 135.0, 131.5, 131.4, 129.2, 128.7, 128.5, 128.4, 128.3, 128.1, 126.8, 125.5, 125.3, 124.3, 123.0, 122.4, 121.6, 116.2, 116.1, 36.3, 21.5 ppm. Found C, 49.33.35; H, 3.36; N, 8.91; S, 2.40. Calc. for $C_{49}H_{35}F_{12}N_7P_2RuS{\bullet}H_2O{\bullet}MeCN$: C, 51.28; H, 3.48; N, 9.20; S, 2.63. HRMS (Micro-ESI pos) calcd. for $C_{50}H_{37}F_6$N7P^{96}RuS [M^+] = 1008.1549. Found 1008.1569.

D4: [Ru(tpy-ptz)(tpy-PhOMe)](PF_6)$_2$ (13.0 mg, 11%)

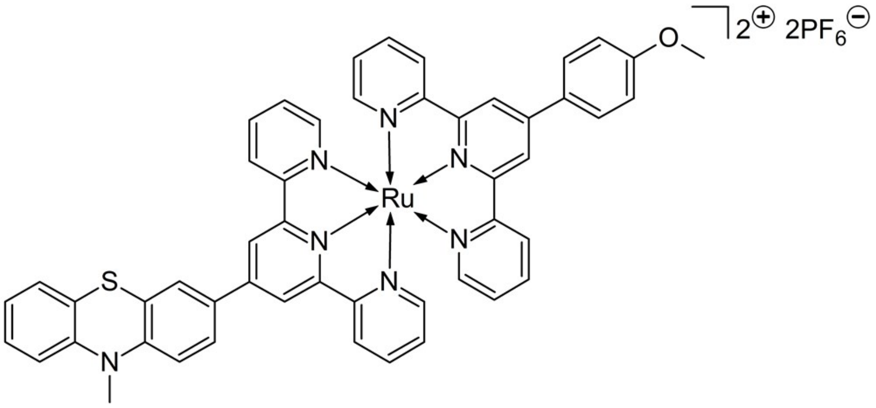

^{1}H NMR (400 MHz, CD_3CN): $\delta = 9.00$ (4H, s), 8.67 (4H, d, $J = 8.2$ Hz), 8.22 (2H, d, $J = 8.8$ Hz), 8.06-8.15 (2H, m), 7.96 (4H, t, $J = 7.7$ Hz), 7.44 (4H, t, $J = 5.6$ Hz), 7.30-7.37 (3H, m), 7.25-7.30 (2H, m), 7.16-7.23 (4H, m), 7.04-7.12 (2H, m), 4.00 (3H, s), 3.55 ppm (3H, s). ^{13}C NMR (101 MHz, CD_3CN): $\delta = 162.8$, 159.4, 156.5, 156.4, 156.4, 153.5, 149.0, 149.0, 148.9, 147.9, 146.0, 139.0, 131.5, 130.3, 129.9, 129.2, 128.5, 128.3, 128.1, 126.8, 125.5, 125.3, 124.3, 123.1, 122.0, 121.6, 116.2, 116.1, 116.1, 56.5, 36.3 ppm. HRMS (Micro-ESI pos) calcd. for $C_{50}H_{37}OF_6N_7P^{96}RuS$ [M^+] = 1024.1498. Found 1024.1501.

Relaxation scheme of dyads and triad upon excitation at 520 nm

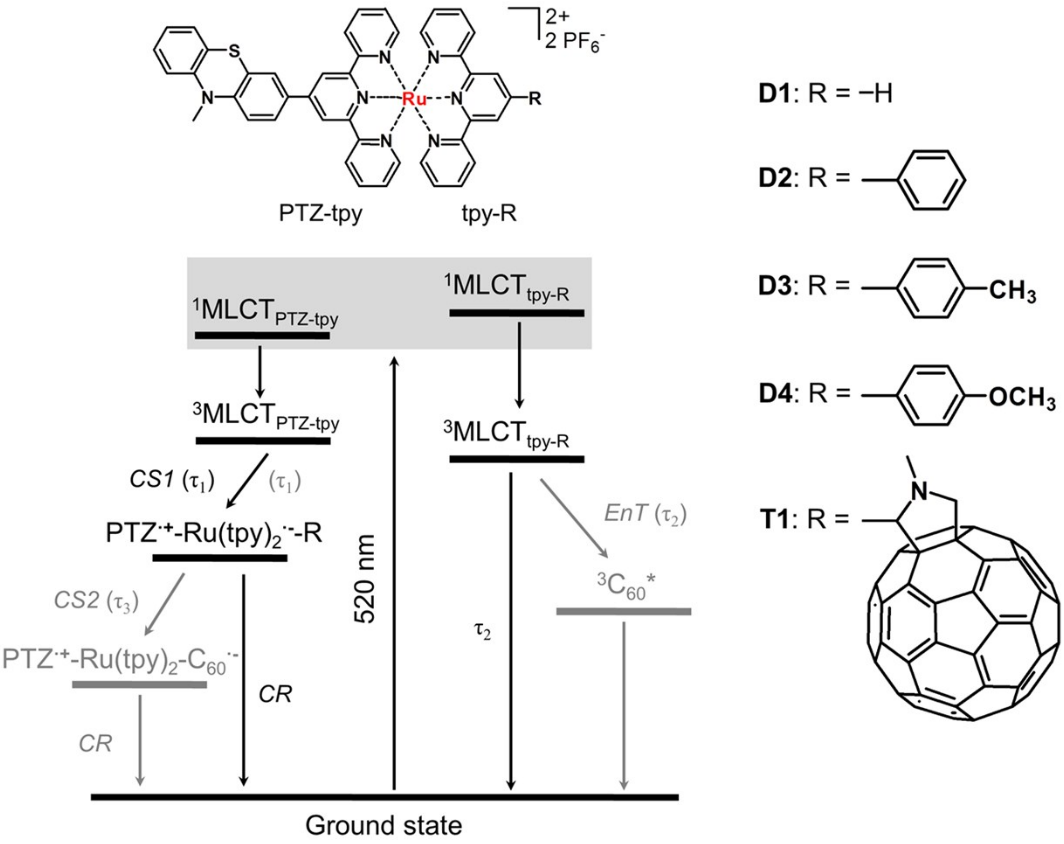

Figure S1. Relaxation processes for **D1-D4** and **T1** refer to the model proposed for **D1** and **T1** at room temperature.[3] Terpyridine (tpy) ligand connected with *N*-methylphenothiazine (PTZ) and other substituents are named as PTZ-tpy and tpy-R, respectively. Excitation of Ru(tpy)$_2$ photosensitizer generates two differently distributed MLCT states, *i.e.* MLCT$_{\text{PTZ-tpy}}$ and MLCT$_{\text{tpy-R}}$. The MLCT$_{\text{PTZ-tpy}}$ state decays *via* electron transfer (τ_1, left side) and the MLCT$_{\text{tpy-R}}$ state decays directly to ground state (τ_2, **D1-D4**, right side) or decays *via* energy transfer (τ_2, **T1**, right side, grey lines).

Temperature dependent fs TA data of **D1**

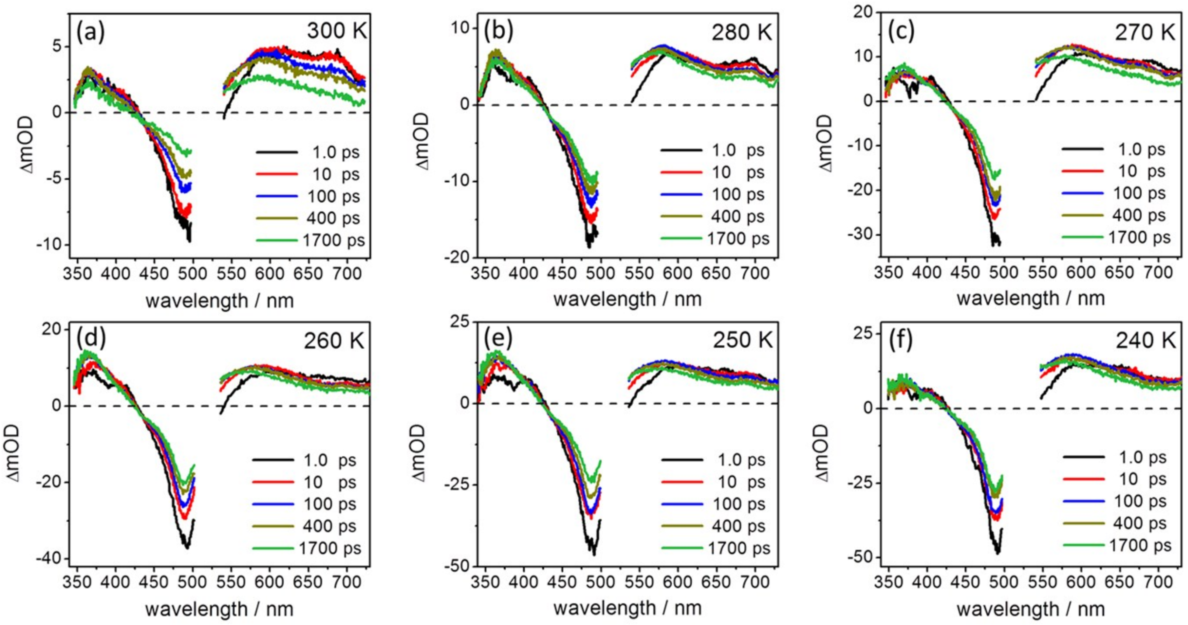

Figure S2. fs transient absorption spectra at selected delay times upon excitation at 520 nm in dichloromethane at temperature regions from 300 to 240 K.

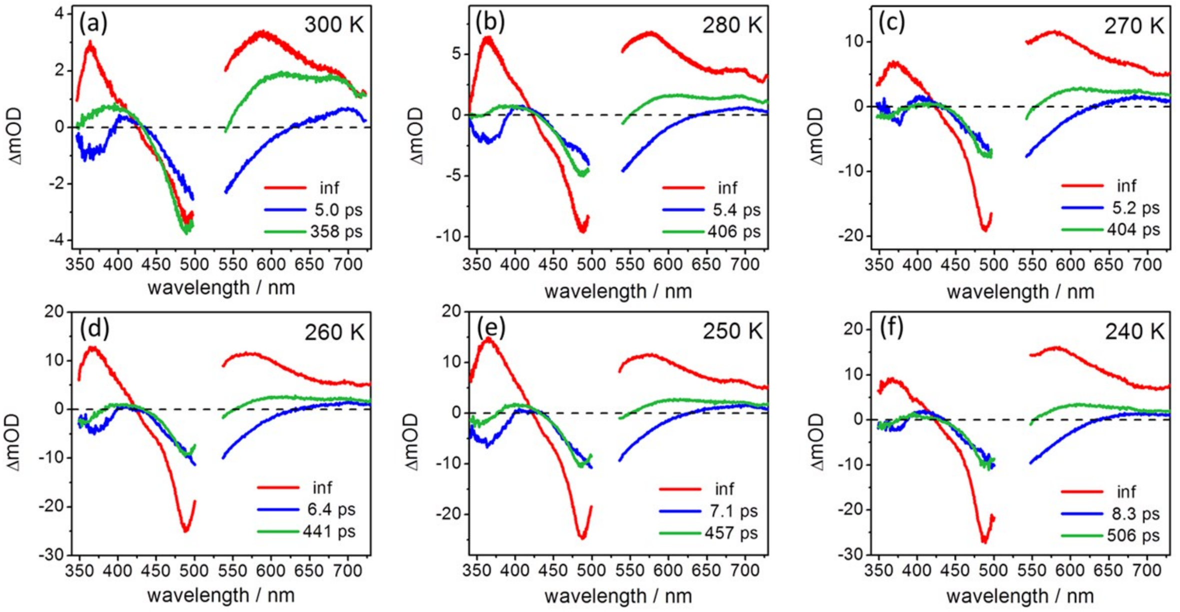

Figure S3. Decay-associated spectra resulting from the global fit of fs TA data upon excitation at 520 nm in dichloromethane.

Temperature dependent fs TA data of **D2**

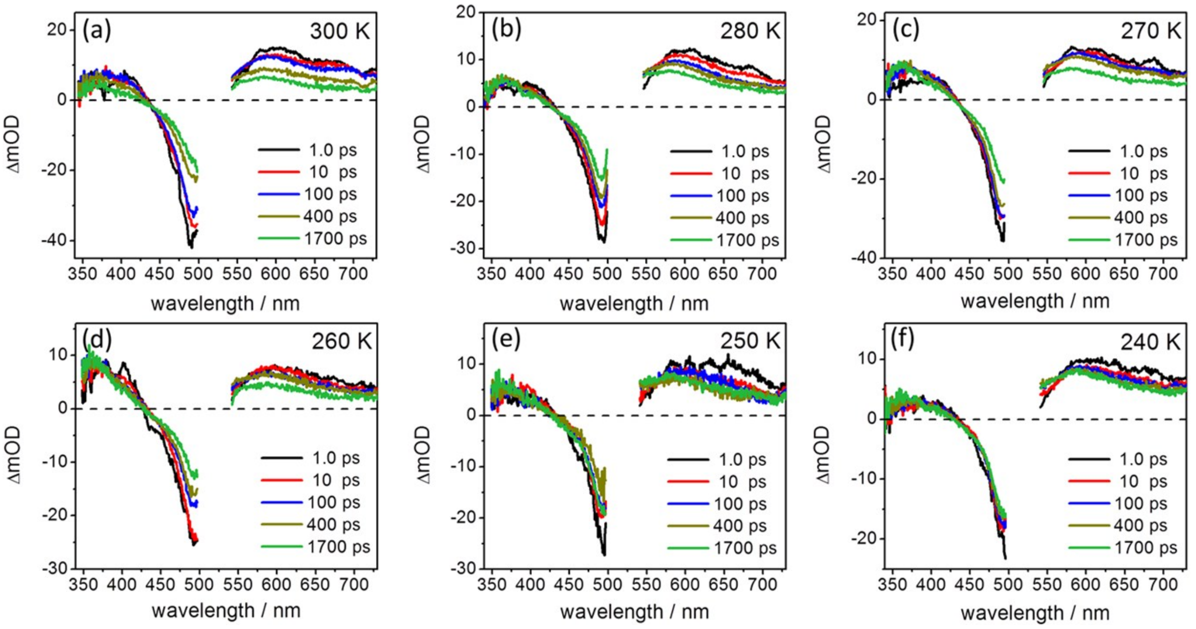

Figure S4. fs transient absorption spectra at selected delay times upon excitation at 520 nm in dichloromethane at temperature regions from 300 to 240 K.

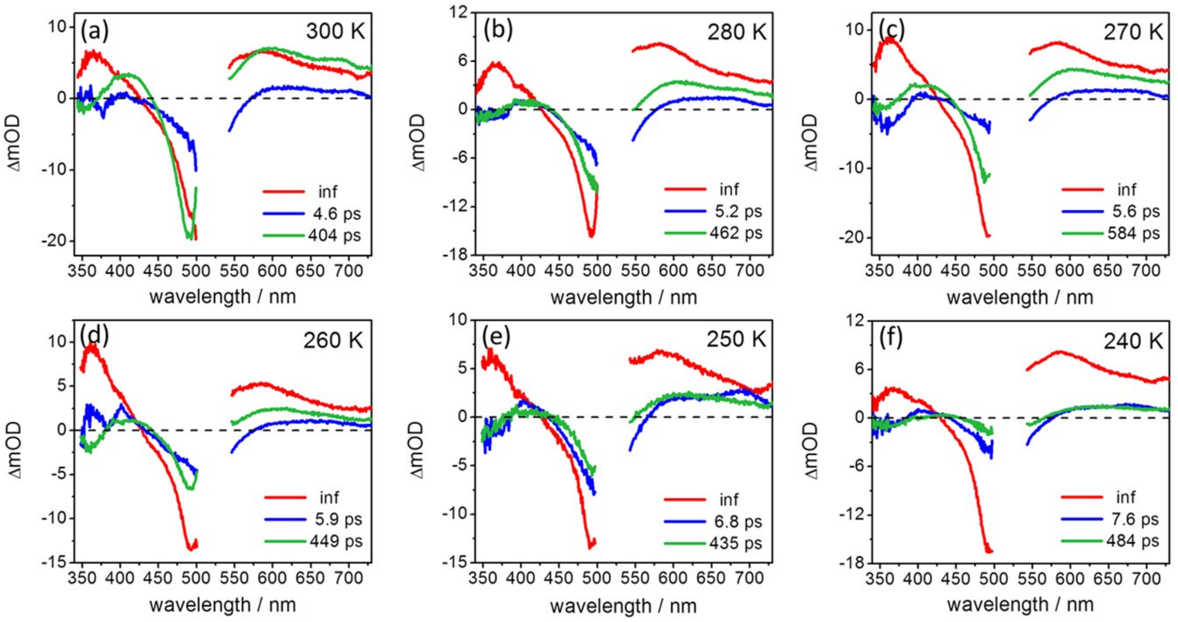

Figure S5. Decay-associated spectra resulting from the global fit of fs TA data upon excitation at 520 nm in dichloromethane.

Temperature dependent fs TA data of **D3**

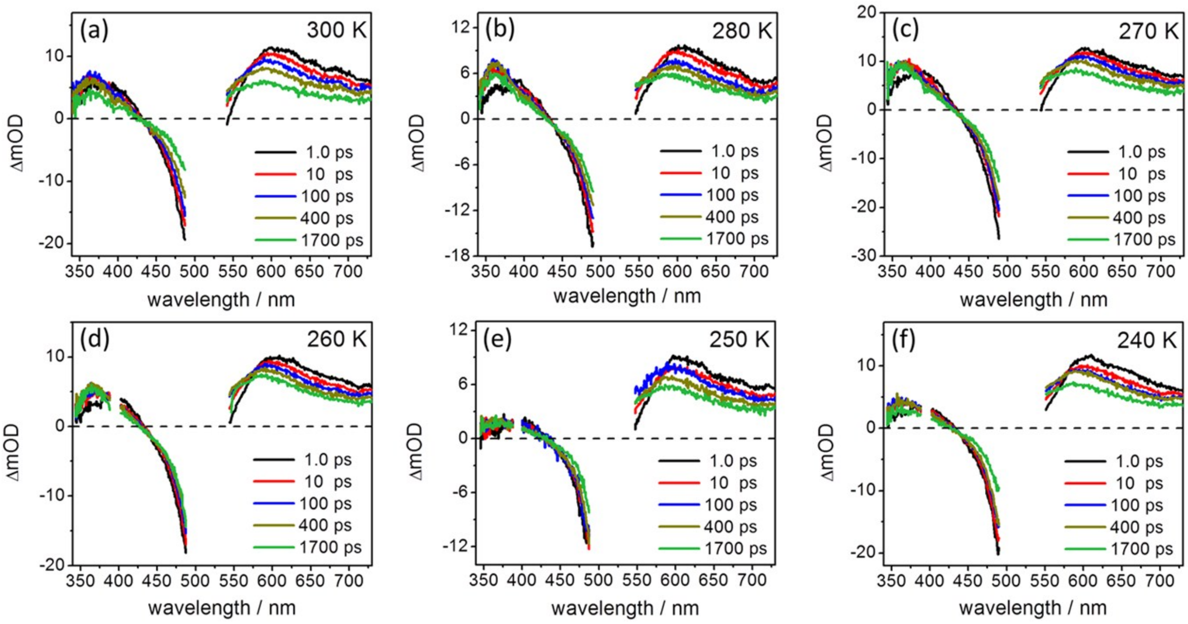

Figure S6. fs transient absorption spectra at selected delay times upon excitation at 520 nm in dichloromethane at temperature regions from 300 to 240 K.

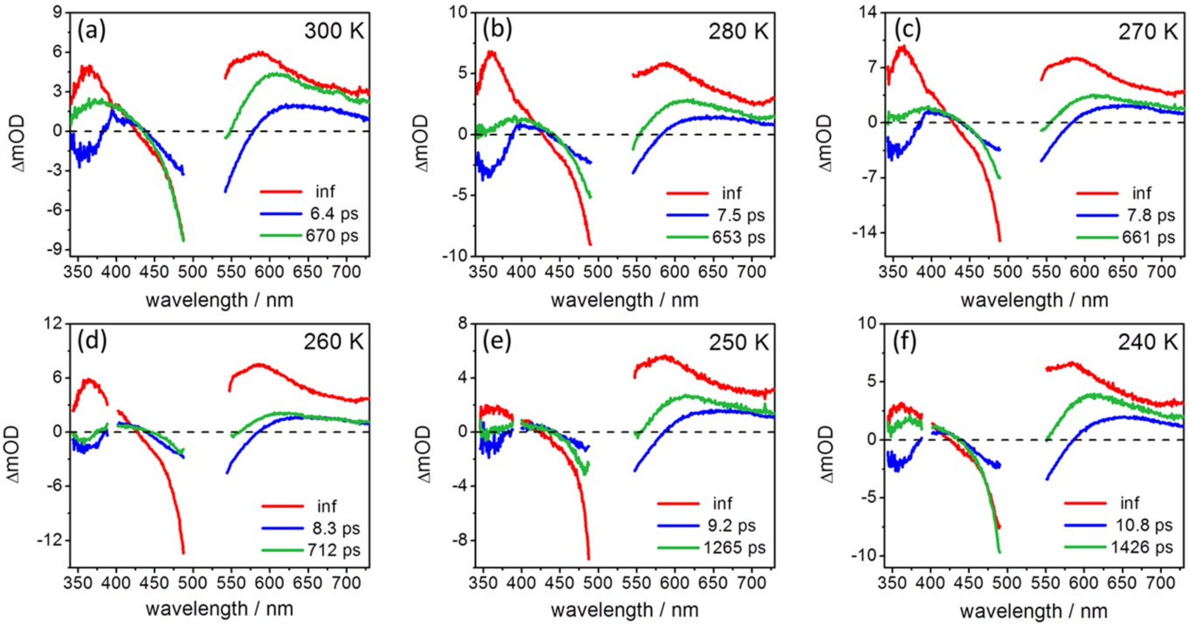

Figure S7. Decay-associated spectra resulting from the global fit of fs TA data upon excitation at 520 nm in dichloromethane.

Temperature dependent fs TA data of **D4**

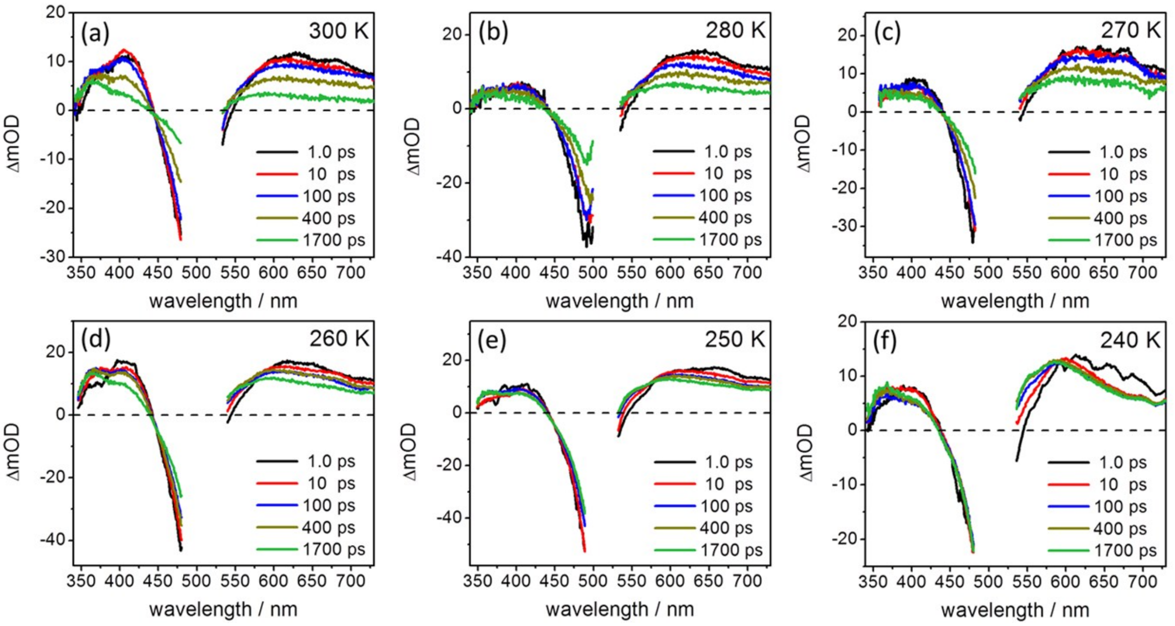

Figure S8. fs transient absorption spectra at selected delay times upon excitation at 520 nm in dichloromethane at temperature regions from 300 to 240 K.

It should be noted that the shape of the fs TA spectra at 240 K changes (*i.e.* 540 to 730 nm) compared to other data at higher temperatures. Meanwhile the corresponding DAS yields two kinetic components which are both faster than others (Figure S9f). The interpretation of the data at 240 K is complicated. Thus for the Marcus analysis the data point at 240 K for **D4** was omitted in the main text.

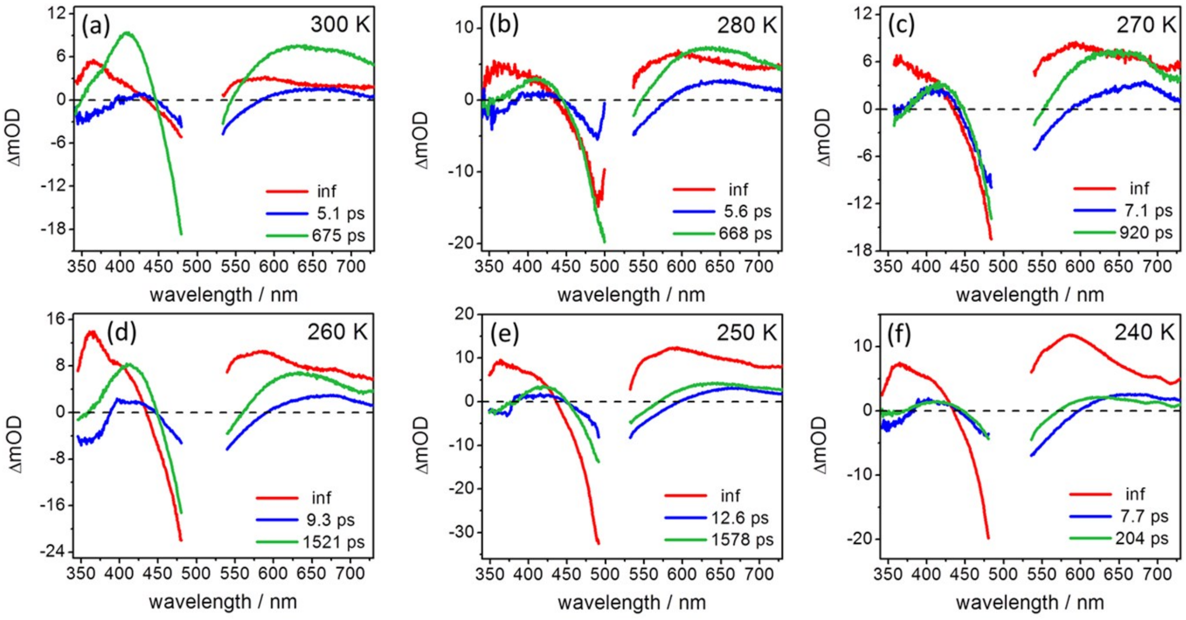

Figure S9. Decay-associated spectra resulting from the global fit of fs TA data upon excitation at 520 nm in dichloromethane.

Temperature dependent fs TA data of **T1**

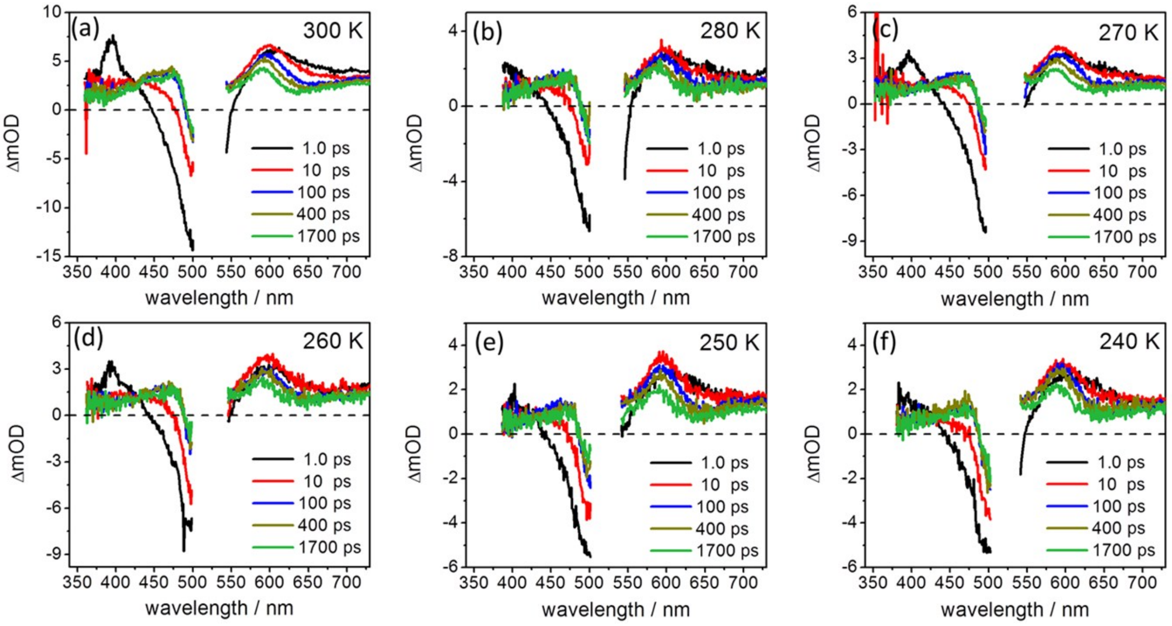

Figure S10. fs transient absorption spectra at selected delay times upon excitation at 520 nm in dichloromethane at temperature regions from 300 to 240 K.

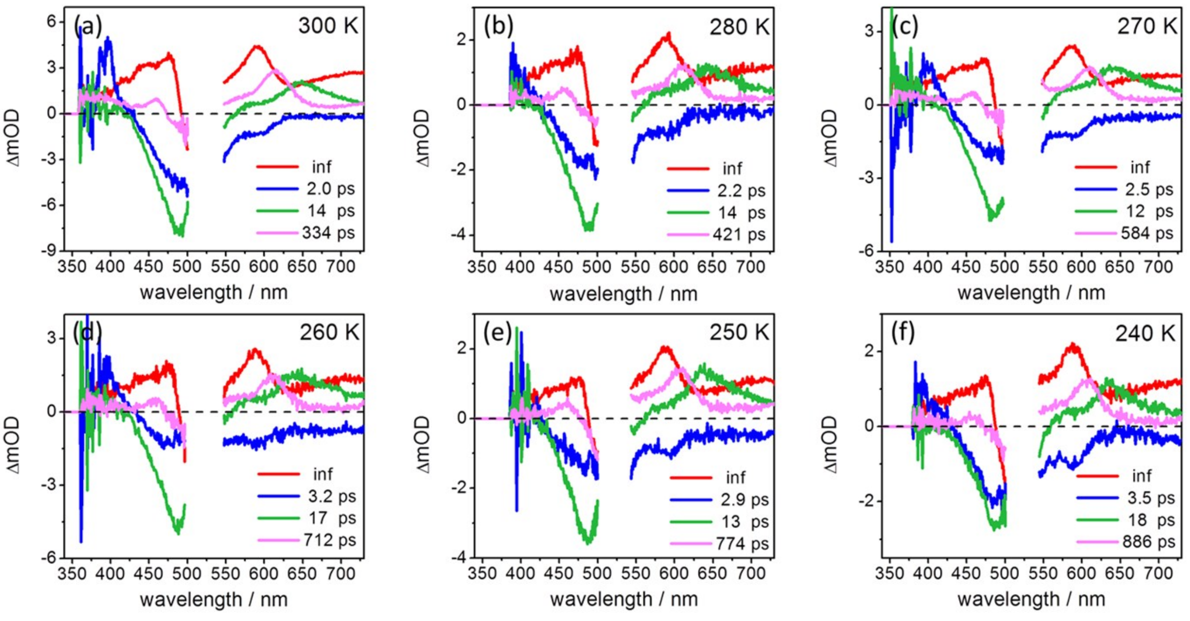

Figure S11. Decay-associated spectra resulting from the global fit of fs TA data upon excitation at 520 nm in dichloromethane.

Summary of the time constants for electron transfer

Table S1. Temperature dependence of the time constants (in ps) for the PTZ→Ru(tpy)$_2^*$ electron transfer process in **D1**–**D4** and **T1** obtained from the global fit of fs TA data.

T / K	**D1**	**D2**	**D3**	**D4**	**T1**
300	5.0	4.6	6.4	5.1	2.0
280	5.4	5.2	7.5	5.6	2.2
270	5.2	5.6	7.8	7.1	2.5
260	6.4	5.9	8.3	9.3	3.2
250	7.1	6.8	9.2	12.6	2.9
240	8.3	7.6	10.8	–	3.5

Estimation of reorganization energy and the temperature dependence

$$\lambda = \lambda_i + \lambda_o \qquad (1)$$

$$\lambda_o = \frac{e^2}{4 \cdot \pi \cdot \varepsilon_0} \cdot \left(\frac{1}{2a_1} + \frac{1}{2a_2} - \frac{1}{R_{DA}}\right) \cdot \left(\frac{1}{n^2} - \frac{1}{\varepsilon_s}\right) \qquad (2)$$

where λ_i and λ_o represent the inner and outer reorganization energy, respectively.[4] λ_i reflects the free energy change associated with the nuclear bond length changes within molecules and λ_o accounts for the reorganization of the surrounding chemical environment, *e.g.* solvent molecules. In the simplest model, electron donor and acceptor are treated as spheres with radii a_1 and a_2 (for more accurate prediction, electron donor and electron acceptor should be treated as ellipsoids).[5] R_{DA} is the donor-acceptor distance. n and ε_s represent refractive index and dielectric constant of the solvent involved during charge transfer, respectively. ε_0 is the vacuum permittivity (8.85×10^{-12} F/m).

For the PTZ-Ru(tpy)$_2$-R system:

1. λ_i is estimated to be 0.1 eV[5,6] and commonly treated as distance[5] and temperature[7,8] independent.

2. Both n and ε_s are temperature dependent, $\varepsilon_s(T) = a + bT + cT^2 + dT^3$, for dichloromethane, $a = 0.40452\times10^2$, $b = -0.17748\times10^0$, $c = 0.23942\times10^{-3}$, $d = 0$;[9]

For dichloromethane, $n(T) = 1.59078 - 5.66\times10^{-4}$ T.[10]

3. For PTZ→Ru(tpy)$_2^*$ electron transfer, PTZ and photo-excited Ru complex are the electron donor (a_1 = 4 Å) and acceptor (a_2 = 5 Å), respectively. The center-to-center distance R_{DA} is 9.6 Å. a_1, a_2 and R_{DA} were estimated from the neutral, optimized molecular structures.[2,11]

As a result, the calculated reorganization energy associated with PTZ→Ru(tpy)$_2^*$ electron transfer as a function of temperature for **D1** and **T1** were summarized in Table S3-4. Only **D1** and **T1** were exemplarily calculated since all compounds have the same electron donor, donor-acceptor distance and chemical linkage.

Estimation of driving forces and the temperature dependence

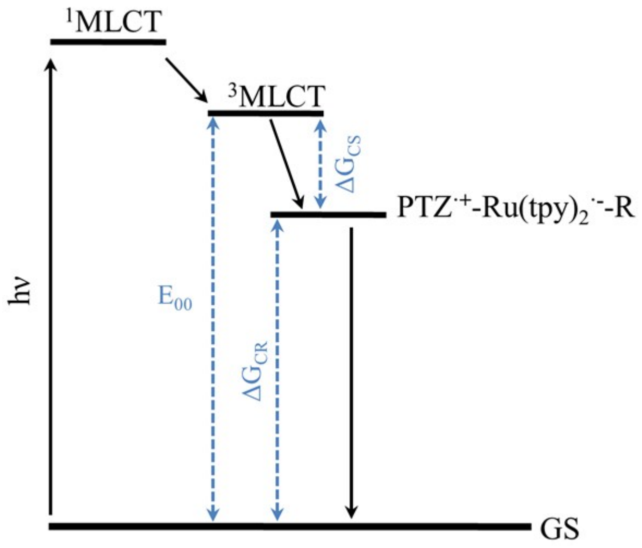

For PTZ→Ru(tpy)$_2$* electron transfer, the radical pairs are PTZ$^{\cdot +}$ / tpy$^{\cdot -}$. E_{00} in Rehm-Weller equation is the energy difference between the excited state (where the electron transfer takes place) and ground state. In our system, as indicated in the relaxation model (see Figure S1) electron transfer occurs from an upper-lying ^{3}MLCT state. Since different ^{3}MLCT states are relatively close in energy, E_{00} is taken to be 2.07 eV which was estimated from the emission spectrum of [Ru(tpy)$_2$](PF$_6$)$_2$ at 77 K (in butyronitrile glass).[12] The Gibbs free energy change of a photoinduced electron transfer process can be estimated by:

$$\Delta G^{\circ}_{CS} = e\,(E_{D^{+}/D} - E_{A/A^{-}}) - E_{00} - \frac{e^2}{4\pi\varepsilon_0\varepsilon R_{DA}} \qquad (3)$$

$$\Delta G^{\circ}_{CR} = -\,\Delta G^{\circ}_{CS} - E_{00} \qquad (4)$$

The values of $E_{PTZ+/PTZ}$ and $E_{tpy/tpy-}$ in **D1** and **T1** were taken from ref 2. For **D2**-**D4** cyclic voltammetry was performed (Figure S12 and Table S2). The influence of temperature on ΔG°_{CS} value is also considered (see Table S3-4).

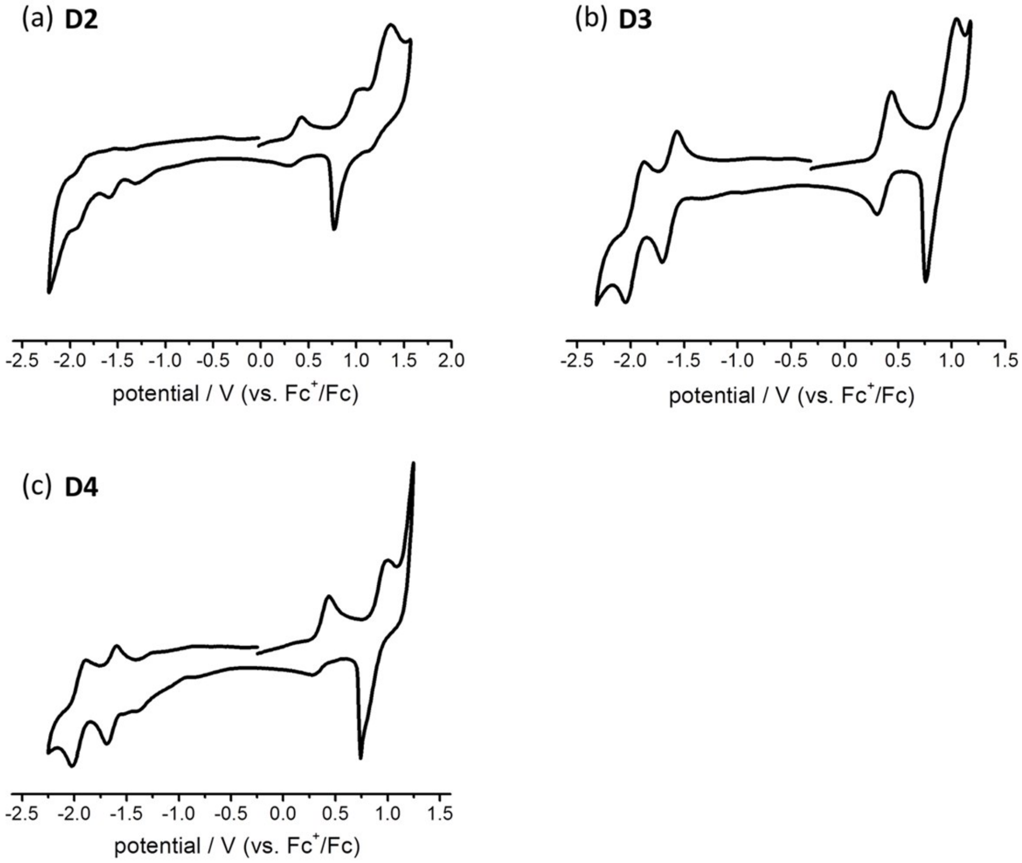

Figure S12. Cyclic voltammetry curves (scan rate 200 mV/s) for **D2**-**D4** in dichloromethane with 0.1 M Bu_4NPF_6 supporting electrolyte.

Table S2. Summary of electrochemical data for **D1**-**D4** and **T1** recorded in dichloromethane with 0.1 M Bu_4NPF_6 supporting electrolyte.

	E^o / V (vs. $Fc^{\cdot+}$/Fc)		
	$PTZ^{\cdot+}$ / PTZ	Ru^{III} / Ru^{II}	tpy / $tpy^{\cdot-}$
D1[a]	0.35	0.87	-1.60
D2	0.35	0.87	-1.63
D3	0.37	0.90	-1.62
D4	0.36	0.86	-1.64
T1[a]	0.34	0.99	-1.67

[a] Electrochemical data were taken from ref 2.

Summary of calculations for PTZ→Ru(tpy)$_2^*$ electron transfer

Table S3. Summary of the calculated temperature dependent dielectric constant (ε) and refractive index (n) of dichloromethane as well as reorganization energy (λ), driving force (–ΔG°) for charge separation, activation energy (ΔG‡) in **D1**.

T / K	ε	n	λ	–ΔG° / eV	ΔG‡ / eV[a]
300	8.7558	1.4210	0.763	0.291	0.073
280	9.5281	1.4323	0.766	0.277	0.078
260	10.4920	1.4436	0.769	0.263	0.083
240	11.6474	1.4549	0.773	0.249	0.089

Table S4. Summary of the calculated temperature dependent dielectric constant (ε) and refractive index (n) of dichloromethane as well as reorganization energy (λ), driving force (–ΔG°) for charge separation, activation energy (ΔG‡) in **T1**.

T / K	ε	n	λ	–ΔG° / eV	ΔG‡ / eV[a]
300	8.7558	1.4210	0.763	0.231	0.093
280	9.5281	1.4323	0.766	0.217	0.098
260	10.4920	1.4436	0.769	0.203	0.104
240	11.6474	1.4549	0.773	0.189	0.110

[a] Activation energy was obtained by $(\lambda+\Delta G°)^2/4\lambda$.[13,14]

The influence of temperature on solvent dielectric properties, *i.e.* dielectric constant ε and refractive index n, which may change λ (eq S1-2) and –ΔG° (eq S3-4), is considered in this work. It should be noted that the single linear relation indicated by the reformed Marcus equation in the main text can really be expected when both λ and the term $(\lambda+\Delta G°)^2/4\lambda$ (*i.e.* activation energy, ΔG‡) are temperature independent.[13,14] Otherwise, deviation from single linear regression would be observed because of the impact of temperature on solvent dielectric properties.[13,14] According to Table S3-4, λ and ΔG‡ are apparently insensitive to temperature variation which show relative small changes of 0.010 and 0.017 eV, respectively. Hence, we conclude that the solvent itself would not cause significant deviations due to temperature change.

Molecular structure of the reference compounds

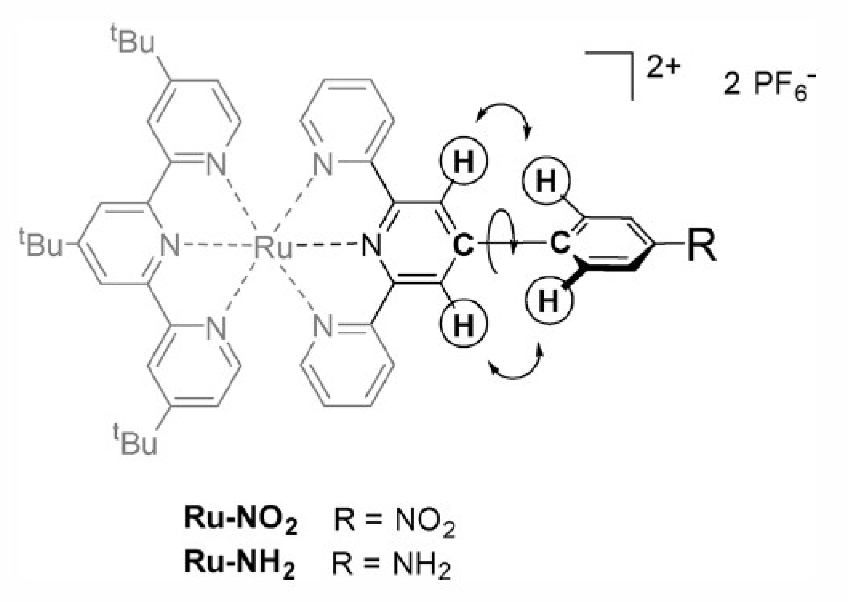

Figure S13. Molecular structure of the functionalized Ru(tpy)$_2$ complexes with a strongly electron donating substituent –NH$_2$ and a strongly electron withdrawing substituent –NO$_2$ referred in the main text.[15,16]

NMR spectra of **D2**

^{1}H NMR (400 MHz, CD_3CN)

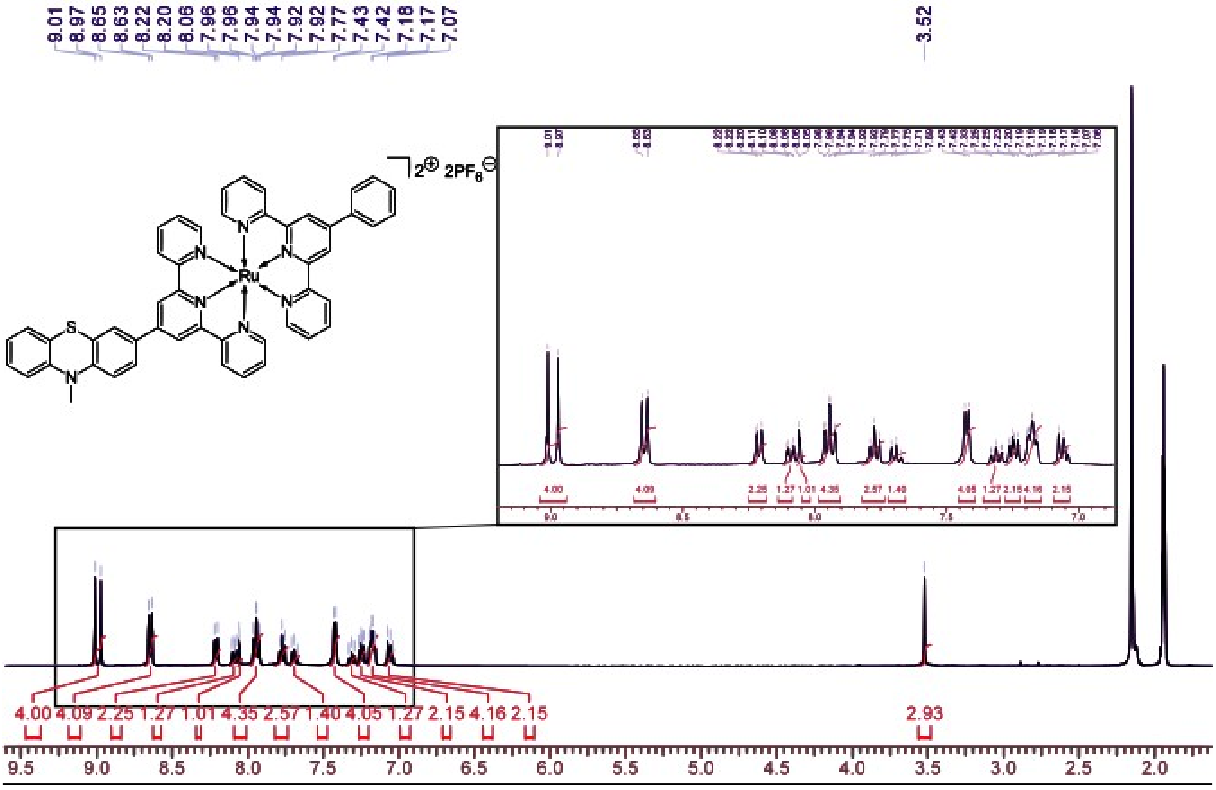

^{13}C NMR (101 MHz, CD_3CN)

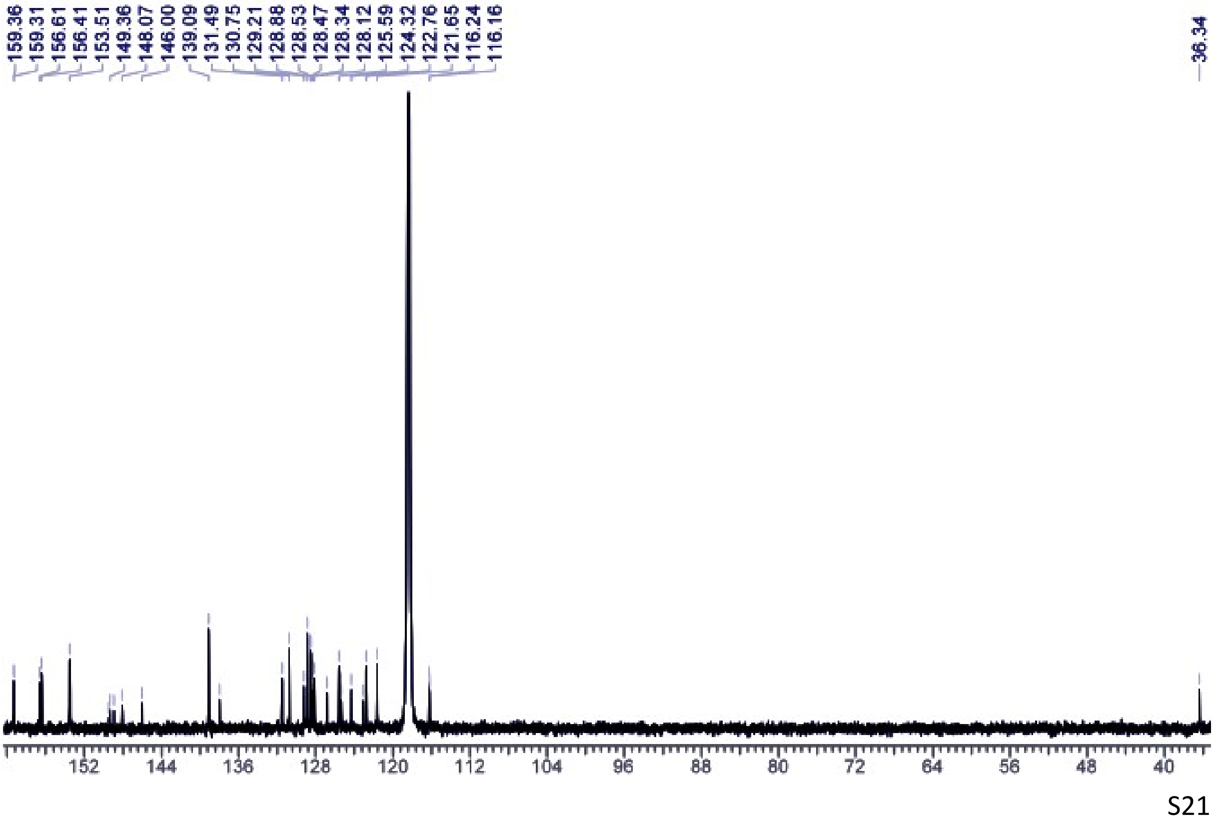

NMR spectra of **D3**

^1H NMR (400 MHz, CD_3CN)

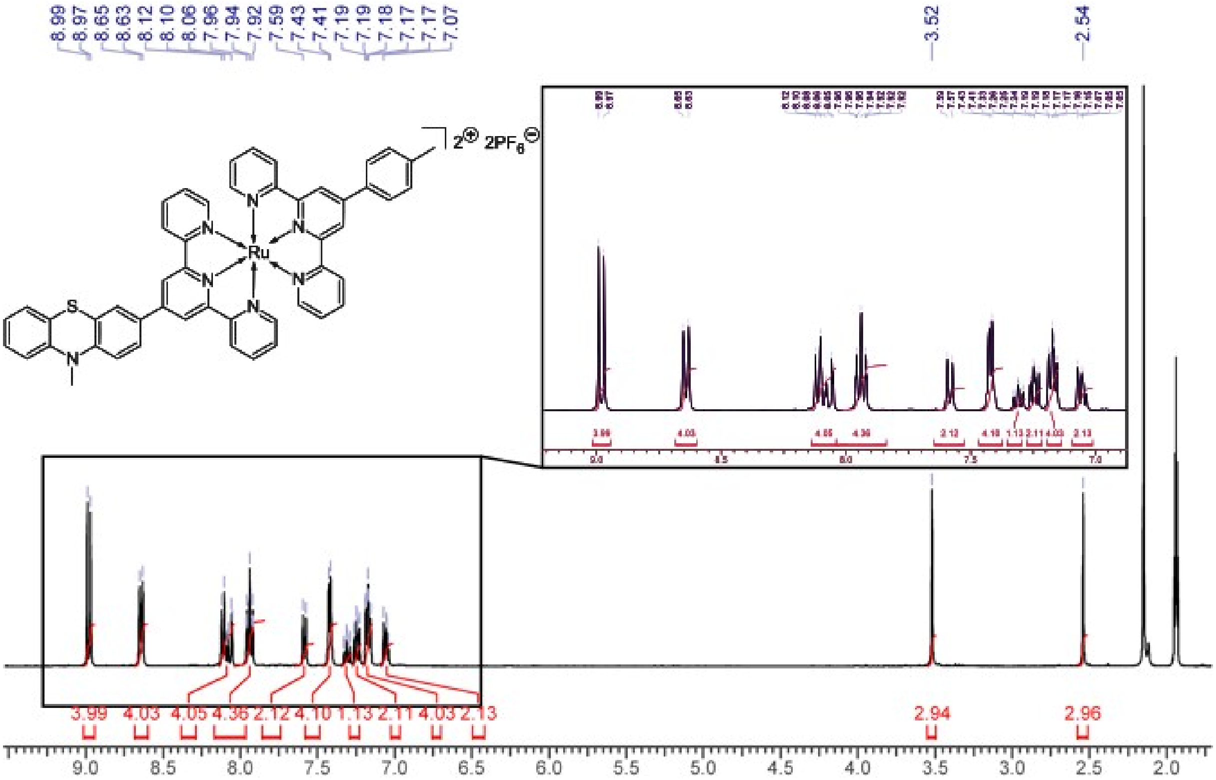

^{13}C NMR (101 MHz, CD_3CN)

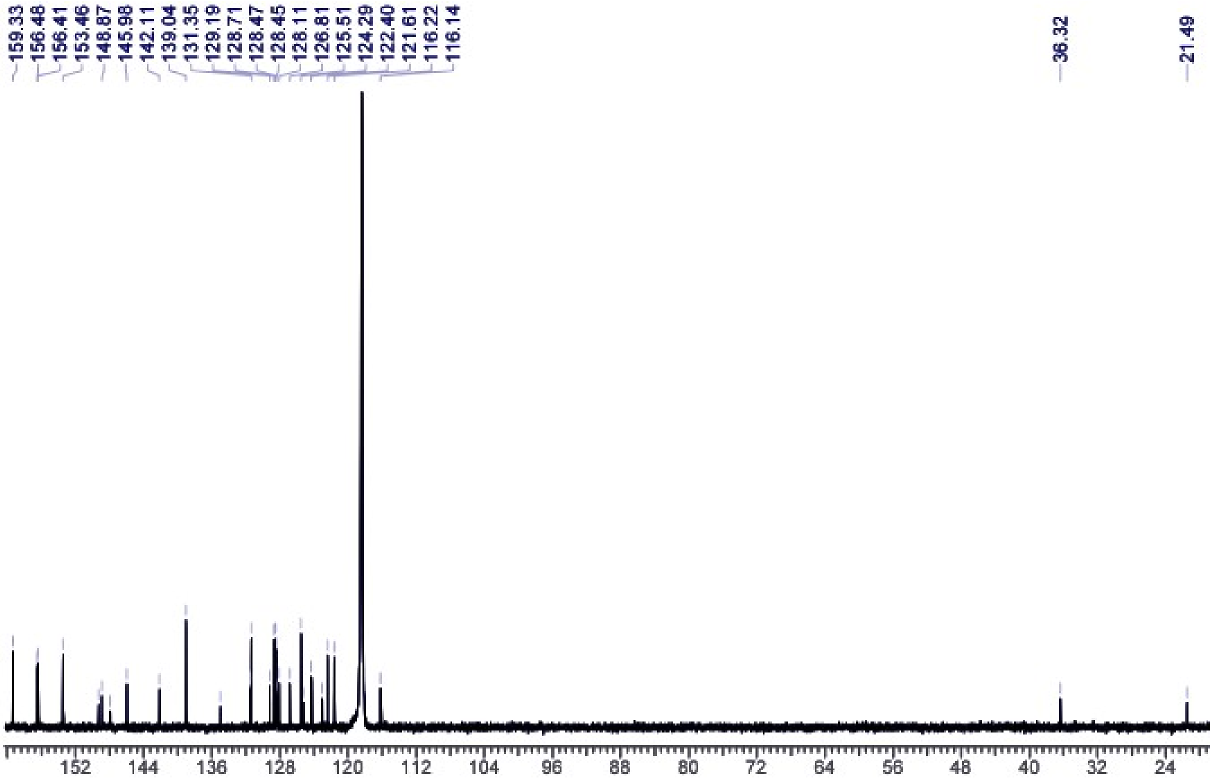

NMR spectra of **D4**

^{1}H NMR (400 MHz, CD$_3$CN)

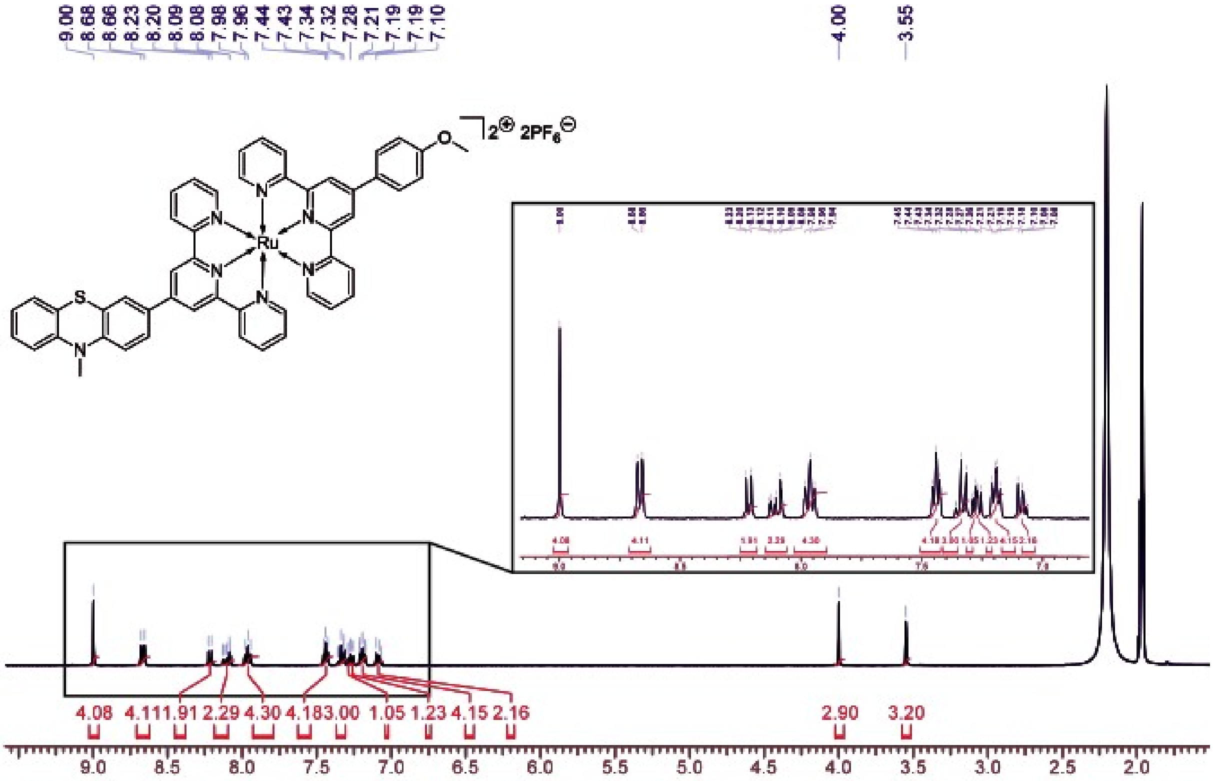

^{13}C NMR (101 MHz, CD$_3$CN)

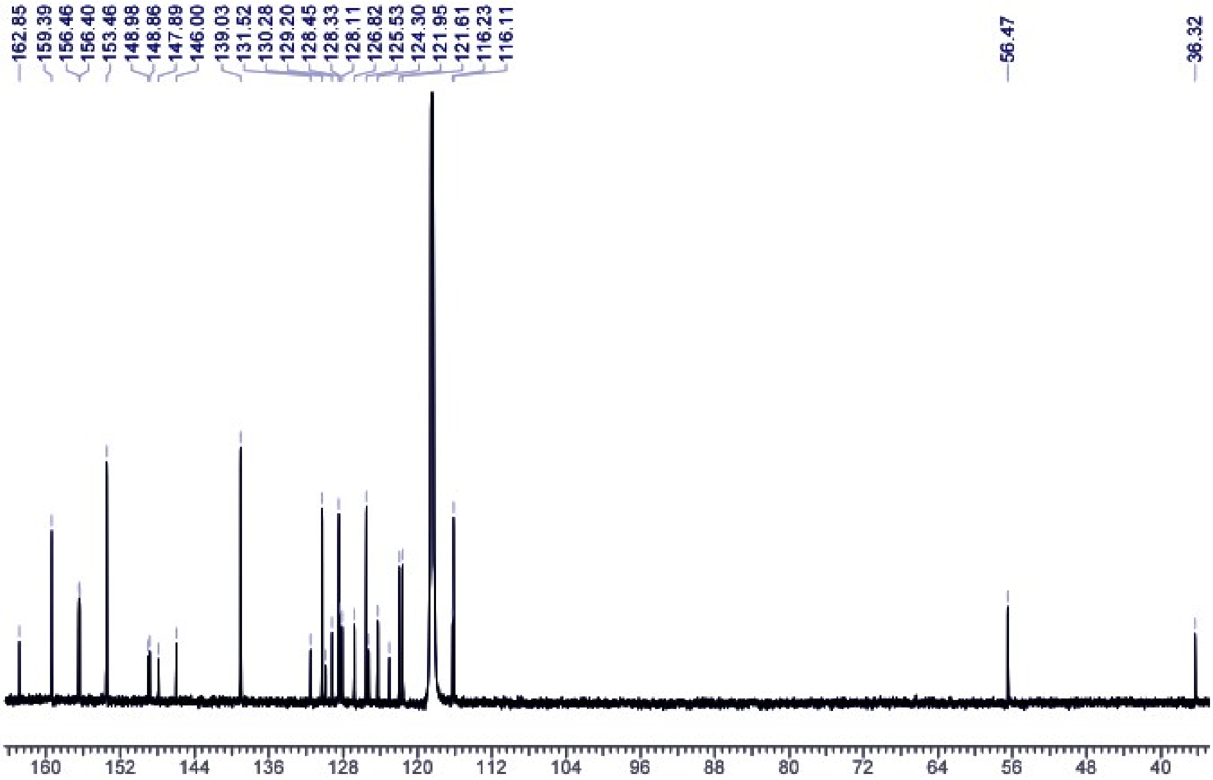

REFERENCES

1. K. Barthelmes, J. Kübel, A. Winter, M. Wächtler, C. Friebe, B. Dietzek and U. S. Schubert, *Inorg. Chem.*, 2015, **54**, 3159−3171.

2. K. Barthelmes, A. Winter and U. S. Schubert, *Eur. J. Inorg. Chem.*, 2016, **2016**, 5132–5142.

3. Y. Luo, K. Barthelmes, M. Wächtler, A. Winter, U. S. Schubert and B. Dietzek, *Chem. Eur. J.*, 2017, **23**, 4917–4922.

4. R. A. Marcus and N. Sutin, *Biochim. Biophys. Acta*, 1985, **811**, 265–322.

5. M. Kuss-Petermann and O. S. Wenger, *Phys. Chem. Chem. Phys.*, 2016, **18**, 18657–18664.

6. E. Göransson, J. Boixel, J. Fortage, D. Jacquemin, H.-C. Becker, E. Blart, L. Hammarström and F. Odobel, *Inorg. Chem.*, 2012, **51**, 11500−11512.

7. J. Kroon, H. Oevering, J. W. Verhoeven, J. M. Warman, A. M. Oliver and M. N. Paddon-Row, *J. Phys. Chem.*, 1993, **97**, 5065–5069.

8. P. Vath, M. B. Zimmt, D. V. Matyushov and G. A. Voth, *J. Phys. Chem. B*, 1999, **103**, 9130–9140.

9. D. R. Lide, *Handbook of Chemistry and Physics*, 84th edition.

10. H. Shekaari, A. Bezaatpour and A. Soltanpour, *J. Chem. Eng. Data*, 2010, **55**, 5927–5931.

11. Y. Luo, K. Barthelmes, M. Wächtler, A. Winter, U. S. Schubert and B. Dietzek, *J. Phys. Chem. C*, 2017, **121**, 9220–9229.

12. J.-P. Sauvage, J.-P. Collin, J.-C. Chambron, S. Guillerez, C. Coudret, V. Baltani, F. Barigelletti, L. D. Cola and L. Flamigni, *Chem. Rev.*, 1994, **94**, 993–1019.

13. J. Kroon, H. Oevering, J. W. Verhoeven, J. M. Warman, A. M. Oliver and M. N. Paddon-Row, *J. Phys. Chem.*, 1993, **97**, 5065–5069.

14. R. H. Goldsmith, O. DeLeon, T. M. Wilson, D. Finkelstein-Shapiro, M. A. Ratner and M. R. Wasielewski, *J. Phys. Chem. A*, 2008, **112**, 4410–4414.

15. M. Presselt, B. Dietzek, M. Schmitt, S. Rau, A. Winter, M. Jäger, U. S. Schubert and J. Popp, *J. Phys. Chem. A*, 2010, **114**, 13163–13174.

16. J. Preiß, M. Jäger, S. Rau, B. Dietzek, J. Popp, T. Martínez and M. Presselt, *ChemPhysChem*, 2015, **16**, 1395–1404.